

COALESCENCE OF BLACK-HOLE BINARIES: FROM
THEORETICAL SOURCE MODELS TO APPLICATIONS
IN GRAVITATIONAL-WAVE ASTRONOMY

DISSERTATION

ZUR ERLANGUNG DES AKADEMISCHEN GRADES
DOKTOR DER NATURWISSENSCHAFTEN
(DR. RER. NAT.)
IN DER WISSENSCHAFTSDISZIPLIN PHYSIK

EINGEREICHT AN DER
MATHEMATISCH-NATURWISSENSCHAFTLICHEN FAKULTÄT
DER UNIVERSITÄT POTSDAM



✱

VON

LUCÍA SANTAMARÍA LARA

GEBOREN AM 23. JULI 1982 IN BURGOS, SPANIEN

POTSDAM, APRIL 2010

Lucía Santamaría Lara

Coalescence of Black-Hole Binaries: from Theoretical Source Models to Applications in Gravitational-Wave Astronomy © April 2010

BETREUER:

Prof. Bernard F. Schutz

SUPERVISOREN:

Dr. Badri Krishnan

Dr. Sascha Husa

GUTACHTER:

Dr. Alberto Vecchio

Asst. Prof. Laura Cadonati

Dr. Chris van den Broeck

INSTITUT:

Max-Planck-Institut für Gravitationsphysik (Albert-Einstein-Institut)

FAKULTÄT:

Mathematisch-Naturwissenschaften Fakultät, Universität Potsdam

Sigue, sigue adelante y no regreses
Fiel hasta el fin del camino y tu vida
No echas de menos un destino más fácil
Tus pies sobre la tierra antes no hollada
Tus ojos frente a lo antes nunca visto

— Luis Cernuda

ABSTRACT

To date, gravitational waves have not yet been observed directly, but strong evidence supports their existence. With current ground-based interferometers operating at their design sensitivity, their upgraded versions approved to be commissioned within the next five years and a space-based antenna in design stages, the need for optimal data analysis strategies becomes pressing. Signals coming from binary systems of compact objects, such as neutron stars and black holes, are expected to stand among the most promising candidates for the first detection of gravitational waves.

This work focuses on improving existing detection techniques for gravitational-wave signals from binaries of black holes. The current post-Newtonian approach is valid until the compact objects become so close to each other that the weak-field approximation to general relativity breaks down. At that point, one needs to resort to full numerical relativity methods in order to solve Einstein's equations. It was only recently that the field succeeded in providing stable solutions and in extracting the gravitational radiation associated to the merger of the binary. Ever since, an increasing number of simulations exploring larger parts of the parameter space have become available.

This dissertation presents a new waveform model to describe the gravitational radiation of the full coalescence of a binary of black holes, from the initial inspiral phase through the merger until the final ringdown to a stationary black hole. Analytical and numerical approaches to the binary black-hole problem are brought together to present a joint description of the coalescence process. The parameter space that our model covers corresponds to that of comparable-mass, spinning, non-precessing binaries. The inclusion of these waveforms as filters in current searches for gravitational waves with ground-based detectors will have an immediate impact in their performance. On one hand, the extension of the waveforms past the post-Newtonian stage would allow more massive systems to be surveyed. On the other hand, the spin of the black-hole system affects its detectability, in a way that can now be quantified.

Further related work contained in this dissertation presents the latest searches for compact binaries in the output of the first-generation ground-based detectors; in addition, we describe the results of a search for numerical relativity signals incorporated into Gaussian data as a way of assessing the performance of current data analysis search strategies; finally, the potential detection and characterization of black-hole binaries with total mass between hundreds and tens of thousands of solar masses is suggested, which could be possible with future-generation interferometers.

The main focus of this dissertation is thus the connection between theoretical solutions of the binary black-hole problem and their direct application in gravitational-wave data analysis and astrophysics.

ZUSAMMENFASSUNG

Bisher wurden Gravitationswellen (GW) noch nicht direkt nachgewiesen, doch gibt es starke Indizien, die auf ihre Existenz hindeuten. Durch die bereits mit hoher Detektorempfindlichkeit arbeitenden Interferometer, deren bereits genehmigten verbesserten Ausbaustufen und das geplante LISA-Projekt, steigt die Notwendigkeit für entsprechende Strategien zur Datenanalyse. Signale von Binärsystemen kompakter Objekte (Neutronensterne und Schwarze Löcher) sind die aussichtsreichsten Kandidaten für den ersten Nachweis von GW.

Diese Arbeit konzentriert sich auf die Verbesserung existierender Detektortechniken für Signale von GW binärer Schwarzer Löcher. Der gegenwärtige post-Newtonsche Ansatz gilt nur bis sich die kompakten Objekte soweit annähern, dass die Schwachfeldnäherung der ART zusammenbricht. An diesem Punkt muss man vollständige numerische Methoden anwenden, um die Einstein-Gleichungen zu lösen. Erst vor kurzem gelang es hier, stabile Lösungen anzubieten und die Gravitationsstrahlung aus der Verschmelzung des Binärsystems zu definieren. Seitdem wurden mehrere Simulationen, die einen größeren Teil des Parameterraums untersuchen, veröffentlicht.

Diese Dissertation stellt ein neues Modell zur Beschreibung der GW einer vollständigen Verschmelzung zweier Schwarzer Löcher vor, von der frühen Annäherungsphase auf einer Spiralbahn, über die Vereinigung, bis zur Phase des Abklingens und der Entstehung eines einzelnen stationären Schwarzen Lochs. Analytische und numerische Ansätze für das Problem binärer Schwarzer Löcher werden zusammengebracht, um eine gemeinsame Beschreibung des Verschmelzungsprozesses zu präsentieren. Der Parameterraum, den unser Modell umfasst, korrespondiert mit dem vergleichbar schwerer, rotierender Binärsysteme ohne Präzession. Die Einbindung dieser Wellenformen als Filter in die derzeitige Suche nach GW wird einen unmittelbaren Einfluss auf deren Ergebnis haben. Zum einen würde es die Erweiterung der Wellenform über die post-Newtonsche Stufe hinaus erlauben, weitaus schwerere Systeme zu beobachten. Zum anderen beeinflusst der Spin die Nachweisbarkeit in einer Art und Weise, die nun quantitativ bestimmt werden kann.

Ein weiterer, damit zusammenhängender Teil dieser Dissertation beschäftigt sich mit der Suche nach Binärsystemen in den Ergebnissen der terrestrischen Detektoren. Zusätzlich beschreiben wir eine Suche nach numerischen Signalen als eine Methode, die Leistungsfähigkeit heutiger Datenanalyse-Strategien zu bewerten. Zuletzt wird der potentielle Nachweis und die Beschreibung von Schwarzen Löchern einer Gesamtmasse von hunderten bis zehntausenden Sonnenmassen erläutert, der mit zukünftigen Interferometern möglich wird.

Der Schwerpunkt dieser Dissertation ist somit die Verbindung von theoretischen Lösungen der Problematik binärer Schwarzer Löcher und deren direkter Anwendung in der Analyse von GW-Daten und der Astrophysik.

ACKNOWLEDGMENTS

My doctoral experience has been tremendously enriching and I owe gratitude to a large number of people and institutions. I am indebted to the Max Planck Society and the Albert Einstein Institute for their continued endorsement in the form of scientific education, facilities and support to pursue my research; to the LIGO Scientific Collaboration for providing a stimulating environment for doing gravitational-wave science; to the Relativity Group at the University of Jena for giving me the opportunity of starting my research in the field of numerical relativity; and to the DAAD (German Academic Exchange Service) for their partial funding over the past years.

I am personally grateful to the director of the Albert Einstein Institute, Professor Bernard F. Schutz, for his strong belief in my capabilities. This work would not have been possible without the guidance I have received from my advisors Badri Krishnan and Sascha Husa, who have made sure I never lacked help and motivation to carry on my doctoral research. I appreciate the support received from the leaders of the groups where I have worked, Bernd Brügmann in Jena; Luciano Rezzolla and Maria Alessandra Papa in Golm; Steve Fairhurst, Patrick Brady, Bangalore Sathyaprakash and Alan Weinstein within the LSC. I am thankful to Laura Cadonati, Chris van den Broeck and Alberto Vecchio for accepting to be external reviewers of this dissertation.

I have had the privilege of finding extraordinary people along the way. I heartily thank Pau Amaro Seoane, Stas Babak, Jolien Creighton, Steve Drasco, Marc Mars, Alberto Sesana and Ed Porter for their mentoring and advice. It has been a pleasure to share time and ideas with Diego Fazi, Nick Fotopoulos, Chad Hanna, Michael Jasiulek, Drew Keppel, Christian Reisswig, Emma Robinson, Jennifer Seiler and John T. Whelan. I especially acknowledge and thank the help of Frank Ohme in the context of our work on phenomenological waveforms. I appreciate the useful comments provided by Ian Hinder, Mark Hannam and Jocelyn Read, who have read and corrected parts of this dissertation. Any remaining errors and mistakes are, nonetheless, my full responsibility. For making my doctoral years truly enjoyable I thank all my fellow students and post-doctoral researchers at the Albert Einstein Institute and the LIGO and Virgo Scientific Collaborations. My friends in Burgos, Salamanca and Berlin have always encouraged me to pursue my goals; I feel privileged for having them close to me, despite the distance. Lastly, words can not express the immense gratitude and love I feel towards my parents and family for their affection and understanding. This dissertation is dedicated to them.

LUCÍA SANTAMARÍA LARA
POTSDAM, APRIL 2010

CONTENTS

OVERVIEW	3
I THE UNIVERSE THROUGH A NEW WINDOW	7
1 GRAVITATIONAL WAVES	9
1.1 Einstein's Theory of Gravitation	9
1.1.1 The Einstein Field Equations	9
1.1.2 Effects of Gravitational Waves on Test Particles	12
1.2 History of Gravitational-Wave Detectors	14
1.3 Gravitational-Wave Interferometry	17
1.4 World-Wide International Network of Detectors	19
1.5 The Future of Gravitational-Wave Astronomy	23
1.5.1 The Advanced Interferometers	23
1.5.2 Third-Generation Ground-Based Detectors	24
1.5.3 LISA: The Space Antenna	25
2 SOURCES OF GRAVITATIONAL WAVES	27
2.1 Stochastic Background	27
2.2 Periodic Sources	28
2.3 Bursts	29
2.4 Coalescing Binaries	30
2.4.1 Evidence for Compact Binaries	30
2.4.2 The Coalescence Process	31
2.4.3 Expected Astrophysical Rates for Compact Binaries	34
II MODELING BINARY BLACK-HOLE COALESCENCES	37
3 ANALYTICAL MODELING OF BLACK-HOLE BINARIES	39
3.1 Post-Newtonian Formalism for Non-Precessing Binaries	39
3.1.1 Energy and Flux	41
3.1.2 TaylorT4 Approximant	42
3.1.3 Stationary Phase Approximation and TaylorF2	43
3.1.4 Amplitude	45
3.2 Ringdown and Quasi-Normal Modes	48
3.2.1 Perturbations from Equilibrium	48
3.2.2 The Ringdown Waveform	49

4	BLACK-HOLE BINARIES IN NUMERICAL RELATIVITY	53
4.1	Solving Einstein Equations Numerically	53
4.1.1	The 3+1 Decomposition	54
4.1.2	The ADM Equations	56
4.1.3	The BSSN Formulation	57
4.1.4	A Recipe for Successful Simulations	59
4.2	Numerical Simulations of Non-Precessing Binaries	65
4.2.1	NR waveforms and Codes	65
4.2.2	Going from Ψ_4 to h	67
5	NEW WAVEFORM MODEL FOR BINARY BLACK HOLES	69
5.1	Full Models for Binary Black-Hole Coalescence	69
5.2	Matching Post-Newtonian and Numerical Relativity	71
5.2.1	Basic Notions	71
5.2.2	Issues in Matching PN with NR	73
5.2.3	An Illustration for Non-Spinning Systems	75
5.2.4	Construction of Hybrids for Aligned-Spin Systems	82
5.3	Phenomenological Model	85
5.3.1	Phase Model	85
5.3.2	Amplitude Model	86
5.3.3	Mapping the Phenomenological Coefficients	87
5.4	Summary and Future Work	89
III	APPLICATIONS	93
6	REAL SEARCHES FOR GRAVITATIONAL WAVES	95
6.1	The Data Analysis Strategy for Coalescing Binaries	95
6.1.1	The Optimal Filter	95
6.1.2	Template Construction	97
6.1.3	Signal-Based Vetoes	97
6.1.4	Coincidence Test and Background Estimation	99
6.1.5	Detection Statistic: False-Alarm Rate	100
6.2	The Low-Mass Search in S5 LIGO Data	101
6.2.1	Description of the Search	102
6.2.2	Search Results	105
6.2.3	Discussion of the Low-Mass Search	109
6.3	The High-Mass Search in S5 LIGO Data	109
6.3.1	Motivation and Strategy for a High-Mass Search	110
6.3.2	Preliminary Results of the High-Mass Search	112

7	NUMERICAL INJECTIONS IN GRAVITATIONAL SEARCHES	117
7.1	The NINJA Project	117
7.1.1	Numerical Waveforms	118
7.1.2	Creation of NINJA Data	121
7.2	Search with a Phenomenological Template Bank	126
7.2.1	The Non-Spinning Phenomenological Waveform Model	126
7.2.2	The Search Strategy	127
7.2.3	Efficiency for Detection	130
7.2.4	Accuracy for Parameter Estimation	133
7.3	Looking Ahead: The NINJA 2 Project	135
8	ASTROPHYSICS OF INTERMEDIATE-MASS BLACK HOLES	137
8.1	Formation of an Intermediate-Mass Black Hole	137
8.2	Life of a Massive Binary	139
8.2.1	Birth	139
8.2.2	Growing Up (Shrinking Down)	140
8.2.3	Death	142
8.3	Horizon Distance and Signal-To-Noise Ratio	144
8.4	Event Rates	146
8.5	Summary and Conclusions	150
9	EPILOGUE	153
	BIBLIOGRAPHY	155
	CURRICULUM VITÆ	169
	PUBLICATIONS	171

LIST OF FIGURES

Figure 1	Effect of the two polarizations of a gravitational wave propagating through a ring of test particles	13
Figure 2	Schematic optical layout of a gravitational-wave interferometer	18
Figure 3	International network of GW interferometers	20
Figure 4	Strain sensitivity curves for the ground-based interferometers in operation during S5/VSR1	23
Figure 5	Expected sources of gravitational waves for future ground-based and space-borne detectors	24
Figure 6	Typical gravitational wave emitted by a coalescing compact binary	33
Figure 7	Pictorial representation of a binary black-hole system in a quasicircular orbit	40
Figure 8	Different variants of constructing the PN Fourier amplitude in the stationary phase approximation for the equal mass case	47
Figure 9	Ringdown signals emitted by sources of total mass $100 M_{\odot}$ and different spin values	50
Figure 10	Foliation of the space-time in the 3+1 decomposition of the Einstein equations	54
Figure 11	Typical numerical relativity waveform for the late inspiral, merger and ringdown of a binary black-hole system	64
Figure 12	Comparison between the double integration in the time domain and the division in the frequency domain for the computation of the gravitational-wave strain	68
Figure 13	Contour plot for the fitting error $\Delta\phi_0$ in the $(f_L, \Delta f)$ plane	76
Figure 14	Dependence of the fitting errors in η , ϕ_0 and t_0 on the frequency window $(f_L, \Delta f)$	77
Figure 15	Best fit value of η as a function of the start frequency f_L of the matching window for the waveform which corresponds nominally to a mass ratio 1 : 2	78
Figure 16	Distinguishability of different hybrid waveforms constructed from Llama equal-mass waveforms at different resolutions	80
Figure 17	Distinguishability of different hybrid waveforms constructed from NR waveforms produced with either BAM or Llama	80
Figure 18	Initial LIGO's ability to distinguish hybrid waveforms constructed from different PN approximants	81
Figure 19	Illustration of the method for constructing PN-NR hybrid waveforms in the frequency domain	83

Figure 20	Comparison of hybrid waveforms with the numerical data used in their construction in the time domain 84
Figure 21	Fitting procedure for the amplitude 87
Figure 22	Map of the phenomenological parameters to the physical parameters of the binary η and χ 88
Figure 23	Overlaps between the hybrid waveforms and the proposed phenomenological fit for Advanced LIGO 90
Figure 24	Overlaps between the NR data-sets #4–7ab and the predicted phenomenological waveforms from our model for advanced LIGO 90
Figure 25	Diagram demonstrating how the χ^2 -test discriminates between true and spurious signals 99
Figure 26	Parameter space of masses surveyed by the low- and high-mass searches for coalescing compact binaries in S5 LIGO data 102
Figure 27	Combined and un-combined inverse false-alarm rates for triple H1H2L1 and double H1L1 triggers in month 4 of the 2nd year S5 low-mass search 104
Figure 28	Horizon distance in Mpc as a function of the binary's total mass for the three interferometers in operation during month 4 of the 2nd year S5 low-mass search 107
Figure 29	The posterior distribution for the rate of BNS coalescences in the S5 LIGO low-mass search 107
Figure 30	The marginalized 90% rate upper limits as a function of mass for the LIGO S5 low-mass search 108
Figure 31	Expected horizon distance of the LIGO detectors for inspiral-only and full signals 111
Figure 32	Found and missed injection during months 1 and 2 of the high-mass S5 LIGO search 113
Figure 33	Plot of SNR versus χ^2 in L1 during months 1 and 2 of the high-mass S5 LIGO search 114
Figure 34	Playground zero-lag events observed compared to background during months 1 and 2 of the high-mass S5 LIGO search 116
Figure 35	Summary of all numerical relativity waveforms submitted to the NINJA project 119
Figure 36	Distribution of power into different spherical harmonics for the waveforms submitted to the NINJA project 120
Figure 37	Design spectra of the first generation LIGO and Virgo detectors and the NINJA noise curves 124
Figure 38	Total mass and distance of the 126 NINJA injections 125
Figure 39	Two time-domain phenomenological waveforms from the template bank used in the NINJA search 128
Figure 40	Found and missed injections in the NINJA search with a phenomenological template bank 131
Figure 41	Accuracy in the recovery of chirp mass and end time of the reduced set of NINJA injections using the phenomenological template bank 134

- Figure 42 Amplitude of equal-mass, non-spinning BBH systems scaled to various total masses of the IMBH binary compared with the sensitivity curves of various detectors 138
- Figure 43 Triaxiality of the resulting merged cluster for different mass fractions and the mass fraction 0.5 141
- Figure 44 Amplitude of the GW emitted by a system of two equal-mass IMBHs of total mass $878.4 M_{\odot}$ placed at 100 Mpc as seen by different GW observatories 143
- Figure 45 Sky-averaged horizon distance versus redshifted mass for three binary configurations obtained with the design sensitivity curves of Advanced LIGO and the Einstein Telescope 144
- Figure 46 Signal-to-noise ratio as a function of the total mass of the BBH for the present and future generations of GW detectors and LISA 145
- Figure 47 Three parameterizations of the stellar formation rate per unit comoving volume compared in the calculation of the event rates 147
- Figure 48 Sky-averaged reach of the Advanced LIGO and the ET detectors up to $z = 5$ versus intrinsic total mass of the IMBH binary 148

LIST OF TABLES

Table 1	Terminology for statements related to astrophysical rates	34
Table 2	Compact binary coalescence rates per Mpc^3 per Myr	35
Table 3	Detection rates for compact binary coalescence sources	36
Table 4	The first QNM frequencies ωM of the spherical, non-spinning Schwarzschild black hole for $l = 2, 3$, given in geometrical units	49
Table 5	Some properties of currently-working NR evolution codes	63
Table 6	NR codes and configurations used for the construction and verification of our hybrid waveforms and phenomenological model	66
Table 7	Coefficients to map the 9 free parameters Λ_k of our phenomenological model to the physical parameters of the BBH binary	89
Table 8	Detailed results from BNS from the S5 LIGO low-mass search	106
Table 9	Overview of results from BNS, BBH and BHNS from the S5 LIGO low-mass search	106
Table 10	Initial conditions for the numerical waveforms submitted to the NINJA project	122
Table 11	Characteristic duration, mass and frequencies of the waveforms submitted to the NINJA project	123
Table 12	Results of the search for NINJA signals using the non-spinning phenomenological template bank	130
Table 13	Overview of the missed injections for the search with a phenomenological template bank	132
Table 14	Event rates for IMBH binaries formed in the single-cluster channel potentially observable by Advanced LIGO and the ET per year	149

ACRONYMS

ADM Arnowitt-Deser-Misner
AIGO Australian International Gravitational Observatory
BBH Binary Black Hole
BHNS Black Hole–Neutron Star Binary
BNS Binary Neutron Stars
BSSN Baumgarte-Shapiro-Shibata-Nakamura
CBC Compact Binary Coalescence
CLIO Cryogenic Laser Interferometer Observatory
CT Conformal Traceless
DQ Data Quality
EOB Effective One Body
ET Einstein Telescope
FAR False-Alarm Rate
GRB Gamma-Ray Burst
GW Gravitational Wave
IFAR Inverse False-Alarm Rate
IFO Interferometer
IMBH Intermediate-Mass Black Hole
IMR Inspiral-Merger-Ringdown
ISCO Innermost Stable Circular Orbit
 Λ CDM Λ Cold Dark Matter
LCGT Large-Scale Cryogenic Gravitational-Wave Telescope
LIGO Laser Interferometer Gravitational-Wave Observatory
LHO LIGO Hanford Observatory
LLO LIGO Livingston Observatory
LISA Laser Interferometer Space Antenna
LSC LIGO Scientific Collaboration
NINJA Numerical Injection Analysis

- NR Numerical Relativity
- PBH Primordial Black-hole Binaries
- PN Post-Newtonian
- QNM Quasi-Normal Mode
- SFR Star Formation Rate
- SMBH Supermassive Black Hole
- SMS Supermassive Star
- SNR Signal-To-Noise Ratio
- SPA Stationary-Phase Approximation
- SPH Smooth Particle Hydrodynamics
- TT Transverse-Traceless
- VMS Very Massive Star
- WMAP Wilkinson Microwave Anisotropy Probe

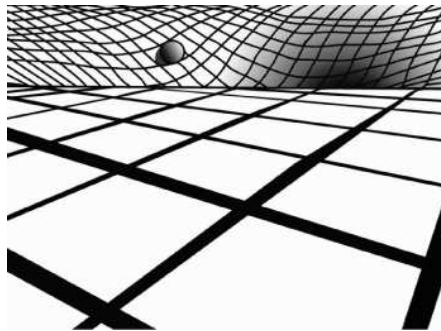
LUCÍA SANTAMARÍA LARA

COALESCENCE OF BLACK-HOLE BINARIES: FROM
THEORETICAL SOURCE MODELS TO APPLICATIONS IN
GRAVITATIONAL-WAVE ASTRONOMY

OVERVIEW

Few other physical laws or mathematical theories have captivated the imagination of generations of scientists the way general relativity has. The geometrical treatment that Einstein proposed to explain the structure of space-time and its connection with the dynamics of matter possesses a special simplicity and elegance. Particularly fascinating are the far-reaching *gedankenexperiments* that Einstein devised in order to arrive at previously unexplored conclusions about the consequences of travelling at velocities comparable to that of light.

General relativity is a theory developed from first principles, which applied novel, abstract mathematical techniques to the understanding of our Universe; nevertheless, when confronted with experimental phenomena, the predictions happened to be in excellent agreement with the observations. Relativity goes one step further than Newton's theory of gravitation and is able to correctly calculate the discrepancies in the precession of Mercury's perihelion. Its accuracy is the basis for the current global positioning systems [44]. And perhaps more significantly: it predicts the existence of gravitational waves, ripples in space-time produced by the accelerated movement of massive objects in the four-dimensional Universe in which we live.



A distorted rubber sheet gives a simple way of visualizing general relativity.
<http://www.jrank.org/space/pages/2362/general-relativity.html>

The discovery of the Hulse-Taylor binary pulsar in 1974 led to the observation of the decay of its orbit, in precise agreement with the loss of energy due to gravitational radiation predicted by general relativity [250]. To date, this constitutes the strongest direct evidence for the existence of gravitational waves. Direct measurement of such radiation has not yet occurred; nevertheless, active experimental and theoretical efforts are underway to detect gravitational emissions for the first time.

The work presented in this dissertation focuses on the characterization of the gravitational radiation emitted by binary systems of black holes. The main focus is the connection of the theoretical predictions for the gravitational radiation emitted by coalescing black-hole binaries with their application in gravitational-wave astronomy. To this end, analytical and numerical approaches to solving the binary black hole problem are brought together with the goal of accurately modelling the gravitational signature of non-precessing binary systems. This research is of immediate relevance to current and future data-analysis efforts in the context of searches for gravitational waves with the detectors LIGO and Virgo.

The object's name is PSR B1913+16, also known as PSR J1915+1606 and PSR 1913+16

This dissertation is structured as follows: chapter 1 introduces the canonical mathematical formulation of the Einstein equations in the weak-field approximation, which predicts the existence of gravitational waves. It is followed by a short description of the history of searches for gravitational radiation, including the development of currently-operating interferometers. Nowadays, an international network of detectors exists that is actively operating at design sensitivity and working towards meeting the challenge of the first direct measurement of gravitational waves. Additionally, a brief overview of the future of gravitational-wave astronomy as it is foreseen for the next decade is given.

Chapter 2 presents various sources of gravitational radiation that can be reasonably expected to exist in our Universe, in particular coalescing binaries, for they are the main focus of this work. An introduction to the coalescence process is given, describing in detail the three stages in which the full process is commonly divided — adiabatic inspiral, non-linear merger and perturbative ringdown to a final Kerr black hole. Finally, the expected astrophysical rates of occurrences of binaries in our Universe are given for the current and future generations of gravitational-wave interferometers.

The in-depth description of the theoretical methods that are employed to solve the binary black hole coalescence can be found in chapters 3 and 4, which respectively present the analytical and the numerical approaches to the problem. Chapter 3 first introduces the post-Newtonian treatment of the inspiral phase to later concentrate on perturbative methods for the final ringdown. Chapter 4 describes the foundations of numerical relativity and its long-awaited success in performing full, non-linear simulations of the late inspiral, merger and ringdown parts of the black-hole binary coalescence.

One of the main results of this dissertation is presented in chapter 5. A new method is proposed to model the full coalescence of non-precessing binary black hole systems in the frequency domain, that accurately incorporates the most up-to-date contributions from post-Newtonian theory and state-of-the-art numerical relativity simulations. The introduction of the novel phenomenological model is accompanied with a general description of the challenges that need to be taken into account when comparing post-Newtonian and numerical methods. A discussion of the different possible sources of error in the construction of hybrid waveforms is provided as well.

In the context of joint work within the LIGO and Virgo Scientific Collaborations, the author has contributed to the analysis of LIGO data corresponding to the period 2005–2007. The description of two searches for coalescing binaries in different regions of the mass parameter range is given in chapter 6. The results of one of them provide the latest upper limits on the rate of compact binaries within the surveyed mass range in our local Universe via direct data-taking with gravitational-wave detectors. For the other search, preliminary results are presented.

Chapter 7 is an introduction to the use of waveforms from numerical relativity in the context of software injections into simulated detector noise, with the primary goal of assessing the reliability of current data analysis techniques to signals that include the merger and ringdown of the binary. In this context, a multi-disciplinary collaboration was established in 2008 with the task of carrying out this program. I participated in this first challenge in two direct ways, firstly, as a co-developer of the software required to perform the injections of numerical data into the detector noise and, secondly, as analyst of such data by means of a family of non-spinning templates modeling

the full binary black hole coalescence. Chapter 7 summarizes the general guidelines under which the project was formulated as well as the findings obtained through our analysis.

Finally, the dissertation concludes with a brief look at astrophysics in chapter 8. The primary goal of gravitational-wave astronomy is to reach a stage when astrophysically-relevant statements can be made once gravitational radiation is measured and a new window to the Universe is opened. Profound knowledge of the expected astrophysical sources is certainly key to reach that stage. Chapter 8 addresses the question of the existence of a particular class of black holes, those with an intermediate mass comprised among hundreds and tens of thousands of solar masses. Observational evidence for binaries formed by two of these objects exists but is not conclusive. Hence, there is an unexplored field where gravitational-wave astronomy with second- and third-generation interferometers might be able to provide further insight. The consequences that the existence of intermediate-mass black-hole binaries could have for Advanced LIGO and other future detectors are explored.

Geometric units are used throughout this dissertation, i.e. $G = c = 1$; thus, mass, time and distance are measured in the same units. The space-time metric is assumed to have signature $(-, +, +, +)$. The mass of our sun is

$$1 M_{\odot} = 1.9891 \times 10^{30} \text{ kg} = 1.4766 \times 10^3 \text{ m} = 4.92549 \times 10^{-6} \text{ s}.$$

Unless otherwise specified, lower case Greek indices ($\mu, \nu, \rho, \sigma, \dots$) range from 0 to 3, whereas lower case Latin indices (i, j, k, \dots) range from 1 to 3.

Part I

THE UNIVERSE THROUGH A NEW WINDOW

GRAVITATIONAL WAVES

Over a century ago, physicist Albert Einstein revolutionized the field of gravitation, introducing a shift of scientific paradigm in our understanding of the structure of space-time. His theory of general relativity is the current description of gravitation in modern physics. It unifies special relativity and Newton’s law of universal gravitation. General relativity also predicts the existence of gravitational waves, which have since been measured indirectly; a direct measurement has not yet occurred, but experiments are currently underway — certain aspects related to this research field constitute the main focus of this thesis.

The field of gravitational-wave research has accumulated a rich and somewhat controversial history over its more than five decades of existence [94]. From the primitive Weber cylinders to the low-temperature bars and spherical resonant detectors, afterwards superseded by sophisticated interferometers, the search for gravitational waves constitutes not only a fascinating theoretical endeavour, but also a challenging experimental enterprise.

In this chapter, Einstein’s theory and its prediction of gravitational waves are introduced, as well as past efforts towards detection of gravitational radiation; in addition, the technology underlying the currently-operating observatories that are expected to grant positive results within the next few years is described.

1.1 EINSTEIN’S THEORY OF GRAVITATION

General relativity asserts that the curvature of space-time causes gravity. The presence of matter curves space-time and the curvature in turn determines the behaviour of matter. Einstein arrived at this revolutionary idea by means of a series of *gedankenexperiments* or thought experiments based on the assumptions that the speed of light was a constant of our universe and that the motion of free-falling objects was universal. Let us have a look in the next sections at the elegant mathematical formulation that expresses this phenomenon.

“Space-time grips mass, telling it how to move, and mass grips space-time, telling it how to curve” — John Archibald Wheeler

1.1.1 The Einstein Field Equations

In geometric units and covariant notation, the Einstein equations for the gravitational field take the abbreviated form [110]

$$G_{\mu\nu} = 8\pi T_{\mu\nu}, \quad (1.1)$$

where $G_{\mu\nu} = R_{\mu\nu} - \frac{1}{2}Rg_{\mu\nu}$ is the Einstein tensor, $g_{\mu\nu}$ is the metric of the four-dimensional space-time and $T_{\mu\nu}$ is the stress-energy tensor that encodes the matter content. In this expression, it is the Einstein tensor $G_{\mu\nu}$ that is used to express the curvature of the Riemann manifold. The Ricci scalar $R = g^{\mu\nu}R_{\mu\nu}$, also known as *scalar curvature*, is the trace of the Ricci tensor, which in turn is defined as the trace over the first and third indices of the *Riemann curvature tensor*, $R_{\mu\nu} = R^{\gamma}_{\mu\gamma\nu}$. The Riemann tensor is a fundamental object in differential geometry that measures the extent to which

the metric tensor is not locally isometric to a Euclidean space. The curvature tensor is given in terms of the Levi-Civita connection ∇ of the space-time as

$$(\nabla_\mu \nabla_\nu - \nabla_\nu \nabla_\mu) v^\rho = R^\rho_{\sigma\mu\nu} v^\sigma, \quad (1.2)$$

for any given vector v^μ . The covariant derivatives commute in a flat manifold but do not if the manifold is curved. The Riemann tensor verifies the following symmetries and identities [259]

$$R_{\mu\nu\rho\sigma} = -R_{\mu\nu\sigma\rho} = -R_{\mu\sigma\rho\nu} = R_{\sigma\rho\mu\nu}, \quad (1.3)$$

$$R_{\mu\nu\rho\sigma} + R_{\mu\rho\sigma\nu} + R_{\mu\sigma\nu\rho} = 0, \quad (1.4)$$

$$\nabla_\lambda R_{\rho\sigma\mu\nu} + \nabla_\rho R_{\sigma\lambda\mu\nu} + \nabla_\sigma R_{\lambda\rho\mu\nu} = 0. \quad (1.5)$$

Equations 1.4 and 1.5 are known as the first and second Bianchi identities

The Bianchi identities imply $\nabla_\mu T^{\mu\nu} = 0$, which is the equation of local conservation of energy and momentum. In absence of sources or in a region far away from them, equation 1.1 further simplifies to $G_{\mu\nu} = 0$.

In this geometric language it is hard to notice that 1.1 represents a set of differential equations. But as a matter of fact, the curvature tensor depends on the metric and its first and second derivatives

$$R^\rho_{\sigma\mu\nu} = \partial_\mu \Gamma^\rho_{\nu\sigma} - \partial_\nu \Gamma^\rho_{\mu\sigma} + \Gamma^\rho_{\mu\alpha} \Gamma^\alpha_{\nu\sigma} - \Gamma^\rho_{\nu\alpha} \Gamma^\alpha_{\mu\sigma} \quad (1.6)$$

$$\Gamma^\rho_{\mu\nu} = \frac{1}{2} g^{\rho\alpha} (\partial_\mu g_{\nu\alpha} + \partial_\nu g_{\mu\alpha} - \partial_\alpha g_{\mu\nu}). \quad (1.7)$$

Furthermore, we are interested in the study of gravitational radiation, treated as a small perturbation that propagates through an otherwise flat space-time. In this weak-field situation there exist coordinate systems where the components of the metric can be decomposed as

$$g_{\mu\nu} = \eta_{\mu\nu} + h_{\mu\nu}, \quad |h_{\mu\nu}| \ll 1 \quad \text{throughout space-time,} \quad (1.8)$$

where $\eta_{\mu\nu}$ is the Minkowski metric that describes a space-time with no curvature. Such coordinates are called nearly Lorentz coordinates and are particularly suitable to solve equation 1.1, which predicts gravitational waves. Einstein showed that the perturbative $h_{\mu\nu}$ field can be calculated in a manner analogous to that of the retarded electrodynamic potentials.

Applying ansatz 1.8 to equation 1.1 and solving for the perturbative radiation field to first order in $h_{\mu\nu}$ yields the linearized Einstein equations

$$-\partial^\alpha \partial_\alpha \bar{h}_{\mu\nu} - \partial^\alpha \partial^\beta \bar{h}_{\alpha\beta} + \partial^\alpha \partial_\mu \bar{h}_{\nu\alpha} + \partial^\alpha \partial_\nu \bar{h}_{\mu\alpha} = 16\pi T_{\mu\nu} \quad (1.9)$$

on the field $\bar{h}_{\mu\nu} \equiv h_{\mu\nu} - \frac{1}{2} \eta_{\mu\nu} h_{\mu\nu}$, which is introduced for simplicity. Note that $\bar{\bar{h}}_{\mu\nu} = h_{\mu\nu}$, and in the case when $\bar{h} (= -h) = 0$, then $\bar{h}_{\mu\nu} = h_{\mu\nu}$. The three last terms on the left-hand side of equation 1.9 serve to keep the expression gauge-invariant. In general relativity there is a gauge freedom corresponding to the group of diffeomorphisms. In the linear approximation this implies that two perturbations $h_{\mu\nu}$ and $h'_{\mu\nu}$ represent the same physical phenomenon if they are related by a transformation of the form

$$h'_{\mu\nu} \rightarrow h_{\mu\nu} + \partial_\mu \xi_\nu + \partial_\nu \xi_\mu, \quad (1.10)$$

where ξ^α is a vector field. Without loss of generality, a field ξ^α can be found such that the following gauge condition is verified

$$\partial^\alpha \bar{h}_{\mu\alpha} = 0 \quad (\text{Lorentz gauge}), \quad (1.11)$$

in clear analogy with the Lorentz gauge condition for the electromagnetic tensor $\partial_\alpha A^\alpha = 0$. However, it is interesting to note that whereas the Maxwell equations in the Lorentz gauge are valid in every source-free region of the space, in the case of the linearized Einstein equations we need to impose the additional condition of being far away from the sources, so that the weak-field condition 1.8 is satisfied. This taken into account, equation 1.9 in the Lorentz gauge simplifies to

$$\partial^\alpha \partial_\alpha \bar{h}_{\mu\nu} = 0 \quad (\text{in vacuum}). \quad (1.12)$$

Aside of the choice of Lorentz gauge, there remains the freedom to make further gauge transformations of the form given in equation 1.10 provided that $\partial^\alpha \partial_\alpha \xi_\beta = 0$, for they leave equation 1.11 unchanged. This means that the Lorentz condition does not uniquely fix the degrees of freedom in the field variables. It can be shown [235] that the gauge can be changed while remaining within the Lorentz class of gauges using any vector solving

$$\left(-\frac{\partial^2}{\partial t^2} + \nabla^2 \right) \xi_\alpha = 0. \quad (1.13)$$

Thus, we can always arrive at the gauge

$$\bar{h} = 0 \quad (1.14)$$

$$\bar{h}_{0i} = 0 \quad (i = 1, 2, 3) \quad \text{in a source-free region} \quad (1.15)$$

$$\bar{h}_{00} = 0 \quad \text{if no sources are present anywhere,} \quad (1.16)$$

which is referred to as Coulomb gauge, also known as radiation gauge. In this transverse-traceless (TT) gauge $\bar{h}_{\mu\nu} = h_{\mu\nu}$, as already noted. The Einstein field equations in vacuum far away from the source of the field take the form

$$\left(-\frac{\partial^2}{\partial t^2} + \nabla^2 \right) h_{\mu\nu} = 0, \quad (1.17)$$

a wave equation for the gravitational radiation that admits the plane-wave solution

$$h_{\mu\nu} = a_{\mu\nu} e^{ik_\alpha x^\alpha}, \quad (1.18)$$

where $a_{\mu\nu}$ is a four-dimensional symmetric tensor containing the amplitude of the different components of the wave and k^α is the wave vector. Substituting 1.18 in 1.17 yields the condition $k_\alpha k^\alpha = 0$, i.e. $k^\alpha = (\omega, \vec{k})$ is a null vector tangent to the world line of a photon, which shows that gravitational waves propagate at the speed of light. The nullity of k^α implies $\omega^2 = |\vec{k}|^2$.

The choice of Coulomb gauge imposes several constraints on the components of the tensor $a_{\mu\nu}$. The traceless condition 1.14 translates to $a = 0$; 1.15 and 1.16 imply that only the spatial components of $a_{\mu\nu}$ are non-zero. If we further orient the direction of propagation of the wave along the z-axis so that $k^\alpha = (\omega, 0, 0, \omega)$ then $a_{\alpha z} = 0$ for all α . These conditions reduce the number of independent components of $a_{\mu\nu}$ from ten to only two

$$a_{\mu\nu} = \begin{pmatrix} 0 & 0 & 0 & 0 \\ 0 & a_{xx} & a_{xy} & 0 \\ 0 & a_{xy} & -a_{xx} & 0 \\ 0 & 0 & 0 & 0 \end{pmatrix}, \quad (1.19)$$

The Lorentz gauge is in fact a class of gauges

It is natural that gravitational waves propagate with speed c, as c is the only relevant speed in the theory. Astrophysicist Sir Arthur Eddington, however, liked to express his skepticism by saying that "gravitational waves propagate at the speed of thought"

hence the final form of the solution to the source-free, linearized Einstein equations for the perturbative field is

$$h_{\mu\nu} = \begin{pmatrix} 0 & 0 & 0 & 0 \\ 0 & h_+ & h_\times & 0 \\ 0 & h_\times & -h_+ & 0 \\ 0 & 0 & 0 & 0 \end{pmatrix} e^{i\omega(z-t)}, \quad (1.20)$$

with h_+ and h_\times representing the two polarization states of the wave. A general gravitational wave can be written as a linear combination of the *plus* and *cross* components $h = h_+ \hat{e}_+ + h_\times \hat{e}_\times$ in the orthonormal basis of vectors

$$\hat{e}_+ = \begin{pmatrix} 1 & 0 \\ 0 & -1 \end{pmatrix} \quad \hat{e}_\times = \begin{pmatrix} 0 & 1 \\ 1 & 0 \end{pmatrix}. \quad (1.21)$$

Rotations of the x - and y -axes in the transverse plan by an angle ψ change the polarization components in the following way

$$\begin{aligned} h'_+ &= h_+ \cos 2\psi + h_\times \sin 2\psi \\ h'_\times &= -h_+ \sin 2\psi + h_\times \cos 2\psi, \end{aligned} \quad (1.22)$$

which indicates that general relativistic gravitational waves have spin two, because the source of gravity is the stress-energy tensor, which is a second-rank tensor. This is of importance for issues related to quantization of gravity, which fall beyond the scope of this thesis.

1.1.2 Effects of Gravitational Waves on Test Particles

The formalism developed in section 1.1.1 shows how gravitational radiation from a far source propagates throughout the universe in the form of ripples in the space-time, deforming its geometry. Thus, in principle, gravitational waves could be detected by accurately tracking the separation of a pair of freely-suspended masses. Using the same principle, one could try to measure the perturbation on the paths of photons coming from a far object —such as a millisecond-period pulsar— when they are affected by a passing gravitational wave. Alternatively, masses connected by a solid piece of material would react to the gravitational tidal forces that stress the material.

Light constitutes an excellent way of measuring proper distances between free-falling objects. Pulses of electromagnetic radiation propagating in a region affected by a gravitational field react to it in a measurable way that can provide us with information about the metric of the space-time. Consider two free-falling particles A and B in a background Lorentz frame and choose the TT gauge introduced in section 1.1.1 associated to this frame. We will work in the TT gauge, for it is the most appropriate when dealing with radiation space-times. Besides, test particles in a given spatial location remain at those same TT coordinates, which is particularly convenient.

We shall denote ξ^α the connecting vector between A and B. Free particles obey the geodesic equation for their 4-velocity u^α [259]

$$u^\alpha \nabla_\alpha u^\beta = 0. \quad (1.23)$$

These three gravitational-wave detection mechanisms are, respectively, the functional principles of interferometers, pulsar timing arrays and resonant bars

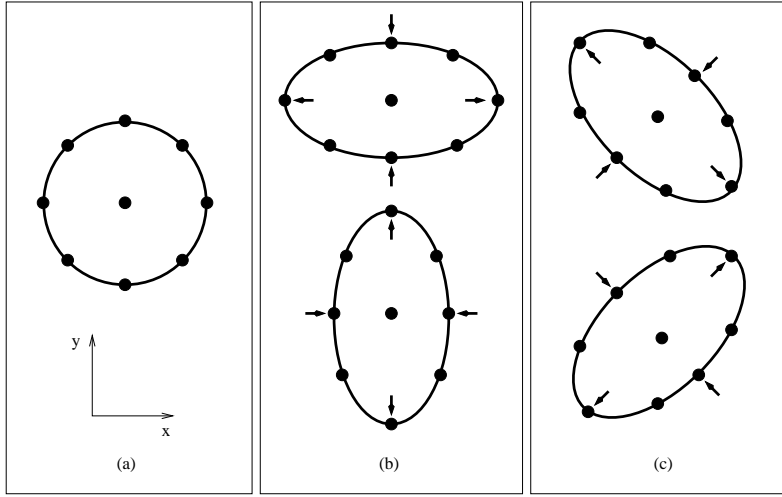


Figure 1: Effect of the two polarizations of a gravitational wave propagating through a ring of test particles. (a) A ring of free particles before a wave travelling in the z -direction reaches them. (b) Distortion produced in the ring by the *plus* polarization h_+ , which modifies the proper distance between the particles in the ring, altering its geometry as the phase of the gravitational wave changes through a complete oscillation cycle. (c) Same as (b) but for the *cross* polarization h_\times . The effects are not drawn to scale but have been greatly magnified.

In a curved space-time, the second derivative of the vector ξ^α is non-zero, which means that there is an acceleration between particles A and B given by the equation of geodesic deviation

$$a^\alpha = \frac{d^2 \xi^\alpha}{dt^2} = -R_{\beta\mu\nu}^\alpha \xi^\beta u^\mu u^\nu = -R_{\beta 0 0}^\alpha \xi^\beta, \quad (1.24)$$

since the 4-velocity u^α has coordinates $(1, 0, 0, 0)$ in this coordinate basis. In the TT gauge, the relevant components of the Riemann tensor, defined in equation 1.6, can be easily calculated

$$R_{\nu 0 0 \mu} = \frac{1}{2} \frac{d^2 h_{\mu\nu}}{dt^2}, \quad (1.25)$$

which, according to equation 1.20, are only non-zero for $\mu\nu = ij$ with $i, j = 1, 2$ representing the x - and y -directions. Thus

$$\frac{d^2 \xi^i}{dt^2} = \frac{1}{2} \frac{d^2 h_{ij}}{dt^2} \xi^j. \quad (1.26)$$

Figure 1 illustrates the meaning of equation 1.26. A ring of particles placed at rest on the xy -plane in an initially wave-free region of space-time encounters a gravitational wave travelling along the z -direction. The arrival of the wave modifies the proper distance between the particles. The *plus* polarization of the wave stretches and squeezes the ring along the x - and y -axes, oscillating between the shapes displayed on panel (b) of figure 1. The *cross* polarization distorts the ring along the directions given by $(\hat{e}_x \pm \hat{e}_y)/\sqrt{2}$. The effects of the two polarizations are rotated 45° relative to one another, in contrast to the electromagnetic field, where the rotation angle is 90° .

Once we know the effect of a passing gravitational wave on a pair of test particles, we can proceed to devise mechanisms for detecting that effect, for

instance, by means of a laser and an interferometer of arm's length L . An assumption that is usually made for ground-based detectors is that the wavelength of the gravitational wave is much larger than the size the interferometer, $\lambda_{\text{GW}} \gg L$. This simplifies the integration of equation 1.26

$$\delta x = \frac{h_{xx}}{2}x, \quad \delta y = \frac{h_{yy}}{2}y. \quad (1.27)$$

Thus, the variation of the proper lengths of the interferometer's arms is proportional to the original distance between them. When a gravitational wave passes along the z -direction with polarization $h_{xx} = -h_{yy} = h_+(t)$, the change in proper distance and the phase difference between the two beams at the origin are

$$\frac{\delta L(t)}{L} = h_+(t), \quad \Delta\phi = 2\pi \frac{L}{\lambda} h_+(t). \quad (1.28)$$

The interferometer response, i.e. the difference in phase between the beams recombining at the beam splitter is proportional to

$$h(t) \propto \delta(\Delta\phi) \equiv F_+ h_+(t) + F_\times h_\times(t), \quad (1.29)$$

where F_+ and F_\times are the antenna patterns of the detector, which encode the projections between the wave's polarizations in the radiation's and detector's reference frames. The quantity h is the *gravitational wave strain*.

In this derivation it is implicitly assumed that the spatial variation of the gravitational wave in the interferometer's arms is negligible. The temporal variation of $h(t)$ during the short time $\approx 2L$ that it takes for the light to travel back and forth to the mirror is not taken into account. The result of the derivation is right, however it is in principle not correct to use the spatial distance. As a matter of fact, the photons travel along null geodesics, not spatial. One can calculate how the frequency of the photon ω changes when travelling through a space-time affected by gravitational radiation:

$$\frac{\delta\omega}{\omega} = -\frac{1}{2} \hat{x}_i \hat{x}_i \dot{h}_{ij} L. \quad (1.30)$$

The passing gravitational wave affects the photon by altering its path; tracking the Doppler shift of a sinusoidal electromagnetic signal allows us to measure the effect of the gravitational radiation. For a complete, general derivation of the Doppler shift of a signal transmitted and transponded from a distant spacecraft, including the results obtained when dropping the assumption of long wavelength, the reader is referred to [113]. This paper is fundamental for understanding the physics that underlie the operation of the space-borne antenna LISA, and also generalizes commonly-used formulations of the effect of gravitational waves on ground-based detectors like LIGO and Virgo.

For concrete examples of correct derivations of the response functions for LIGO and LISA we refer the reader to the articles [226] and [117] respectively

1.2 HISTORY OF GRAVITATIONAL-WAVE DETECTORS

Weber studied gravitational radiation with Wheeler and pioneered the field of gravitational-wave detectors at a time —late 1950s and early 1960s— when the mere existence of gravitational waves was not widely accepted. He designed and built the first gravitational-wave detector in the form of an aluminum cylinder carefully suspended and connected to instrumentation to observe

oscillations of the bar's fundamental mode [261]. A passing gravitational wave would set the cylinder vibrating at its resonant frequency —about 1660 Hz— and piezoelectric crystals firmly attached around the cylinder's waist would convert that ringing into an electrical signal. Due to the extreme weakness of the gravitational radiation, the cylinder had to be massive and the piezoelectric sensors very sensitive and capable of detecting a change in the cylinder's length by about 10^{-16} meters.

This is indeed what Weber reported a couple of years after the construction of his first detector [262, 263]. By that time his group in Maryland had built several cylindrical bars and moved one of them to Argonne National Laboratory, near Chicago, about 1000 km away. Reported were observations of above-background coincidences between both detectors with very low false alarm probability, which were interpreted as “good evidence” for gravitational waves. In his publication from 1970 [263], Weber even claimed to have measured largely anisotropic radiation that peaked in the direction of the galactic center.

In the years subsequent to Weber's detection claim, a number of independent groups built their own bars and tried to reproduce his results. None of the instruments —located in Argonne, Glasgow, Moscow, Reading, Rutherford, Tokyo, Munich, Frascati, Stanford, Rochester and the Bell Laboratories in New Jersey— were able to measure anything other than random noise, thus discrediting Weber's work. By the late 1970s the consensus in the scientific community was that Weber's results were spurious. His recognition as father of gravitational-wave detection efforts is nevertheless well deserved, for he drew many others into the field.

Soon it became evident that improved detectors were needed in order to approach the sensitivity region that would allow astrophysicists' predictions to be tested. Resonant bars cooled to liquid helium temperatures of ~ 3 K and below at millikelvin —cryogenic bars— promised to reach a sensitivity five orders of magnitude better than that of Weber's bars. Ideally, that would make them sensitive to the strongest potential sources of gravitational waves in our Galaxy and in the local group. Thus, a number of ultra-low temperature bars were designed and constructed during the 1980s and 1990s: the cryogenic resonant gravitational radiation detector ALLEGRO [180] at Louisiana State University, the Italian-built bar EXPLORER [46] located at CERN in Geneva, the coldest and more sensitive AURIGA [215] in Legnaro near Padua, the niobium-made bar NIOBE [63] at the University of Western Australia, the millidegree bar NAUTILUS [47] at Frascati.

The experimental challenge faced by the groups operating resonant detectors is better understood with a simple calculation of the tiny effects induced in the bars by gravitational radiation. Gravitational waves are generated by the acceleration of masses with quadrupolar distributions. A very simple upper limit for the amplitude of the gravitational waves can be given by

$$h \ll \frac{1}{c^4} \left(\frac{GM}{r} \right) \left(\frac{GM}{R} \right), \quad (1.31)$$

where M is the mass, r is the distance and R is the radius of the astrophysical object. Hence, a neutron star with a typical mass of $1M_{\odot}$ and $R = 10$ km located at a distance of 10 Mpc would produce a strain $h \ll 10^{-21}$. The energy flux of a gravitational wave is given by

$$\mathcal{F} = \frac{c^3}{16\pi G} |\dot{h}|^2. \quad (1.32)$$

Physicist Joseph Weber (1919–2000) studied electronics before joining the engineering faculty of the University of Maryland, College Park, where he completed his PhD with a thesis on microwave spectrometry. He gave the earliest public lecture on the principles behind the laser and the maser

The creativity of bar researchers is shown in the made-up acronyms of their detectors.

ALLEGRO: A Louisiana Large Experimental Gravitational Radiation Observatory

AURIGA: Antenna Ultracriogenica Risonante per l'Indagine Gravitazionale Astronomica

NAUTILUS: Nuova Antenna a Ultrabassa Temperatura per Investigare nel Lontano Universo le Supernovae

For a wave of $h = 10^{-21}$ and frequency 1 kHz the energy flux is about $0.3\text{W}/\text{m}^2$. This flux is comparable to that of the Moon light on the Earth, however it is very difficult to detect with a resonant bar detector, given the very small absorption cross section of matter.

One way to improve the detectability of weak signals is to increase the size of the effect they induce in the detector, which depends on the length of the bar, the amplitude of the wave and the quality factor Q of the material. The value of Q is a characteristic of each oscillator, defined as the ratio of the stored energy to the energy dissipated per one radian of the oscillation. Unfortunately, the size of a bar detector can not be increased arbitrarily, for an object of dimensions larger than a few meters would be almost impossible to isolate from external noise sources. The amplitude of the gravitational waves is likewise determined by the position, distance and characteristics of the sources. Hence, the only alternative to achieve a larger and easier-to-measure effect in the detector is to build it of a high Q -value material, such as sapphire. A high Q means that the bar stays for a longer time in an excited state, which results in an increased signal-to-noise ratio. Bars made of sapphire were proposed and constructed, but no substantially superior results were reported.

In fact, a major drawback of cylindrical detectors comes intrinsically from their geometric design: when a bar is hit by gravitational wave, it rings; more specifically it expands and contracts along its length. These detectors are therefore relatively insensitive to gravitational waves travelling along their axes, since gravitational waves are transverse waves. A more optimal design choice is that of spherical detectors, which are responsive to radiation arriving from any direction. The transducers that measure the small disturbances in the detector can be placed everywhere on the sphere. As a matter of fact, a basis of five tensors suffices to determine all directions, polarizations, and magnitudes of incident gravitational waves.

Two projects based on spherical detectors are currently operating or preparing commissioning runs. The pioneer is MiniGRAIL [106], located at the Leiden University in the Netherlands. The MiniGRAIL detector is a cryogenic 68 cm diameter spherical gravitational wave antenna made of CuAl with a mass of 1400 kg, a resonance frequency of 2.9 kHz and a bandwidth around 230 Hz. It aims to operate at 20 mK. The “Mario Schenberg” detector [21] at the University of São Paulo in Brazil has a diameter of 65 cm and weights 1150 kg. The two detectors will ideally operate in coincidence, searching for high frequency events in the 3.0–3.4 kHz frequency bandwidth, such as rotating neutron star instabilities or small black hole mergers. The quantum-limited strain sensitivity dL/L of these antennas ranges from 4×10^{-21} to 10^{-22} .

The theory of how to detect below the quantum limit and the challenge of how to manipulate the Heisenberg uncertainty principle in a macroscopic object has not yet been met in practice and that is one aspect that makes detection of gravitational waves with resonant detectors so fascinating and yet so arduous. Another serious problem bars encounter is the narrow frequency band—around their resonance frequency, typically above 600 Hz—that they are capable of surveying. Most strong sources of gravitational waves, such as binaries of moderate to massive black holes, emit at lower frequencies than that and on a wide range of frequencies. Moreover, the relatively small dimensions of resonant detectors seriously limit the maximum size of the tidal stretching induced in them by a passing gravitational wave and make

See [119] for a description of the possible orthogonal sets proposed by Forward

MiniGRAIL:
Gravitational Radiation
Antenna In Leiden

them more prone to be affected by quantum, thermal and vibration noise sources. All these inherent difficulties for measuring gravitational radiation with resonant detectors have led the field to a gradual decline after the year 2000, while gravitational-wave interferometry has progressively taken the leading role in the detection effort.

1.3 GRAVITATIONAL-WAVE INTERFEROMETRY

Laser interferometers use light to measure the distance between two free-falling mirrors. Nowadays they are the most sensitive operating gravitational-wave detectors and constitute the most promising technology for performing the first measurements within the next years. Their superiority over resonant detectors comes from their larger size, which translates in an inherently better sensitivity, and from their ability to detect signals in a broad range of frequencies.

A typical astrophysical source of interest for gravitational-wave astronomy has frequency components at $f_{\text{GW}} \sim 100$ Hz, corresponding to a wavelength of $\lambda_{\text{GW}} \sim 3000$ km. Maximum sensitivity of the interferometer is achieved when the wave spends half of its period in the arms, this is

$$L = \frac{\lambda_{\text{GW}}}{2} \sim 1500 \text{ km}, \quad (1.33)$$

an unrealistic length for a ground-based detector. In practice, a simple Michelson interferometer is enhanced by means of two additional near mirrors placed near the beam splitter. The Fabry–Pérot cavities store the beams and increase the effective path length.

A simple diagram showing the basics of a gravitational-wave interferometer is given in figure 2. The design consists of a power-recycled Michelson interferometer with Fabry–Pérot arms. Two mirrors are suspended at each end of the L-shaped detector arms. The light originates in a pre-stabilized laser that passes through an optical mode cleaner and is divided in two paths at the beam splitter, travelling back and forth within the Fabry–Pérot cavities. The two arms form cavities that trap much of the light that enters, due to the almost perfect reflectance of the near mirrors. The associated power gain increases the sensitivity. All mirrors, including the beam splitter, are suspended in order to remove noise associated to mechanical vibration. The light that exits the cavity after being reflected in the far mirrors eventually returns to the beam splitter and the two separate beams recombine. The returning beams are kept out of phase so that when the arms are both in resonance — when there is no gravitational wave passing through — their light waves subtract, and no light should arrive at the photodiode.

When a gravitational wave passes through the interferometer, the distances along the arms of the interferometer are shortened and lengthened as shown in section 1.1.2, causing the beams to become slightly less out of phase, so some light arrives at the photodiode, indicating a signal. Light that does not contain a signal is not wasted but it is returned to the interferometer using a power recycling mirror, thus increasing the power of the light in the arms. During normal operation of the interferometer, noise sources can cause movement in the optics, producing similar effects to real gravitational waves — as a matter of fact, a major complexity factor in the effort of detecting gravitational

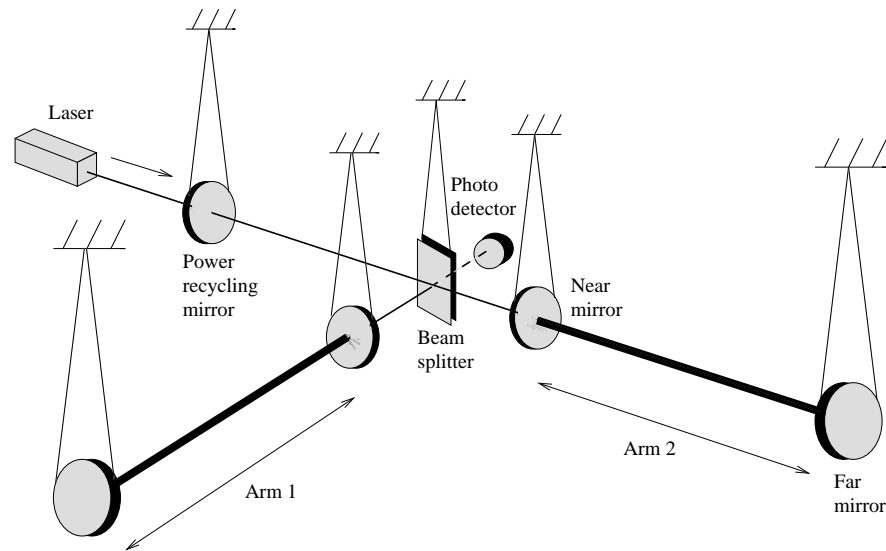


Figure 2: Schematic optical layout of a gravitational-wave interferometer, showing its main components. The diagram is not to scale and does not display other refinements of the optical design.

radiation is finding ways to extract the real signals without confusing them with these spurious motions of the mirrors.

In designing an interferometer for gravitational waves, the same principles operating on bar detectors apply: an increase in the instrument's size entails a larger signal and thus a reduction in the noise. Contrary to resonant detectors, interferometers can expand in size and obtain a larger signal by means of a longer arm. Nevertheless, the signal will always be masked by a variety of instrumental sources of noise. The significance of the main noise sources will be briefly reviewed in the next subsections.

Seismic Noise

Undesired ground vibrations, due to seismic and human activities, limit the sensitivity of the interferometers at low frequencies. To filter out these disturbances, the optical components are suspended to a series of several pendulums, each hanging from the above. Above their resonance frequency, a simple pendulum is actually a second-order low-pass filter, with a response function attenuated as $1/f^2$ for the mirror motion. The interferometer Virgo [257] uses seven-stage pendulums — called superattenuators — which effectively filter out the seismic noise, enabling detection down to ~ 4 Hz. In the case of the LIGO [173] and GEO600 [127] detectors, double and triple pendulums are used. The lower cut-off frequencies below which the seismic noise dominates are slightly larger than that of Virgo, around 40 and 50 Hz respectively.

Thermal Noise

This source of noise is associated to thermal vibrations of the mirrors and their suspensions. The steel wire that suspends the mirror is at room temperature, in thermal equilibrium with the environment. Its thermal fluctuations induce a motion in the mirror that changes the length of the interferometer's arm. In order to keep thermal noise as low as possible, the use of ultra-high-Q

materials in the construction of mirrors and suspension wires is advisable. Suspension thermal noise limits the sensitivity of the detectors mainly in the 50–200 Hz band.

Shot Noise

Photon shot noise is the major limiting source of disturbance at frequencies above 200 Hz and results from the finite number of photons arriving at the photo-detector. Phase and amplitude of the light field are conjugate variables which can not be determined simultaneously with arbitrary precision. Thus, the power of the light beam is expected to fluctuate randomly, affecting the measurements in the photodiode. Shot noise can be reduced by increasing the laser power. In order to be able to detect gravitational waves with frequency ~ 100 Hz, the intensity of the laser would need to be of the order of ~ 100 W, a value beyond the capability of any existing continuous laser. To circumvent this limitation, power recycling techniques are used to increase the power in the interferometer's arm and Fabry–Pérot cavities are installed which amplify the phase shift accumulated. Using such a design, the typically-used 10 W lasers suffice to achieve the desired sensitivity at high frequencies.

Other Quantum Sources of Noise

Although photon shot noise can be reduced by increasing the laser power, this in turn will increase the size of the fluctuations in the laser intensity and in the laser pressure on the mirrors. This quantum limit does eventually become the limiting noise factor at high powers. Future-generation interferometers will need to deal with this source of noise by means of signal recycling and the use of squeezed light. Such investigations are already taking place in currently-operating interferometers, like the GEO600 detector.

1.4 THE WORLD-WIDE INTERNATIONAL NETWORK OF DETECTORS

As noted in section 1.3, the extreme sensitivity required for measuring the tiny effects that gravitational radiation induce in matter, together with the unavoidable presence of spurious noise sources in the detector imply that random internal disturbances might masquerade as real signals. In practice, any kind of detection claim needs to be corroborated by coincident observations from more than one interferometer in order for the scientists to have confidence. Besides, it is convenient to have more than one detection instrument, since the millisecond-scale time delays between observations at different sites can provide information on the location of the source on the sky, a crucial aspect for gravitational-wave astronomy. Each new interferometer improves the sensitivity of all existing ones.

In this spirit, several independent projects that now form an international network of ground-based gravitational-wave interferometers have been designed, funded, constructed and brought into operation in the course of the last 20 years. In figure 3 the locations of both currently-operating and planned detectors all over the world are marked. They correspond to the sites of the LIGO [173], Virgo [257], GEO600 [127], TAMA300 [249] and AIGO [48] detectors.

LIGO operates two gravitational wave observatories taking data simultaneously: the LIGO Livingston Observatory ($30^{\circ}33'46.42''$ N $90^{\circ}46'27.27''$ W)

*LIGO: Laser
Interferometer
Gravitational-wave
Observatory*



Figure 3: International network of gravitational-wave interferometers. Shown in the map are the locations of the three American LIGO detectors at two sites, LHO in Hanford, WA and LLO in Livingston, LA, the Dutch-French-Italian Virgo detector in Cascina near Pisa, the British-German GEO600 located near Hannover, the Japanese detector TAMA300 in Tokyo and the Australian AIGO project near Perth.

in Livingston, Louisiana, USA and the LIGO Hanford Observatory, on the Hanford Nuclear Reservation (coordinates of central complex: $46^{\circ}27'18.52''$ N $119^{\circ}24'27.56''$ W), located near Richland, Washington, USA. LHO hosts two detectors of arm lengths 2 km and 4 km; LLO hosts one 4 km-arm detector. The two LIGO sites are separated by 3002 km. Since gravitational waves travel at the speed of light, this distance corresponds to a difference in gravitational-wave arrival times of up to ten milliseconds. LIGO is the largest and most ambitious project ever funded by the American National Science Foundation. The construction of the facilities was completed in 1999, a series of science data-taking runs started in 2002 and the LIGO design sensitivity was reached in November 2005, initiating a two-year period that culminated after one full year of coincident data among the three LIGO detectors was taken, the S5 run. As of spring 2010 the analysis of these data, split in searches for stochastic, continuous, burst and inspiral signals is close to completion. Chapter 6 of this thesis focuses on the work done by the author in the context of two searches for coalescent binaries in S5 data.

From its beginnings, LIGO was envisioned not as a one-shot experiment, but as an ongoing scientific quest with increasing reach. To that end, the two 4 km-arm LHO and LLO detectors have undergone equipment upgrades and system improvements that have led to LIGO's sixth science run (S6), in progress since July 2009. The enhanced interferometers have been boosted by new optics, increased laser power, advanced seismic isolation tables, and improved signal sensing. But this is by no means the end of LIGO's potential. In addition to enlarging the present scope of gravitational-wave searches, Enhanced LIGO and S6 are already providing an important testing ground for yet a new set of improvements, which is expected to be fully implemented in 2015. This advanced-generation upgrade program, known as Advanced LIGO, will increase the detectors' sensitivities by a factor of 10 and probe a volume of space a thousand times greater than initial LIGO. If our present knowledge of general relativity and expected rates of astrophysical sources in the local universe are correct, the advanced interferometers should be able to detect gravitational waves within the next five years.

Virgo, named after the Virgo Cluster, is located within the site of EGO (European Gravitational Observatory) at Cascina, Italy ($43^{\circ}37'53''$ N $10^{\circ}30'16''$ E). With its 3 km-long arms, it is the largest interferometer built outside the USA. Virgo is funded by EGO, a consortium created by CNRS for France and INFN for Italy with the aim of fostering gravitational-wave research in Europe. The construction of Virgo finalized in 2003 and the detector started its first science run, VSR1, in May 2007, joining LIGO's S5 run in a three-site data-taking effort that extended until October 2007. In contrast to LIGO, that is built around having two facilities and using the combined power to make observations, Virgo is a single powerful detector optimized to extend the bandwidth to lower frequencies with a very sophisticated seismic isolation system.

In a manner similar to that of LIGO, Virgo has planned a two-step upgrade towards a second-generation detector. Virgo+, the enhanced version of Virgo, includes a system for thermal compensation and a laser with increased power. In this configuration, a VSR2 data-taking period started coincidentally with LIGO's S6 in July 2009. A one- to two-year joint S6/VSR2 science run with these enhanced interferometers is foreseen, that will extend until the beginning of 2011. New payloads — dielectric reference mass, fused silica fibers, new mirrors allowing to achieve a higher cavity finesse — will be installed in 2010. The interferometer optical configuration does not change at this stage. On the contrary, the second-generation detector, Advanced Virgo, will require a major upgrade, with the goal of increasing the sensitivity by about one order of magnitude with respect to Virgo in the whole detection band. Its starting operation date, most likely around 2015, shall be selected in agreement with the Advanced LIGO installation in order to optimize the efficiency of the world-wide network of gravitational-wave detectors.

The British-German gravitational-wave detector GEO600 is situated near Sarstedt in the proximity of Hannover, Germany ($52^{\circ}14'49''$ N $9^{\circ}48'30''$ E). Its construction started in September 1995 with funds from the Max Planck Society, the Federal republic of Germany and the Particle Physics and Astronomy Research Council of the UK. With its 600 m-long arms, GEO600 is the first large-scale instrument already now using second-generation technology, such as electro-static actuators and signal recycling. Between 2002 and 2006 GEO600 participated in several data runs in coincidence with the LIGO detectors, the last of which had GEO600 joining S5 from May to October 2006. In November 2007, as soon as the LIGO and Virgo detectors went off-line, GEO600 entered continuous operations — the “Astrowatch mode” — supplemented when possible by the 2-km LHO detector. Astrowatch terminated when the enhanced detectors began operating in July 2009.

Due to limiting infrastructure and the topology of the site, which prevents any increase in the arm length, GEO600 can not undergo a major upgrade in the fashion of the advanced LIGO and Virgo detectors. However, significant improvements through small sequential changes can be made to reduce noise sources at high frequencies in the kHz region where, for example, normal modes in neutron stars or quasi-normal modes in black holes provide interesting gravitational wave sources. The goal of this GEO-HF program [265] is to improve the sensitivity of the detector in the high-frequency mode by reducing the effect of two limiting noise sources, namely shot noise and coating thermal noise. In such a configuration, GEO will be the most sensitive detector at high frequencies and will be used to search for sources whenever the detection strategy of the worldwide detector network allows it.

*CNRS: Centre national
de la recherche
scientifique*

*INFN: Istituto
Nazionale di Fisica
Nucleare*

Tama is the area of Tokyo where the observatory is situated, and “tamatama” is Japanese for “casually, unexpectedly, by chance”

CLIO: Cryogenic Laser Interferometer Observatory

AIGO: Australian International Gravitational Observatory

“Sweet spot” is the common name to refer to the most sensitive part of the detector

TAMA300 is a 300-m baseline gravitational-wave detector located at the Mitaka campus of the National Astronomical Observatory of Japan ($35^{\circ}40'31''$ N $139^{\circ}32'4''$ E). It is a project of the gravitational-wave studies group at the Institute for Cosmic Ray Research (ICRR) of the University of Tokyo. Its construction started in 1995; joint operation with LIGO and GEO600 took place until 2004. Due to its modest size, TAMA300 is seen as a step towards a larger-scale interferometer in the sense of technology and construction budget. That future project is the Large Scale Cryogenic Gravitational Wave Telescope (LCGT), which pursues the goal of detecting at least one gravitational wave event per year at a sensitivity comparable to that of Advanced LIGO and Virgo and two orders of magnitude better than TAMA300. LCGT is currently being constructed and will consist of two sets of interferometers with 3 km-long arms located underground in a tunnel of the Kamioka mine in Japan. Whereas TAMA300 plays an important role as test bed for interferometer operations and advanced vibration-isolation systems, CLIO, a 100 m-baseline underground cryogenic interferometer, shall prove the feasibility of a cryogenic installation in the Kamioka mine. The LCGT mirrors, made of sapphire and cooled down to temperatures of 20 K, will reduce thermal vibrations of the material.

Given the fact that all the detectors described so far are located in the Northern hemisphere, it becomes apparent that the addition of one in the Southern hemisphere would greatly improve the world-wide network of interferometers [236]. The AIGO site at Gingin, north of Perth in Western Australia ($31^{\circ}21'27.6''$ S $115^{\circ}42'50''$ E) was carefully chosen for its convenience to host such a facility. Currently, the AIGO research facility consists of a 80 m interferometer, but a proposal is underway to build a 5 km-long detector which could join Advanced LIGO, Advanced Virgo, GEO-HF and LCGT in what would constitute the most sensitive gravitational-wave data-taking effort to date.

The sensitivity of currently-operating gravitational-wave interferometers has steadily improved over the last decade. With every new experimental challenge, an improved noise curve has been obtained, which means that the detectors' reach to astrophysical sources of gravitational radiation increases. Figure 4 displays the strain sensitivity curves corresponding to the ground-based interferometers in operation during S5/VSR1. The curves show the status of the three LIGO detectors in summer 2007 in red, blue and green, the Virgo detector in May 2008 in purple and the GEO600 detector in June 2006 in black.

Figure 4 illustrates in practice the diverse noise sources affecting the detectors that were described in section 1.3. At low frequencies below 50 Hz for GEO600 and 40 Hz for LIGO, the seismic wall appears. The special suspension technology of Virgo makes it specially competitive down to 10 Hz, which should enable the observation of many more cycles for the merger of compact objects and a broader frequency band to search for signals from spinning pulsars. In the intermediate frequency band between 50 and 200 Hz, the suspension thermal noise becomes dominant. The LIGO detectors are the most sensitive in this region, with their *sweet spot* of maximum sensitivity located at around 150 Hz. At high frequencies, the sensitivity of all detectors worsens again due to the presence of photon shot noise. The future GEO-HF will be optimized for these high frequencies and is expected to show improved sensitivity in the kHz region. For comparison, the design sensitivity curves

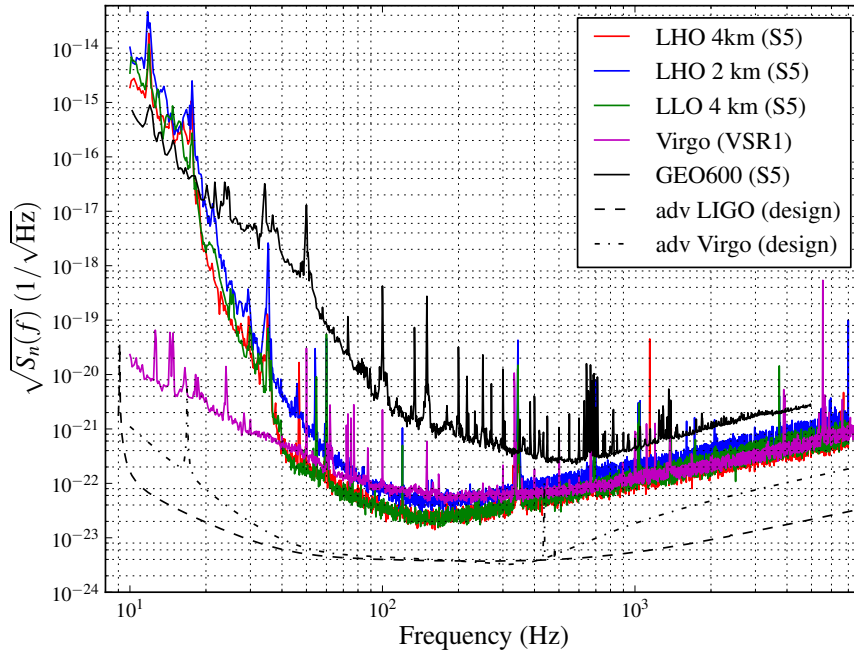


Figure 4: Strain sensitivity curves for the ground-based interferometers in operation during S_5/VSR_1 , the last run before the LIGO and Virgo detectors underwent their “enhancement” upgrades. The solid curves correspond to the three LIGO detectors as of summer 2007, the Virgo detector as of May 2008 and the GEO600 detector as of June 2006. For comparison, the dashed curves show the design reference noise budget of Advanced LIGO and Virgo.

of the second-generation detectors Advanced LIGO and Virgo described in section 1.5.1 are shown in figure 4 as well.

1.5 THE FUTURE OF GRAVITATIONAL-WAVE ASTRONOMY

1.5.1 *The Advanced Interferometers*

The following years will see significant sensitivity improvement of the detectors and more extensive upgrades in what will constitute a second generation of gravitational-wave interferometers. Advanced LIGO and Virgo will replace their existing hardware with new technology, with the goal of gaining a factor of 10 in improved sensitivity with respect to the first-generation detectors. One of the most significant consequences of the upgrades in the suspension systems of LIGO will be the reduction of the seismic cut-off frequency from the existing 40 Hz value in initial LIGO to 10 Hz for the advanced detector. To improve the sensitivity limited by the quantum noise, the laser power will be increased from the 10 W of initial LIGO to ~ 200 W. A signal recycling mirror will give the advanced detectors the ability to tune the interferometer frequency response, so that the sensitivity can be optimized for detection of different kinds of astrophysical sources.

The second generation of ground-based interferometers will most likely inaugurate an era of routine gravitational-wave observations, as its physical reach during their first several hours of operation will exceed the integrated observations of the first year LIGO science run. If the current instruments do

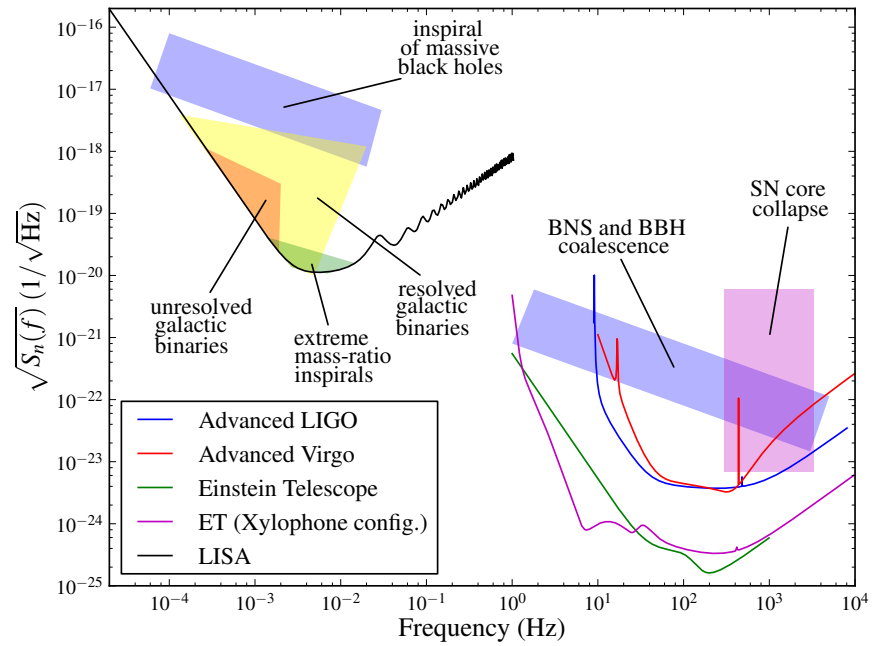


Figure 5: Expected sources of gravitational waves for future ground-based and space-borne detectors. Advanced and third-generation ground-based detectors are expected to detect compact binaries formed by neutron stars, stellar-mass black holes and, eventually, intermediate-mass black holes, as well as signals from supernovæ core collapse. The space antenna LISA focuses on low-frequency signals coming from coalescence of supermassive black holes, extreme mass-ratio inspirals and galactic binaries.

not make the first detection of GWs, the second-generation interferometers should succeed.

1.5.2 Third-Generation Ground-Based Detectors

The fundamental low-frequency limitations of the second-generation detectors are given by thermal, gravity gradient and seismic noise, as explained in section 1.3. To circumvent these problems, yet a third generation of interferometers to be operated underground is currently being proposed. The Einstein Telescope (ET) will be a 10 km laser-interferometer with a sensitivity 100 times larger than that of the current detectors. Moreover it will cover the frequency range between 1 Hz and 10^4 Hz, increasing the ability to detect massive BBHs which merge at frequencies lower than the cut-off values of LIGO and Virgo. Once the design study and the technical preparation phase are completed, construction could begin after the second-generation observatories have started operation, probably before the end of the next decade.

The frequency range that the ET will be able to probe and its expected sensitivity could make this third-generation, ground-based interferometer a complementary companion for the space antenna LISA described in section 1.5.3, a very advantageous fact, since these two detectors might well be operating simultaneously in the future. Whereas the geometry of the current ground-based detectors requires a multi-site network to measure the polarization of the GW signal, the ET design will be able to do so by itself,

<http://www.et-gw.eu/>

benefiting from two coaligned, coplanar detectors at a single site. The currently favored design contains three independent detectors arranged in an equilateral-triangle geometry. The expected sensitivity curve for this “baseline” design of the ET is shown in Figure 5. An alternative “xylophone” configuration of the ET has been proposed [151], which trades off improved sensitivity near 10 Hz for decreased sensitivity at higher frequencies. The ability to operate either in broad- or narrow-band mode —within the frequency range where the noise budget is limited by photon-shot noise— in order to optimize the sensitivity to targeted astrophysical sources is a common characteristic of the proposed ET and the Advanced LIGO and Virgo detectors.

1.5.3 *LISA: The Space Antenna*

LISA completes the family of gravitational-wave detectors and represents a qualitative step forward in the exploration of the gravitational-wave spectrum. LISA will operate in orbit around the Sun, and will consist of three widely separated spacecrafts arranged in a triangular configuration. The entire arrangement has been designed with a size ten times larger than the orbit of the Moon.

*LISA: Laser
Interferometer Space
Antenna*

LISA will perform low-frequency gravitational-wave astronomy in the band from 0.03 mHz to above 0.1 Hz; its sources are massive black holes merging at the center of galaxies, binaries of compact stars and stellar remnants in our Galaxy, extreme mass-ratio inspirals in which a star-sized compact object falls into a massive black hole at the center of a distant galaxy and, eventually, other sources of cosmological origin, including the relic radiation from the very early phase of the Big Bang, and speculative astrophysical objects such as cosmic strings. The antenna is expected to be launched within the next ten years. A schematic depiction of the expected sources for the advanced, third-generation and space-borne gravitational-wave detectors is shown in figure 5, including galactic binaries, extreme mass-ratio inspirals, supernovæ core collapse and compact binary coalescences.

Chapter 2 describes the main sources of gravitational radiation reasonably expected to exist in our local universe. According to our present understanding of general relativity and the current progress in the detectors’ sensitivity figures, signals arriving from these sources ought to be detected with the enhanced or advanced detectors over the course of the next years.

Astrophysicists and gravitational-wave physicists work towards understanding the kind of potentially-detectable sources that exist in our Universe. Through the study of electromagnetic radiation by means of traditional astronomy, enormous progress and discoveries of exciting phenomena have taken place during the last century. Most regions of the electromagnetic spectrum have been studied at some level of sensitivity.

The gravitational-wave spectrum constitutes a completely new scenario on its own. In the case of gravity, the conservation of energy, linear momentum and angular momentum prevent radiation due to the acceleration of mass monopoles, mass dipoles and current dipoles respectively. This implies that the leading order radiation comes from the acceleration of mass quadrupoles. Our current knowledge of the composition of the Universe states that only 4% of the mass-energy of the Universe exists in the form of charged particles capable of emitting electromagnetic radiation. Nevertheless, the remaining 96% does couple with gravity and could perhaps emit gravitational waves. Nearly all interesting astrophysical phenomena indeed do so, and usually in copious amounts. The information encoded in gravitational waves is pristine; it comes to us unaffected by the matter it encounters, from the heart of the most fabulous astrophysical events, such as supernovæ explosions or mergers of black-hole binaries.

This chapter succinctly describes the principal sources of gravitational waves that are being searched for with the currently-operating interferometers. These are *stochastic* signals that fluctuate randomly over a long time compared to an observing run; *periodic* waves modeled as superposition of sinusoids that are roughly constant over a long time compared to an observing run; *bursts* that last only a few cycles or for short times compared to an observing run; signals from *coalescing binaries* corresponding to systems that inspiral and/or merge within the observation time. Special emphasis shall be placed on coalescing black-hole binaries, as they constitute the main focus of this thesis.

2.1 STOCHASTIC BACKGROUND

The very early Universe must have been the source of a random sea of gravitational radiation that even today permeates space and acts as an omnidirectional background. Once produced, gravitational waves emitted shortly after the Big Bang would forever carry unaltered information about the physical processes that generated them. The waves are expected to be originated in a large number of unresolved sources, nowadays superimposed forming a stochastic gravitational-wave background. Examples of this type of radiation are relic gravitational waves from inflation, from Galactic binary white-dwarf systems and from slow-spinning Galactic pulsars. Estimations of the stochastic background are usually made by considering the relation between the

Quasars, pulsars, gamma-ray bursts and the cosmic microwave background radiation were not discovered until after 1950

energy density of the gravitational waves Ω_{GW} and the one needed to close the Universe

$$\Omega_{\text{GW}}(f) = \frac{f}{\rho_c} \frac{d\rho_{\text{GW}}}{df}. \quad (2.1)$$

The quantity $d\rho_{\text{GW}}$ is the energy density of gravitational radiation contained in the frequency range f to $f + df$ and ρ_c is the critical density of the Universe.

The expansion of the Universe has cooled down the stochastic radiation — an uncertain aspect in our knowledge of it is its current intensity. Theoretical predictions for the value of Ω_{GW} are affected by large uncertainties depending on the applied model. The optimum detection and characterization strategy for this kind of signal is based on a cross-correlated analysis. A stochastic gravitational-wave background signal would cause random fluctuations in the phase of the output laser, which are indistinguishable from various instrumental noise sources. If a signal is present, however, the randomness is correlated among detectors. Such an analysis has been performed in the LIGO S5 data [12], resulting in a constraint for Ω_{GW} of $\sim 6.9 \times 10^{-6}$ at 95% confidence in the frequency band around 100 Hz, a result that already rules out certain cosmic (super)string models. It is hoped that the advanced detectors will be able to push the upper limit on Ω_{GW} down to 10^{-10} , a result that would lead to further meaningful constraints on other theories of the early Universe. A measurement of the stochastic background of gravitational waves is possibly the most important observation that gravitational-wave detectors can make from the point of view of fundamental cosmology.

2.2 PERIODIC SOURCES

Neutron stars are very compact objects originated from the gravitational collapse of massive stars. Pulsars are highly magnetized, rotating neutron stars that emit a beam of electromagnetic radiation. X-ray observations indicate that most of the rapidly accreting, weakly magnetic neutron stars in the Galaxy have a rotation frequency contained within a narrow band. This apparently remarkable fact can be explained by assuming that the loss of angular momentum is due to emission of gravitation waves [61] through some given mechanism. Currently there are over 200 known pulsars with frequencies larger than 20 Hz, which would fall in the detection band of the ground-based interferometers.

These objects radiate gravitational waves due to a variety of physical processes. Regardless of their origin, they emit a quasiperiodic continuous signal of slowly-changing frequency over the observation time, due to loss of energy in the form of gravitational radiation and, possibly, other mechanisms. Thus, the period of the pulsar steadily lengthens as the pulsar loses energy, a phenomenon known as *spindown*. By measuring the pulsar's spindown rate via electromagnetic observations, an upper limit on its gravitational emission can be set. One of the most relevant results from the LIGO detectors to date has been the determination of a new upper limit on the gravitational wave emission from the Crab pulsar that beats indirect limits inferred from spindown and energy conservation arguments [9].

The mechanisms responsible for an accreting neutron star developing a quadrupolar asymmetry are numerous. Among those that have been proposed are internal r-mode oscillations, magnetic deformations and crustal

The word “pulsar” is a contraction of “pulsating star”. The first pulsar was observed in 1967 by astrophysicist Jocelyn Bell Burnell

mountains. A rapidly rotating neutron star with small deformations from its axially-symmetric shape emits quasiperiodic gravitational waves. This deviation can be expressed by the ellipticity $\varepsilon \equiv (I_{xx} - I_{yy})/I_{zz}$, where I_{xx} , I_{yy} are the components of the star's quadrupole moment along the principal axes in its equatorial plane and I_{zz} is the moment of inertia along its rotation axis. Typical neutron stars with masses $M \sim 1.4 M_{\odot}$ have $3 \times 10^{44} \text{ g cm}^2 \lesssim I_{zz} \lesssim 3 \times 10^{45} \text{ g cm}^2$, depending on the assumed equation of state. The uncertainties in the typical values of ε are much larger. The gravitational wave emitted by a neutron star located at a distance r has a frequency twice its rotation frequency f and can be expressed as [253]

$$h \sim \frac{4\pi^2 G}{c^4} \frac{I_{zz} f^2}{r} \varepsilon \sim 2 \times 10^{-26} \left(\frac{10 \text{ kpc}}{r} \right) \left(\frac{\varepsilon}{10^{-6}} \right) \left(\frac{f}{1 \text{ kHz}} \right)^2. \quad (2.2)$$

The intrinsic amplitude of the signal associated to rotating neutron stars is very small, of the order of $h \sim 10^{-25}$ for a pulsar of $f = 60 \text{ Hz}$ and $\varepsilon = 10^{-5}$ at $r = 1 \text{ kpc}$. Detection can therefore only be achieved by means of long, day-to-weeks integration times that allow to extract the signal from the noise it is buried in. The Doppler effect due to the Earth changing its position by a non-negligible fraction during this long observation times needs to be taken into account. In practice, this kind of searches might become computationally prohibitive, and thus, distributed methods of computation, such as the project ‘‘Einstein@Home’’ are being developed. If gravitational waves from rotating neutron stars are detected, they will provide important information about the star's structure.

<http://www.einsteinathome.org/>

2.3 BURSTS

Our Universe's violent nature manifests itself sporadically in the form of highly-energetic, short-duration bursts of radiation. A variety of astrophysical sources can give rise to such gravitational-wave bursts, being supernovae explosions and other generic gamma-ray bursts the canonical examples. A supernova explosion happens when the compact core of a giant star collapses after having exhausted its supply of energy from nuclear reactions. The burst of radiation released in such an explosion is so energetic that it might outshine an entire galaxy. The exact mechanisms that commence in the star's core and trigger the explosion are unfortunately not yet fully understood. The complexity of the problem requires that any realistic simulation incorporates a large number of physical phenomena: three-dimensional hydrodynamics, neutrino transport, realistic nuclear physics, magnetic fields, rotation. At present the computation of a detailed waveform is not feasible, thus making optimal searches using matched filtering unattainable.

In absence of complete models for the gravitational emission, typical data-analysis strategies to search for gravitational-wave bursts involve looking for excess power in certain frequency bands at specific times, which might or might not be correlated with electromagnetic or neutrino observations — these are known as *externally-triggered* searches. Additionally, burst searches rely on finding evidence of transient signals in coincidence among several gravitational-wave detectors. An estimate of the amplitude of the radiation

from a typical supernova at 10 kpc that emits in 1 ms the energy equivalent of $10^{-7} M_{\odot}$ at 1 kHz can be given by [230]

$$h \sim 6 \times 10^{-21} \left(\frac{E}{10^{-7} M_{\odot}} \right)^{1/2} \left(\frac{1 \text{ ms}}{T} \right)^{1/2} \left(\frac{1 \text{ kHz}}{f} \right) \left(\frac{10 \text{ kpc}}{r} \right). \quad (2.3)$$

A typical search for burst signals in the detectors' output consists on the combination of a signal-processing algorithm together with post-processing and diagnostics tools. The output of a search is a list of “triggers” that are subject to consistency and coincident tests. Upon passing those tests, they are considered gravitational-wave candidates. By definition, and due to their unmodeled nature, burst searches make use of non-optimal and therefore less sensitive detection methods than match-filtered searches. However, they have the advantage that, by not making any assumption on the functional form of the wave to be detected, they might allow detection of sources that we are so far unaware of. Certainly, if another supernova explosion like SN1987a occurred in our galaxy within the next decade, burst detection algorithms would turn out to be excellent tools for its characterization.

2.4 COALESCING BINARIES

Gravitationally-bound binaries formed by compact objects orbiting around each other —such as neutron stars or black holes— undergo a coalescence process in the course of which they emit part of their energy as gravitational radiation. These coalescing binaries are of particular interest to gravitational-wave astronomy because they are among the most promising candidates to be detected in the first place. The gravitational radiation emitted by pairs of neutron stars and/or black holes can be accurately modeled by a variety of analytical and numerical theoretical methods. This implies that searches for these systems can be designed that employ optimal algorithms based on the expected waveforms to be detected. Additionally, coalescing binaries can be used as standard candles for measuring astrophysical distances, since their amplitude is uniquely determined by their phase evolution and the luminosity distance to the source. Finally, coalescing binaries can serve as test probes of General Relativity, for their gravitational-wave signature originates from objects which massively curve space-time and travel at speeds approaching that of light.

2.4.1 Evidence for Compact Binaries

Both observational and theoretical reasons strongly support the existence of neutron stars and black holes in our Universe, as well as their occurrence in gravitationally-bound binary systems, formed either by two neutron stars, two black holes or a neutron star and a black hole. The Chandrasekhar limit of $\sim 1.4 M_{\odot}$ gives a theoretical upper bound for the mass of an electron-degenerate star. This limit is of importance in multiple processes of stellar explosion, such as Type Ia/b/c and II supernovæ, in particular processes that end up in a white dwarf (Type Ia) or when the core of a massive star explodes (Type Ib/c II).

Compact objects with an orbiting companion in a tightly gravitationally-bound orbit have been observed and measured. By tracking down the elliptical

movement of the binary components, an estimation of the masses of both objects is possible. If the masses of the compact objects are larger than the Chandrasekhar limit, then the binary must be formed by either neutron stars or black holes. Associated phenomena such as thermonuclear explosions observed as matter falls onto the compact object help determine whether we are dealing with neutron stars. In absence of matter-associated processes, the binary is formed by black holes, whose spins, among other values, can be determined.

Further experimental evidence, for instance the observation of the orbital period of the Hulse-Taylor pulsar [155, 250], supports the existence of inspiralling compact objects. Determination of the orbital energy loss due to emission of gravitational waves allows for the masses of the binary to be estimated as roughly $1.44 M_{\odot}$ and $1.39 M_{\odot}$. The two objects orbit each other with a period of 8 hours, which corresponds to a separation of $\sim 1 R_{\odot}$. At this separation and given their orbital frequency, it is ruled out that the objects could be ordinary stars, for a much weaker force would result if they were. On the other hand, the absence of observations of electromagnetic counterparts excludes the possibility that these objects were white dwarfs. Recently, the observation of the highly relativistic double pulsar system PSR J0737-3039A/B [171] has provided the most stringent test to date of strong-field gravity. Its mean orbital velocities and accelerations are much higher than those of other known binary pulsars. This system is unique in the sense that both neutron stars are detectable as radio pulsars. Precise timing observations taken over the first few years since its discovery have turned this object into an excellent candidate for testing general relativity.

Confident in the existence of gravitationally-bound binary systems formed by neutron stars and/or black holes in our Universe, the next sections proceed to describe the coalescence process as well as the expected event rates for coalescing binaries.

2.4.2 The Coalescence Process

For a number of practical and theoretical reasons, the process of coalescence of a compact binary is usually divided upon three distinct phases. During the first stage, the two objects are still far from each other and move with non-relativistic velocities in orbits that slowly spiral inwards. This adiabatic phase can be treated perturbatively under the assumptions of a weak gravitational field inside the source and of slow internal motions. The typical velocity of the system is the orbital velocity $v/c \sim \epsilon$, which can be thought of as a perturbative parameter indicating the deviation from the Newtonian regime.

When the Einstein equations introduced in section 1.1.1 are expanded in terms of ϵ , an approximation which is valid if the deviation from the Minkowski flat metric is small, the result is the post-Newtonian formalism. The lowest term in this expansion, corresponding to $\epsilon \rightarrow 0$, gives the well-known quadrupole formula for the gravitational field in the TT coordinate system [64]

$$h_{ij}^{\text{TT}} = \frac{2G}{c^4 D} \mathcal{P}_{ijmn}(\hat{n}) \frac{d^2}{dt^2} Q_{mn}(t - D/c), \quad (2.4)$$

where D is the distance from the observer to the source, $\hat{n} = \vec{x}/D$ is the unit vector in the direction connecting the source with the observer and the symbol

$\mathcal{P}_{ijmn} = \mathcal{P}_{im}\mathcal{P}_{jn} - \frac{1}{2}\delta_{ij}\mathcal{P}_{ij}\mathcal{P}_{mn}$ with
 $\mathcal{P}_{ij} = \delta_{ij} - n_i n_j$ the
 projector operator

\mathcal{P}_{ijmn} represents the TT projection operator onto the plane orthogonal to \hat{n} . The object Q_{ij} is the quadrupole moment of the source, which can be written in terms of the mass density ρ as follows

$$Q_{ij} = \int \rho(\vec{x}, t) \left(x_i x_j - \frac{1}{3} \delta_{ij} x^2 \right) d^3x. \quad (2.5)$$

During the long inspiral phase, the two compact objects forming the binary follow an adiabatic sequence of quasi-circular orbits. The movement of their center of mass can be modelled by a series expansion on two variables, the parameter ϵ and the symmetric mass ratio of the system, defined as

$$\eta = \frac{m_1 m_2}{M}, \quad M = m_1 + m_2. \quad (2.6)$$

The parameter η ranges from 1/4 in the equal-mass case to 0 in the test-mass limit. The validity of the post-Newtonian expansion is limited to situations where $\epsilon \rightarrow 0$ and $\eta \rightarrow 1/4$. This implies that the series does not converge as the two bodies draw closer and enter the strong-field regime — likewise, the approximation is more exact the more similar the masses of the two compact objects are. The more detailed description of the post-Newtonian formulation applied to the binary black-hole problem is given in section 3.1 of chapter 3.

The emission of gravitational radiation progressively leads to the shrinking of the orbit of the binary system, as the two bodies follow the quasi-circular trajectory and enter the strong-curvature phase, when their motion becomes more and more relativistic. Eventually, the system transitions from the adiabatic inspiral to the plunge phase, being the frequency associated to the Innermost Stable Circular Orbit (ISCO) of a test particle in a Schwarzschild space-time a traditionally-used transition point. The ISCO frequency is reached when the two bodies are separated by a distance of $R = 6M$ resulting in

$$f_{\text{ISCO}} = \frac{c^3}{6\sqrt{6}\pi GM}. \quad (2.7)$$

This mass-dependent frequency can be computed for several systems of interest for ground-based interferometers. For instance, $f_{\text{ISCO}}|_{M=2.8 M_\odot} \approx 1570$ Hz whereas $f_{\text{ISCO}}|_{M=30 M_\odot} \approx 150$ Hz. The merger of binaries of neutron stars occurs at frequencies at which the detector's response is dominated by shot noise — the post-Newtonian description is then adequate to describe such binaries while they are within the most sensitive band of the detectors. On the contrary, binaries formed by solar-mass black holes reach the plunge and ringdown stages of their coalescence *while* in the LIGO/Virgo/GEO600 band, hence the corresponding post-Newtonian waveforms terminate too early. Intermediate-mass and supermassive black-hole binaries merge at much lower frequencies and are therefore the target of advanced and/or space-borne detectors, as discussed in chapter 8.

Beyond the ISCO frequency, the real evolution of the system starts diverging significantly from the predictions given by the post-Newtonian formalism. The orbital frequency of the inspiralling system speeds up and the power series breaks up. Non-perturbative methods need to be employed and a full-GR approach is required, i.e. the exact, non-truncated equations for the gravitational field need to be solved. An analytical solution of the Einstein equations is unfortunately not available for the two-body problem and thus, numerical methods become very relevant in this regime. The particular 4-dimensional

At approximately $v/c \sim 0.3$ one can consider that the system is in the strong-field regime

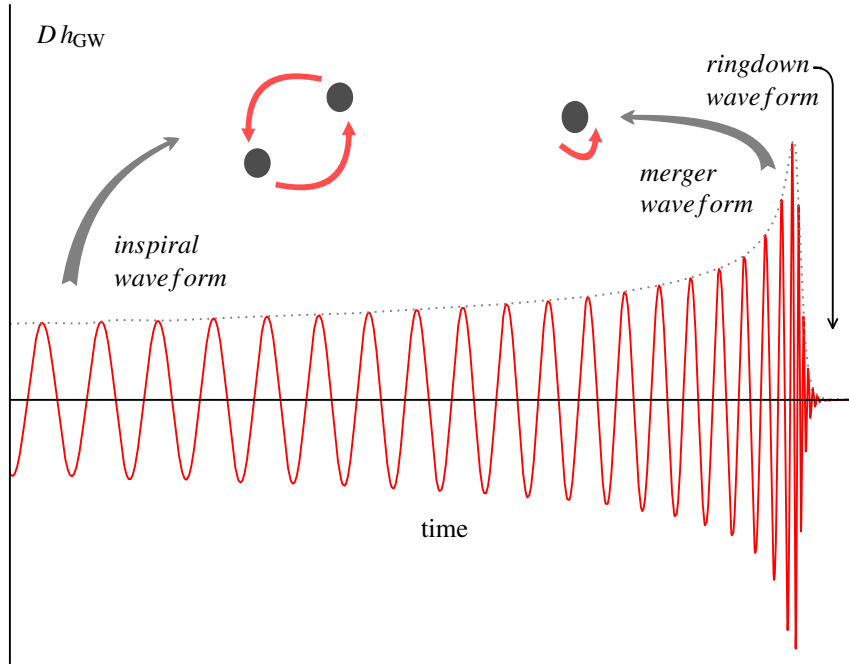


Figure 6: Typical gravitational wave emitted by a coalescing compact binary. The system undergoes a long adiabatic inspiral phase (only the last piece of which is plotted here) while the two bodies approach each other due to loss of energy in the form of gravitational radiation. The inspiral terminates when the two bodies merge, after which they ring down to a final Kerr black hole. The wave depicted in this plot is a hybrid waveform corresponding to an equal-mass, non-spinning, binary black-hole system.

nature of the Einstein equations imply that a 3+1 decomposition in their spatial and time components is required before any attempt of discretizing them is made. This fact has given rise to a whole field of research on well-posedness of the diverse formulations of the decomposed Einstein equations, ever since the first numerical simulations of black-hole binaries were performed by Hahn and Lindquist [139] in the 1960s.

A large body of research exists that studies the plunge of coalescing binaries, both those formed by neutrons stars, black holes and mixed binaries. The presence of a non-zero stress-energy tensor on the right-hand side of equation 1.1 makes numerical simulations with matter considerably more complex than those of black-hole binaries. Nevertheless, and for a number of reasons, fully self-consistent numerical relativity simulations of binary black-hole space-times were inviable in practice until a few years ago — after a series of breakthroughs occurred in 2005 [212, 88, 52], complete numerical simulations of the last stages of the binary black-hole coalescence finally became feasible. The field has quickly blossomed ever since, turning into a powerful tool to test predictions of general relativity in the strong-curvature regime, and becoming an important element in the obtaining of accurate and complete waveform templates for binary black-hole coalescence to be used in gravitational-wave searches. The key results achieved by the numerical relativity community over the past years, which constitute one of the pillars of the work developed in this dissertation, are presented in chapter 4.

The final fate of the binary after its plunge and merger is a single spinning black hole that relaxes towards stationarity while it radiates all their perturbations away, a process usually called ringdown. The end-state is the only possible axisymmetric and stationary solution in vacuum, the Kerr black hole [164], that according to the *no-hair* theorem only carries information about its mass and spin. The gravitational wave emitted by the system can be analytically calculated making use of perturbation theory, as explained in section 3.2 of chapter 3.

Figure 6 summarizes in a graphical way what has been exposed so far about the gravitational signature of compact binaries. Plotted is the typical gravitational wave emitted by a coalescing compact binary formed by a pair of black holes. The figure shows the last part of the long adiabatic inspiral phase that eventually transitions into the plunge regime after which the two objects merge and ring down to the final Kerr black hole. The increasing frequency and amplitude of the wave as the two coalescing objects approach each other is clearly visible. The signal displayed in figure 6 is a hybrid waveform corresponding to a non-spinning, equal-mass black-hole binary system obtained with the method described in chapter 5.

2.4.3 Expected Astrophysical Rates for Compact Binaries

The volume of the Universe that current gravitational-wave detectors are capable of surveying and the increased observable volume that the advanced detectors would be able to explore make a natural question arise: what are the expected rates of coalescing binaries thought to exist in our neighbouring Universe? Theoretical predictions of astrophysical event rates are crucial to the detection process. A clear understanding of these numbers can provide essential input for questions relevant to which one of the various possible configurations of the advanced detectors is optimal. Additionally, as the sensitivity of the detectors improve, gravitational-wave observations will start yielding astrophysically-interesting upper limits. Some models that predict high detection rates could be ruled out, and constraints could be placed on quantities such of the strength of massive-star winds and the kick velocities of merged compact objects.

Based on the ample work done in the field of predictions of astrophysical rates for compact binaries, a compilation of the state-of-the-art expectations is presented here. The results follow the discussion presented in [1]. Significant uncertainties affect the predictions of astrophysical rates for compact binary coalescences, that can have an error bar of a couple of orders of magnitude.

Table 1: Terminology for statements related to astrophysical rates. The symbols R refer to rates per galaxy; the symbols N represent detection rates

Abbreviation	Rate statement	Physical significance
R_{\max}, \dot{N}_{\max}	Upper limit	Rates should be no higher than...
$R_{\text{high}}, \dot{N}_{\text{high}}$	Plausible optimistic estimate	Rates could reasonably be as high as...
$R_{\text{re}}, \dot{N}_{\text{re}}$	Realistic estimate	Rates are likely to be...
$R_{\text{low}}, \dot{N}_{\text{low}}$	Plausible pessimistic estimate	Rates could reasonably be as low as...

Table 2: Compact binary coalescence rates per Mpc^3 per Myr. Quoted are the expected rates for neutron-star, mixed and black-hole binaries, where the latest are taken to be stellar-mass black holes of $10 M_{\odot}$. For a discussion on the expected rates of intermediate-mass black-hole binaries, see chapter 8.

Source	R_{low}	R_{re}	R_{high}	R_{max}
NS-NS ($\text{Mpc}^{-3} \text{ Myr}^{-1}$)	0.01 [162]	1 [162]	10 [162]	50 [166]
NS-BH ($\text{Mpc}^{-3} \text{ Myr}^{-1}$)	6×10^{-4} [196]	0.03 [196]	1 [196]	—
BH-BH ($\text{Mpc}^{-3} \text{ Myr}^{-1}$)	1×10^{-4} [160]	0.005 [160]	0.3 [160]	—

Nevertheless, a range of rates can be quoted that expresses the plausible optimistic, likely and plausible pessimistic estimates. Table 1 introduces the terminology used to refer to these concepts. R_{re} refers to the mean of the posterior probability density function for the rates, R_{low} and R_{high} are the 95% pessimistic and optimistic confidence intervals, respectively, and R_{max} is the upper limit.

Rates are usually expressed in events per Myr per Milky Way Equivalent Galaxy, events per Myr per Mpc^3 or events per Myr per L_{10} , where L_{10} is 10^{10} times the blue solar luminosity $L_{B,\odot}$. Here we present the most up-to-date compact binary merger rates per unit volume. The references in table 2 provide further information on the assumptions that these rates are based on.

$$L_{B,\odot} = 2.16 \times 10^{33} \text{ erg/s}$$

In order to convert these merger rates into detector rates, a number of assumptions need to be made regarding the characteristic of the detectors, the network of interferometers and the data analysis strategies that are followed in the searches. The figures quoted in table 3 have been computed considering a volume of the observable Universe such that the LIGO/Virgo network would detect a compact binary with a signal-to-noise ratio of 8. This is a conservative choice if the detector noise is Gaussian and stationary and if there are two or more detectors operating in coincidence. Additionally, a post-Newtonian stationary-phase approximation is assumed for the functional form of the gravitational wave originated by the binary coalescence. This neglects the fact that the most massive binaries merge and ring down within the detector band and thus, the signal-to-noise ratio is underestimated. A further assumption is made by considering that all neutron stars have a mass of $1.4 M_{\odot}$ and all black holes a mass of $10 M_{\odot}$ — our knowledge of the mass distribution is not sufficient at present to warrant more detailed models, and the uncertainties in the coalescence rates dominate errors from the simplified assumptions about component masses.

Given the constraints mentioned above, the detection rates expected for the initial and advanced ground-based interferometers are quoted in table 3 for neutron-star, mixed and black-hole binaries of stellar mass. It is immediate to note that even the most optimistic estimates predict relatively low for the initial interferometers; nonetheless, a lucky detection with the enhanced detectors should not be ruled out. The chances that compact binaries are detected with the advanced detectors look however much more promising, for tens to hundreds of compact binaries are realistically expected to exist within the reach of the interferometers. In this section we have concentrated on neutron-stars and stellar-mass black-hole binaries. For a more detailed discussion on

Table 3: Detection rates for compact binary coalescence sources. Even the optimist estimates predict low rates in the initial interferometers — however, detection is plausible with the advanced instruments.

Detector	Source	\dot{N}_{low} (yr ⁻¹)	\dot{N}_{re} (yr ⁻¹)	\dot{N}_{high} (yr ⁻¹)	\dot{N}_{max} (yr ⁻¹)
Initial	NS-NS	2×10^{-4}	0.02	0.2	0.6
	NS-BH	7×10^{-5}	0.004	0.1	—
	BH-BH	2×10^{-4}	0.007	0.5	—
Advanced	NS-NS	0.4	40	400	1000
	NS-BH	0.2	10	300	—
	BH-BH	0.4	20	1000	—

rates and possible detection of *intermediate-mass* black holes with advanced detectors we refer the reader to chapter 8.

This chapter has provided an overview of the possible sources of gravitational waves that are being searched for in the output of the current interferometers. The focus has been put on the description of coalescing binaries, for they are the main topic of this thesis. The next chapters describe in more detail the analytical and numerical tools relevant for computing the gravitational radiation associated to black-hole binaries with aligned spins and introduce the phenomenological model developed for these systems.

Part II

MODELING BINARY BLACK-HOLE COALESCENCES

The complex, non-linear structure of the Einstein equations poses a non-trivial challenge when one tries to find an exact analytical solution. The final object to search for is a suitable metric describing the structure of the space-time, including the inertial motion of objects in it. In order to do so, the stress-energy tensor on the right-hand side needs to be calculated, which in turn depends on the *unknown* metric. If only interested in the weak-field limit of the theory, the dynamics of matter can be computed using special relativity methods and/or Newtonian laws of gravity and then placing the resulting stress-energy tensor into the Einstein field equations. But if the exact solution is required or a solution describing strong fields, the evolution of the metric and the stress-energy tensor must be solved for together.

The particular case of the two-body problem —the dynamics of two structureless point-particles, characterized solely by their masses and, possibly, their spins, moving under their mutual, purely gravitational interaction— has no known complete solution. Even writing down the equations of motion for this system is difficult. Unlike in Newton's theory, it is impossible to express the acceleration by means of the positions and velocities, in a way which would be valid within the exact theory. Therefore we are obliged to resort to approximation methods. The nature of the adiabatic inspiral phase of the binary black-hole coalescence makes the post-Newtonian approximation particularly suitable to describe the evolution of the system until the two compact objects approach the merger and the strong-field regime dominates. Likewise, once the two compact objects merge, the final state is reduced to a single black hole, for which known, exact solutions to the Einstein equations do exist. Perturbations of these solutions around the equilibrium give rise to emission of gravitational radiation, and analytical methods exist to describe this phenomenon.

In this chapter these two analytical approaches to the modeling of the inspiral and ringdown stages of the binary black-hole coalescence are reviewed. These formalisms are of importance for the construction of the phenomenological model presented in chapter 5.

3.1 POST-NEWTONIAN FORMALISM FOR NON-PRECESSING BINARIES

Coalescing compact binaries such as the binary black-hole system can be accurately modeled by the post-Newtonian approximation to general relativity at least during the major part of the long inspiral phase, under the assumptions of a weak gravitational field. The full general relativity equations are approximated by a series on the expansion parameter $\epsilon \sim (v/c)^2 \sim (Gm/rc^2)$, where r is the separation between the two point masses and v the magnitude of their relative velocity. In order to compute a post-Newtonian waveform for the gravitational radiation, it is necessary to solve the equations of motion and the generation of gravitational waves.

The two-body equations of motion can be reduced to relative equations of motion in the center-of-mass frame, and expressions for them up to dif-

This approach is based on a formal expansion of the Einstein equations when the velocity of light c tends to infinity

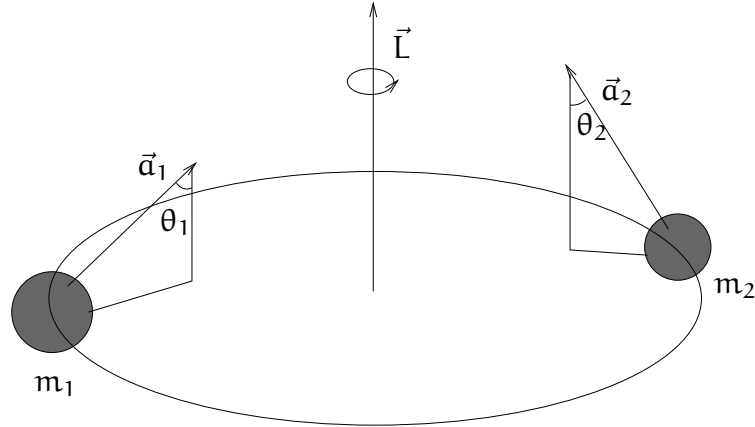


Figure 7: Pictorial representation of a binary black-hole system in a quasicircular orbit. In the most general case the black holes are rotating with their spins given by \vec{a}_1 and \vec{a}_2 . The particular subset of physical configurations that we are interested in modeling here are those for which the orbit is non-precessing, i.e. $\theta_1 = \theta_2 = 0$.

PN orders are named according to the power in the $(v/c)^n$ expansion. Thus, 3.5PN represents terms of order $(v/c)^7$ beyond quadrupole

See e.g. [40]

ferent PN orders can be found in the literature. For a complete overview and description of the achievements in the field, the reader is referred to the review article [64]. In the most general configuration of the binary black-hole problem, the spins of the black holes are randomly oriented and, thus, the orbit precesses. A pictorial representation can be seen in figure 7.

The dimensionality of the parameter space of a spinning binary is considerably larger than the equivalent non-spinning system. Assuming the black holes to be well described by a mass and a spin vector (ignoring higher multipoles), and their trajectory to be well described by adiabatically evolving Keplerian orbits, we need 17 parameters to describe the binary system. Besides the two masses and spin vectors, we also need a fiducial time t_0 and orbital phase ϕ_0 at t_0 , the distance to the source and its sky-location, two parameters for the unit vector normal to the orbital plane, and finally if we consider eccentricity then we additionally need the eccentricity and the direction of the semi-major axis. Sufficiently close to or during the merger, this description in terms of Keplerian orbit will break down, and higher order black hole multipoles might play a role as well.

As a first step towards the understanding of the full parameter space, a subset of configurations can be studied. This dissertation deals with the study of binaries where both black holes have *aligned* or *antialigned* spins with respect to the direction of the total angular momentum. Previous works on post-Newtonian evolutions show evidence that, given generic initial conditions, the system evolves towards stable configurations with spin vectors around a fixed orientation [233], although this restriction seems to apply only to certain sections of the parameter space. Similar hints pointing to the existence of a rich structure for some regions of initial inspiral conditions have been presented in [176, 150].

Hence, as a natural expansion of the parameter space encompassed by our waveform models, the physical configurations that we will study in this dissertation are those corresponding to non-precessing, spinning binaries.

Additionally we will work in the frequency rather than in the time domain. The justification for this choice will become clear in view of the matching and fitting techniques developed in chapter 5.

In this chapter we focus on the post-Newtonian treatment for this kind of systems, which we know is accurate at least during the major part of the long inspiral part of the coalescence, under the assumptions of a weak gravitational field [64]. In order to obtain an analytical description of the early inspiral in the Fourier domain we construct the *TaylorF2* phase [100, 101, 102, 43] and the 3PN amplitude [67, 42] for compact binaries with comparable masses and spins aligned with the orbital angular momentum. Each black hole is characterized by its mass m_i and the magnitude of its spin vector

$$S_i = |\chi_i| m_i^2, \quad i = 1, 2. \quad (3.1)$$

The spin vectors are aligned or antialigned with the orbital angular momentum \vec{L} , where the sign of $\vec{L} \cdot \vec{S}_i$ is given by the sign of χ_i . Useful quantities in the post-Newtonian formalism are the symmetric mass ratio 2.6, the total mass and the chirp mass

$$\mathcal{M} = \eta^{3/5} M. \quad (3.2)$$

The PN expansion is written in the dimensionless variable x , which is related to the orbital frequency ω of the binary via

$$x = \omega^{2/3}. \quad (3.3)$$

3.1.1 Energy and Flux

Two key quantities in the post-Newtonian formalism are the binding energy of the center-of-mass E and the gravitational-wave flux \mathcal{L} . The post-Newtonian expansion for the energy of inspiralling compact binary systems in the adiabatic approximation is published in the literature, see for instance [64, 104, 66, 81] and references therein. For our purposes we include leading order and next-to-leading order spin-orbit effects [165, 40, 65] as well as spin-spin effects that appear at relative 2PN order [165, 97, 205]. The explicit expression for the energy for non-precessing spinning black-hole binaries can be written as

$$E = -\frac{x\eta}{2} \sum_{k=0}^6 e_k x^{k/2}, \quad (3.4)$$

with

$$\begin{aligned} e_0 &= 1, & e_1 &= 0, & e_2 &= -\frac{3}{4} - \frac{\eta}{12}, \\ e_3 &= \frac{8}{3} (S_1 + S_2) + 2\eta(\chi_1 + \chi_2), \\ e_4 &= -\frac{27}{8} - (\chi_1^2 m_1^2 + \chi_2^2 m_2^2) + \eta \left(\frac{19}{8} - 2\chi_1 \chi_2 \right) - \frac{\eta^2}{24}, \\ e_5 &= \frac{72 - 31\eta}{9} (S_1 + S_2) + \frac{\eta(9 - 10\eta)}{3} (\chi_1 + \chi_2), \\ e_6 &= -\frac{675}{64} + \eta \left(\frac{34445}{576} - \frac{205\pi^2}{96} \right) - \frac{155\eta^2}{96} - \frac{35\eta^3}{5184}. \end{aligned}$$

Note that the square terms in the individual spins are only valid for black holes, as discussed in [97, 205, 81]

Since the numerical relativity data that we will use in our phenomenological model presents constant spin magnitudes, we use here the corresponding post-Newtonian spin definition [116, 65].

The other necessary component in the description of an inspiralling black-hole binary as a sequence of quasi-circular orbits is the flux \mathcal{L} , which we take at 3.5PN order including the same spin effects as for the energy. Additionally, we take into account the 2.5PN correction of the flux due to the energy flow into the black holes, as calculated in [32]. The final expression reads

$$\mathcal{L} = \frac{32}{5}\eta^2 x^5 \sum_{k=0}^7 \ell_k x^{k/2}, \quad (3.5)$$

with the coefficients ℓ_k given by

$$\begin{aligned} \ell_0 &= 1, & \ell_1 &= 0, & \ell_2 &= -\frac{1247}{336} - \frac{35\eta}{12}, \\ \ell_3 &= 4\pi - \frac{11}{4}(S_1 + S_2) - \frac{5\eta}{4}(\chi_1 + \chi_2), \\ \ell_4 &= -\frac{44711}{9072} + 2(\chi_1^2 m_1^2 + \chi_2^2 m_2^2) \\ &\quad + \eta \left(\frac{9271}{504} + \frac{31}{8}\chi_1\chi_2 \right) + \frac{65\eta^2}{18}, \\ \ell_5 &= -\pi \left(\frac{8191}{672} + \frac{583}{24}\eta \right) + (S_1 + S_2) \left(\frac{135}{112} + \frac{1189}{126}\eta \right) \\ &\quad + (\chi_1 + \chi_2) \left(\frac{51}{16}\eta - \frac{15}{7}\eta^2 \right) - \frac{3}{4}(\chi_1^3 m_1^3 + \chi_2^3 m_2^3), \\ \ell_6 &= \frac{16\pi^2}{3} + \frac{6643739519}{69854400} - \frac{1712\gamma_E}{105} - \frac{856}{105} \ln(16x) \\ &\quad + \eta \left(\frac{41\pi^2}{48} - \frac{134543}{7776} \right) - \frac{94403\eta^2}{3024} - \frac{775\eta^3}{324}, \\ \ell_7 &= \pi \left(-\frac{16285}{504} + \frac{214745\eta}{1728} + \frac{193385\eta^2}{3024} \right). \end{aligned} \quad (3.6)$$

The symbol $\gamma_E \approx 0.5772$ represents the Euler constant.

3.1.2 TaylorT4 Approximant

The post-Newtonian adiabatic model assumes that the motion of the binary components proceeds along an adiabatic sequence of quasi-circular orbits. In particular, the assumption is that $\dot{r} = 0$ and the following energy-balance equation holds

$$\frac{dE(t)}{dt} = -\mathcal{L}(t), \quad (3.7)$$

which, when using 3.3, translates into an evolution equation for the orbital frequency, or equivalently

$$\frac{dx}{dt} = -\frac{\mathcal{L}(x)}{dE(x)/dx}. \quad (3.8)$$

Taking equation 3.8 as starting point, diverse manipulations can be made that lead to different waveform models, as summarized in [69, 86]. For instance,

numerically solving 3.8 leads to the *TaylorT1* post-Newtonian approximant. Alternatively, we may explicitly construct the *TaylorT4* approximant, which is obtained by expanding the right-hand side of 3.8 to 3.5PN order.

$$\frac{dx}{dt} = \frac{64}{5} \eta x^5 \sum_{k=0}^7 a_k x^{k/2}, \quad (3.9)$$

with the following coefficients

$$\begin{aligned} a_0 &= 1, & a_1 &= 0, & a_2 &= -\frac{743}{336} - \frac{11\eta}{4}, \\ a_3 &= 4\pi - \frac{113}{12} (S_1 + S_2) - \frac{25\eta}{4} (\chi_1 + \chi_2), \\ a_4 &= \frac{34103}{18144} + 5 (\chi_1^2 m_1^2 + \chi_2^2 m_2^2) \\ &\quad + \eta \left(\frac{13661}{2016} + \frac{79}{8} \chi_1 \chi_2 \right) + \frac{59\eta^2}{18}, \\ a_5 &= -\pi \left(\frac{4159}{672} + \frac{189}{8} \eta \right) - (S_1 + S_2) \left(\frac{26387}{1008} - \frac{6427}{168} \eta \right) \\ &\quad - (\chi_1 + \chi_2) \left(\frac{473}{84} \eta - \frac{1245}{56} \eta^2 \right) - \frac{3}{4} (\chi_1^3 m_1^3 + \chi_2^3 m_2^3), \\ a_6 &= \frac{16447322263}{139708800} - \frac{1712}{105} \gamma_E + \frac{16\pi^2}{3} - \frac{856}{105} \ln(16x) \\ &\quad + \eta \left(\frac{451\pi^2}{48} - \frac{56198689}{217728} \right) + \frac{541}{896} \eta^2 - \frac{5605}{2592} \eta^3, \\ a_7 &= -\pi \left(\frac{4415}{4032} - \frac{358675}{6048} \eta - \frac{91495}{1512} \eta^2 \right). \end{aligned} \quad (3.10)$$

Note that the formal re-expansion of the denominator and the multiplication with the numerator in 3.8 yields contributions to higher orders than those in 3.9. However, since 4PN and higher terms in flux and energy are not completely determined so far, the expressions that one can compute for a_k with $k > 7$ are incomplete. The same applies for contributions of the spins at relative PN orders higher than 2.5PN. When we later use the *TaylorT4* expression 3.9, we only expand it to 3.5PN order but keep all the spin expressions, i.e. (incomplete) contributions in a_6 and a_7 are not neglected.

3.1.3 Stationary Phase Approximation and TaylorF2

Consider a gravitational-wave complex signal in the time domain of the form

$$h(t) = A(t) e^{i\Phi(t)}. \quad (3.11)$$

If the amplitude of the signal varies slowly in a time scale compatible with the frequency of the oscillation, i.e.

$$\frac{\dot{A}}{A} \ll \dot{\Phi} \quad \forall t, \quad (3.12)$$

then the analytical Fourier transform of the wave can be easily calculated. This stationary phase approximation holds well in the case of the long adiabatic

inspiral. As a result, the *TaylorF2* expression for the phase can be obtained [100, 101, 102, 43]. Firstly, the expansion of the the inverse of equation 3.8,

$$\frac{dt}{dx} = -\frac{dE/dx}{\mathcal{L}}, \quad (3.13)$$

allows us to analytically integrate $t(x)$. The orbital phase ϕ can be integrated via

$$\frac{d\phi}{dt} = \omega = x^{3/2} \Rightarrow \frac{d\phi}{dx} = -x^{3/2} \frac{dE(x)/dx}{\mathcal{L}(x)} \quad (3.14)$$

to obtain $\phi(x)$. This is the *TaylorT2* approximant. The decomposition of the gravitational wave into modes using spin-weighted spherical harmonics ${}^{-2}Y_{lm}$ allows us to express each component in the time domain as [67]

$$h^{lm}(t) = A^{lm}(t) e^{-im\phi(t)}, \quad (3.15)$$

The transformation to the frequency domain is made in the framework of the stationary phase approximation,

$$\tilde{h}^{lm}(f) = \int_{-\infty}^{\infty} h^{lm}(t) e^{2\pi i f t} dt \approx A^{lm}(t_f) \sqrt{\frac{2\pi}{m\ddot{\phi}(t_f)}} e^{i\psi^{lm}(f)}, \quad (3.16)$$

where t_f is defined as the moment of time at which the instantaneous frequency coincides with the Fourier variable, i.e., $m\omega(t_f) = 2\pi f$. The phase in the frequency domain is given by

$$\psi^{lm}(f) = 2\pi f t_f - m\phi(t_f) - \frac{\pi}{4}. \quad (3.17)$$

Given $t(x)$ and $\phi(x)$ the change to the Fourier variable is done through the change

$$x(t_f) = [\omega(t_f)]^{2/3} = \left(\frac{2\pi f}{m}\right)^{2/3}. \quad (3.18)$$

Applying this machinery to the energy 3.4 and flux 3.5 leads to an expression for the phase of the dominant mode $l = 2$, $m = 2$ of the gravitational-wave signal

$$\psi^{22}(f) = 2\pi f t_0 - \phi_0 - \frac{\pi}{4} + \frac{3}{128\eta} (\pi f)^{-5/3} \sum_{k=0}^7 \alpha_k (\pi f)^{k/3}, \quad (3.19)$$

with

$$\begin{aligned} \alpha_0 &= 1, & \alpha_1 &= 0, & \alpha_2 &= \frac{3715}{756} + \frac{55\eta}{9}, \\ \alpha_3 &= -16\pi + \frac{113}{3}(S_1 + S_2) + 25\eta(\chi_1 + \chi_2), \\ \alpha_4 &= \frac{15293365}{508032} - 50(\chi_1^2 m_1^2 + \chi_2^2 m_2^2) \\ &\quad + \eta \left(\frac{27145}{504} - \frac{395}{4} \chi_1 \chi_2 \right) + \frac{3085\eta^2}{72}, \end{aligned}$$

$$\begin{aligned}
\alpha_5 &= \ln(\pi f) \left[\pi \left(\frac{38645}{756} + \frac{65}{9} \eta \right) - (S_1 + S_2) \left(\frac{683665}{2268} + \frac{3790}{63} \eta \right) \right. \\
&\quad \left. - (\chi_1 + \chi_2) \left(\frac{37265}{252} \eta + \frac{3400}{63} \eta^2 \right) \right. \\
&\quad \left. - \frac{10}{3} (\chi_1^3 m_1^3 + \chi_2^3 m_2^3) \right], \\
\alpha_6 &= \frac{11583231236531}{4694215680} - \frac{640\pi^2}{3} - \frac{6848}{21} \gamma_E - \frac{6848}{63} \ln(64\pi f) \\
&\quad + \eta \left(\frac{2255\pi^2}{12} - \frac{15737765635}{3048192} \right) + \frac{76055}{1728} \eta^2 - \frac{127825}{1296} \eta^3, \\
\alpha_7 &= \pi \left(\frac{77096675}{254016} + \frac{378515}{1512} \eta - \frac{74045}{756} \eta^2 \right). \tag{3.20}
\end{aligned}$$

From 3.17 it can be noticed that, in fact, the expression for the phase 3.19 is valid not only for the $l = 2$, $m = 2$ mode, but also for all spherical harmonics with $m = 2$. The quantities t_0 and ϕ_0 are arbitrary and arise as constants of integration when calculating $t(x)$ and $\phi(x)$. Note that the calculation of α_5 also leads to contributions not proportional to $\ln(\pi f)$. For given mass ratio and spins, however, these terms are just an additional constant due the pre-factor of the sum in 3.19 and we absorb them in the definition of ϕ_0 . In our implementation of this Fourier-domain phase we also take into account the spin terms that appear after re-expanding at 3PN and 3.5PN order, although they are not complete and therefore not given here.

A similar discussion can be found in [43]

3.1.4 Amplitude

The time-domain amplitude of the gravitational wave has been recently calculated at 3PN order by Blanchet *et al.* [67]. We use the expression given there for the $l = 2$, $m = 2$ mode in combination with the spin corrections provided in [58, 42]. In our notation, the time-domain amplitude is expressed as

$$A^{22}(x) = \frac{8\eta x}{D_L} \sqrt{\frac{\pi}{5}} \sum_{k=0}^6 \mathcal{A}_k x^{k/2}, \tag{3.21}$$

where D_L is the luminosity distance between the source and the observer and the coefficients are given by

$$\begin{aligned}
\mathcal{A}_0 &= 1, \quad \mathcal{A}_1 = 0, \quad \mathcal{A}_2 = -\frac{107}{42} + \frac{55}{42} \eta, \\
\mathcal{A}_3 &= 2\pi + \frac{2}{3} (m_2 - m_1) (\chi_1 - \chi_2) - \frac{2}{3} (1 - \eta) (\chi_1 + \chi_2), \\
\mathcal{A}_4 &= -\frac{2173}{1512} - \eta \left(\frac{1069}{216} - 2\chi_1 \chi_2 \right) + \frac{2047}{1512} \eta^2, \\
\mathcal{A}_5 &= -\frac{107\pi}{21} + \eta \left(\frac{34\pi}{21} - 24i \right), \\
\mathcal{A}_6 &= \frac{27027409}{646800} - \frac{856\gamma_E}{105} + \frac{428i\pi}{105} + \frac{2\pi^2}{3} + \eta \left(\frac{41\pi^2}{96} - \frac{278185}{33264} \right) \\
&\quad - \frac{20261\eta^2}{2772} + \frac{114635\eta^3}{99792} - \frac{428}{105} \ln(16x). \tag{3.22}
\end{aligned}$$

In order to construct the Fourier-domain amplitude as given by 3.16, an explicit expression for $\ddot{\phi} = d^2\phi/dt^2 = \dot{\omega}$ is needed in the denominator. In [42]

the approach consists of a re-expansion of $\sqrt{1/\dot{\omega}}$ using the same ingredients as those underlying the *TaylorTn* approximants. One could, however, take a different route, since $\dot{\omega} = 3\sqrt{\chi\dot{\chi}}/2$ allows to choose different prescriptions for $\dot{\chi}$ without re-expanding the quotient.

One can for instance use the Newtonian $\dot{\chi}$, i.e. the leading term given by

$$\dot{\chi} = \frac{64\eta}{5M} x^5. \quad (3.23)$$

Incorporating 3.23 in 3.16 leads to the following expression for the 3PN amplitude in the frequency domain assuming a Newtonian $\dot{\chi}$

$$\tilde{A}^{22}(f) \simeq \frac{M^2\pi}{R} \sqrt{\frac{\eta}{6}} (\pi M f)^{-7/6} A^{22}(t_f). \quad (3.24)$$

Alternatively, one can re-expand the denominator as

$$\sqrt{\frac{2\pi}{\ddot{\phi}}} \simeq \sqrt{\frac{5\pi}{96\eta}} M (\pi M f)^{-11/6} \mathcal{J}[(\pi M f)^{1/3}, 5], \quad (3.25)$$

where $\mathcal{J}[u, n]$ represents a Taylor series in the variable u up to order u^n . Finally, we might as well replace $\dot{\chi}$ by its *TaylorT1* or *TaylorT4* description and the re-expansion of the form [42]

$$\sqrt{\frac{\pi}{\dot{\omega}}} \simeq \sqrt{\frac{5\pi}{96\eta}} x^{-11/4} \sum_{k=0}^5 S_k x^{k/2}, \quad (3.26)$$

with

$$\begin{aligned} S_0 &= 1, & S_1 &= 0, & S_2 &= \frac{743}{672} + \frac{11}{8}\eta, \\ S_3 &= -2\pi + \left(\frac{113}{24} - \frac{19}{6}\eta\right) \chi_s + \frac{113\delta}{24} \chi_a, \\ S_4 &= \frac{7266251}{8128512} + \frac{18913}{16128}\eta + \frac{1379}{1152}\eta^2 - \frac{79}{16}\eta (\chi_s^2 - \chi_a^2), \\ S_5 &= \pi \left(-\frac{4757}{1344} + \frac{57}{16}\eta\right). \end{aligned} \quad (3.27)$$

In the expression above, we have introduced the three auxiliary variables $\delta = (m_1 - m_2)/M$, $\chi_s = (\chi_1 + \chi_2)/2$, $\chi_a = (\chi_1 - \chi_2)/2$. The transfer to the the Fourier domain is completed by using 3.21 in 3.16 in combination with 3.18. Let us recall that these expressions are only valid for systems with *aligned* or *antialigned* spins.

This finally allows to write down the expression for the Fourier-domain amplitude of the dominant mode for the *TaylorT4* approximant as

$$\tilde{A}^{22}(f) = \left| \sqrt{\frac{2\eta}{3}} \frac{\pi M^2}{D_L} \Omega^{-7/6} \sum_{k=0}^5 \tilde{A}_k \Omega^{k/3} \right|, \quad (3.28)$$

where $\Omega \equiv \pi M f$ and

$$\begin{aligned} \tilde{A}_0 &= 1, & \tilde{A}_1 &= 0, & \tilde{A}_2 &= \left(-\frac{323}{224} + \frac{451}{168}\eta\right), \\ \tilde{A}_3 &= \frac{27\delta}{8} \chi_a + \left(\frac{27}{8} - \frac{11}{6}\eta\right) \chi_s, \end{aligned}$$

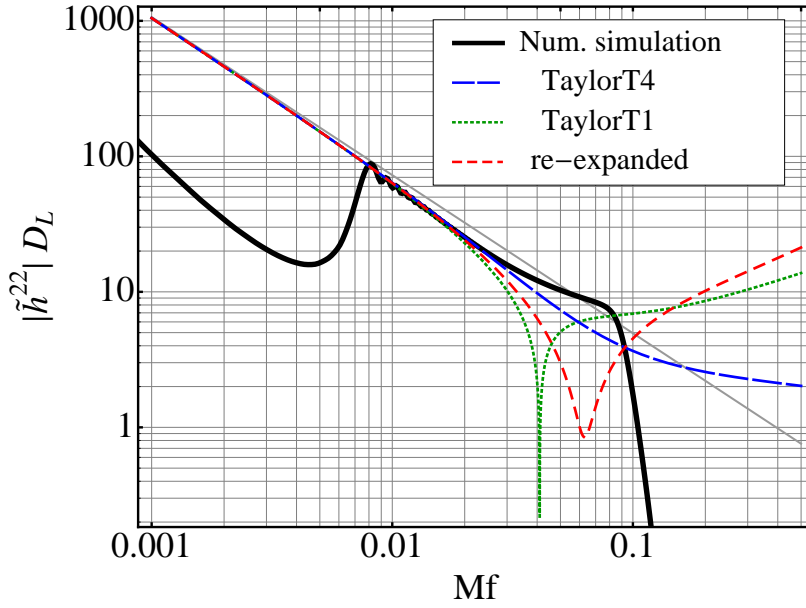


Figure 8: Different variants of constructing the PN Fourier amplitude in the stationary phase approximation for the equal mass case. The labels refer to the different ways of treating $(\pi/\dot{\phi})^{1/2}$ in equation 3.16. The thick curve shows data obtained by a numerical simulation in full general relativity. The straight gray line illustrates the restricted PN amplitude, $|\tilde{h}^{22}|_{D_L} = \pi\sqrt{2\eta/3}(\pi f)^{-7/6}$

$$\begin{aligned}\tilde{A}_4 &= -\frac{27312085}{8128512} - \frac{1975055}{338688}\eta + \frac{105271}{24192}\eta^2 + \frac{79}{16}\eta(\chi_a^2 - \chi_s^2), \\ \tilde{A}_5 &= -\frac{85\pi}{64}(1 - 4\eta) - 24i\eta - \frac{13577}{1008}(\chi_s + \delta\chi_a) \\ &\quad + \frac{4367\delta\chi_a + 13985\chi_s}{1008}\eta - \frac{583\chi_s}{252}\eta^2.\end{aligned}\quad (3.29)$$

Taking the norm in 3.28 is necessary due to a small imaginary contribution at the highest PN order.

The comparison between the different approaches proposed to deal with the presence of $\dot{\phi}$ in the denominator of 3.16 is shown in figure 8. We plot the Fourier-domain amplitude of the dominant mode in the case of re-expanded, *TaylorT1* and *TaylorT4* $\dot{\phi}$. Additionally, the restricted post-Newtonian amplitude that scales like $f^{-7/6}$ is shown, together with the Fourier-transform of data from a numerical relativity simulation. It is interesting to observe that the corrections to the restricted amplitude are already noticeable at frequencies below $Mf = 0.005$, therefore affecting the reliability of gravitational-wave searches based on templates without amplitude corrections for parameter estimation of stellar-mass black-hole binaries.

From figure 8 it can be concluded that all variants of the 3PN Fourier amplitude agree reasonably well with the numerical relativity data roughly up to the frequency of the last stable circular orbit in Schwarzschild given by equation 2.7, $f_{\text{ISCO}} \approx 0.022$. Due to the comparable behavior even beyond this point we choose to construct the Fourier-domain amplitude of our post-Newtonian model by using the *TaylorT4* for $\dot{\chi}$ given in 3.9. This is the final choice that will be employed in the construction of our inspiral-merger-ringdown waveform model described in detail in chapter 5.

3.2 RINGDOWN AND QUASI-NORMAL MODES

The name “ringdown” reminds of a bell that, when struck, rings at a given frequency before returning to equilibrium

The final fate of two compact objects undergoing an inspiral process during which they emit a fraction of their energy in the form of gravitational waves is the eventual merge into a single, distorted black hole. When the two objects that form the binary merge into the final black hole, this becomes perturbed and undergoes a *ringdown* process in the course of which gravitational radiation is emitted. During the ringdown, all perturbations are radiated away until a state of stationary, spinning black hole is reached, after an infinite amount of time. By means of the *no-hair* theorem, the final black hole can be completely characterized by only three externally observable classical parameters: mass, electric charge, and angular momentum. All other information—for which “hair” is a metaphor—about the matter which formed a black hole or is falling into it, *disappears* behind the black-hole event horizon.

The following sections introduce the concept of quasi-normal modes and the associated gravitational radiation. The interested reader will find a comprehensive review of this topic, including both black holes and neutron stars, in [168].

3.2.1 Perturbations from Equilibrium

The first studies on stability of Schwarzschild black holes date back from 1957, when Regge and Wheeler [216] discovered that a disturbance from the black hole’s sphericity would not grow with time, but would oscillate about the equilibrium configuration. Zerilli [267] extended this study for the even-parity case. The existence of the associated quasi-normal modes was pointed out by Vishveshwara [258] in calculations of the scattering of gravitational waves by a Schwarzschild black hole. Solving the Einstein equations for perturbations around a spherically-symmetric solution leads to wave equations, assuming a decomposition of the full solution $\chi(t, r, \theta, \phi)$ into spherical harmonics $Y_{lm}(\theta, \phi)$

$$\chi(t, r, \theta, \phi) = \sum_{l,m} \frac{\chi_{lm}(t, r)}{r} Y_{lm}(\theta, \phi). \quad (3.30)$$

Essentially, the equation to solve is of the form

$$s^2 \chi - \chi'' + V\chi = 0, \quad (3.31)$$

where prime denotes differentiation with respect to a radial variable and V is an effective potential depending on the nature of the perturbations under study. The solutions for the quasi-normal ringing can be approximated by a damped exponential. Thus, for each mode there exists a characteristic complex angular frequency ω_{lm} ; the real part is the angular frequency of the oscillation and the imaginary part is the decay rate, or the inverse of the damping time τ . It is perhaps more common to express these physical characteristics in terms of the oscillation frequency f_{lm} and the quality factor Q_{lm}

$$\omega_{lm} = 2\pi f_{lm} - i\tau^{-1} = 2\pi f_{lm} - i\pi \frac{f_{lm}}{Q_{lm}} \quad (3.32)$$

The solutions present a $2l + 1$ degeneracy on m

Leaver [174] determined the fundamental $l = 2, 3$ frequencies of the oscillations of a black hole around the Schwarzschild solution, as well as the

Table 4: The first QNM frequencies ωM of the spherical, non-spinning Schwarzschild black hole for $l = 2, 3$, given in geometrical units.

n	$l = 2$	$l = 3$
0	$0.3737 - i0.0890$	$0.5994 - i0.0927$
1	$0.3467 - i0.2739$	$0.5826 - i0.2813$
2	$0.3011 - i0.4783$	$0.5517 - i0.4791$
3	$0.2515 - i0.7051$	$0.5120 - i0.6903$

overtones, classified by an index n . The values of the first quasi-normal frequencies are given in table 4. The fundamental $l = 2$, $n = 0$ mode is the most slowly-damped mode, i.e. the one with the lowest value of the imaginary part of the frequency. When n increases, it can be shown that also the imaginary part of the frequency grows very quickly. This indicates that higher-order modes do not contribute significantly to the emitted gravitational radiation; the statement is true as well for the higher l modes (octupole, etc). In contrast, the real part of the frequency asymptotes to a constant value.

So far, we have dealt with Schwarzschild black holes only; however, the axisymmetric, black hole solution to the source free Einstein equations, i.e. the Kerr solution, is a more accurate description of a spinning black hole, which is the case that we intend to model in chapter 5. The problem of the perturbations from a spinning black hole was addressed by Teukolsky [251]. The solution for the separation in angular and radial variables is of the form

$$\chi(r, \theta, \phi) = R(r, \omega)S(\theta, \omega)e^{i m \phi}, \quad (3.33)$$

which, unlike the Schwarzschild case, entails a dependency in ω . The solutions decouple into spin-weighted *spheroidal*, rather than spherical, harmonics ${}_s S_{lm}$ with $s = -2$. For real ω^2 , the spheroidal harmonics can be expanded into spherical harmonics of fixed m .

The calculation of the quasi-normal frequencies of the Kerr black hole is considerably more involved than the Schwarzschild case. The reason is the complexity of the perturbation equations and, in particular, their non-separability. For this reason, only partial results for these frequencies are available in the literature. In [174], Leaver presented the $l = 2$ modes for different m and spin, showing that the spin removes the $2l + 1$ degeneracy in m . In particular, for the $l = 2$, $m = 2$ mode, the value of the real part of the orbital frequency ranges from $M\omega_R = 0.37$ for a non-spinning black hole to $M\omega_R = 0.9$ for a maximally-spinning black hole. This fact will be of importance as theoretical input for the phenomenological model developed in chapter 5.

3.2.2 The Ringdown Waveform

Since the gravitational waves emitted by a ringing black hole will be dominated, after an initial transient period, by a superposition of quasi-normal modes, it seems reasonable to try to model the ringdown radiation in such a way. If the characteristic parameters of the radiation — ω and τ — introduced in

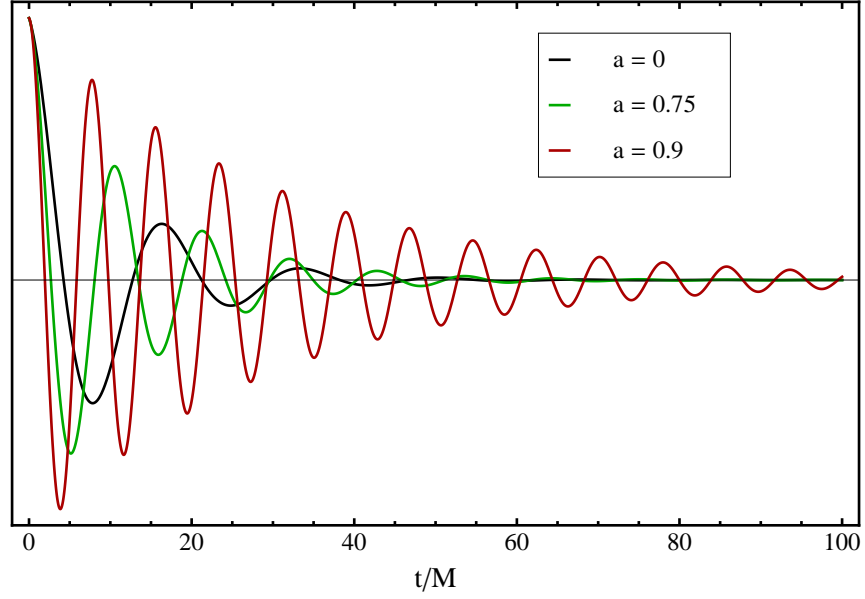


Figure 9: Ringdown signals emitted by sources of total mass $100 M_{\odot}$ and spin values $a = 0, 0.75$ and 0.9 , corresponding to frequencies 119, 189 and 221 Hz and Q -factors 2, 3.73 and 5.67 respectively. The amplitude of the waveforms has been arbitrarily rescaled.

section 3.2.1, could be expressed as a function of the black hole's M and a , then it would be certainly possible to infer its physical parameters in terms of the emitted waves. In fact, this approach constitutes the basis of the modeled ringdown searches made by the LIGO and Virgo collaborations [14].

Motivated by the fact that a coalescing binary has a rotating shape corresponding to the spheroidal harmonic $l = 2, m = 2$, Echeverria [109] performed an analytical fit to Leaver's data for the fundamental quasi-normal frequency in terms of the black hole's physical parameters

$$f_{220}(a, M) = \frac{1}{2\pi} \frac{c^3}{GM} \left[1 - 0.63(1 - a)^{3/10} \right] \quad (3.34)$$

$$Q_{220}(a) = 2(1 - a)^{-9/20}, \quad (3.35)$$

with aM^2 being the spin of the final black hole after the binary has merged. These relations can be inverted to yield the mass and spin of the black hole in terms of the characteristic parameters of the radiation, which motivates the already-mentioned ringdown searches with LIGO and Virgo.

Assuming that the gravitational radiation of a ringing black hole far from the source can be approximated by the most slowly damped mode, then higher order contributions can be neglected. The central frequency of the waveform is given by $f_0 \equiv f_{220}$ and the quality factor is $Q \equiv Q_{220}$. The waveform for the fundamental mode at large distances can be expressed as an exponential damped sinusoidal

$$h_{\text{ring}}^{22}(t) = \frac{\mathcal{A}_{\text{ring}} M}{r} e^{-\pi f_0 t / Q} \cos(2\pi f_0 t), \quad (3.36)$$

where the amplitude depends on the mass of the black hole and its distance to the detector, and the frequency and damping factor of the sinusoidal wave

are related to the physical parameters of the hole via 3.34 and 3.35. The peak amplitude $\mathcal{A}_{\text{ring}}$ can be computed from the stress-energy tensor, assuming that a fraction ε of the black hole's mass is radiated away in the form of gravitational waves

$$\mathcal{A}_{\text{ring}} = \sqrt{\frac{5}{2}} \varepsilon \left(\frac{GM}{c^2} \right) Q^{-1/2} F(Q)^{-1/2} g(a)^{-1/2}, \quad (3.37)$$

where

$$F(Q) = 1 + \frac{7}{24Q^2} \quad (3.38)$$

$$g(a) = 1 - 0.63(1 - a)^{3/10}. \quad (3.39)$$

Figure 9 displays the shape of the ringdown waveform $h_{\text{ring}}^{22}(t)$ for three different values of the spin of the black hole. As the spin increases, so do the frequency and the quality factor. Highly-spinning black holes spend a significantly longer time in their perturbed state before reaching the equilibrium, therefore emitting more radiation, which increases their detectability. In fact, it can be shown from numerical relativity simulations, that a particular configuration with spin —known as *hang-up*— provides the maximally spinning black hole in the final state, and it can be as “loud” as three times a non-spinning black hole [220].

We refer to “loud” in a gravitational-wave detection sense

In this chapter, two analytical approaches have been introduced that describe parts of the coalescence process of a black-hole binary. The adiabatic nature of the quasi-circular inspiral stage calls for a post-Newtonian approach, whereas the perturbative nature of the ringdown oscillations towards the final Kerr black hole after the merger motivates the introduction of the quasi-normal modes formalism. In chapter 4 we will see how the strong-field regime around the black holes' merger calls for full numerical relativity methods as the only feasible approach to solving the Einstein equations.

Numerical relativity is a fascinating research field astride general relativity and computational physics. In the many situations where an analytical solution to the Einstein equations cannot be found, numerical relativity resorts to numerical methods and algorithms that are usually run on supercomputers. A primary goal of numerical relativity is to study space-times whose exact form is not known analytically. As described in chapter 3, this is precisely the case for the merger of two black holes. Although much work has been done within the effective-one-body approach, the analytical approximations that are valid in the perturbative inspiral and ringdown stages do not perform well in the strong-field regime, and full-GR approaches such as that given by numerical relativity are required.

The field of numerical relativity has a long and riveting history, much as the field of gravitational-wave detection does. The pioneering attempts to evolve wormhole initial data in a computer by Hahn and Lindquist in the 1960s [139] were followed by the work of Smarr and York [243, 242, 241] in the 1970s and gave rise to a large body of research as the computational power of the machines increased in the 1990s. A particular combination of choice of formulation for the Einstein equations and technicalities in the treatment of the numerics finally led to successful simulations of the last orbits of the binary black-hole coalescence by Pretorius [212] and later by two other groups [88, 52] in 2005. Ever since, the field has entered a new phase, characterized by the study of previously-unexplored physical phenomena, such as the computation of the recoil velocities —*kicks*— of black-hole mergers, the determination of the final spin after the coalescence and the development of new methods to extract the most accurate gravitational radiation emitted by the binary system. The direct applicability of these results to improved methods on gravitational-wave astronomy opens a promising era of synergistic collaborations between numerical relativity and gravitational-wave data analysis.

This chapter presents a review of the key components that have made this golden age of numerical relativity possible and describes the simulations that will be used to construct the hybrid model of chapter 5.

4.1 SOLVING EINSTEIN EQUATIONS NUMERICALLY

The covariant nature of the Einstein equations, when written in the compact formulation given by equation 1.1, is evident. Time and spatial coordinates are indistinguishable, which is only natural given the geometrical meaning of the equations in a space-time thought of as 4-dimensional manifold. If these equations need to be integrated numerically, however, they need to be rewritten in a more appropriate form. One way to proceed is to split the 4-dimensional covariant structure of the equations in such a way that a time evolution can be performed, exploiting the special nature of time. There are a number of other ways of dealing with the full Einstein equations, such as characteristic methods or the use of harmonic coordinates. But here we will only present the method commonly known as the *space-plus-time* $3+1$

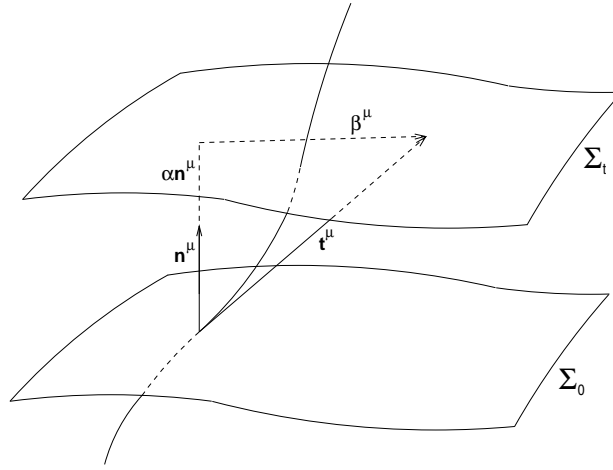


Figure 10: Foliation of the space-time in the 3+1 decomposition of the Einstein equations. Σ_0 and Σ_t represent two hypersurfaces of the foliation. n^μ is the orthogonal vector to Σ_0 and t^μ the tangent to the curves threading the foliation. The relation between these vectors is given by the lapse function and the shift vector as $t^\mu = \alpha n^\mu + \beta^\mu$.

decomposition of space-time, whose development in the 1960s and 1970s was of the most importance to establish the basis and formalism needed for the subsequent emergence of numerical relativity. The next sections succinctly describe this formalism.

4.1.1 The 3+1 Decomposition

The 3+1 decomposition was first introduced by Arnowitt, Deser and Misner in 1962 [41], together with other important concepts regarding the canonical formulation of general relativity, now commonly referred to as the ADM formalism. Ever since, other researchers have studied the well-posedness of the Cauchy problem, thus clarifying the physical meaning of the problem and supplying practical algorithms to find its solution. As a result of the 3+1 decomposition, the Einstein equations are split into constraint equations which are solved to provide initial data on some initial slice, and evolution equations which permit us to evolve the data from slice to slice [266].

As depicted in figure 10, the globally hyperbolic 4-dimensional space-time $(M, g_{\mu\nu})$ can be foliated by a set of 3-dimensional space-like hypersurfaces Σ_t that completely fill the space. The foliation can be identified with the level sets of a parameter t , which is a *universal time function*.

Consider now the future-pointing, time-like unit normal vector field to the hypersurfaces, n^μ , which corresponds by definition to the 4-velocity of the Eulerian observers. This vector n^μ , defined as

$$n^\mu = -\alpha g^{\mu\nu} \nabla_\nu t, \quad (4.1)$$

allows us to introduce the 3-dimensional metric $\gamma_{\mu\nu}$ induced onto the hypersurfaces by the 4-metric $g_{\mu\nu}$

$$\gamma_{\mu\nu} = g_{\mu\nu} + n_\mu n_\nu, \quad (4.2)$$

and its contravariant form $\gamma^{\mu\nu} = g^{\mu\alpha}g^{\nu\beta}\gamma_{\alpha\beta}$. The mixed tensor $\gamma_{\nu}^{\mu} = \delta_{\nu}^{\mu} + n^{\mu}n_{\nu}$ is a projector onto the slices. The α function of equation 4.1

$$\alpha^{-2} \equiv -g^{\mu\nu}\nabla_{\mu}t \nabla_{\nu}t, \quad (4.3)$$

is the *lapse function*.

We can construct a time vector field t^{μ} which is tangent to the time lines, i.e. the lines of constant coordinates as

$$t^{\mu} = \alpha n^{\mu} + \beta^{\mu}, \quad (4.4)$$

where the spatial vector $\beta^{\mu} = (0, \beta^i)$ is the *shift vector*. From the above definition we find that $t^{\mu}n_{\mu} = -\alpha$, which implies $t^{\mu}\nabla_{\mu} = 1$. The shift then corresponds to the projection of t^{μ} onto the spatial hypersurface. Explicitly, the vector t^{μ} can be decomposed into its normal and tangent components relative to the hypersurfaces

$$\alpha = -t^{\mu}n_{\mu}, \quad (4.5)$$

$$\beta^i = \gamma_j^i t^j. \quad (4.6)$$

As a matter of fact, the lapse function α and shift vector β^i are *gauge functions* that define how coordinates move forward in time from slice Σ_0 to Σ_t . This is a reflection of the covariant character of the Einstein equations, which assures that any coordinate system is as valid as any other one when it comes to describing the geometry of the space-time. The lapse sets the proper time between successive hypersurfaces and the shift vector determines the relative velocity between Eulerian observers and the lines of constant spatial coordinates.

Equipped with the above-defined $\{\alpha, \beta^i, \gamma_{ij}\}$, we can now rewrite the line element of the metric in terms of its time and spatial components as

$$ds^2 = -\alpha^2 dt^2 + \gamma_{ij}(dx^i + \beta^i dt)(dx^j + \beta^j dt). \quad (4.7)$$

In this coordinate basis, the normal vector n^{μ} is of the form

$$n_{\mu} = (-\alpha, 0, 0, 0), \quad n^{\mu} = \frac{1}{\alpha}(1, -\beta^i). \quad (4.8)$$

Given the 3-metric γ_{ij} it is possible to define a covariant derivative and associated 3-dimensional Riemann tensor in a manner analogous to the 4-dimensional expression given in equation 1.6. The spatial Riemann tensor accounts for the *intrinsic* curvature of the slice Σ_t . However, one should not forget that the slice is embedded in a 4-dimensional space, hence possessing *extrinsic* curvature as well. It is intuitively clear that, whereas the 4-dimensional Riemann tensor is a space-time object containing time derivatives of the 4-metric $g_{\mu\nu}$, the 3-dimensional Riemann is a spatial object, and can be computed only from derivatives of the spatial metric alone. There must certainly be some information missing when projecting the full Riemann tensor into the 3-dimensional slices, and that missing information that tells us how the hypersurfaces are embedded in the space-time is called *extrinsic curvature*.

The extrinsic curvature $K_{\mu\nu}$ of the slice is defined via the projection of the gradient of the surface normal field and can also be expressed in terms of the Lie derivative along the normal vector n^{μ}

$$K_{\mu\nu} \equiv -\gamma_{\nu}^{\alpha}\nabla_{\mu}n_{\nu} = -\frac{1}{2}\mathcal{L}_n\gamma_{\mu\nu}, \quad (4.9)$$

The covariant derivative compatible with γ_{ij} will be denoted \mathbb{D}

The intrinsic and extrinsic curvatures of the slices and the curvature of the background space are not independent, but they are related by means of the Gauss-Codazzi equations

and is a symmetric and purely spatial tensor. The last equality clarifies the meaning of the extrinsic curvature; it provides information on the rate of change of the spatial metric $\gamma_{\mu\nu}$ as we move along the vector n^μ along the hypersurfaces Σ . The complete geometry of a slice embedded in a 4-dimensional space-time is represented by the triplet $\{\Sigma_t, \gamma, K\}$, which will turn out to be an initial data set for the space-time. Obviously, not every set of 3-dimensional slices can fit into the 4-dimensional space-time. Certain integrability conditions, called the *Gauss-Codazzi equations*, represent the sufficient and necessary geometrical identities that must be *locally* satisfied in order for the foliation Σ to be correctly embedded in the full space-time.

4.1.2 The ADM Equations

The ADM equations encode the same physical content as the Einstein equations 1.1 but split in space and time and given in terms of the variables

$$\alpha, \quad \beta^i, \quad \gamma_{ij}, \quad K_{ij}. \quad (4.10)$$

As a result of this projection of the full equations onto the hypersurfaces Σ and the normal field n^μ , a set of four equations arises that can be classified in two categories: *evolution* equations for the variables γ_{ij} and K_{ij} and *constraints* that need to be satisfied on every hypersurface. In principle one can compute the quantities 4.10 for an initial slice Σ_0 and evolve the data to the next slice Σ_t by means of the time derivatives of γ_{ij} and K_{ij} . This process will eventually lead to the complete specification of the geometry of the space-time, providing at the same time a suitable algorithm to construct and numerically evolve any physically relevant data.

The stress-energy tensor that appears on the right hand side of 1.1 includes all the relevant information related to the matter content of the space-time. The component $T^{\mu\nu}$ of the tensor refers to the μ -th component of the 4-momentum tensor across a surface with constant x^ν coordinate. The stress-energy tensor is a symmetric object and its different components can be associated with well-known physical quantities. Thus, T^{00} is the energy density, T^{0i} represents the flux of energy across the x^i surface, equivalent to T^{i0} , which is the density of the i^{th} momentum component. In addition, T^{ij} ($i \neq j$) is the shear stress and T^{ii} represents a pressure-like quantity, the normal stress. According to our intention of splitting the Einstein equations by projecting them, it will be necessary to operate on their right-hand side, too. For this purpose the energy density ρ , the momentum density j_μ and the spatial stress $S_{\mu\nu}$ are introduced and defined as follows

$$\rho \equiv n^\mu n^\nu T_{\mu\nu}, \quad (4.11)$$

$$j_\mu \equiv \gamma_\mu^\sigma n^\rho T_{\sigma\rho}, \quad (4.12)$$

$$S_{\mu\nu} \equiv \gamma_{\mu\sigma} \gamma_{\nu\rho} T^{\sigma\rho}. \quad (4.13)$$

Thus we can finally write the ADM equations. The evolution equations for the spatial metric and the extrinsic curvature read

$$\partial_t \gamma_{ij} = -2\alpha K_{ij} + D_i \beta_j + D_j \beta_i \quad (4.14)$$

$$\begin{aligned} \partial_t K_{ij} = & \beta^k D_k K_{ij} + K_{ik} D_j \beta^k + K_{kj} D_i \beta^k - D_i D_j \alpha \\ & + \alpha \left({}^{(3)}R_{ij} - 2K_{ik} K_j^k + K K_{ij} \right) \\ & - 8\pi\alpha \left(S_{ij} - \frac{1}{2} \gamma_{ij} (S - \rho) \right). \end{aligned} \quad (4.15)$$

In 4.15, ${}^{(3)}R_{ij}$ is the associated Ricci tensor with the metric γ_{ij} . In addition to these evolution equations, the *Hamiltonian* and *momentum* constraint equations read

$${}^{(3)}R + K^2 + K_{ij} K^{ij} = 16\pi\rho \quad (4.16)$$

$$D_j K_i^j - D_i K = 8\pi j_i \quad (4.17)$$

where ${}^{(3)}R$ and K denote the trace of the Ricci tensor and extrinsic curvature respectively. In vacuum, the energy and momentum densities are zero, i.e. $\rho = 0$ and $j_\mu = 0$.

In the set of equations 4.14—4.17, the gauge functions α and β^i can be freely specified. One of the issues to address when running numerical relativity simulations is the choice of a well-behaved gauge that leads to a successful numerical evolution. As it turns out, regardless of the chosen gauge, the ADM system of equations is only weakly hyperbolic and thus does not give rise to a well-posed initial value problem in the most general case. Correspondingly, the growth of high-frequency components in numerical simulations cannot be bounded and reliable numerical simulations are not possible. Next section describes an alternative formulation that has proven to be better suited in this context.

Only for particular cases—like for instance spherical symmetry—can the ADM equations be made well-posed

4.1.3 The BSSN Formulation

A large number of alternative, hyperbolic formulations of the Einstein equations have been proposed to solve the problem of the weak hyperbolicity of the ADM formulation. A system that has been found to behave in a satisfactory manner, at least in binary black hole evolutions, is the one developed by Baumgarte and Shapiro [54] based on that of Shibata and Nakamura [239] after Nakamura, Oohara and Kojima presented a reformulation of the ADM equations introducing a conformal transformation [187]. This alternative evolution system is nowadays broadly known as the BSSN formulation.

The BSSN system belongs to the class of conformal traceless formulations. Besides the use of conformal transformations and a traceless decomposition of the extrinsic curvature, possibly the most important aspect is the promotion of the conformal connection to an independent variable. The idea behind the BSSN formulation is to evolve a conformal factor and the trace of the extrinsic curvature separately. Modifying the equations by using the constraints is the crucial step to make the system hyperbolic. An alternative version of the BSSN equations exists that does not include the conformal traceless transformation but is equally strongly hyperbolic; this approach is known as the NOR system [186].

In geometry, two Riemannian metrics g and h on a smooth manifold \mathcal{M} are called conformally equivalent if $g = u h$ for some positive function u on \mathcal{M} . The function u is called the conformal factor.

Traceless refers to the fact that the extrinsic curvature is split in its trace-free and trace parts, and it is the former that is conformally transformed.

In the traditional BSSN formulation, the conformal factor is written as $\Psi = e^\phi$ so that the conformal metric is

$$\tilde{\gamma}_{ij} = e^{-4\phi} \gamma_{ij}, \quad \phi = \frac{1}{12} \ln \det \gamma_{ij}, \quad (4.18)$$

requiring as an auxiliary constraint that the determinant of the conformal metric $\tilde{\gamma}_{ij}$ is unity. The trace-free part of the intrinsic curvature

$$A_{ij} \equiv K_{ij} - \frac{1}{3}\gamma_{ij}K, \quad (4.19)$$

is rescaled like the metric itself

$$\tilde{A}_{ij} = e^{-4\phi}A_{ij}. \quad (4.20)$$

Indices of this conformally transformed object 4.20 will be raised and lowered with the conformal metric 4.18. We can now find the evolution equations for ϕ and K making use of 4.14 and 4.15 and taking their trace

$$\frac{d}{dt}\phi = -\frac{1}{6}\alpha K, \quad (4.21)$$

$$\frac{d}{dt}K = -\gamma^{ij}D_j D_i \alpha + \alpha \left(\tilde{A}_{ij}\tilde{A}^{ij} + \frac{1}{3}K^2 + 4\pi\alpha(\rho + S) \right), \quad (4.22)$$

where

$$\frac{d}{dt} = \frac{\partial}{\partial t} - \mathcal{L}_\beta = \frac{\partial}{\partial t} - \beta^i \frac{\partial}{\partial x^i} \quad (4.23)$$

and the Hamiltonian constraint 4.16 has been used to eliminate the Ricci scalar from 4.22. Now the trace-free parts of the equations yield

$$\frac{d}{dt}\tilde{\gamma}_{ij} = -2\alpha\tilde{A}_{ij}, \quad (4.24)$$

$$\begin{aligned} \frac{d}{dt}\tilde{A}_{ij} = e^{-4\phi} \left(-(D_i D_j \alpha)^{TF} + \alpha(R_{ij}^{TF} - S_{ij}^{TF}) \right) \\ + \alpha(K\tilde{A}_{ij} - 2\tilde{A}_{il}\tilde{A}_j^l). \end{aligned} \quad (4.25)$$

The superscript ^{TF} in the last equation denotes the trace-free part of a tensor. The Ricci tensor R_{ij} can now be decomposed into two terms

$$R_{ij} = \tilde{R}_{ij} + R_{ij}^\phi, \quad (4.26)$$

where

$$\begin{aligned} R_{ij}^\phi = -2\tilde{D}_i \tilde{D}_j \phi - 2\tilde{\gamma}_{ij}\tilde{D}^l \tilde{D}_l \phi + 4(\tilde{D}_i \phi)(\tilde{D}_j \phi) \\ - 4\tilde{\gamma}_{ij}(\tilde{D}^l \phi)(\tilde{D}_l \phi), \end{aligned} \quad (4.27)$$

and \tilde{D}_i is the covariant derivative operator associated with $\tilde{\gamma}_{ij}$. The operator \tilde{R}_{ij} can be brought into a manifestly elliptic form by introducing the *conformal connection functions*

$$\tilde{\Gamma}^i \equiv \tilde{\gamma}^{jk}\tilde{\Gamma}_{jk}^i = -\partial_j \tilde{\gamma}^{ij}, \quad (4.28)$$

where the $\tilde{\Gamma}_{jk}^i$ are the connection coefficients associated with $\tilde{\gamma}_{ij}$. In terms of these objects, the Ricci tensor can be written as

$$\begin{aligned} \tilde{R}_{ij} = -\frac{1}{2}\tilde{\gamma}^{lm}\partial_l \partial_m \tilde{\gamma}_{ij} + \tilde{\gamma}_{k(i}\partial_{j)}\tilde{\Gamma}^k + \tilde{\Gamma}^k\tilde{\Gamma}_{(ij)k} \\ + \tilde{\gamma}^{lm} \left(2\tilde{\Gamma}_{l(i}\tilde{\Gamma}_{j)km} + \tilde{\Gamma}_{im}^k\tilde{\Gamma}_{klj} \right). \end{aligned} \quad (4.29)$$

The symmetrization operator is denoted by parentheses around the indices that are to be interchanged: $A_{(\mu\nu)} \equiv \frac{1}{2}(A_{\mu\nu} + A_{\nu\mu})$

We can now appreciate the convenience of introducing the connection functions 4.28, because this way only the Laplace operator $\tilde{\gamma}^{lm}\partial_l\partial_m\tilde{\gamma}_{ij}$ remains in the Ricci tensor 4.29. The other second derivatives have been absorbed in the derivatives of $\tilde{\Gamma}^i$. One can get rid of these second derivatives if the connection functions are now promoted to independent functions, and an evolution equation for them can be derived by permuting a time derivative with the space derivative in equation 4.28

$$\frac{d}{dt}\tilde{\Gamma}^i = -\partial_j \left(2\alpha\tilde{A}^{ij} - 2\tilde{\gamma}^{m(j}\partial_m\beta^{i)} + \frac{2}{3}\tilde{\gamma}^{ij}\partial_l\beta^l + \beta^l\partial_l\tilde{\gamma}^{ij} \right). \quad (4.30)$$

Finally, eliminating the divergence of \tilde{A}^{ij} with the help of the momentum constraint 4.17 yields

$$\begin{aligned} \frac{\partial}{\partial t}\tilde{\Gamma}^i = & -2\tilde{A}^{ij}\partial_j\alpha + 2\alpha \left(\tilde{\Gamma}_{jk}^i\tilde{A}^{jk} - \frac{2}{3}\tilde{\gamma}^{ij}\partial_j K - \tilde{\gamma}^{ij}S_j + 6\tilde{A}^{ij}\partial_j\phi \right) \\ & - \partial_j \left(\beta^l\partial_l\tilde{\gamma}^{ij} - 2\tilde{\gamma}^{m(j}\partial_m\beta^{i)} + \frac{2}{3}\tilde{\gamma}^{ij}\partial_l\beta^l \right). \quad (4.31) \end{aligned}$$

Equations 4.21 through 4.25 together with 4.31 form the BSSN system of evolution equations, equivalent to 4.14 and 4.15 but for the set of variables

$$\phi, \quad K, \quad \tilde{\gamma}_{ij}, \quad \tilde{A}_{ij}, \quad \tilde{\Gamma}^i. \quad (4.32)$$

Since the connection functions are evolved as independent functions, their original definition 4.28 serves as a new constraint equation, in addition to 4.16 and 4.17. Obviously, not all the variables of this system are independent, in particular the determinant of $\tilde{\gamma}_{ij}$ has to be unity and the trace of \tilde{A}_{ij} has to vanish. These conditions can either be used to reduce the number of evolved quantities or, alternatively, all quantities can be evolved and the conditions can be used as a numerical check. Precisely this question of how the constraints are used in the evolution equations is known to be a subtlety in obtaining numerically stable evolutions with the BSSN formulation.

4.1.4 A Recipe for Successful Simulations

The long history of numerical evolutions of non-trivial space-times tells a story full of exciting research milestones on theoretical and numerical methods, major breakthroughs, dead ends and fresh starts that, as a matter of fact, eventually led to a happy end. A complete description of all relevant research milestones falls beyond the scope of this dissertation. It would not be inaccurate to say that some of the progress in numerical relativity was achieved by trial and error. This section briefly presents some of the ingredients that, *a posteriori* resulted fundamental for obtaining numerical codes able to successfully evolve a binary of black holes through the late inspiral to the merger and ringdown.

Choice of Gauge

Many years of intense research on numerical methods and stability were needed to enable the transition between a theoretical formulation of general relativity which was suitable for implementation in a computer and the desired result of a well-behaved, stable simulation of the black holes' merger. The

We mean good in the sense of being adequate for numerical implementations

use of appropriate gauge conditions was crucial to reach the final goal. As mentioned in section 4.1.1, the choice of the lapse function α and the shift vector β^i is left free, since the choice of coordinates in Einstein's theory is arbitrary. Good gauge conditions should, when possible, be adapted to the underlying symmetries of the problem, avoid the formation of numerical singularities and be mathematically well behaved [26].

An apparently simple gauge condition, known as *geodesic slicing*, defined by the equations

$$\alpha = 1, \quad \beta^i = 0, \quad (4.33)$$

is by no means a good choice of gauge to evolve a black-hole space-time. In this gauge, any coordinate observer, starting from rest, will fall into the black-hole singularity. A superior choice is the *maximal* slicing, derived by imposing that the volume of the spatial hypersurfaces is maximal, which is equivalent to the condition

$$K = \gamma^{ij} K_{ij} = \frac{\partial K}{\partial t} = 0. \quad (4.34)$$

Possibly the main disadvantage of this gauge choice is that it leads to an elliptic equation for the lapse α , whose numerical solution might be computationally prohibitive.

The simulations used for the construction of the full coalescence waveform model presented in chapter 5 make use of a particular member of a family of slicing conditions proposed by Bona *et al.* [68], resulting in a hyperbolic equation for the lapse which is easy to solve numerically. The lapse α is chosen to satisfy the evolution equation

$$\frac{d}{dt} \alpha = \frac{\partial}{\partial t} \alpha - \beta^i \partial_i \alpha = -\alpha^2 f(\alpha) K, \quad (4.35)$$

with $f(\alpha)$ a positive but otherwise arbitrary function of α . The particular choice implemented in the numerical codes that have produced the simulations employed in this thesis is $f(\alpha) = 2/\alpha$, which leads to

$$\alpha = 1 + \log \gamma, \quad (4.36)$$

a very easy-to-implement condition that, additionally, is tremendously robust.

Regarding the conditions for the shift vector β^i , the mainstream way to proceed in the context of the most recent BSSN black hole evolutions—in particular in the ones used in this work—has been based on the Γ -freezing condition

$$\frac{\partial}{\partial t} \tilde{\Gamma}^i = 0, \quad (4.37)$$

proposed as a natural choice for the shift in the BSSN formulation, as it freezes three of the independent degrees of freedom. The Γ -freezing condition is equivalent to the minimal distortion condition and introduces an elliptic equation for the shift, which is again computationally disadvantageous. An innovative solution for the numerical implementation of the shift condition was introduced by Alcubierre *et al.* [27] by means of a Γ -driver condition, inspired by the idea of transforming the elliptic equation for the shift into

The minimal distortion condition minimizes changes in the shape of volume elements during an evolution

a parabolic one by making $\partial_t \beta^i$ or $\partial_t^2 \beta^i$ proportional to the given elliptic operator. The Γ -driver can be written as

$$\partial_t \beta^i - \beta^j \partial_j \beta^i = \frac{3}{4} \alpha B^i \quad (4.38)$$

$$\partial_t B^i - \beta^j \partial_j B^i = \partial_t \tilde{\Gamma}^i - \beta^j \partial_j \tilde{\Gamma}^i - \eta B^i, \quad (4.39)$$

where η —do not mistake it for the symmetric mass ratio for binary systems introduced in equation 2.6— is a freely-specifiable damping coefficient which helps avoid strong oscillations in the shift.

Excision and Punctures

There is still more to the problem than the choice of a suitable set of gauge conditions. For years, the field of numerical relativity struggled to maintain stable evolutions, the instabilities propagating through the computational grid and eventually ending the simulation. The existence of infinities is obviously problematic for a numerical code, and it would be desirable to find a proper way of dealing with the black-hole singularities. At least two techniques were implemented to deal with problems associated with the existence of physical singularities in the solutions to the equations. The *excision* method consists of removing a portion of a space-time inside of the event horizon surrounding the singularity of a black hole, simply not evolving it. Due to the principle of causality and properties of the event horizon, this procedure should in theory not affect the solutions of the equations outside of the event horizon. Additionally, ingoing boundary conditions on a boundary surrounding the singularity but inside the horizon are imposed. This approach presents some problems; while physical effects cannot propagate from inside to outside, coordinate effects could. Besides, as the black holes move, the location of the excision region needs to be continually adjusted to move with the black hole. The full development of this technique, together with suitable gauge conditions to increase stability and to allow the excised regions to move along the grid was carried out for several years. The efforts did eventually pay off, and the first stable, long-term evolution of the orbit and merger of two black holes using this technique was published by Pretorius in 2005 [212]. This undoubtedly constituted a major breakthrough in the field of numerical relativity.

The second method that proved successful —and the one on which the simulations used in this dissertation are based— was developed by Brandt and Brügmann [73] and is known as the *puncture* approach. This method is a generalization of the Brill-Lynden prescription for initial data [74]. One of the advantages of the puncture method is the absence of inner boundary conditions; the solution is factored into an analytical part, which contains the singularity of the black hole, and a numerically constructed part, which is then singularity free. The procedure can be viewed as follows: we know that the simplest solution for a Schwarzschild space-time in isotropic coordinates implies a conformal factor $\Psi = e^\Phi$ of the form

$$\phi = 1 + \frac{m}{2r}, \quad (4.40)$$

Pretorius did not use BSSN, but rather a generalized harmonic formulation of the Einstein equations, not based on the 3+1 scheme, which we do not discuss here

The Schwarzschild solution describes the gravitational field outside a spherical, non-rotating mass, which can be a black hole

on a conformally-flat space-time $\gamma_{ij} = \Psi^4 \eta_{ij}$. A generalization for N black holes for time-symmetric initial data can be made exploiting the linearity of the Hamiltonian constraint

$$\phi = 1 + \sum_{i=1}^N \frac{m_i}{2|\vec{r} - \vec{r}_i|}. \quad (4.41)$$

With this insight, the basic idea behind the puncture method is the explicit separation of the singular part in the expression for the conformal factor

$$\phi = \phi_{\text{BL}} + u, \quad \phi_{\text{BL}} = \sum_{i=1}^N \frac{m_i}{2|\vec{r} - \vec{r}_i|}. \quad (4.42)$$

Thus, we can solve this equation for u and we would need to impose appropriate boundary conditions at infinity and, in principle, also at the holes' location. The key observation, and what was proved by Brandt and Brügmann, is that there is no need for special boundary conditions *at the punctures*; they can be ignored when solving for u without further complications. For the purpose of this dissertation it suffices to say that this fact simplifies enormously the treatment of the singularities in the numerical domain; for a full discussion of the implications of the punctures method for the geometry of the space-time we refer the reader to [140, 141, 26].

At this point it is important to remember the following caveat: the methods described above assume that the conformal geometry of the space-time is flat. This might not necessarily be compatible with the physical system under study. In particular, the method does not generate a Kerr solution for a single spinning black hole, since the Kerr space-time is not a conformally-flat geometry. Conformally flat initial data always contain a dynamical component, which will be radiated away in the form of *non-physical* gravitational radiation as the simulation progresses. This pulse of “junk” radiation will propagate away from the computational domain; however, appropriate boundary conditions at the external edge of the grid are crucial to avoid contamination of the physical gravitational radiation content of the system.

One last ingredient separates us from the goal of successful evolutions of black-hole binaries in the BSSN framework: for many years the opinion held by a subset of the community was that corotating coordinates were a good solution to deal with the binary black hole problem. The idea was that working out how to work with a corotating grid seemed easier than working out how to move the black holes. This was also motivated by the assumption that keeping the holes fixed in the grid would lead to more stable dynamics. Elaborate gauge conditions for the shift vector β^i in order to prevent the holes from moving were required as a result. The corotating scheme was known to present fundamental problems, especially regarding the outer boundaries, for which no physically meaningful conditions could be applied. Additionally, extraction of the gravitational-radiation content of the space-time was technically more involved.

The solution to this puzzle might appear obvious in view of what has been said so far: why not letting the punctures move across the computational grid while keeping the coordinate frame fixed. But an old issue with the moving puncture approach was the lack of knowledge about what to do with the conformal factor, which blows up at the puncture. The puncture method factored out the singular piece, and in order to maintain that analytical singular piece

In a corotating frame the coordinate positions of the black holes remain fixed while the reference frame rotates with some angular velocity

Table 5: Some properties of currently-working NR evolution codes. The table reflects the status of published results at the time of writing. The columns list the name of the code, the employed evolution system (GH stands for generalized harmonic formulation), the numerical technique (FD-k stands for finite differences using k-th order stencils in the bulk), the η choices for the $\tilde{\Gamma}$ -driver shift 4.39, the approximate location of the outer boundary and the finest grid-spacing. Several of these parameters —such as the stencil order, the damping η or the details of the grid— are tunable; we report characteristic values that have been employed in the codes to obtain published results. For the SpEC code, r_{\max} decreases during the run.

Code	Reference	System	Technique	$M \eta$	r_{\max}/M
AMSS-NCKU	[91, 126]	BSSN	FD-6	2	128
BAM	[77]	BSSN	FD-6	2	773
CCATIE	[206]	BSSN	FD-4	1	819
Hahndol	[158, 256]	BSSN	FD-4, 6	2	> 1000
LazEv	[269, 88]	BSSN	FD-4, 8	6	1281
Lean	[244]	BSSN	FD-4, 6	1	256
Llama	[207]	BSSN	FD-8	1	3600
MayaKranc	[153]	BSSN	FD-4, 6	2	317.4
PU	[213, 212]	GH	FD-2	n/a	∞
SpEC	[69, 232]	GH	Spectral	n/a	450 \rightarrow 230
UIUC	[114]	BSSN	FD-4	0.25	409.6

stable, there was a strong belief in favour of keeping the punctures fixed. The breakthrough was to realize that evolving the singular conformal factor was actually quite easy. In fact, this was what indeed solved the problem and allowed the black holes to evolve from the last inspiral orbits through the plunge. Two independent groups arrived at this same conclusion independently, using slightly different, but essentially equivalent methods. The results appeared in 2005, by Campanelli *et al.* [88] and Baker *et al.* [52], shortly after Pretorius' letter, and confirmed that indeed the problem of numerically simulating the binary black hole merger had finally been solved. Since then, a number of numerical relativity groups across the world have presented their own versions of successful simulations, giving rise to a handful of working codes that can be used to compare results, produce new physics and test general relativity predictions. A summary of such codes is presented in table 5, together with references and brief annotations about their technical aspects. Table 10 provides further information about these codes.

In the *moving punctures* approach, employed by the majority of the codes of table 5, the singular part of the conformal factor is not factored out; instead, the dynamical conformal factor has a logarithmic singularity which is directly evolved. Rather than dealing with the conformal factor directly —as implemented in the CCATIE code—, the approach followed in Campanelli *et al.* —and also in the BAM simulation shown in figure 20— is to evolve an auxiliary variable defined as $\chi = \Psi^{-4} = e^{-4\phi}$.

Later it was realized that the fixed-puncture approach is problematic, even if the black holes do not move. Their codes are labelled LazEv and Hahndol respectively in table 5. Pretorius' code is labelled PU.

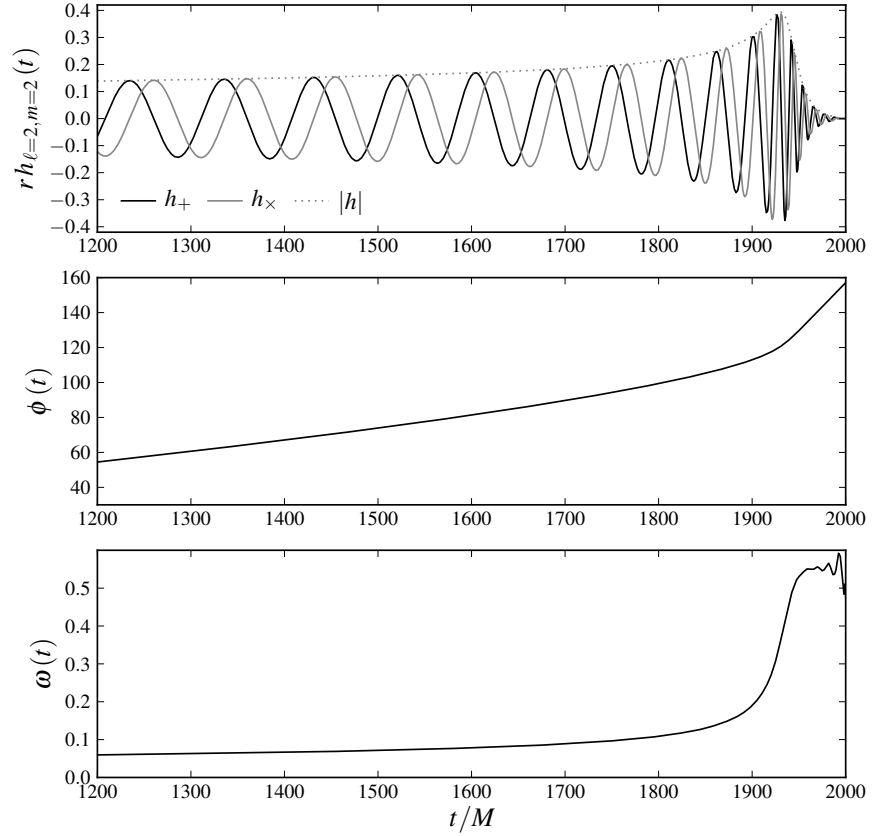


Figure 11: Typical numerical relativity waveform for the late inspiral, merger and ringdown of a binary black-hole system. The upper panel shows the two polarizations h_+ and h_\times of the gravitational-wave strain as well as the amplitude in dimensionless units as a function of time in units of the total mass of the system. The middle and lower panels show the phase of the waveform $\phi(t)$ and its instantaneous frequency $\omega(t)$. The chirp is clearly noticeable. The data corresponds to a non-spinning, equal-mass simulation made with the BAM code.

M is the total ADM
mass of the space-time

Contrary to the initial intuition of many numerical relativists, the moving puncture approach leads to robust and stable simulations of black-hole spacetimes lasting for many hundreds of M , allowing to follow the inspiral, merger and ringdown of a binary and accurately extract their gravitational radiation. Figure 20 shows one example for an equal-mass, non-spinning system evolved with the BAM code. The simulation starts $\sim 2000 M$ before the merger —the pulse of junk radiation is clearly visible, although it is not shown here—, when the two black holes are separated by a distance of $12 M$. The holes are given initial data compatible with a quasi-circular orbit, making use of a method inspired in post-Newtonian evolutions [157] that reduces the eccentricity to a small value of $e < 0.002$. The system is evolved using the BSSN equations and the moving puncture approach described above. Gravitational radiation is extracted at $r_{\text{ext}} = 90 M$ by means of the Newman-Penrose scalar Ψ_4 as described in [77]. The two polarizations of the gravitational-wave strain $h_{+,\times}(t)$ are plotted in the upper panel, together with the amplitude, for the dominant mode $l = 2$, $m = 2$ of the radiation. The phase $\phi(t)$ and angular frequency $\omega(t)$ of the wave are shown as well.

4.2 NUMERICAL SIMULATIONS OF NON-PRECESSING BINARIES

Having seen that numerical simulations of black-hole binaries are possible, there is nothing to prevent us from further exploring the parameter space of physical configurations of the binary. Since the already-mentioned first successful numerical simulations of equal-mass, non-spinning binary black hole mergers were published [212, 88, 52] the NR community has continued exploring the parameter space of the BBH system. It is well known that astrophysically relevant black-hole binaries ought to have components with non-negligible spins. Likewise, systems with very different mass ratios and eccentric orbits are thought to exist in our Universe.

Aware of the complexity of parameter spaces with multiple degrees of freedom, most match-filtered searches for coalescing binaries have so far employed non-spinning templates, neglecting the effect of the spin by assuming a small, tolerable loss in SNR [10, 15, 16]. Dedicated searches for spinning binaries have attempted to model an enlarged parameter space by using a phenomenological template family designed to capture the spin-induced modulations of the gravitational waveform [11]. It would be desirable to understand the mapping between phenomenological and physical parameters, and to devise searches for spinning systems based on strictly physical parameters.

As a first step towards the general case, the phenomenological model constructed in chapter 5 shall be restricted to a subset of possible physical configurations, those in circular orbits and with spins aligned or anti-aligned with the angular momentum, as we justified in section 3.1. There are a number of NR simulations reported for non-precessing systems for a variety of spin values and mass ratios. Results with the BAM code are reported in [145] for the orbital hang-up case and in [144] for anti-aligned spins. The CCATTIE simulations are presented in [206, 221, 223]; a long spectral simulation with anti-aligned spins can be found in [92]. In this section we summarize all these numerical waveforms used in the construction of our phenomenological model.

4.2.1 *NR waveforms and Codes*

The NR waveforms employed in the construction of the hybrid model used in this paper are summarized in Table 6. They have been produced with four independent NR codes, BAM, CCATIE, Llama and SpEC. The first 3 codes use the moving-puncture approach [52, 88] to solving the Einstein equations in a decomposed 3+1 space-time while the last implements the generalized harmonic formulation [213, 69]. BAM and CCATIE use computational domains based on Cartesian coordinates, and the SpEC code use a sophisticated series of spherical and cylindrical domains; in the wave zone, the outer computational domains have the same angular resolution, thus the computational cost only increases linearly as the radius of the outermost shell is increased. The Llama code is based on finite differencing but the set-up of the numerical grid in the outer wave zone, as in SpEC, is also based on spherical coordinates with a constant angular separation. The large wave-zone enables accurate waveform extraction at large distances, accurate extraction of higher angular modes of the radiation, and it allows the outer boundary to be far enough away so that it is causally disconnected from the sphere where the radiation is extracted. A summary of the properties of all three codes is given in [143].

Table 6: NR codes and configurations used for the construction and verification of our hybrid waveforms and phenomenological model. The mass ratio q is defined as m_1/m_2 , assuming $m_1 \geq m_2$; $\chi_{1,2}$ are the dimensionless spins defined in equation. 3.1; a positive value of $\chi_{1,2}$ means that the spin is aligned with the orbital angular momentum L , and negative values are anti-aligned.

Set	Code	Mass ratios	Spins	GW extraction
#1	BAM [77, 157]	$q \in \{1 - 4\}$	$(0, 0)$	$R = 90M$
#2	"	$q = 1$	$(a, a), a \in \pm\{0.25, 0.5, 0.75, 0.85\}$	"
#3	"	$q = 2, 3, 4$	$(a, a), a \in \{\pm 0.5, 0.75\}$	"
#4	"	$q = 3$	$(-0.75, 0.75)$	"
#5	CCATIE [206]	$q = 1$	$(a, a), a \in \{0, 0.2, 0.4, 0.6\}$	$R = 160M$
#6	"	$q = 1$	$(a, -a), a \in \{0, 0.2, 0.4, 0.6\}$	"
#7ab	"	$q = 1$	$(\pm 0.6, a), a \in \{\pm 0.3, 0, -0.6\}$	"
#8	Llama [207]	$q \in \{1, 2\}$	$(0, 0)$	Null Infinity ¹
#9	SpEC [231]	$q = 1$	$(0, 0)$	$R = 225M$

The BAM data-set #1 covers the parameter space of non-spinning systems for several mass ratios during at least the last 5 orbits before merger (length $\sim 1100 - 1450 M$, where M is the total ADM mass of the space-time) [146, 23, 22, 144]. Data-set #2 consists of moderately long simulations covering at least the last 8 orbits before merger (length $\sim 1500 - 2200 M$) for equal-mass systems with equal spins, and are described in depth in [145, 144]. Data-set #3 consists of unequal-mass, unequal-spins simulations [25]. Data-set #4 is a simulation with unequal mass and unequal spins employed in the verification of our fitting mode [25]. For the sets #1–4, initial momenta for quasi-circular orbits were computed for non-spinning cases according to the procedures described in [157], leading to low-eccentricity ($e \approx 0.006$) inspiral evolutions. A number of different methods were used for the spinning cases [76, 145, 144], depending on which method gave the lowest eccentricity for a given configuration. The GW radiation is calculated from the Weyl tensor component Ψ_4 (see e.g. [202]) and extracted at a sphere with radius $R = 90 M$.

The CCATIE data-sets #5, #6 and #7ab correspond to the s -, u -, r - and t -sequences studied in [220]. They span the last $\sim 4 - 5$ orbits before merger (length $\sim 500 - 1000 M$) and are in fact not sufficiently long for being used in the hybrid construction. They are still useful to independently verify the reliability of our phenomenological fit. Data-set #5 corresponds to the hang-up configuration analogous to the BAM set #1; data-set #6 consists of configurations with $(\chi_1, \chi_2) = (a, -a)$, i.e. zero net spin; data-set #7a was analyzed in [206] in the context of the study of the recoil velocity (“kick”) of the final merged black hole. GW radiation is extracted at $R = 160 M$ via the Regge-Wheeler-Zerilli formalism for perturbations of a Schwarzschild black hole [217, 268, 17, 18].

¹ Only the GW radiation corresponding to the Llama $q = 1$ simulation has been extracted at future null-infinity using the Cauchy-characteristic method; the $q = 2$ waveform has been extracted at finite radius and extrapolated to $r \rightarrow \infty$.

Data-set #8 consists of two waveforms for non-spinning black holes with mass ratios $q = 1, 2$. The black holes are evolved with the `Llama` code according to the set-up reported in [207]. The outer boundary is placed at $3600M$ and the initial separation is $11M$, corresponding to 8 orbits in the inspiral phase followed by the merger and ringdown. The wave-extraction for the $q = 1$ configuration uses the Cauchy-characteristic method [218, 219], taking boundary data from the numerical space-time for a subsequent characteristic evolution of the metric to null-infinity, thereby obtaining waveforms that are unambiguously free of any systematic gauge effects. The only remaining source of error is then due to numerical discretization. The equal mass waveform using this code was reported in [219], while the $q = 2$ waveform is new.

Data-set #9 consists of a long non-spinning, equal-mass simulation that follows 16 orbits of the binary plus merger and ringdown of the merged black hole (length $\sim 4300M$). It was computed using the `SpEC` code with negligible initial orbital eccentricity ($\sim 5 \times 10^{-5}$). The GW radiation is extracted via Ψ_4 at $R = 225M$ in a similar manner to #1–4. A full description of this simulation is given in [232]. The long duration of the waveform allows for its use in the estimation of the errors associated to the length of the NR data. In particular, since it contains physical information at lower frequencies, an earlier matching is possible that reduces the ambiguities introduced by PN.

4.2.2 Going from Ψ_4 to h

The gravitational waveforms calculated using NR codes are typically reported in terms of the Weyl tensor component Ψ_4 , which is a complex function encoding the two polarizations of the outgoing transverse radiation. Ψ_4 is related to the two polarizations of the gravitational wave perturbation $h_{+, \times}$ (in the transverse-traceless gauge) via two time derivatives

$$\Psi_4 = \frac{d^2}{dt^2} [h_+(t) - ih_\times(t)] \quad (4.43)$$

Going from Ψ_4 to $h_{+, \times}$ thus involves two time integrations and requires us to fix two integration constants appropriately. The frequency domain offers a straightforward way of calculating the strain

$$h = h_+ - ih_\times \quad (4.44)$$

from Ψ_4 , since integration is replaced by division:

$$\tilde{h}^{\text{NR}}(f) = -\frac{\tilde{\Psi}_4^{\text{NR}}(f)}{4\pi^2 f^2} = A^{\text{NR}}(f) e^{i\Phi^{\text{NR}}(f)}, \quad (4.45)$$

where $\tilde{x}(f)$ denotes the Fourier transform of $x(t)$ as defined later in equation 5.2. Choosing the integration constants can be avoided by removing low frequency components via a suitable high-pass filter. This turns out to be a convenient, accurate and possibly less cumbersome method of calculating the strain h from Ψ_4 . An illustration is given in Fig. 12, where Ψ_4 data corresponding to a `Llama` simulation has been double-integrated in the time and in the frequency domain to yield h . In the case of the time-domain integration, a fitting procedure is needed to determine the two integration constants [60]; however, yet a small overall drift in $h(t)$ remains. When performing the division in the frequency domain, tanh-window functions are employed to

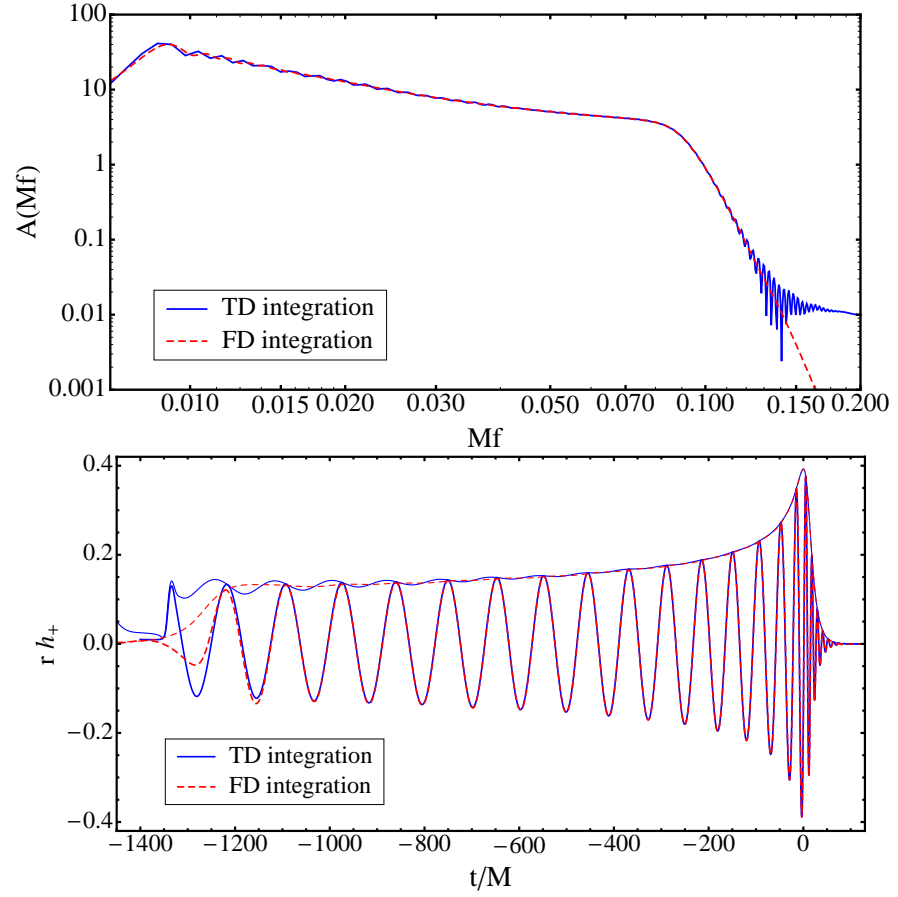


Figure 12: Comparison between the double integration in the time domain (solid line) and the division in the frequency domain (dashed line). Plotted is a NR simulation from data-set #8 of Table 6 with $q = 1$. The upper panel shows $|\tilde{h}(f)|$; we observe cleaner high-frequency components when performing the FD division, in contrast to the TD integration. The lower panel shows $h_+(t)$ and $|h(t)| = \sqrt{h_+^2(t) + h_\times^2(t)}$; the window function employed by our inverse Fourier transform algorithm is responsible for the loss of the first cycle of the waveform. Nevertheless, an overall cleaner $|h(t)|$ during the rest of the inspiral is observed when using the FD division.

pass-filter the data before computing the Fourier transform. Both methods involve a certain degree of fine-tuning in order to produce clean results; in this paper we use the frequency-domain version of the integration process.

This chapter concludes the description of the theoretical tools needed for the construction of the waveform model for the full coalescence of non-precessing binary black-hole systems introduced in chapter 5.

Coalescences of black-hole binaries are expected to be powerful sources of gravitational waves. Analytical and numerical models of the radiation emitted by these systems are crucial for detection and parameter estimation in matched-filter searches. The description and present status of both approaches has been discussed in the preceding chapters. Here, both methods are brought together in order to construct a model capable of describing the full binary black-hole coalescence process.

We present a novel approach to the construction of phenomenological gravitational waveform template models for non-precessing spinning black-hole binaries. Our method is based on a frequency domain matching of post-Newtonian inspiral waveforms with numerical relativity-based binary black hole coalescence waveforms. After introducing the need for full waveform models, section 5.2 outlines the conceptual differences between the analytical and numerical approaches to the binary black-hole problem. We quantify the various possible sources of systematic errors that arise in matching post-Newtonian and numerical relativity waveforms, and we use a matching criteria based on minimizing these errors. In section 5.3, an analytical formula for the dominant mode of the gravitational radiation of non-precessing black-hole binaries is presented that captures the phenomenology of the hybrid waveforms. This model constitutes one of the main achievements in this dissertation. Its implementation in current searches for gravitational waves should allow cross-checks of other inspiral-merger-ringdown waveform families and improve the reach of gravitational wave searches.

This chapter summarizes the work presented in [227]

5.1 FULL MODELS FOR BINARY BLACK-HOLE COALESCENCE

As a generalization of the classic Kepler problem in Newtonian gravity, the binary black hole (BBH) system in general relativity is of great interest from a fundamental physics viewpoint. Equally importantly, this system has received a great deal of attention for its relevance in astrophysics and, in particular, as one of the most promising sources of detectable gravitational radiation for the present and future generation of gravitational-wave detectors, such as LIGO [13], Virgo [19], GEO600 [136] or LISA [238]. The Kepler problem can be solved exactly in Newtonian gravity and it leads to the well-known elliptical orbits when the system is gravitationally bound. In contrast, in general relativity, the BBH system is not stable; it emits gravitational waves which carry energy away, thereby causing the black holes to inspiral inwards, and to eventually coalesce. The emitted GWs are expected to carry important information about this process, and it is one of the goals of gravitational-wave astronomy to detect these signals and decode them.

No analytic solutions of Einstein's equations of general relativity are known for the full inspiral and merger of two black holes. Post-Newtonian methods can be used to calculate an accurate approximation to the early inspiral phase, using an expansion in powers of v/c . As for the coalescence phase, starting with [212, 88, 52], the late inspiral and merger has been calculated by large-

*v is the orbital velocity;
 c is the speed of light*

A summary of the published “long” waveforms is given in the review [142], and a complete catalog of waveforms is being compiled at [189]; more recent work is summarized in [152]

scale numerical solutions of the full Einstein field equations. Since the initial breakthrough, there has been dramatic progress in numerical relativity simulations for GW astronomy, including many more orbits before merger, greater accuracy, and a growing sampling of the black-hole-binary parameter space. NR results are now accurate enough for GW astronomy applications over the next few years [143], and have started playing a role in gravitational wave searches [87, 49].

Given PN and NR results, it is promising to try and combine them to produce “complete” inspiral-merger-ringdown waveforms. PN techniques in their standard formulation become less accurate as the binary shrinks, and the approximation breaks down completely somewhere prior to the merger. NR waveforms, on the other hand, become more and more computationally expensive the larger the number of cycles that one wishes to simulate; the current record is 16 orbits for the equal-mass non-spinning case [232]. We therefore would hope to combine PN and NR results in the region between the point where NR simulations start, and where PN breaks down. To do this it is critical to verify that the PN and NR results are in good agreement in this region, and that there is a consistent PN-NR matching procedure. Much work has been done in comparing PN and NR results over the last 5-15 orbits before merger, so far focusing on the equal-mass non-spinning case [82, 53, 146, 135, 69, 70], the equal-mass non-precessing-spin case [145], and one unequal-mass precessing-spin case [89]; these studies suggest that a sufficiently accurate combination of PN and NR results should be possible. One topic that has not received much attention, however, is the systematic errors that are introduced by different choices of matching procedure.

One of the aims of this chapter is to further understand and quantify the various systematic errors that arise in the matching procedure. There are thus far two kinds of approaches to the NR-PN matching problem, both of which have yielded successful results. The first is the Effective-One-Body approach [80, 83, 98, 103]. Originally motivated by similar techniques in quantum field theory, the idea is to map the two body problem into an effective one-body system with an appropriate potential, and with the same energy levels as the two-body system. It was shown [80] that the appropriate one-body problem (for non-spinning black holes) is that of a single particle moving in a deformed Schwarzschild space-time. It turns out that most parameters of this one-body system can be found by using the appropriate PN calculations, and the remaining parameters are calculated by calibrating to numerical relativity simulations. This approach has been successful so far for non-spinning systems where only a single parameter needs to be calibrated by NR simulations [84, 85]. The spinning case is more complicated, and work is underway to extend the parameter space described by the model [199].

This window could be either in the time or frequency domain

A complementary approach is to perform a phenomenological matching of the GW waveforms in a window where both PN and NR are expected to be good approximations to the true waveform. The first step is to construct a hybrid NR+PN waveform by matching the two waveforms within the matching window. The waveform is completely PN before this window, completely NR afterwards, and it interpolates between the two in the matching window. Once the hybrid waveform is constructed and we are confident about the matching procedure, the second step is to fit the hybrid waveform to a parameterized model containing a number of phenomenological coefficients and finally to map them to the physical parameters of the system. The resulting

model would thus be parameterized by the masses and spins of the two black holes. Most of the work in this approach has thus far been in the time domain [24, 22, 23, 25].

In the work presented here we take a complementary approach; both the construction of the PN+NR hybrid waveform and the matching to a phenomenological model are carried out in the frequency domain. The reasons for this are twofold. Firstly, the errors in the matching procedure are technically easier to estimate in the frequency domain. Secondly and more importantly, in light of these potential errors, comparing results between two independent methods is a valuable way of ensuring that the matching procedure is robust.

The main results of this chapter are, firstly, to construct hybrid waveforms for binary black hole systems with aligned spins in the frequency domain. We do this by combining 3.5PN waveforms in the stationary phase approximation with a number of NR results. We show that this construction is internally consistent and it yields hybrids which are, for the most part, sufficiently accurate for the initial and advanced LIGO detectors. The difference between the various PN approximants is a more significant source of error than the numerical errors in the NR waveforms. Using these hybrid waveforms, we construct a phenomenological frequency-domain waveform model depending on three parameters that covers the space of aligned spins and moderate mass ratios. We show that the model fits the original hybrid waveforms with overlaps better than 98% for Advanced LIGO, and for the most part, better than 99% for essentially all black hole systems observable with Advanced LIGO, i.e. for systems with total mass ranging from ~ 10 to $\sim 400M_{\odot}$.

The post-Newtonian waveform model and the numerical waveforms that we employ have been already described in preceding chapters. Section 5.2 describes the fitting method and the various systematic errors that appear in this procedure. It quantifies the reliability of the waveforms for specific GW detector and signal-to-noise ratios. Section 5.3 fits these hybrid waveforms to an analytic model. It shows that the model provides a good representation of the hybrid waveforms and can be used in GW searches in the appropriate parameter space. Finally, section 5.4 concludes with a summary and suggestions for future work.

Eccentricity would need to be added, if appropriate

We use the same parameters as in [25]

5.2 MATCHING POST-NEWTONIAN AND NUMERICAL RELATIVITY

5.2.1 Basic Notions

The basic criteria for evaluating the goodness of fit for the hybrid waveform requires a notion of distance between two GW signals $h(t)$ and $h'(t)$. The simplest notion is the distance in the least-squares sense over an interval $t_1 \leq t \leq t_2$

$$\delta_{t_1, t_2}(h, h') = \int_{t_1}^{t_2} |h(t) - h'(t)|^2 dt. \quad (5.1)$$

We shall use this for the numerical relativity waveform $h_{\text{NR}}(t)$ and the post-Newtonian waveform $h_{\text{PN}}(t)$, with the interval $[t_1, t_2]$ being chosen so that both waveforms are reasonably good approximations (in a sense to be quantified later). Thus, the PN waveform is taken up to t_2 and the NR waveform is taken to start at t_1 ; they overlap within the interval $[t_1, t_2]$.

Let us consider the frequency domain equivalent. Our convention for the Fourier transform of a signal $x(t)$ is

$$\tilde{x}(f) = \int_{-\infty}^{\infty} x(t) e^{2\pi i f t} dt. \quad (5.2)$$

One needs to be careful in converting the time interval $[t_1, t_2]$ to a frequency interval $[f_1, f_2]$. In principle, the Fourier transform is “global” in time, and signals which have compact support in time cannot have compact support in frequency, and vice versa. However, for the binary black hole waveforms that we are considering, the frequency always increases in time, so that we can sensibly associate a frequency interval $[f_1, f_2]$ with a given time interval $[t_1, t_2]$. For these waveforms, we can consider the above distance definition in the frequency domain:

$$\delta_{f_1, f_2}(h, h') = \int_{f_1}^{f_2} |\tilde{h}(f) - \tilde{h}'(f)|^2 df. \quad (5.3)$$

We shall use such a norm (applied to the phase) for constructing the hybrid waveform.

When evaluating the goodness of a hybrid waveform for a particular detector, we need to consider detector-specific inner products, which are convenient to describe in the frequency domain. Let $S_n(f)$ be the single-sided power spectral density of the noise in a GW detector defined as

$$E[\tilde{n}(f)\tilde{n}^*(f')] = \frac{1}{2} S_n(f) \delta(f - f'). \quad (5.4)$$

Here $n(t)$ is the detector noise time series with $\tilde{n}(f)$ its Fourier transform and E refers to the expectation value over an ensemble of independent realizations of the noise, which is assumed to be a zero-mean, stationary, stochastic process. This equation implies that data at different frequencies are independent, and is one of the reasons why working in the frequency domain is so useful in data analysis. The time domain description of the noise is more complicated; $n(t)$ and $n(t + \tau)$ are in general not independent; $E[n(t)n(t + \tau)]$ is generally non-zero. For stationary noise this is a function $C(\tau)$ only of τ , and is related to $S_n(f)$ via a Fourier transform.

See e.g. Papoulis [201]

Given $S_n(f)$, we use the following definition of an inner product between two signals $x(t)$ and $y(t)$

$$\langle x|y \rangle \equiv 4\Re \int_0^{\infty} \frac{\tilde{x}(f)\tilde{y}^*(f)}{S_n(f)} df \quad (5.5)$$

where $\tilde{x}(f)$, $\tilde{y}(f)$ are the Fourier transforms of $x(t)$, $y(t)$ respectively. This inner product is appropriate for Gaussian noise and forms the basis for matched filtering. It can be used to define a suitable notion of distance between two signals $h(t)$ and $h'(t)$ as $\langle \delta h|\delta h \rangle$, where $\delta h(t) = h'(t) - h(t)$.

See e.g. Helstrom [149]

Following [175], we define a one-parameter family of waveforms which interpolates between $h(t)$ and $h'(t)$ as

$$h''(t; \lambda) = h(t) + \lambda \delta h(t). \quad (5.6)$$

If we use an unbiased estimator for λ , the variance σ_λ^2 of the estimator is bounded from below by the Cramer-Rao bound

See e.g. Kendalls [247]

$$\sigma_\lambda^2 \geq \langle \delta h | \delta h \rangle^{-1}. \quad (5.7)$$

This can be a useful bound for large SNRs which is in fact what we are interested in here; it is easier to distinguish between two loud waveforms and demands on the waveform model are correspondingly more stringent. Thus, a useful condition for being able to distinguish between the two waveforms is $\sigma_\lambda < 1$. Thus, if $h(t)$ is the true waveform and $h'(t)$ our approximation to it, then we say that $h'(t)$ is a sufficiently accurate approximation if $\langle \delta h | \delta h \rangle \leq 1$. It is clear that $\langle \delta h | \delta h \rangle \propto \rho^2$ where $\rho = \langle h | h \rangle^{1/2}$ is the optimal SNR. Hence, as we just remarked, the two signals are easier to distinguish when the detector is more sensitive, or when the signal amplitude is larger. It will be convenient to normalize the norm of δh and write this distinguishability criterion as

$$\frac{1}{\rho^2} \langle \delta h | \delta h \rangle \geq \frac{1}{\rho^2}. \quad (5.8)$$

Thus, for a given detector, we choose a reasonable guess ρ_0 for the largest expected SNR and we compute the normalized distance between the two waveforms $\langle \delta h | \delta h \rangle / \rho^2$. If this exceeds $1/\rho_0^2$, then we consider that the detector is able to distinguish between the two waveforms.

If we are interested in the less stringent requirement of detection rather than in strict distinguishability, then a sufficient condition is [175]

$$\frac{1}{\rho^2} \langle \delta h | \delta h \rangle < 2\epsilon, \quad (5.9)$$

where ϵ is the maximum tolerated fractional loss in SNR. If we are willing to accept e.g. a 10% loss in detection rate, then a suitable choice is $\epsilon \approx 0.03$.

A useful way to describe the efficacy of approximate waveform models is through the concepts of effectualness and faithfulness introduced in [98]. Let $h_\lambda(t)$ be the exact waveform with parameters λ and the approximate waveform model be $h_\lambda^{\text{app}}(t)$. The ambiguity function is defined as the normalized inner product maximized over extrinsic parameters

$$\mathcal{A}(\lambda, \lambda') = \max_{t_0, \phi_0} \frac{\langle h_\lambda | h_{\lambda'}^{\text{app}} \rangle}{\sqrt{\langle h_\lambda | h_\lambda \rangle \langle h_{\lambda'}^{\text{app}} | h_{\lambda'}^{\text{app}} \rangle}} \quad (5.10)$$

where t_0 is the time offset between the two waveforms, and ϕ_0 is the initial phase. Performing a further maximization over the parameters λ' of the model waveforms, we define $\hat{\mathcal{A}}(\lambda) = \max_{\lambda'} \mathcal{A}(\lambda, \lambda')$. If $\hat{\mathcal{A}}(\lambda)$ exceeds a chosen threshold, e.g. 0.97, then the waveform model h^{app} is said to be *effectual*. In order to be able to estimate parameters we also need the model to be *faithful*. This means that the value of λ' which maximizes $\mathcal{A}(\lambda, \lambda')$ should not be biased too far away from λ .

This corresponds to sources uniformly distributed in space

Effectual models are sufficient for detection

5.2.2 Issues in Matching PN with NR

It is useful at this stage to discuss some of the issues that arise in combining PN and NR results. Since PN and NR are both used to address the BBH problem, one can use start with the two black holes very far apart, evolve them using appropriate PN equations of motion and compute the resulting waveforms. As one gets close to the merger, terminate the PN evolution and use this end-point to construct initial data for the full NR simulation which

then evolves the black holes through the merger and ringdown. However, the formalisms and methods employed in the two cases are radically different and there are potential difficulties in carrying out this procedure.

See e.g. [134, 211]

In fact it can be persuasively argued that the cosmological setting is more relevant to GW observations than strict asymptotic flatness

PN is based on a perturbative expansion in powers of the small parameter $\epsilon = v/c$, where v is the orbital velocity and c is the speed of light. In the usual formulations, PN theory uses a point-particle description of the black holes, and their parameters can be viewed as effective parameters which couple in the appropriate manner with the external background gravitational field. The goal of PN theory is to find a one-parameter sequence of solutions to the field equations $g_{\mu\nu}^\epsilon$ to any specified order in ϵ . It has recently been shown rigorously [192] that, in the cosmological setting with gravitating perfect fluids, the one-parameter family of solutions exists and admits an expansion in ϵ^n to any order. While similar results in the asymptotically-flat case are not yet available, it is certainly reassuring to know that PN works as advertised in this non-trivial setting. The errors in PN waveforms are then due to the systematic differences between the true waveform and the asymptotic series expansion in ϵ^n truncated at a finite order, and this error depends on which particular PN expansion one chooses to use.

In contrast, numerical relativity is based on the 3+1 formulation of general relativity as an initial value problem, and one solves the resulting partial differential equations numerically. The GW signal is typically extracted at large distances from the source by calculating the outgoing transverse component of the gravitational radiation encoded in the Weyl tensor component Ψ_4 . For a given physical configuration (choice of masses, spins, separation etc.), one specifies the initial data consisting of the spatial metric and extrinsic curvature of the initial spatial slice. The initial data should be chosen to be as compatible as possible with the space-time computed in the PN formalism, and significant progress has been made in this regard [156, 260]. The black holes here are not point particles but rather black hole horizons. The parameters of the black hole are often computed as integrals over the apparent horizon, and in most cases the parameters used in constructing the initial data are also useful approximations to the true ones. There are however possible systematic errors. For example, if we are using the quasi-local horizon definitions, an important requirement is that the horizon should locally be approximately axisymmetric. The methods for finding the approximate symmetry vectors have become increasingly accurate and reliable [107, 159, 55, 147, 177]. However, it should be kept in mind that the assumption of approximate axisymmetry is expected to become increasingly worse closer to the merger. Furthermore, the very use of apparent horizons is gauge dependent; using a different time coordinate will lead to a different set of apparent horizons and possibly also different values of the parameters. In the inspiral phase when the horizons are sufficiently isolated this gauge issue is not expected to be a problem, but as we get closer to the merger, the variation in the parameters due to gauge choices could become significant [188].

This has not yet been quantified

Let us elaborate a little more on the spin. Most post-Newtonian treatments are based on the equations of motion derived in [95, 200]. The starting point is the spin tensor $S^{\mu\nu}$ constructed from moments of the stress energy tensor $T^{\mu\nu}$. Since $S^{\mu\nu}$ has potentially 6 non-zero independent components, the system for the 4 equations of motion $\nabla_\mu T^{\mu\nu} = 0$ is over-determined. One thus imposes the so-called spin supplementary conditions such as $S^{\mu\nu}p_\nu = 0$ or $S^{\mu\nu}u_\nu = 0$ with p_μ being the 4-momentum and u_ν the 4-velocity.

These different conditions lead to physically different equations of motion and trajectories [172]. On the other hand, for black holes in NR, a common method for evaluating spin employs the formalism of quasi-local horizons [45]. The final result for the magnitude of the horizon angular momentum is an integral over the apparent horizon S :

$$J = -\frac{1}{8\pi} \oint_S K_{\mu\nu} \phi^\mu dS^\nu, \quad (5.11)$$

where $K_{\mu\nu}$ is the extrinsic curvature of the Cauchy slice, ϕ^μ is a suitable approximate axial symmetry vector on S [107, 159, 55, 147, 177], and dS^b is the area element on the apparent horizon. The direction of the spin is harder to find, but some approximate methods are available [90, 159]. There is yet no detailed study of possible analogs of the spin supplementary conditions in this formalism, or on the equations of motion for horizons with a given set of multipole moments. For a horizon with area A and spin magnitude J , the mass is given by the Christodoulou formula

$$m = \sqrt{\frac{A}{16\pi} + \frac{4\pi J^2}{A}}. \quad (5.12)$$

Hence, uncertainties in spin can also lead to uncertainties in the mass.

As long as we are dealing with just the numerical or PN waveforms by themselves, small effects in the definitions of mass and spin are not important for most applications. In fact, we can treat them as just convenient parameterizations of the waveform without worrying about their detailed physical interpretation. However, when we wish to compare the results from frameworks as different as PN and NR this may no longer work. Depending on the details of the matching procedure, systematic differences between the various definitions might need to be taken into account, or at the very least they should be quantified. One valid approach is to not assume *a priori* that the PN and NR parameters are equal to each other but rather, for a given numerical waveform, we search over PN waveforms in a particular PN approximant and find the best fit values.

5.2.3 An Illustration for Non-Spinning Systems

Let us now move to a concrete case of constructing hybrid waveforms, considering the non-spinning Llama waveforms, i.e. data set #7 in Table 6. Recall that this data set consists of two waveforms with non-spinning black holes with mass ratios 1 : 1 —used in figures 16 and 17— and 1 : 2 —figures 13, 14, 15 and 18—. Since these waveforms are calculated using the Llama code with extraction at future null-infinity with the Cauchy-characteristic method for the equal mass case, or well into the wave zone for the 1 : 2 case, we have a high degree of belief that systematic effects of waveform extraction are small. Even for these waveforms, based on the discussion above, in principle we should not rule out a small mismatch in the values of the spin (and perhaps also eccentricity) between the NR and PN waveforms. For simplicity, let us consider only the possibility that the symmetric mass ratio η could be different, and restrict ourselves to non-spinning black holes and zero eccentricity. We would like to match the Llama waveforms with the frequency domain PN waveforms discussed in section 3.1 with the values of the spins set to zero. The total mass M sets the scale for the time (and frequency); in addition

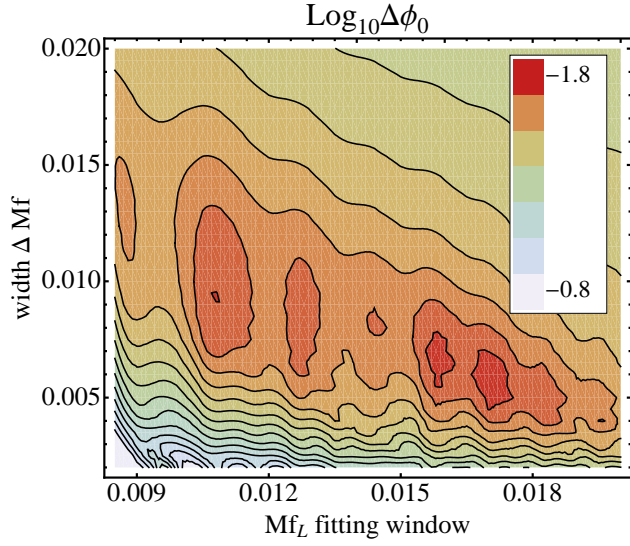


Figure 13: Contour plot for the fitting error $\Delta\phi_0$ in the $(f_L, \Delta f)$ plane. Here η is kept fixed to the NR value and we optimize over ϕ_0 and t_0 .

we have the extrinsic parameters for the time offset and initial phase t_0 and ϕ_0 . Furthermore, we only consider the $\ell = m = 2$ mode, so that the PN waveform is of the form $\tilde{h}^{\text{PN}}(Mf; \phi_0, t_0, \eta_{\text{PN}})$ in the frequency domain.

Fitting Errors

For a given NR waveform $h_{\text{NR}}(t)$ we consider a time window $(t_0, t_0 + \Delta t)$ or, alternatively, in the frequency domain the matching region consists of a lower starting frequency f_L and a width Δf . We match the two waveforms in a least-squares sense by minimizing the phase difference in Fourier space

$$\delta = \min_{t_0, \phi_0, \eta_{\text{PN}}} \int_{f_L}^{f_L + \Delta f} |\delta\phi(f; \eta_{\text{NR}}, \eta_{\text{PN}}, t_0, \phi_0)|^2 Mdf, \quad (5.13)$$

$$\delta\phi(f) \equiv \phi_{\text{NR}}(f; \eta_{\text{NR}}) - \phi_{\text{PN}}(f; t_0, \phi_0, \eta_{\text{PN}}).$$

We optimize δ over all allowed time and phase shifts, i.e. (t_0, ϕ_0) , and the PN intrinsic parameters λ_{PN} . Given the previous discussion on the possible differences between the intrinsic parameters λ between the PN and NR frameworks, here we have distinguished between the intrinsic parameter η of equation 2.6 appearing in h_{PN} and h_{NR} . Note that we are not only neglecting spins and eccentricity but also assume $M_{\text{PN}} = M_{\text{NR}} = M$. Future analyses should successively drop these simplifications.

Let us now consider the choice of the optimal matching window $(f_L, f_L + \Delta f)$, and the best fit values of $(\phi_0, t_0, \eta_{\text{PN}})$. For each window, the least squares procedure gives a best fit value $\eta_{\text{PN}} = \eta(f_L, \Delta f)$ and $1\text{-}\sigma$ error estimates $\Delta\eta, \Delta\phi_0, \Delta t_0$. Our principle for choosing $(f_L, \Delta f)$ is to pick the one for which the quality of fit between the NR and PN waveforms is the best, i.e. to minimize the fitting errors.

We first fix $\eta_{\text{PN}} = \eta_{\text{NR}}$, choosing the 1 : 2 waveform, and consider fitting for (ϕ_0, t_0) . The result for $\Delta\phi_0$ is shown in figure 13 as a contour plot in the $(f_L, \Delta f)$ plane. There are clearly multiple best-fit islands but we already see that the optimal window choice turns out to be a long frequency width starting

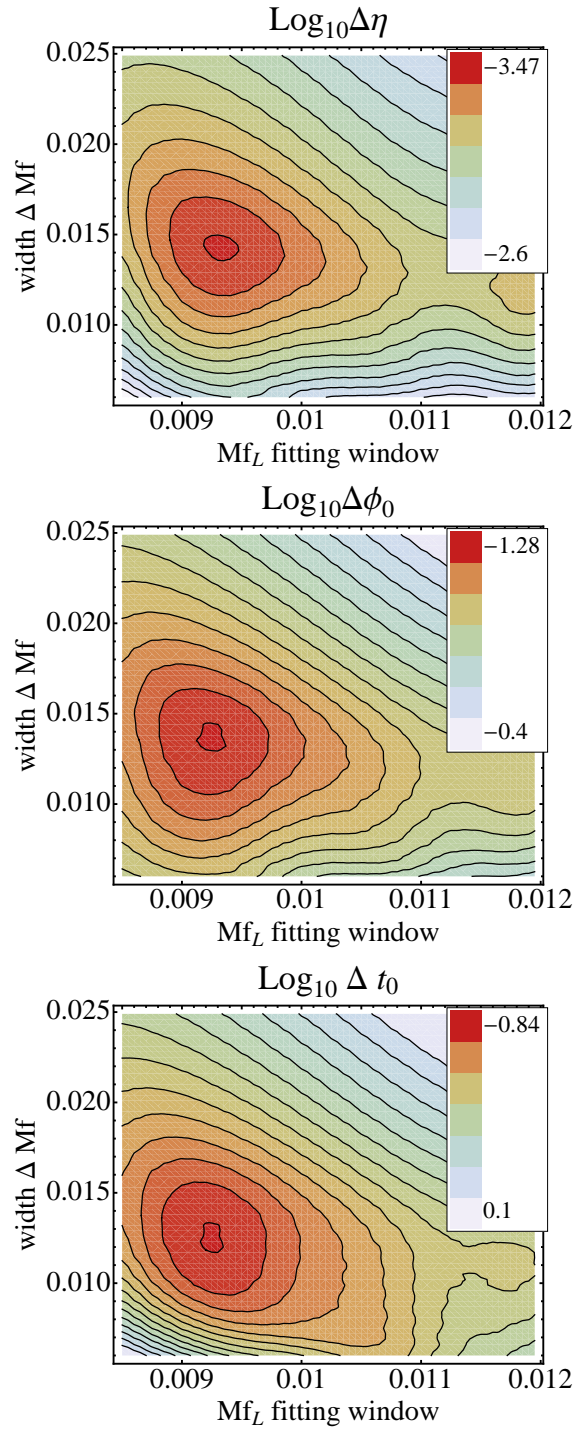


Figure 14: Dependence of the fitting errors in η , ϕ_0 and t_0 on the frequency window ($f_L, \Delta f$). Note that there is a clear choice of $(f_L, \Delta f)$ which optimizes the fit between the NR waveform and the PN waveforms with different η . At the best fit point, the accuracy in η by this fitting procedure is better than 10^{-3} .

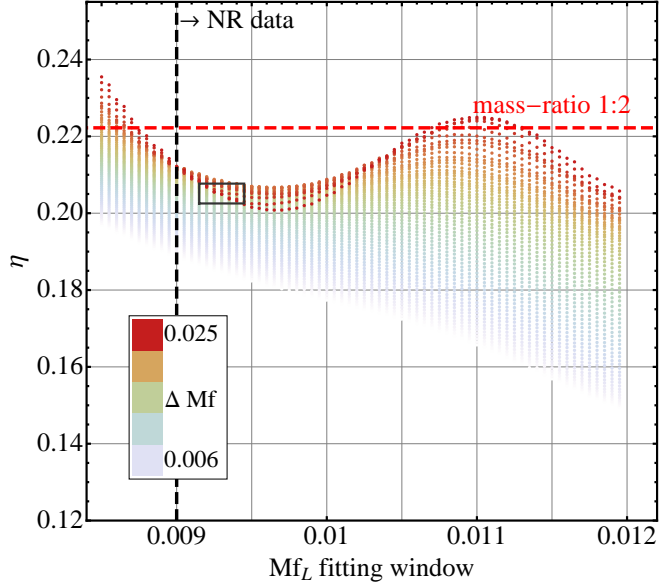


Figure 15: Best fit value of η as a function of the start frequency f_L of the matching window for the waveform which corresponds nominally to a mass ratio 1 : 2, i.e. $\eta_{\text{NR}} = 2/9 = 0.222 \dots$; this is shown by a horizontal dashed line. The vertical dashed line at $Mf_L = 0.009$ is the start frequency of the NR waveform. A rectangle highlights the region of minimal fitting errors from figure 14. We see that the best determined values of η are clearly smaller than η_{NR} .

at low frequencies, or a relatively short window starting closer to the merger. Regarding the increasing error PN that most likely introduces towards higher frequencies, we prefer using an early and long matching window. Though we do not show it here, the result is similar for the time offset t_0 .

It is more interesting instead to generalize this and allow all three parameters ($\eta_{\text{PN}}, \phi_0, t_0$) to vary. The main result is displayed in figure 14, which shows contour plots of the fitting errors $\Delta\eta, \Delta\phi_0$ and Δt_0 in the $(f_L, \Delta f)$ plane. There are now clear and consistent minima for all errors and thus a clear best choice for f_L and Δf . At this optimal choice, we see that we can fit η, ϕ_0 and t_0 to better than $10^{-3}, 0.06$ and $0.15M$, respectively. Apart from the error $\Delta\eta$, the actual best fit value η is also of great interest. Figure 15 shows the value of η as a function of the start frequency of the matching window f_L and Δf . The x-axis on this plot is the start point of the fitting window f_L , and the color bar indicates Δf . The most trustworthy values correspond to the optimal choice of $(f_L, \Delta f)$ obtained in figure 14; we indicate the union of all three minimal-error islands as a rectangle in figure 15.

To summarize, from figures 14 and 15 we deduce that, if we were to ignore η_{NR} (the value that the numerical simulation nominally assumes) and simply try to find the best fit with the PN waveforms described in section 3.1, then we can clearly estimate the best matching region $(f_L, f_L + \Delta f)$ and a best fit value $\eta_{\text{PN}} = \eta \pm \Delta\eta$. This procedure illustrates a trade-off between trying to match at early frequencies, where our PN model is more reliable and having a sufficiently long fitting window, in which a considerable frequency evolution leads to an accurate estimate of the fitting parameters.

Accuracy of the Hybrid Waveform

Later we shall show a phenomenological fit for the hybrid waveform and we shall claim that the fit reproduces the hybrid waveform sufficiently accurately, but here we first ask whether the hybrid waveform is itself sufficiently accurate subject to various errors. The basic criteria for evaluating this is the notion of a distance between two signals whose difference is δh , as given in equation 5.8. For two signals h and h' , we shall consider the normalized distance squared $\langle \delta h | \delta h \rangle / \rho^2$, where ρ is calculated from our best model. Now the total mass M becomes important. Previously, when we looked at the least square fits in equation 5.13, the total mass appeared just as a scale factor. However, in the inner product equation 5.5, the power spectral density $S_n(f)$ sets a frequency scale, and the value for $\langle \delta h | \delta h \rangle$ becomes mass-dependent. We shall consider two design noise curves, Initial and Advanced LIGO [3, 20]. We are then addressing the question of how different our hybrids would be if we were to use a slightly different result on either the NR or PN side.

On the NR side, we first consider data computed at different resolutions. The Llama waveforms for the equal-mass case have been computed at low, medium and high resolutions corresponding to spacing $h = 0.96, 0.80$ and 0.64 on the wave extraction grid. We combine them with the TaylorF2 model from section 3.1 by using the optimal matching window discussed around figure 13 and $\eta_{\text{PN}} = \eta_{\text{NR}}$. The result is shown in figure 16. Hybrids constructed with medium- and high-resolution waveforms would be indistinguishable even with Advanced LIGO at a SNR of 80 over the considered mass range. Thus, we conclude that the numerical errors related to a finite resolution are not relevant in the hybrid construction process.

The uncertainties increase when comparing NR data produced by different codes. Similar to the analysis of different resolutions we calculate the distance of hybrid waveforms for non-spinning black holes with mass ratio 1 : 1 and 1 : 2. Results from data set #1 and #8 (see Table 6) were used, and the distance plot in figure 17 shows that the 1 : 2 waveform would be distinguishable for Advanced LIGO at SNR 20 for a total masses between $\sim 30M_\odot$ and $\sim 65M_\odot$. Note that these errors are dominated by our matching to PN which possibly yields different fit parameters for the PN model and therefore amplifies small differences in the NR data. Towards higher masses, the influence of this matching decreases as well as the distance of both waveform. However, as we shall show next, all these errors are still small compared to the intrinsic uncertainties introduced by PN and they do not matter for Initial LIGO. If we care only about detection with a minimal match $\epsilon = 0.03$ [see equation 5.9], we have even less to worry about.

The errors on the PN side turn out to be much more important. figure 18 illustrates the effect of using different PN approximants combined with the same Llama 1 : 2 simulation. The dashed curve shows the difference in the hybrid waveforms when we match 3PN or 3.5PN phase following the TaylorF2 frequency domain approximants described in section 3.1. We see that the difference between the 3PN and 3.5PN hybrids becomes significant even for Initial LIGO at SNR of 8 between a total mass of $\sim 5M_\odot$ and $\sim 35M_\odot$. Similarly, the differences between the F2 and Taylor T1 & T4 approximants are also significant. For detection with $\epsilon = 0.03$ (see equation 5.9), we need to look at the horizontal line with $\langle \delta h | \delta h \rangle / \rho^2 = 0.06$ in figure 18. For all the curves except the hybrid constructed with the SpEC waveform, there is a small

3PN amplitude, 3.5PN TaylorF2 phase combined with highest resolution NR waveform

The amplitude is taken at 3PN order in both cases

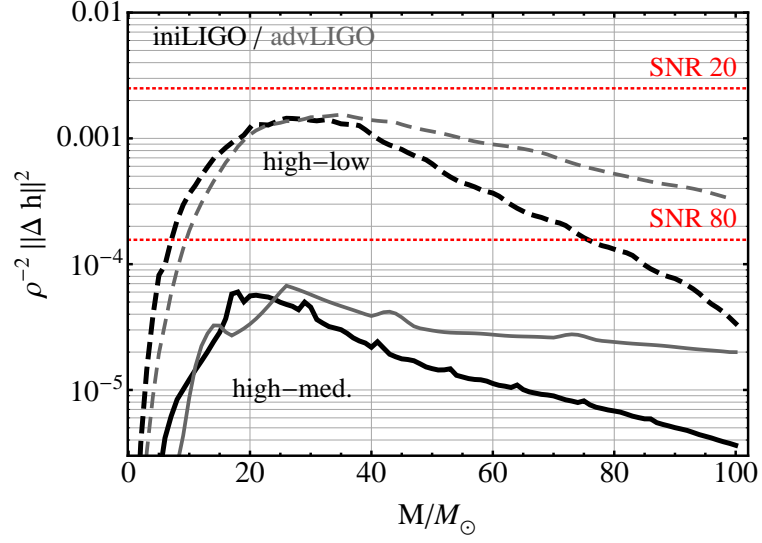


Figure 16: Distinguishability of different hybrid waveforms constructed from Llama equal-mass waveforms at different resolutions. The two sets of curves are for Initial and Advanced LIGO, and we consider the difference between the high-medium resolution waveforms, and the high-low waveform resolutions. The horizontal lines are the lines of constant SNR (in fact it is $1/\text{SNR}^2$). If the distance measure goes above these lines, then the waveforms can be distinguished from each other.

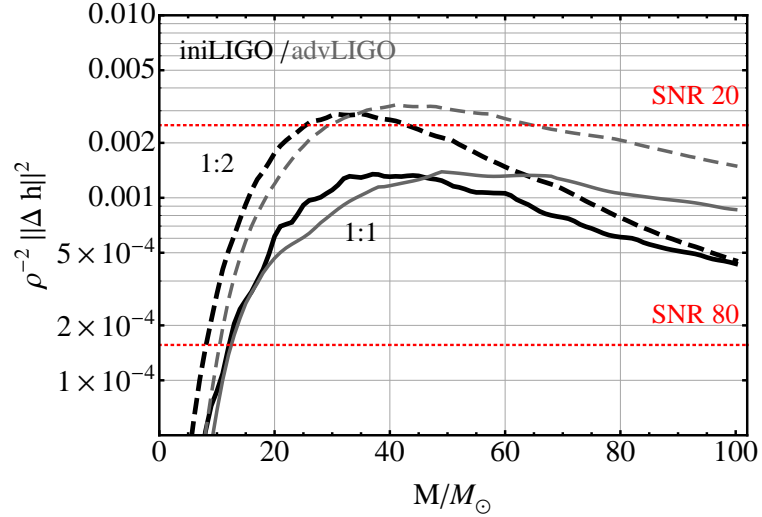


Figure 17: Distinguishability of different hybrid waveforms constructed from NR waveforms produced with either BAM or Llama. The solid lines indicate the normalized distance in the equal-mass case, dashed lines show the case of mass-ratio 1 : 2. The highest available resolution was always used.

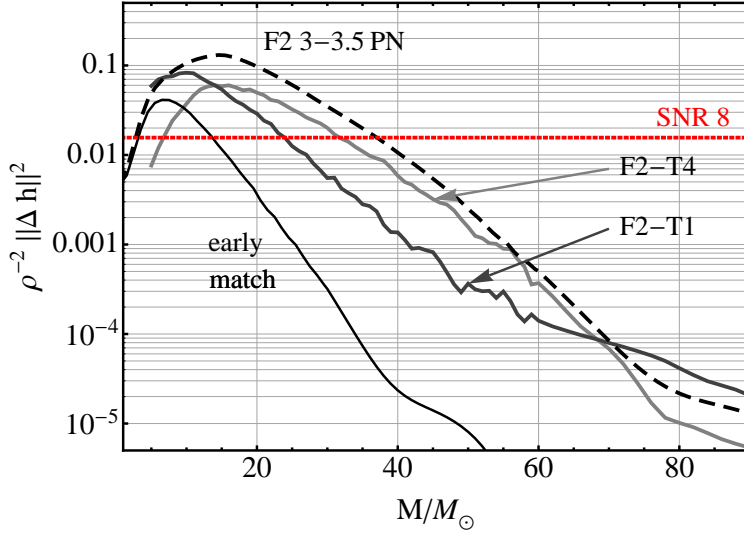


Figure 18: Initial LIGO’s ability to distinguish hybrid waveforms constructed from different PN approximants. This plot shows that the hybrids are not sufficient for detection at the $\epsilon = 0.03$ level [equation 5.9] only for a small range of masses. “Early match” is a reference for matching 3PN or 3.5PN F2 at early frequencies to the long equal mass SpEC waveform.

range of masses for which the difference between the hybrids would matter even for detection.

As a reference, we employ the same procedure for the longest equal mass waveform available, i.e. the data-set #9 based on the SpEC code which covers ~ 16 orbits before merger. For this longer waveform, we again match the TaylorF2 phase at 3PN and 3.5PN order. Figure 18 shows that the hybrid remains accurate for a larger range of total masses; this is mainly because the waveform is considerably longer than the Llama waveforms used above, hence it allows us to use an earlier and longer matching window.

Having carried out this study of errors for non-spinning waveforms, we can now draw some conclusions for the aligned-spin case. In principle, the procedure outlined here remains valid; we should search over not only $\{\eta, t_0, \phi_0\}$, but now also over the spins $\{\chi_1, \chi_2\}$. We would not expect the results to be *better* than shown here for non-spinning waveforms because (i) we are adding two more parameters and (ii) the waveforms #1-4 are expected to have more wave-extraction systematic errors than the Llama results considered here. Most importantly, as we have just seen, the intrinsic errors in PN are more significant whereas the numerical accuracy is not the bottleneck. The intrinsic parameter biases in PN also show up when different PN models are compared with each other. An extensive comparison of different PN models is made in [86]; this paper quantifies the mutual effectualness and faithfulness of the different PN models and shows that errors of $\sim 20\%$ are not uncommon for Advanced LIGO. The less than 10% error in η shown in figure 15 are thus entirely consistent with the differences between different PN models. To address this, one needs either improved PN models or a greater variety of longer NR waveforms such as the long SpEC simulation.

As a simplification, in what follows below we will choose the matching window based on maximizing over the extrinsic parameters (t_0, ϕ_0) motivated by figure 13. In that figure, we observe the best fit region extending

diagonally from $M\Delta f \approx 0.013$ on the y -axis, to the bottom right corner. It turns out that for this diagonal, the upper frequency of the window does not vary much, $0.020 \lesssim Mf_L + M\Delta f \lesssim 0.024$, and we shall use this fact below for constructing hybrid waveforms for aligned spinning systems.

5.2.4 Construction of Hybrid Waveforms for Aligned-Spin Systems

Let us now proceed to the construction of a hybrid waveform model for non-precessing, spinning systems with comparable mass. Again, the waveforms described in section 3.1 will be the basis for our model at low frequencies corresponding to the inspiral stage. On the other hand, the NR simulations described as data-sets #1–3 in Table 6 contain physical information for frequencies above $Mf \approx 0.008$. We will refer to figure 13 to justify our choice of an overlapping window at $Mf \in (0.01, 0.02)$. Once this interval is fixed, we use the freedom in t_0 and ϕ_0 to align the PN and NR phases; both transformations keep the overlap invariant and are therefore irrelevant from the point of view of template construction.

Having identified the appropriate overlapping window, we now carry out the following matching procedure for all NR simulations of data-sets #1–3: PN and NR phases are aligned in the interval $Mf \in (0.01, 0.02)$ by adjusting t_0 and ϕ_0 ; the middle point is taken as matching point between PN and NR and we construct a hybrid phase consisting of TaylorF2 at low frequencies and NR data at high ones. An analogous procedure is applied to the amplitude, but in this case there is no freedom for adjusting any parameter. Hence, we use an educated guess for the matching frequency and find the frequency which minimizes $A^{\text{NR}}(f_{\text{match}}) - A^{\text{PN}}(f_{\text{match}})$. Due to the existence of a common region where PN and NR overlap, such a point can always be found. The hybrid amplitude consists of PN before and NR after f_{match} . Small wiggles in the NR amplitude, due to the Fourier transform, do not affect the phenomenological fit significantly. The most important ingredient for arriving at an effectual model is the phase.

We make a choice compatible with that for the phase

Figure 19 illustrates the above-described hybrid construction method for matching PN and NR data in the frequency domain. The procedure introduces no resizing of neither data and allows for the construction of waveforms containing all the information from the TaylorF2 approximant at low frequencies and input from the NR simulations for the late inspiral, merger and ringdown. The matching procedure has been applied to NR data-sets #1–3. The resulting hybrid PN-NR data cover a part of the parameter space corresponding to equal-valued, (anti-)aligned spins for $0.16 \leq \eta \leq 0.25$ and constitute the “target” waveforms to be fitted by the analytical phenomenological model described in section 5.3.

A fundamental check to assess the validity of our matching procedure is the verification that the hybrid waveforms do not contain irregularities arising from the way PN and NR are stitched together. We show that this is indeed not the case by performing the inverse Fourier transform of our hybrids and comparing them with the numerical data they were created from in the vicinity of the merger. The results of the perfect agreement in the time domain can be seen in figure 20.

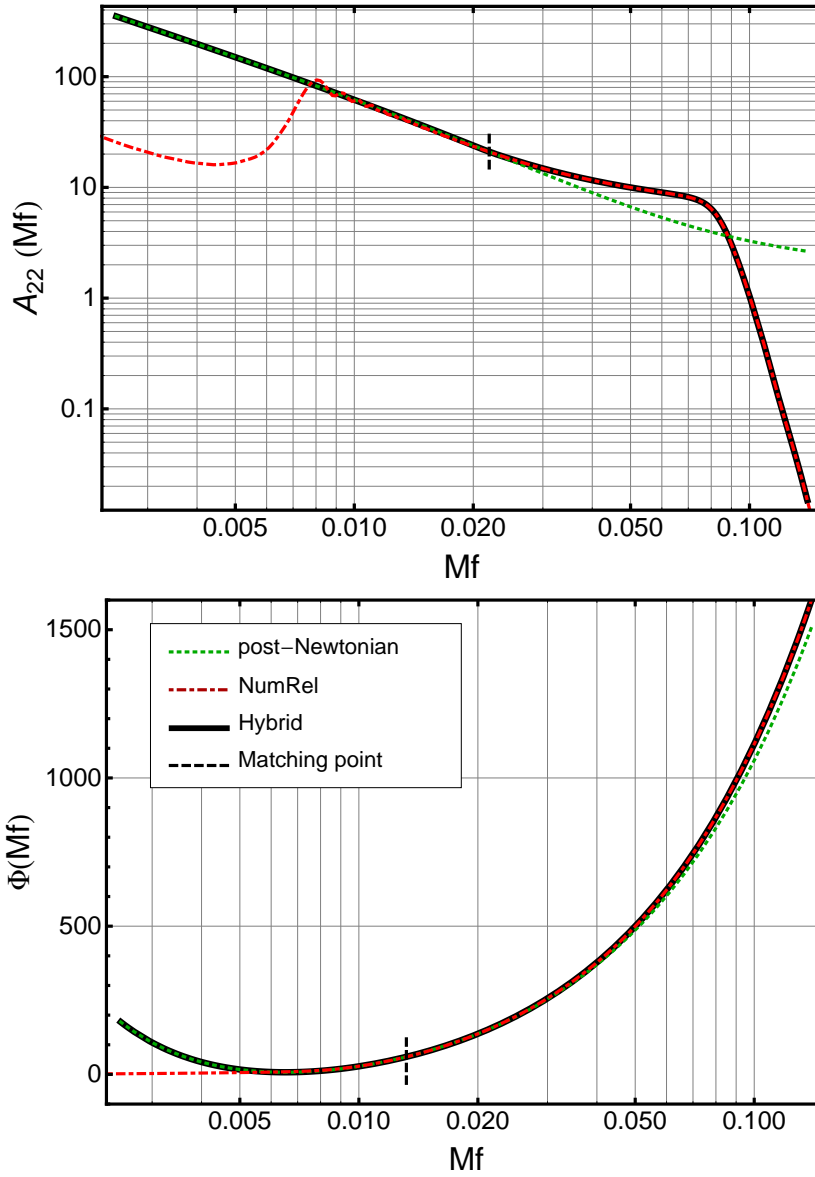


Figure 19: Illustration of the method for constructing PN-NR hybrid waveforms in the frequency domain. The data corresponds to an equal-mass binary with aligned spins $\chi_1 = \chi_2 = -0.25$. The left panel shows the amplitude and the right displays the phase of the dominant $\ell = 2$, $m = 2$ mode of the GW complex strain $\tilde{h}(f)$. The green dotted lines correspond to the TaylorF2 PN approximant and the red dot-dashed curve is the NR data. The hybrid waveform is depicted in solid black and the matching points for amplitude and phase are indicated with a dashed line.

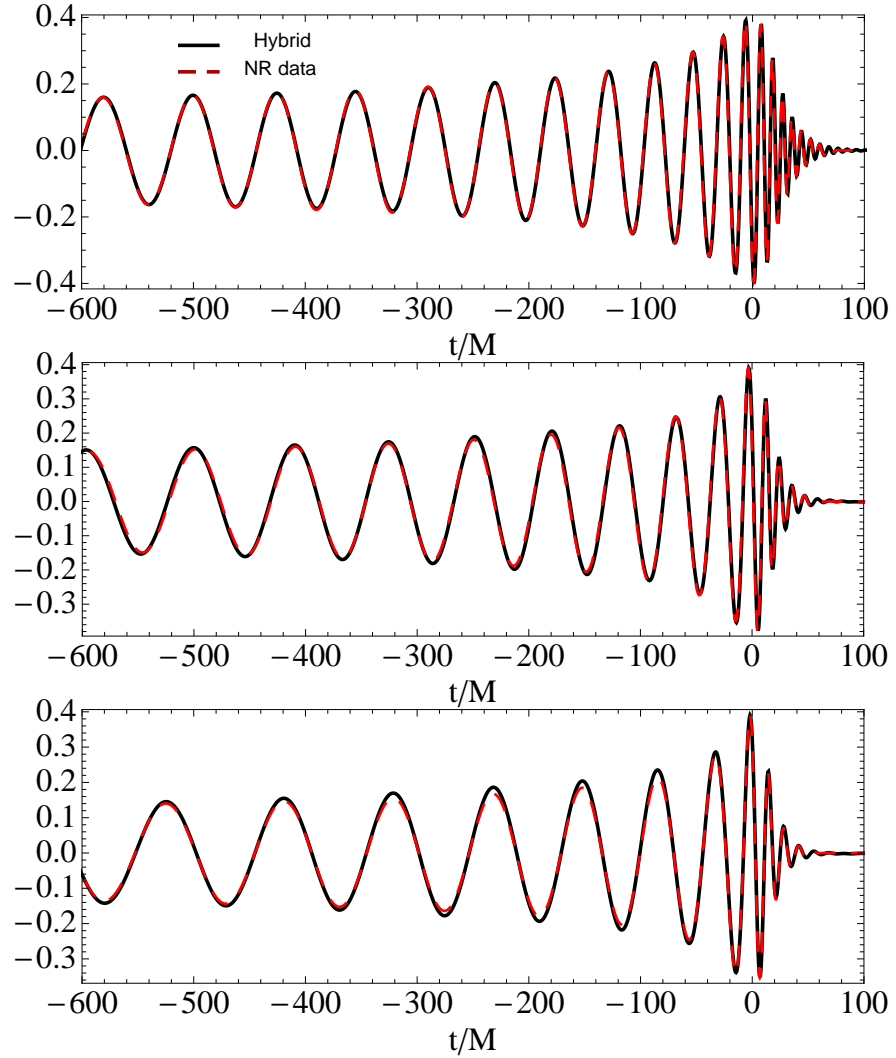


Figure 20: Comparison of hybrid waveforms with the numerical data used in their construction in the time domain. The three waveforms correspond to equal-mass simulations of spins $\chi_1 = \chi_2 = 0.85, 0$ and -0.75 in the upper, mid and bottom panel respectively. We plot the final cycles of the hybrid waveforms in the time domain, with the corresponding numerical simulation on top of them. The agreement in the time domain confirms that our matching procedure does not introduce irregularities in the final hybrid waveform. Additionally, the accumulation of orbits in the *hang-up* configuration displayed in the upper panel is also clearly visible.

5.3 PHENOMENOLOGICAL MODEL

In this section we present the phenomenological model developed in order to fit the hybrid PN-NR waveforms of section 5.2 to an analytical formula. A geometric description of the procedure for constructing phenomenological waveforms parameterized by just the physical parameters is detailed in [23], and here we just summarize it. Let \mathcal{M} be the space of intrinsic physical parameters that we are interested in. In the present case, this is the four-dimensional space of the component masses and spins $\lambda = \{M, \eta, \chi_1, \chi_2\}$. For each point λ in \mathcal{M} , let $h(t; \lambda)$ be the true physical waveform that we wish to approximate; in particular we consider only the dominant $\ell = m = 2$ mode in this paper. We start with some known signals in this parameter space at N points $\lambda_1, \lambda_2, \dots, \lambda_N$. We take these known signals to be the hybrid waveforms whose construction we described earlier. Here the NR waveforms are the BAM waveforms of data sets #1-3 summarized in Table 6, and the PN model is the 3.5PN frequency domain model for aligned spins described in section 3.1. Given the finite set of hybrid waveforms constructed from these ingredients, we wish to propose a phenomenological model $h_{\text{phen}}(t; \lambda)$ that interpolates between the hybrid waveforms with sufficient accuracy. In constructing this phenomenological model, it is convenient to work not with the physical parameters λ , but rather with a larger set of phenomenological parameters $\tilde{\lambda}$, which we shall shortly describe. If $\tilde{\mathcal{M}}$ is the space of phenomenological parameters, then we need to find a one-to-one mapping $\mathcal{M} \rightarrow \tilde{\mathcal{M}}$ denoted $\tilde{\lambda}(\lambda)$, and thus the subspace of $\tilde{\mathcal{M}}$ corresponding to the physical parameters. As the end result of this construction, for every physical parameter λ , we will know the corresponding phenomenological parameter $\tilde{\lambda}(\lambda)$ and thus the corresponding phenomenological waveform $h_{\text{phen}}(t; \tilde{\lambda}(\lambda))$.

Following the construction procedure of section 5.2.4, we split our waveforms in amplitude and phase, both of which shall be fitted to a phenomenological model

$$\tilde{h}_{\text{phen}}(f) = A_{\text{phen}}(f) e^{i\Phi_{\text{phen}}(f)}. \quad (5.14)$$

For both the amplitude and the phase of the dominant mode of the GW radiation, we make use of the insight from PN and perturbation theory for the description of the inspiral and ringdown of the BBH coalescence respectively, and introduce a phenomenological model to complete the description of the waveforms in the merger.

5.3.1 Phase Model

The PN approach for the GW radiation based on the stationary phase approximation, introduced in equation 3.19 of section 3.1, gives an adequate representation of the phase of the dominant mode during the adiabatic inspiral stage of the BBH coalescence $\psi_{\text{SPA}}^{22}(f)$. As the system transitions towards the merger phase, it is expected that further terms in the expansion are required to capture the features of the evolution. With this *ansatz* in mind, we propose a pre-merger phase $\psi_{\text{PM}}^{22}(f)$ of the form

$$\psi_{\text{PM}}^{22}(f) = \frac{1}{\eta} \left(\alpha_1 f^{-1/3} + \alpha_2 + \alpha_3 f + \alpha_4 f^{2/3} \right), \quad (5.15)$$

where the α_k coefficients are inspired by the SPA phase, redefined and phenomenologically fitted to agree with the hybrid waveforms in the region between the frequencies f_{ISCO} of equation 2.7 and f_{RD} of equation 3.34. As for the post-merger phase, the Teukolsky equation [252] describes the ring-down of a slightly distorted spinning black hole. The metric perturbation for the fundamental mode at large distances can be expressed as an exponential damped sinusoidal

$$h_{\text{ring}}^{22}(t) = \frac{A_{\text{ring}} M}{r} e^{-\pi f_{\text{RD}} t / Q} \cos(2\pi f_{\text{RD}} t), \quad (5.16)$$

where M is the mass of the ringing black-hole, r the distance from the source, and Q and f_{RD} correspond, respectively, to the quality factor of the ringing down and the central frequency of the quasi-normal mode. These can be approximated by the fit formulas given by equations 3.34 and 3.35. The spin of the final black hole after the binary has merged can be inferred from the spins of the two black holes. In our case, we use the fit presented in [223], which maps the mass-ratio and spins of the binary to the total spin a of the final black hole. This analytical treatment of the ringdown motivates a linear ansatz for the post-merger phase $\psi_{\text{RD}}^{22}(f)$ of the form

$$\psi_{\text{RD}}^{22}(f) = \beta_1 f + \beta_2. \quad (5.17)$$

The transition between the different regimes is smoothed by means of tanh-window functions

$$w_{f_0}^{\pm} = \frac{1}{4} \left[1 \pm \tanh \left(\frac{4(f - f_0)}{\sigma} \right) \right] \quad (5.18)$$

to produce the final phenomenological phase

$$\Phi_{\text{phen}}(f) = 2\psi_{\text{SPA}}^{22} w_{f_1}^- + w_{f_1}^+ w_{f_2}^- \psi_{\text{PM}}^{22} + 2\psi_{\text{RD}}^{22} w_{f_2}^+, \quad (5.19)$$

with $f_1 = 0.93f_{\text{ISCO}}$, $f_2 = 1.1f_{\text{RD}}$ and $\sigma = 0.015$. We choose these particular transition points after having found them to provide the best match between the hybrids and the phenomenological model.

5.3.2 Amplitude Model

In a similar manner to the phase, we approach the problem of fitting the amplitude of the GW wave by noting that the PN amplitude obtained from the SPA expression could be formally re-expanded as

$$\tilde{A}_{\text{PN}}(f) = C\Omega^{-7/6} \left(1 + \sum_{k=2}^5 \gamma_k \Omega^{k/3} \right), \quad (5.20)$$

where $\Omega = \pi M f$. We introduce a higher-order term to model the pre-merger amplitude $\tilde{A}_{\text{PM}}(f)$

$$\tilde{A}_{\text{PM}}(f) = \tilde{A}_{\text{PN}}(f) + \gamma_1 f^{5/6}, \quad (5.21)$$

where the γ_1 coefficient is introduced to model the amplitude in the pre-merger regime. The *ansatz* for the amplitude during the ringdown is

$$\tilde{A}_{\text{RD}}(f) = \delta_1 \mathcal{L}(f, f_{\text{RD}}(a, M), \delta_2 Q(a)) f^{-7/6}, \quad (5.22)$$

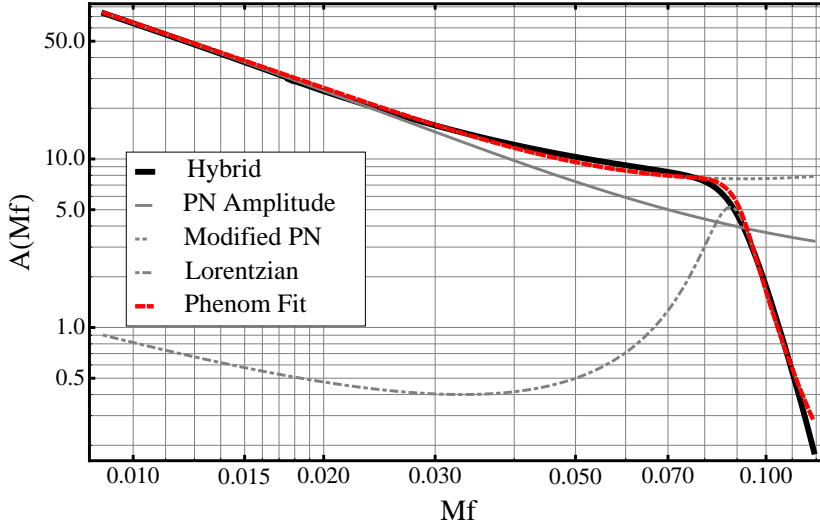


Figure 21: Fitting procedure for the amplitude. The γ_1 term of equation 5.21 is introduced to follow the behavior of the amplitude in the pre-merger regime whereas the Lorentzian curve correctly describes the post-merger. The two pieces are glued together in a smooth manner using tanh-windows.

where only the width and overall magnitude of the Lorentzian function

$$\mathcal{L}(f, f_0, \sigma) \equiv \frac{\sigma^2}{(f - f_0)^2 + \sigma^2/4} \quad (5.23)$$

are fitted to the hybrid data. The factor $f^{-7/6}$ is introduced to correct the Lorentzian at high frequencies, since the hybrid data shows a faster fall-off. The phenomenological amplitude is constructed from these two pieces in a manner analogous to the phase

$$\tilde{A}_{\text{phen}}(f) = 2 \left[\tilde{A}_{\text{PM}}(f)w_{f_0}^- + \tilde{A}_{\text{RD}}(f)w_{f_0}^+ \right], \quad (5.24)$$

with $f_0 = 0.98f_{\text{RD}}$ and $\sigma = 0.015$. Figure 21 demonstrates how this phenomenological *ansatz* fits the hybrid amplitude in a smooth manner through the late inspiral, merger and ringdown.

5.3.3 Mapping the Phenomenological Coefficients

Our models for the amplitude and phase involve 9 phenomenological parameters $\{\alpha_1, \alpha_2, \alpha_3, \alpha_4, \beta_1, \beta_2, \gamma_1, \delta_1, \delta_2\}$ defined in equations 5.15, 5.17, 5.21 and 5.22. We now need to find the mapping $\mathcal{M} \rightarrow \tilde{\mathcal{M}}$ from the physical to these phenomenological parameters. Following [25] we construct the quantity

$$\chi \equiv \frac{1 + \delta}{2}\chi_1 + \frac{1 - \delta}{2}\chi_2 \quad \text{with } \delta \equiv \frac{m_1 - m_2}{M}, \quad (5.25)$$

that encodes the BH spins weighted by their relative masses. Thus, our phenomenological waveforms are parameterized only by the symmetric mass ratio η and the spin parameter χ , as well as by the total mass of the system M through a trivial rescaling. Figure 22 shows the mapping of $\alpha_k, \beta_k, \gamma_k$ and δ_k to surfaces in the (η, χ) -plane.

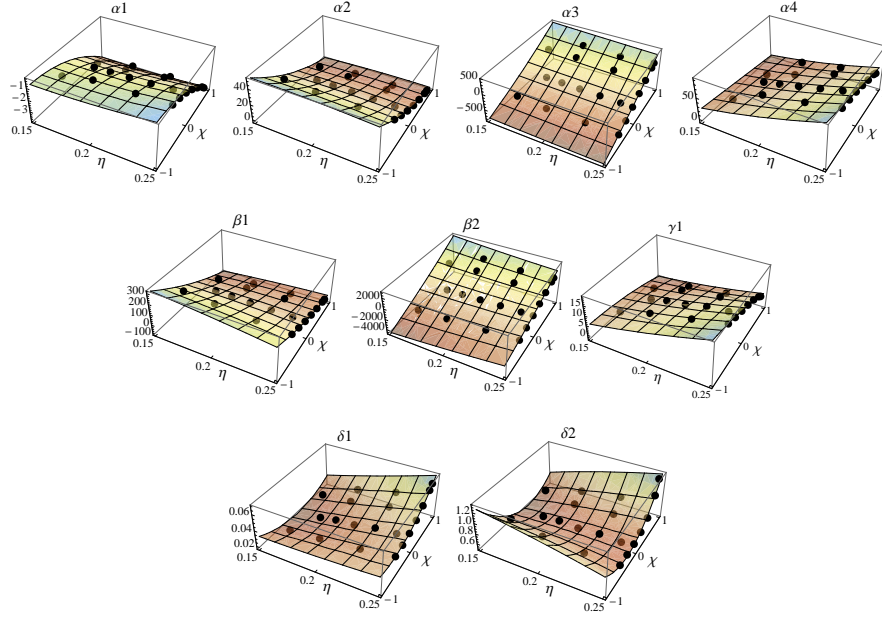


Figure 22: Map of the phenomenological parameters to the physical parameters of the binary η and χ .

The 9 phenomenological coefficients introduced in our model, denoted generically by Λ_k , are expressed in terms of the physical parameters of the binary as

$$\Lambda_k = \sum_{i+j \in \{1,2\}} \zeta_k^{(ij)} \eta^i \chi^j, \quad (5.26)$$

which yields 5 coefficients $\zeta^{(ij)}$ for each of the 9 parameters, as given in table 7.

We evaluate the goodness of fit between the phenomenological model and the hybrid waveforms in terms of the overlap, i.e. the ambiguity function $\mathcal{A}(\lambda, \lambda')$ defined in equation 5.10. In evaluating the overlap, we maximize over the extrinsic parameters t_0, ϕ_0 as indicated in equation 5.10, but in this paper we do not perform the additional maximization over the model parameters λ' . Thus, the results in this section can be viewed as a lower bound on the effectualness. We shall study the effectualness and faithfulness in greater detail in a forthcoming paper.

Figures 23 and 24 illustrate this fact using the design curve of the Advanced LIGO detector. The first plot shows the overlap between hybrid waveforms constructed in section 5.2.4 and their corresponding phenomenological fit. The match approaches unity by construction at low masses and degrades with increasing total mass. Nevertheless, for none of the hybrid waveforms employed in the construction of our model does the overlap fall below a value of 0.98, thus reflecting the fact that the phenomenological waveforms effectually represent the target signals. In figure 24, and as a further test to assess the robustness of our model for systems with unequal-spin configurations, we compute the overlap between the phenomenological waveforms and the NR data-sets #4-7 that were *not* used in the construction of the model. At low masses there is no contribution of the short NR waveforms, therefore the overlaps can not be computed; however, at the masses for which the NR part falls within the Advanced LIGO band we obtain overlaps > 0.97 , which

Table 7: Coefficients to map the 9 free parameters Λ_k of our phenomenological model to the physical parameters of the BBH binary.

Λ_k	$\zeta^{(01)}$	$\zeta^{(02)}$	$\zeta^{(11)}$	$\zeta^{(10)}$	$\zeta^{(20)}$
α_1	-1.68	0.77	0.11	16.53	-47.74
α_2	-32.35	-8.63	-31.87	-182.27	480.58
α_3	790.19	-44.11	751.89	2018.15	-2847.51
α_4	-14.44	-2.01	33.46	163.11	-1753.92
β_1	-347.25	-37.21	-920.76	-930.65	2784.18
β_2	6930.34	-194.52	18935.20	14960.90	-47393.80
γ_1	-1.85	-3.13	-64.08	-60.89	686.61
δ_1	0.06	0.03	0.37	0.10	0.83
δ_2	1.01	0.44	5.00	5.43	-11.43

indicate that our phenomenological model can reliably be extrapolated to physical configurations with unequal spins, where the spins of the black holes are encoded in the single parameter χ .

5.4 SUMMARY AND FUTURE WORK

The aim of the central part of this dissertation has been to construct an analytical model for the inspiral and coalescence of binary black hole systems with aligned spins and comparable masses in circular orbits. Since this requires merging post-Newtonian and numerical relativity waveforms, one of the main themes has been to quantify the internal consistency of hybrid waveforms. This is important because even if one succeeds in finding a useful fit for a family of hybrid waveforms, one still needs to show that the hybrid one started with is a sufficiently good approximation to the true physical waveforms. We investigated the systematics of constructing hybrid waveforms for accurate non-spinning waveforms based on the Llama code and we saw that numerical errors are not significant. This suggests that in order to improve the accuracy of hybrid waveforms, it would be useful for numerical relativists to calculate longer waveforms so that the matching with PN can be done earlier in the inspiral phase.

With the hybrid waveforms for non-precessing systems at hand, we constructed an analytical model for the waveform which has an overlap of better than 98% for Advanced LIGO with the hybrid waveforms for systems with a total mass ranging from ~ 10 to $\sim 400M_\odot$. In the future we will study in greater detail the effectualness and faithfulness of this waveform model, thereby quantifying more precisely its performance for detection and parameter estimation. We will also quantify the behavior of these templates in real non-Gaussian detector noise, and use them in real searches for gravitational wave signals. Eventually, work is underway in extending the model to include precessing spins. Our phenomenological model for can be readily applied to existent GW detection efforts within the LIGO/Virgo Scientific Collaborations. Ongoing searches are already making use of IMR waveforms, such as

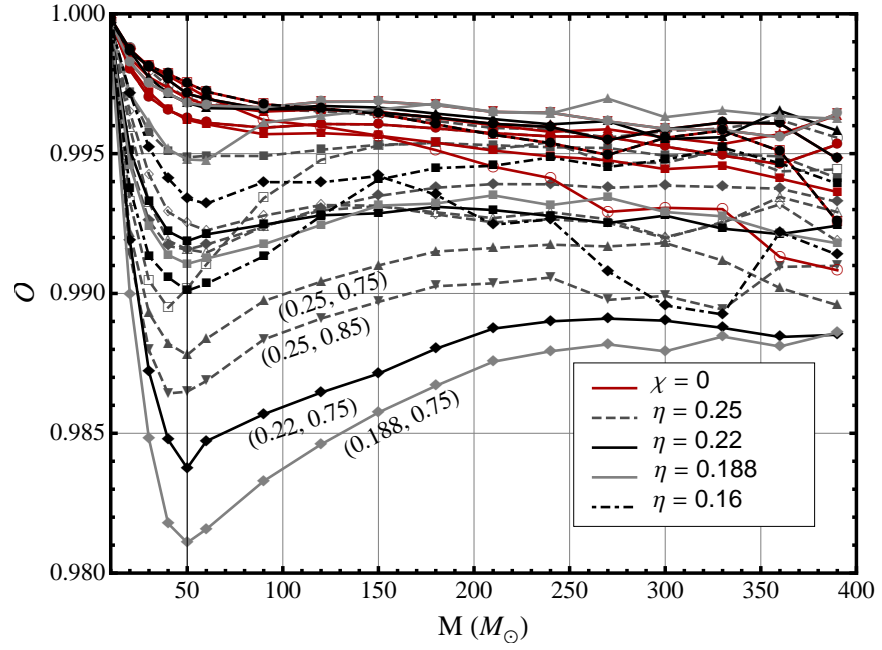


Figure 23: Overlaps between the hybrid waveforms constructed according to the procedure described in section 5.2.4 and the proposed phenomenological fit for Advanced LIGO. The labels indicate the values of (η, χ) for some configurations. We plot $\mathcal{O}(\lambda) = \mathcal{A}(\lambda, \lambda)$, i.e. we compute the ambiguity function (equation 5.10) without maximizing over the parameters of the model waveform; this is a lower bound on the effectualness.

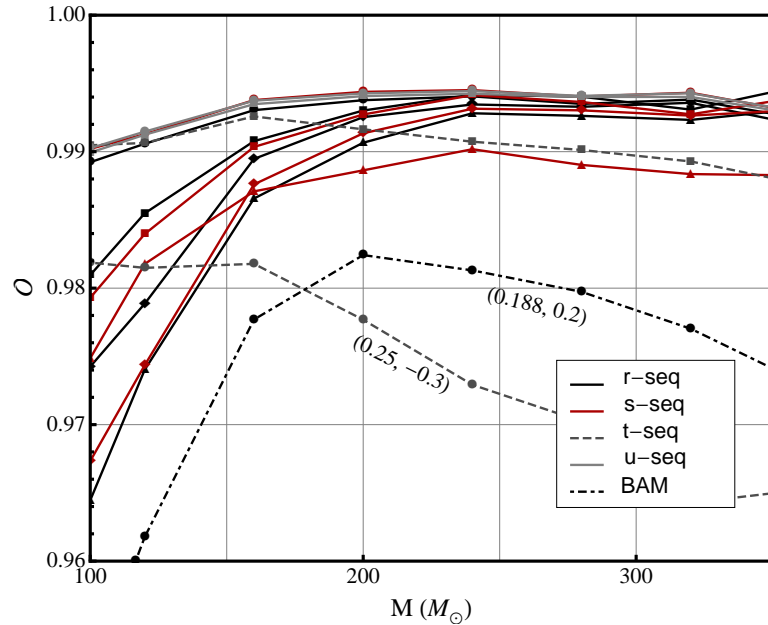


Figure 24: Overlaps between the NR data-sets #4–7ab and the predicted phenomenological waveforms from our model for advanced LIGO. The labels indicate the values of (η, χ) for some configurations. Note that the short duration of the NR data prevents us from computing overlaps at lower masses.

the EOBNR family and the phenomenological family of [24, 23, 22, 25], in the form of software injections and as filter approximants. Our newly developed frequency-domain matching procedure should serve to cross-check the validity of these alternative approaches and to complement them.

This chapter concludes the part of this dissertation devoted to theoretical modelling of gravitational-wave sources. The next chapter focus on applications for real gravitational-wave searches, transfer of numerical relativity results into current data analysis efforts and implications for gravitational-wave astronomy.

Part III

APPLICATIONS

In November 2005 the three first-generation LIGO detectors described in section 1.4 reached their design sensitivity and began a two-year period of observations which concluded in October 2007 [13]. Although the astrophysical estimates for rates of coalescing binaries presented in section 2.4.3 depend on a number of assumptions and unknown model parameters, and are still uncertain at present, searches for these signals in the real output of the interferometers constitute a promising avenue towards detection or, at worst, upper limit estimation.

The inspiral group of the LIGO Scientific Collaboration is engaged in the challenge of analyzing the LIGO data and searching for coalescing binaries. Results from searches for gravitational waves associated to neutron-star, black-hole and mixed binaries using data from previous science runs with ever-increasing sensitivity are reported in [5, 4, 6, 7, 10]. The strategy followed to analyze the S5 data has consisted in splitting up the parameter space of the binaries to be searched for. A search for signals from binaries with component masses greater than or equal to 1 solar mass (M_{\odot}) and total mass ranging from 2 to 35 M_{\odot} is carried out using inspiral templates from post-Newtonian theory; a partially-overlapping search for systems with component masses between 1–99 M_{\odot} and total masses between 25–100 M_{\odot} is the first effort to incorporate a filter family of waveforms modelling the three stages —inspiral, merger and ringdown— of the full binary black-hole coalescence.

This chapter describes the data analysis strategy carried out in these two detection efforts and presents the outcome of the low-mass search, which yielded no plausible detection of gravitational-wave signals but placed a stringent limit on the merger rate of binaries in its correspondent mass range.

This period is known as the fifth LIGO science run, or S5

These two searches are commonly referred to as low-mass and high-mass search

6.1 THE DATA ANALYSIS STRATEGY FOR COALESCING BINARIES

This section explains the infrastructure developed within the inspiral group of the LIGO Scientific Collaboration to search for signals from binary coalescences in the output of the LIGO detector. The detection algorithm has been applied to searches from the third LIGO science run [10] onward. The code, often referred to as the *inspiral pipeline* performs a series of hierarchical operations in order to search for real signals buried in the detector noise. The most relevant steps are briefly described in the next sections.

6.1.1 The Optimal Filter

The optimal detection method for modulated sinusoidal signals of known form buried into stationary Gaussian noise is known to be the *matched filter* algorithm [148]. In the case of coalescing black-hole or neutron-star binaries, the signal might not be precisely known, but it is parameterized by a number of physical characteristics of the binary, such as the masses, initial phase, time of arrival, distance, sky location, orientation and, eventually, spins. The *exact* parameters are not known a priori, but the output of the detector can be filtered

with a family of *templates* that discretely cover the parameter space to be searched for. In the most realistic scenario, the actual noise of the detector is not perfectly described by a stationary Gaussian process and additional methods need to be employed in order to make the matched filter process more robust again non-Gaussian features.

Let us for the moment assume that the output signal of the detector is fairly well represented by stationary Gaussian noise plus a gravitational-wave signal

$$s(t) = n(t) + h(t) \tag{6.1}$$

The one-sided power spectral density $S_n(|f|)$ of the Gaussian noise process $n(t)$ is given by equation 5.4. The typical sensitivity curves of the LIGO and Virgo detectors over the course of the S5/VSR1 data-taking period can be seen in figure 4. The matched filter output of a data stream $s(t)$ with a filter template of the form $h(t)$ is the complex quantity

$$z(t) = 4 \int_0^\infty \frac{\tilde{s}(f)\tilde{h}^*(f)}{S_n(f)} e^{2\pi i f t} df. \tag{6.2}$$

The inner product in the space of template waveforms is given by equation 5.5. To construct a well-defined signal-to-noise ratio (SNR), a normalization for the template has to be calculated

$$\sigma^2 = \langle h|h \rangle = 4 \int_0^\infty \frac{\tilde{h}(f)\tilde{h}^*(f)}{S_n(f)} df. \tag{6.3}$$

In all the above integral expressions, the limits of the integration are usually replaced by f_{low} and f_{final} , with f_{low} given by the corresponding lower cut-off frequency of the detector —40 Hz for initial LIGO, 30 Hz for initial Virgo and 10 Hz for the advanced detectors— and f_{final} determined by the ending frequency of the template, such as the f_{ISCO} or any other characteristic frequency related to the post-Newtonian dynamics, or possibly the Nyquist frequency in the more general case of a full inspiral-merger-ringdown template. We will discuss the choice of this frequency when describing the differences between the two searches presented in sections 6.2 and 6.3.

Thus the real quantity

$$\rho(t) = \frac{|z(t)|}{\sigma} \tag{6.4}$$

is the signal-to-noise ratio (SNR) of the matched filter, which acts as the optimal detection statistic in the presence of stationary, Gaussian noise. To determine whether a signal is present in a given segment of detector data, a threshold in SNR ρ^* is chosen such that

$$\text{if } \rho \begin{cases} \geq \rho^* & \text{assume signal is present} \\ < \rho^* & \text{assume signal is absent.} \end{cases} \tag{6.5}$$

This classification allows for the events for which the SNR crosses the threshold to be listed as *triggers* and ranked according to their significance. The probability that the SNR exceed some given value falls exponentially with increasing threshold

$$p(\rho > \rho^*) = e^{-\rho^{*2}/2} \tag{6.6}$$

This lower frequency is associated to the seismic noise of the interferometer

It is optimal in the Neyman-Pearson sense; it yields maximum detection probability for a given false-alarm rate

and it follows that high SNR values have low probability of having been produced by noise and thus are a reasonably good indicator that a real signal is present.

Nevertheless, not every trigger is necessarily connected to a true gravitational-wave event. The probability that $\rho \geq \rho^*$ and yet no signal is present is called *false-alarm probability* and that of $\rho < \rho^*$ when a signal is present is the *false-dismissal probability*. One of the goals pursued when tuning gravitational-wave searches is to choose the value of ρ^* carefully so that these probabilities are minimal. The threshold is set by the maximal false-alarm rate tolerated in a given search, which in turn is decided by the expected event rate. On a practical level, the presence of non-Gaussian and non-stationary features in the detector noise implies that further methods—such as signal-based-vetoes—are needed to reduce the rate of false alarms and false dismissal.

6.1.2 *Template Construction*

Ideally, the gravitational signal to be measured and the template waveform used for filtering should have the same functional form. In practice, however, theoretical uncertainties, the use of approximations to solve the Einstein equations, and the fact that the parameter space of the signal is continuous but the search is done with a finite set of templates prevent the signal-to-noise ratio from reaching its maximum. The real signals lie outside the submanifold of the search templates that lives in the full manifold of all possible detector outputs [197]. An important question is, thus, how to lay down a set of templates so that the loss of SNR from the mismatch between signal and template does not result in excessive missed detection candidates.

The metric

$$g_{\mu\nu} = \langle h_\mu | h_\nu \rangle \quad (6.7)$$

allows to compute the mismatch in the space of template waveforms. Templates on this space can now be placed, ensuring that the furthest distance from any point to a template is less than a tolerance value ϵ . The loss of SNR due to the discretization of the parameter space is thus bound by ϵ .

Due to the fact that the metric 6.7 takes a more convenient form in a particular system of coordinates than in others, the space is usually parameterized in terms of auxiliary variables related to \mathcal{M} and η , the chirp mass 3.2 and symmetric mass ratio 2.6 of the binary. An hexagonal placement algorithm [93] is employed when laying out the templates, for it provides the highest coverage efficiency. The searches described in sections 6.2 and 6.3 set a value of 0.97 for the fitting factor between elements of the template bank, which ensures that no more than 10% of the signals are lost due to mismatch.

6.1.3 *Signal-Based Vetoes*

In the more realistic case of non-stationary, non-Gaussian detector noise, spurious signals might cause events with unusually high SNR. The presence of environmental or instrumental sources of disturbances in the detector can give rise to loud events that the analysis pipelines might easily confuse with real signals and erroneously classify as triggers. The noise of the detector often presents “glitchy” features that might arise from a number of sources, such as

environmental disturbances or technicalities associated to the instrumentation. A matched filter algorithm will respond to these glitches by giving a large SNR response, although the features of the glitch might bear no resemblance to a true gravitational-wave signal.

In order to overcome this problem, which could have undesired effects in the reliability of the search algorithm, several signal-based vetoes can be implemented, that aim at differentiating between glitches and real signals.

The commonly used vetoes are the χ^2 -discriminator test [30] and the r^2 veto

The χ^2 -test responds to the intention of constructing a detection statistic capable of indicating if the filter template and the signal match sufficiently well, and discard spurious triggers if they do not. An orthogonal decomposition of the template $\tilde{h}(f)$ can be made so that the complete set of p templates $\tilde{h}_i(f)$ satisfies

$$\langle \tilde{h}_i(f) | \tilde{h}_j(f) \rangle = \frac{\delta_{ij}}{p} \quad (6.8)$$

$$\sum_{i=1}^p \langle \tilde{h}_i(f) | \tilde{h}_i(f) \rangle = 1 \quad (6.9)$$

If the signal perfectly matched the template $\tilde{h}(f)$, then a SNR of ρ/p would be expected for each projection $\tilde{h}_i(f)$. Under that expectation, the following quantity can be constructed

$$\chi^2 = \sum_{i=1}^p \left(\rho_i - \frac{\rho}{p} \right)^2, \quad (6.10)$$

where ρ_i is the SNR associated to the i^{th} bin of the orthonormal set, ρ is the total SNR and p is the number of χ^2 bins. Figure 25 illustrates how the test works in the case of a simulated inspiral signal and a spurious glitch. Although both events present a similar SNR value, the decomposition in bins — $p = 4$ in this case — allows for discriminating between the two. While the chirp presents a value of $\chi^2 = 1.296$, the spurious signal has $\chi^2 = 68.4$ [30], hence it is clear that thresholding in χ^2 separates both events.

In Gaussian noise this test is χ^2 -distributed with an expectation value $\langle \chi^2 \rangle = p - 1$, which does not coincide with the actual expectation value when signals are present, due to the use of a *discrete* template bank to search for gravitational waves. If δ is the mismatch between the template and the signal, then the expectation value of χ^2 in the presence of signal without noise at the time of the maximum SNR is $\langle \chi^2 \rangle_{\text{signal}} = \delta \rho^2$. This quadratical scale of the expectation for χ^2 with the SNR introduces the possibility that a loud real signal also presents a large χ^2 . The final threshold is hence done on a normalized quantity defined as

$$\xi^2 = \frac{\chi^2}{p + \delta \rho^2}. \quad (6.11)$$

The condition $\xi^2 \leq \xi^{*2}$ is required for a trigger to pass the χ^2 -test. The parameters δ , p and ξ^{*2} can be tuned. In practice, δ accounts not only for the discrete template bank but also for possible inaccuracies of the waveform model, and is chosen so that no simulated signals are rejected.

The r^2 -test is another reliable signal-processing technique to discriminate between real and spurious triggers. The veto evaluates the time-dependent quantity $r^2 = \chi^2/p$ during a certain amount of seconds before the inferred

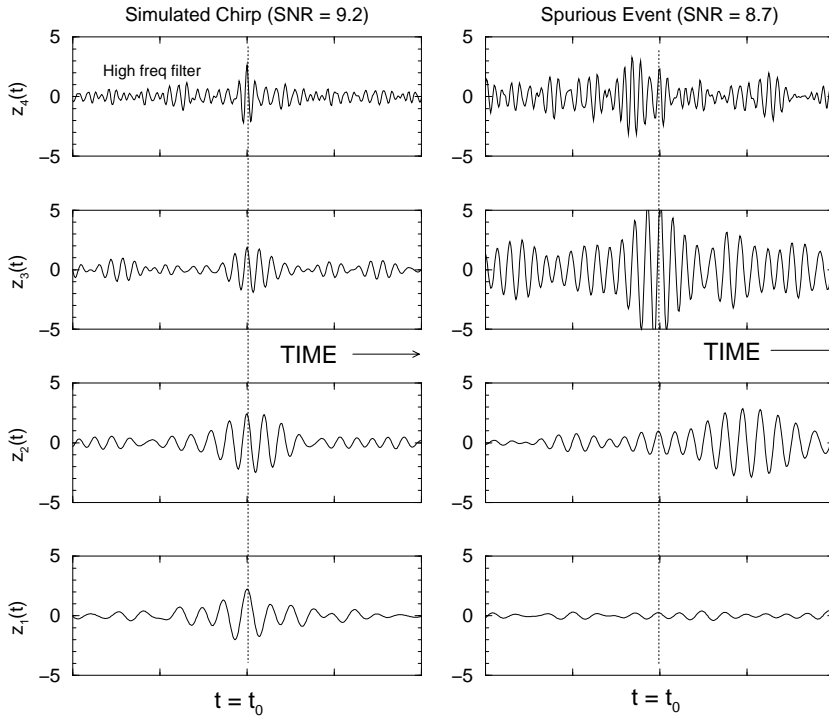


Figure 25: Diagram demonstrating how the χ^2 -test discriminates between true and spurious signals. For the simulated chirp, all filters in the different frequency bands peak at the same time offset t_0 which maximizes the SNR. At this instant in time, all of the contributions z_j —corresponding to the ρ_i defined in the text—are approximately the same value. However when the filter was triggered by the transient burst, the filters in the different frequency bands peak at different times. *Figure credit: B. Allen [30].*

merger time of the trigger. A true signal spends less time above a given threshold than a spurious glitch, so that the condition $r^2 \leq r^{*2}$ acts as a powerful discriminator among the two.

6.1.4 Coincidence Test and Background Estimation

Even when signal-based vetoes are applied to the candidates that exceed a given SNR threshold, the fundamentally noisy nature of the detectors' output gives rise to a substantial number of accidental triggers. In order to increase confidence in these detection candidates, coincidence at two or more detectors is required. Actually, for a gravitational-wave detection to be reliably claimed and verified, it will have to be found in various detectors and also by other means—associated neutrino or electromagnetic observations—. For events to be considered coincident, the time of coalescence and masses of the triggers recorded in different detectors are required to agree within a certain tolerance. The tuning of the diverse parameters that control those thresholds is crucial to ensure a reasonably large number of events that allows for reliable statistics but without this number being so large that the software infrastructure overflows.

The coincident algorithm implemented in the low- and high-mass searches described below creates a time-sorted list of triggers from the multiple detectors whose data are being analyzed. For each single trigger found at a time t_i , all triggers occurred within a time $t \in (t_i, t_i + T)$, where T is some time

A triple trigger is also a double trigger for every pair of detectors that can be formed from the triplet

These are called time-shifted triggers, in contrast to the potential candidates, zero-lag triggers

window, are found. This step is repeated over all single triggers until a list of coincident triggers is found. Finally, the algorithm loops over the coincident triggers and removes coincident triggers that are subsets of higher order coincident triggers.

Again due to the unpredictability of the detectors, purely accidental coincidences might still occur, giving rise to an undetermined number of background triggers that need to be separated from the potential real gravitational-wave signals. The estimation of this background is carried out by a *time-slides* procedure. Most certainly, if the outputs of multiple detectors were to be shifted by a number of seconds with respect to each other and a search was performed in the time-shifted data, *none* of the recorded coincident triggers could ever be claimed to be a real gravitational wave. Thus, time slides provide an accurate estimation of the background due to accidental coincidences, provided that the outputs of the detectors are uncorrelated. Unfortunately, this is not the case for the pair of interferometers H1H2, since they are situated at the same physical location and therefore share common sources of noise.

6.1.5 Detection Statistic: False-Alarm Rate

In purely Gaussian, stationary noise, the SNR as defined in section 6.1.1 provides a way of measuring the false-alarm rate that is *independent* of the filter. In real data, this is not true, and a better statistic needs to be devised. This is the reason why previous searches for gravitational waves from inspiralling binaries [5, 4, 6, 7, 10] have made use of an improved detection statistic constructed with input not only from SNR, but also from χ^2 . This statistic, known as *effective SNR*, improves separation of signals from background and is defined as

$$\rho_{\text{eff}}^2 = \frac{\rho^2}{\sqrt{\left(1 + \frac{\rho}{\rho_0}\right) \left(\frac{\chi^2}{\chi_{\text{dof}}}\right)}}, \quad (6.12)$$

p is the number of bins used in the χ^2 veto

where ρ_0 is a free parameter and $\chi_{\text{dof}} = 2p - 2$ is the number of degrees of freedom of the χ^2 veto in Gaussian noise. Values of $\rho_0 = 250$ and $\rho_0 = 50$ are commonly used in the low- and high-mass searches respectively. The effective SNRs for the single-detector triggers that form a N -detector coincident trigger are then added to yield the combined effective SNR as final detection statistic

$$\rho_c^2 = \sum_{i=1}^N \rho_{\text{eff},i}^2. \quad (6.13)$$

Past searches explored a smaller part of the mass parameter space. For an extended parameter space FAR provides superior performance

Yet superior efficiency is obtained if a different statistic is used, namely the false-alarm-rate (FAR) or its inverse (IFAR) statistic. If an estimation for the background triggers exists — which is our case, since we employ the time-slides method of section 6.1.4 —, then the time-shifted triggers provide a measure of the false-alarm rate for every zero-lag coincident trigger. The statistic is calculated by counting the number of time-shifted, i.e. non-real, triggers with a combined SNR 6.13 greater than or equal to that of the zero-lag, i.e. potentially real, coincident triggers. Since the time-shifted, background triggers were generated by multiple time slides, we have to divide among the number of time slides that were performed. For this number to be a meaningful rate that can be easily compared with results from other searches,

we normalize by a time of observation of one year. This provides a number—the false-alarm rate, or FAR—as a function of effective SNR for each zero-lag trigger, that ranks its significance with respect to the background.

$$\text{FAR}(\rho_{\text{eff}}) = \frac{1 \text{ yr}}{T_{\text{analyzed}}} \frac{N \left[\rho_{\text{eff}}^{\text{bg}} \geq \rho_{\text{eff}}^{\text{zero-lag}} \right]}{N_{\text{slides}}}. \quad (6.14)$$

If using the *inverse* false-alarm statistic, or IFAR, the inverse of FAR is calculated. The meaning of this statistic is as follows: for some given effective SNR, we expect a certain number of zero-lag triggers. For instance, at a normalized IFAR of 0.1—i.e. a normalized FAR of 10—, we expect 10 zero-lag triggers per year with an effective SNR greater than or equal to the effective SNR that corresponds to that IFAR. For an IFAR of 1, we expect 1 foreground trigger, and so on. Plotting the number of triggers versus their IFAR should yield a function of the form $1/x$, allowing us to conclude whether the actual zero-lag triggers are consistent with their expected behaviour or if, on the contrary, an unusual result—and, hence, a candidate—is found.

The subtlety here, and the reason why FAR supersedes combined SNR, is that different types of triggers present different backgrounds. Firstly, a triple coincidence trigger is much more unlikely to occur than a double, hence the background with which it can be compared is very different in these two situations. In particular, for H1H2 triggers we are not even in the position of providing a reliable background estimate, due to already-mentioned correlated sources of noise. All these differences are taken into account when computing FAR, since each trigger is compared with the background triggers in its category only.

Perhaps more importantly, FAR also allows to differentiate triggers according to their mass. Due to the extended mass range surveyed by the searches presented in this chapter, a large number of templates are employed for filtering. Higher-mass templates correspond to binaries that merge at lower frequencies within the LIGO/Virgo bands, hence spanning a shorter duration than templates corresponding to lower-mass binaries. As a consequence, they are more likely to be confused with noise glitches and present a higher sensitivity to non-stationary noise transients in the detector. If we ranked the associated candidates according to their combined effective SNR 6.13, they would dominate the statistic, possibly shadowing potentially interesting lower-mass triggers. In short, the FAR is not only dependent on the type of trigger—double, triple— under consideration, but also on the chirp mass. All this results in a biased false-alarm rate that we can correct by splitting computation of the FAR in several mass-dependent populations. A subsequent combination method among all different kinds of triggers allows to quote a final, single number for the FAR or IFAR of any potential candidate. This is the final ranking statistic employed in the searches described in the following sections.

In our searches, we separate them according to their chirp mass \mathcal{M}

6.2 THE LOW-MASS SEARCH IN S5 LIGO DATA

In this section we present a search for gravitational-waves from binaries with total mass between 2 and $35 M_{\odot}$ and a minimum component mass of $1 M_{\odot}$ in LIGO observations between November 14, 2006 and May 18, 2007 [16]. The mass parameter space surveyed by this search can be visualized in figure 26 in

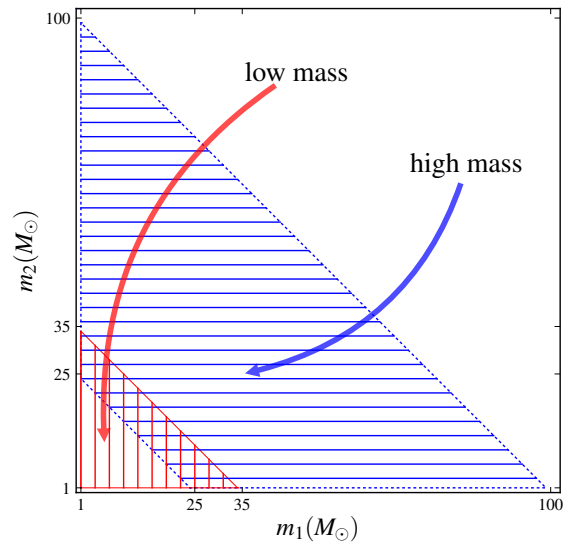


Figure 26: Parameter space of masses surveyed by the low- and high-mass searches for coalescing compact binaries in S5 LIGO data.

red. Prior results from a search for systems with the same mass distribution in data taken from November 4, 2005 to November 14, 2006 were reported in [15]. No gravitational-wave signals were observed during this search and so upper limits on rates for coalescences of compact binaries are reported, using the results of [15] as prior rate distributions. The final results quoted here are thus derived from LIGO observations in the period November 4, 2005 to May 18, 2007.

6.2.1 Description of the Search

The data-analysis pipeline used in this search consists fundamentally of the main stages described in section 6.1, thus this section only describes the most specific characteristics of this concrete search, referring to [10, 15] for extended details. The most substantial change in this analysis is a modification to the way in which the significance of candidate events is compared to instrumental noise background. In previous searches, the noise background was computed *using the entire observation period*. Using this method, the non-stationarity of the noise could lead to candidates being compared to a background that does not correctly represent the state of the detector at a given time. This is especially noticeable for candidates found at the end of the observation period, when the sensitivity of the detector is likely to have improved. In the search presented here, the observation period is instead split into six four-week segments and one 18 day segment and the instrumental background is measured *independently in each month*, as the detector behavior varied over the course of the S5 run. Candidate triggers are therefore compared to a background that better reflects the instrumental behaviour at the particular time of the trigger. Each month was searched independently for gravitational-wave candidates and in the absence of detections, the results from the months are combined—together with the results from [15]—to set an upper limit on the CBC rate.

These segments are referred to as “months”

The author performed the analysis of “month 4”, from March 6 to April 3, 2007

The search for gravitational waves is done at times when at least two of the LIGO detectors were operational, which comprises a total of 0.28 yr when all three detectors were operational —H1H2L1 coincident data—, 0.10 yr of H1H2 coincident data, 0.02 yr of H1L1 coincident data, and 0.01 yr of H2L1 coincident data. Due to above-mentioned noise correlations between the co-located H1 and H2 detectors, the estimation of instrumental background using time-shifted data fails. Therefore no search is done at times when only the H1H2 detectors are operating. Approximately 10% of data is designated *playground*.

Inspiralling low-mass binaries targeted in this search radiate at frequencies that sweep across the sensitive band of the LIGO detectors and their merge happens at the end of the LIGO band. An appropriate choice for the match-filtered search is the use of PN templates terminated at f_{ISCO} . This method is suboptimal if a true signal differs from our template family due to unforeseen physical effects. Matter effects in BNS and BHNS are not included in our templates, but are expected to be important only at higher frequencies [240, 167]. We construct template banks [93] of restricted second order PN waveforms in the frequency domain [253, 229, 108] such that no more than 3% of the SNR is lost due to the discreteness of the bank [198]. A “trigger” is generated if the matched-filter SNR of the strain data filtered against the template exceeds a threshold of 5.5 [31]. The triggers are subject to a coincident test such as the one described in 6.1.4, rejecting those that do not appear in at least two of the three LIGO detectors [224]. There are in principle four possible types of coincidence for three simultaneous detectors: H1H2L1 triple coincident triggers and three different double coincident types: H1H2, H1L1 and H2L1. We discard H1H2 double coincident triggers, due to the problems estimating the background for these triggers and discard H2L1 triggers when the H1 detector is operating nominally, since the 4 km H1 detector is more sensitive than the 2 km H2 detector.

Coincident triggers are subjected to consistency checks using the signal-based vetoes described in 6.1.3 [8, 30, 225]. All triggers occurred at times of poor detector data quality are flagged using environmental and auxiliary data and vetoed [15]. Depending on the severity of the instrumental artifact, we apply two categories of data-quality vetoes, one being more severe than the other. The triggers that survive these vetoes an effective SNR statistic, computed from the trigger’s matched-filter SNR and the value of the χ^2 signal-based veto for that trigger as indicated by equation 6.12. After discarding playground data and times in both veto categories, a total of 0.21 yr of triple coincident H1H2L1 data, 0.02 yr of H1L1 coincident data, and 0.01 yr of H2L1 coincident data remain. In the absence of a detection, these data are used to compute upper limits on the rate of coalescences of neutron-star, black-hole and mixed binaries.

As explained in section 6.1.4, the rate of instrumental noise artifacts is measured by time-shifting data from the Livingston and Hanford observatories. The data are offset by more than the light-travel time between observatories, thus triggers which survive the pipeline are due to noise alone. We performed 100 such time-shifts to obtain a good estimate of the noise background in our search. It is important to recall here what we said in section 6.1.5: binaries of higher masses merger at a lower frequency and thus contain fewer gravitational-wave cycles in the sensitive band of our detectors; this means that our signal-based vetoes are not as powerful as for long, lower-mass sys-

The 4 and 2 km Hanford and the 4 km Livingston detector are denoted H1, H2 and L1 respectively

The playground data consists of 600 of every 6370 s of data that are used to check and tune the pipeline

These templates do not contain the amplitude corrections discussed in chapter 3

H1 and H2 data are kept fixed with respect to each other

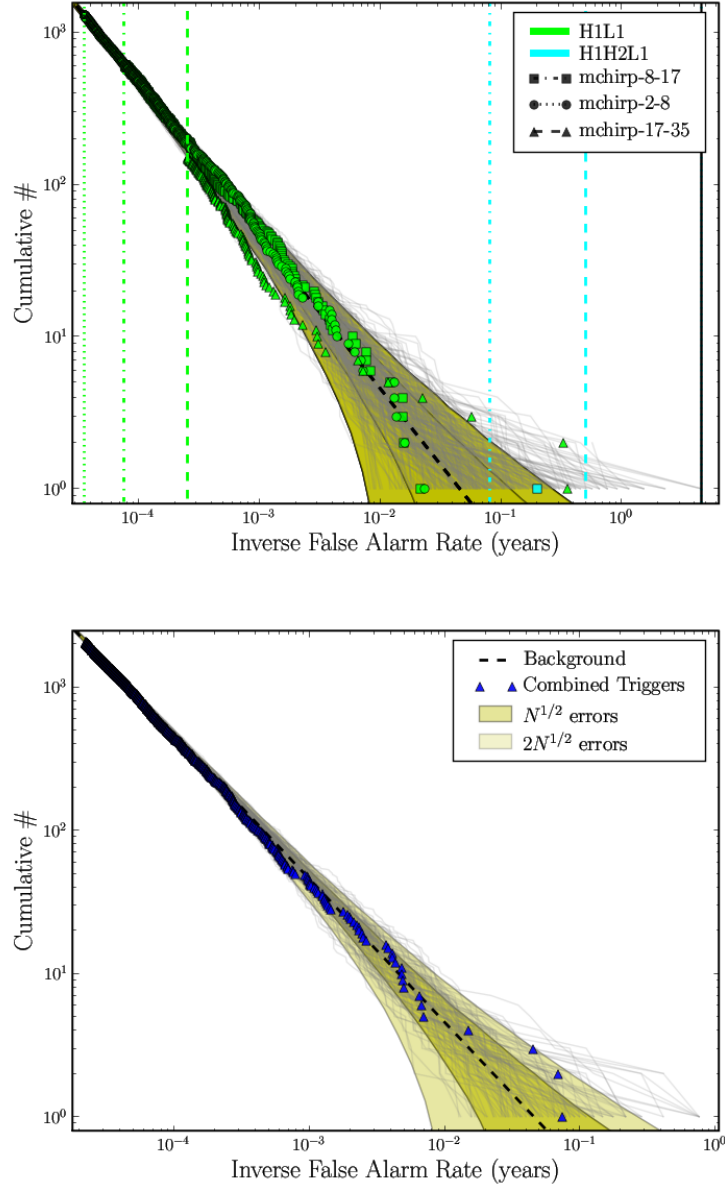


Figure 27: Combined and un-combined inverse false-alarm rates for triple H1H2L1 and double H1L1 triggers in month 4 of the 2nd year S5 low-mass search. The upper panel shows the IFAR of the triggers separated in three chirp mass categories. The lower panel shows the combined results. No candidates stand significantly above the expected background, depicted by a dashed line. The shadowed areas denote regions at one and two standard deviations of the expectation value.

These regions are defined by the chirp mass: $\mathcal{M}_{\text{low}} \leq 3.48 \leq \mathcal{M}_{\text{mid}} \leq 7.40 \leq \mathcal{M}_{\text{high}}$

tems. High-mass templates are therefore more sensitive to non-stationary noise transients and hence our false-alarm rate for them is larger. In order to account for this mass-dependent behavior we compute the background for three different mass regions and compare foreground and background within each of these ranges. Specifically, in each region we count the number of background triggers with effective SNR greater than or equal to a given foreground trigger; dividing this number by the amount of background time

analyzed gives us the false-alarm rate for that trigger. This allows us to define a single detection statistic for every trigger in each of the mass categories. The false-alarm rate can then be directly compared to obtain a ranking of the significance of the triggers, regardless of their mass [15].

The results of the IFAR calculation for month 4 of this search are shown in figure 27. In the upper panel we see the triple H1H2L1 and double H1L1 triggers with their un-combined IFAR values plotted on top of the expected background. The three different mass regions are delimited by the chirp mass of a $8 - 8 M_{\odot}$ and $17 - 17 M_{\odot}$ binary. In the lower plot, all results are combined to produce final IFAR values. No candidate stands significantly above the background for this month. We proceed to the discussion of the final results of the full seven-month search, namely the calculation of upper limits on the rate of binary coalescences.

6.2.2 Search Results

The seven months of data were analyzed separately using the procedure described above. No gravitational-wave candidates were observed with a FAR significantly above those expected from the noise background. The loudest trigger in this search was a triple coincident trigger with a FAR of 6 per year. This is consistent with the expected background, since we searched 0.21 yr of data. The second and third loudest triggers had FAR values of 10 and 11 per year respectively. Although we did not have any detection candidates, we exercised our follow-up procedures by examining any triggers with a FAR of less than 50 per year. This exercise prepares us for future detections and often identifies areas where our search pipeline can be improved to exclude noise transients.

In the absence of detection candidates, we use our observations to set an upper limit on the CBC rate. We follow the procedure described in [72, 71, 62] and use the results reported in [15] as prior information on the rates. We present five different classes of upper limits. The first three limits are placed on binaries of neutron stars and/or black holes assuming canonical mass distributions systems. We also present upper limits as a function of the total mass of the binary and, for BHNS binaries, as a function of the black hole mass. We combine the results from each of the seven months, along with the prior results from the first year analysis, in a Bayesian manner, using the same procedure as described in [15].

We first calculate upper limits on BNS, BBH and BHNS systems assuming the objects have no spin, and summarize the results Tables 8 and 9. The rate of binary coalescences in a galaxy is expected to be proportional to the blue light luminosity of the galaxy [169]. Therefore, we place limits on the rate per L_{10} per year, where L_{10} is 10^{10} times the blue solar luminosity. To calculate the search sensitivity, the analysis was repeated numerous times adding simulated signals with a range of masses, distance and other astrophysical parameters to the data. Table 9 shows the sensitivity of the LIGO detectors to coalescing binaries quoted in terms of the horizon distance i.e., the distance at which an optimally oriented and located binary would produce an SNR of 8. Similar information is graphically shown in figure 28 for month 4 of this search. The plot shows the comparable reach of the H1 and L1 detectors in Megaparsecs, which is about twice as large as that of H2. The horizon distance is computed assuming signals terminating before the merger, and it reaches its maximum

BNS:

$$m_1 = m_2 = (1.35 \pm 0.04) M_{\odot}$$

BBH:

$$m_{1,2} = (5 \pm 1) M_{\odot} M_{\odot}$$

BHNS:

$$m_1 = (5 \pm 1) M_{\odot}, \\ m_2 = (1.35 \pm 0.04) M_{\odot}$$

The Milky Way contains
 $\sim 1.7 L_{10}$ [163]

Table 8: Detailed results from the BNS search. The observation time is the time used in the upper limit analysis. The cumulative luminosity is the luminosity to which the search is sensitive above the loudest event for each coincidence time. The errors in this table are listed as one-sigma logarithmic error bars (expressed as percentages) in luminosity associated with each source error.

BNS Search			
Coincidence time	H1H2L1	H1L1	H2L1
Observation time (yr)	0.21	0.02	0.01
Cumulative luminosity (L_{10})	490	410	110
Calibration error	23%	23%	26%
Monte Carlo error	3%	7%	10%
Waveform error	31%	32%	31%
Galaxy distance error	16%	16%	3%
Galaxy magnitude error	19%	19%	17%

Table 9: Overview of results from BNS, BBH and BHNS searches. D_{horizon} is the horizon distance averaged over the time of the search. The cumulative luminosity is the luminosity to which the search is sensitive above the loudest event for times when all three LIGO detectors were operational. The first set of upper limits are those obtained for binaries with non-spinning components. The second set of upper limits are produced using black holes with a spin uniformly distributed between zero and the maximal value of Gm^2/c .

BNS, BBH and BHNS Searches			
Component masses (M_{\odot})	1.35/1.35	5.0/5.0	5.0/1.35
D_{horizon} (Mpc)	~ 30	~ 100	~ 60
Cumulative luminosity (L_{10})	490	11000	2100
Non-spinning upper limit ($\text{yr}^{-1} L_{10}^{-1}$)	1.4×10^{-2}	7.3×10^{-4}	3.6×10^{-3}
Spinning upper limit ($\text{yr}^{-1} L_{10}^{-1}$)	...	9.0×10^{-4}	4.4×10^{-3}

for binaries with total mass $\sim 30 M_{\odot}$. If the merger and ringdown were taken into account, the peak would shift towards larger masses.

There are a number of uncertainties which affect the upper limit calculation, including Monte Carlo statistics, detector calibration, distances and luminosities of galaxies listed in the galaxy catalog [169] and differences between the PN templates used to evaluate efficiency of the search and the actual waveforms. The effect of these errors on the cumulative luminosity are summarized for the BNS search in Table 8. We marginalize over all of the uncertainties [72] to obtain a posterior distribution on the rate of binary coalescences.

In figure 29, we show the derived distribution of the rate of BNS coalescences. The distribution is peaked at zero rate because there are no detection candidates. We include the distribution for all searches previous to this one (which is our prior). In addition, we present the result that would be obtained from each month, were it analyzed independently of the others and of the previous searches. This provides an illustration of the amount that each month contributes to the final upper limit result and demonstrates the improvement

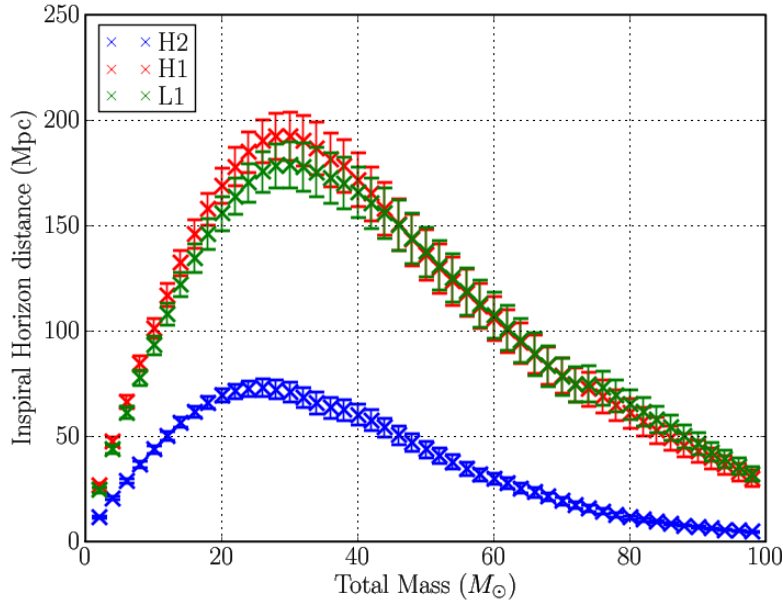


Figure 28: Horizon distance in Mpc as a function of the binary’s total mass for the three interferometers in operation during month 4 of the 2nd year S5 low-mass search. The horizon distance is defined as the distance at which a detector measures $\rho = 8$ for an optimally- oriented and optimally-located binary, i.e. an overhead, face- on orbit.

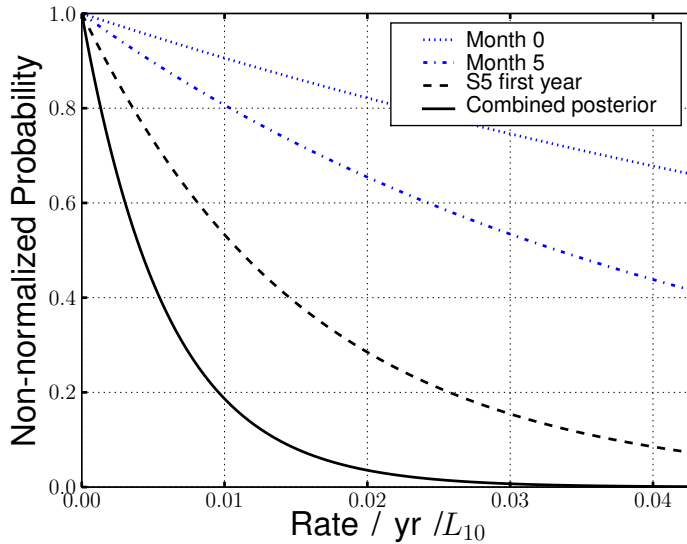


Figure 29: The posterior distribution for the rate of BNS coalescences. The dashed black curve shows the rate computed in [15]. The solid black curve shows the result of this search using the previous analysis as a prior. The figure also shows the rate distributions for two of the individual months computed using a uniform prior. The improvement from month 0 to month 5 is due to increasing detector sensitivity during this search.

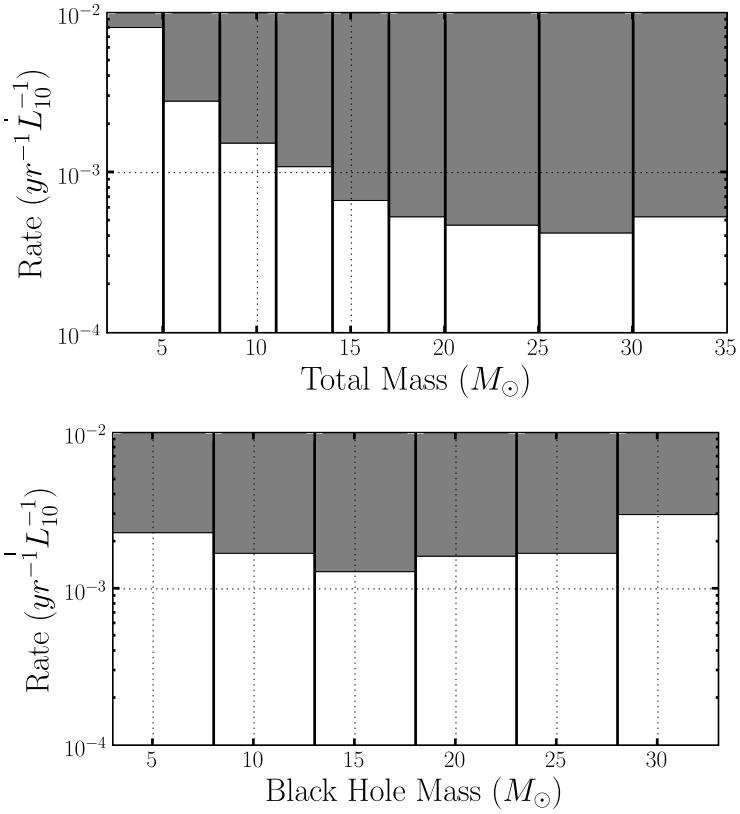


Figure 30: The marginalized 90% rate upper limits as a function of mass. The upper plot shows limits for BBH systems as a function of the total mass of the system. The lower plot shows limits for BHNS systems as a function of the black hole mass, assuming a fixed neutron star mass of $1.35M_{\odot}$. Here the upper limits are calculated using only H1H2L1 data since the relatively small amount of H1L1 and H2L1 data makes it difficult to evaluate the cumulative luminosity in the individual mass bins.

in sensitivity of the detectors during the search. The upper limit is finally obtained by integrating the distribution from zero to $\mathcal{R}_{90\%}$ so that 90% of the probability is contained in the interval. The results obtained in this way are $\mathcal{R}_{90\%,\text{BNS}} = 1.4 \times 10^{-2} \text{ yr}^{-1} L_{10}^{-1}$, $\mathcal{R}_{90\%,\text{BBH}} = 7.3 \times 10^{-4} \text{ yr}^{-1} L_{10}^{-1}$ and $\mathcal{R}_{90\%,\text{BHNS}} = 3.6 \times 10^{-3} \text{ yr}^{-1} L_{10}^{-1}$.

Additionally we calculate the upper limit for BBH systems as a function of the total mass of the binary, assuming a uniform distribution of the component masses. For BHNS systems, we construct an upper limit as a function of the black hole mass, assuming a fixed neutron star mass of $m_{\text{NS}} = 1.35 M_{\odot}$. These upper limits are shown in Fig 30.

Finally, we present upper limits on coalescence rates where the spin of the components of the binary is taken into account. Astrophysical observations of neutron stars indicate that their spins will not be large enough to have a significant effect on the BNS waveform observed in the LIGO band [179, 40]. Theoretical considerations limit the magnitude of the spin S of a black hole to lie within the range $0 \leq S \leq Gm^2/c$. However, the astrophysical distribution of black hole spins, and spin orientations, is not well constrained. Therefore, we provide a sample upper limit for spinning systems using a spin magnitude and orientation distributed uniformly within the allowed values. This gives

upper limits on the rate of BBH and BHNS systems of $\mathcal{R}_{90\%,\text{BBH}} = 9.0 \times 10^{-4} \text{ yr}^{-1} L_{10}^{-1}$ and $\mathcal{R}_{90\%,\text{BHNS}} = 4.4 \times 10^{-3} \text{ yr}^{-1} L_{10}^{-1}$. These rates are about 20% larger than the non-spinning rates.

6.2.3 Discussion of the Low-Mass Search

By combining the results of this search with our previous results, we set a new upper limit on the rate of coalescences in the local universe which is approximately a factor of 3 lower than that reported in [15]. This improvement is significant, even though we searched only two thirds as much data as in [15]. It is due, in part, to improvements in detector sensitivity during S5 which increased the horizon distance. Moreover, the shorter analysis time and improved stationarity of the data, led to many of the months having a less significant loudest event than in the previous search. Both of these effects increased the luminosity to which the search was sensitive, thereby improving the upper limit.

Astrophysical estimates for CBC rates depend on a number of assumptions and unknown model parameters, and are still uncertain at present. In the simplest models, the coalescence rates should be proportional to the stellar birth rate in nearby spiral galaxies, which can be estimated from their blue luminosity [169]. The optimistic, upper end of the plausible rate range for BNS is $5 \times 10^{-4} \text{ yr}^{-1} L_{10}^{-1}$ [162, 161] and $6 \times 10^{-5} \text{ yr}^{-1} L_{10}^{-1}$ for BBH and BHNS [196, 195]. The upper limits reported here are ~ 1 – 2 orders of magnitude above the optimistic expected rates. With the next run that started in summer 2009, the improved Enhanced LIGO and Virgo are expected to bring us close to the optimistic rates. The most confident BNS rate predictions are based on extrapolations from observed binary pulsars in our Galaxy; these yield realistic BNS rates of $5 \times 10^{-5} \text{ yr}^{-1} L_{10}^{-1}$ [162, 161]. Rate estimates for BBH and BHNS are less well constrained, but realistic estimates are $2 \times 10^{-6} \text{ yr}^{-1} L_{10}^{-1}$ for BHNS [196] and $4 \times 10^{-7} \text{ yr}^{-1} L_{10}^{-1}$ for BBH [195]. Thus, the expected rates are ~ 2 – 3 orders of magnitude lower than the limits presented here. The Advanced LIGO and Virgo detectors, currently under construction, will increase our horizon distance by an order of magnitude or more, allowing us to explore the validity of the astrophysical predictions.

6.3 THE HIGH-MASS SEARCH IN S5 LIGO DATA

The upper limits obtained in section 6.2 constitute the most up-to-date results for the rate of coalescences of low-mass binaries obtained via gravitational-wave measurements. The use of post-Newtonian templates is perfectly justified in such a search, since binaries with masses within the surveyed range are well described by inspiral-only models; hence, matched-filter searches employing inspiral-only approximants are a reasonable choice. Searches for more massive systems require instead filters incorporating the last stages of the coalescence. Breakthroughs in numerical relativity have enabled the development of full waveform models that can be applied to such searches.

This section describes a search for signals from binary black hole coalescences in LIGO S5 data when both LIGO sites were operating and collecting coincident data. The search covers systems with total mass $25 M_{\odot} \leq M \leq 100 M_{\odot}$ and component masses $1 M_{\odot} \leq m_1, m_2 \leq 99 M_{\odot}$ with negligible black hole spins. For black holes with this total mass, the merger occurs in

the LIGO detectors' most sensitive frequency region. This is the first analysis that incorporates a template family of waveforms modeling the three stages—inspiral, merger and ringdown—of the full coalescence process. At the time when this dissertation was printed out, the final results had not yet been made public. Hence, this section summarizes the search strategy, describes the main novelties involved in a search for higher-mass systems and presents preliminary results corresponding to the playground data analyzed by the author. The definitive results of the search will be published in [2].

6.3.1 Motivation and Strategy for a High-Mass Search

The existence of binaries formed by compact objects of mass below $10\text{--}15 M_{\odot}$ is well established through X-ray observations [193]; population-synthesis models suggest chirp masses of $\sim 5\text{--}10 M_{\odot}$ for black-hole binaries that merge within 10 Gyr [79, 194]. Nevertheless, it has also been suggested that significantly more massive black-hole binaries could form through a number of alternative channels. In this dissertation, the question of the existence of black holes with masses larger than hundreds of solar masses is investigated in chapter 8; this section focuses instead on a search for binary systems with total mass between 25 and $100 M_{\odot}$. Several simulations over the past years have indicated that dense stellar environments—such as globular and nuclear star clusters—could contribute to the expected rates of compact binary coalescences via dynamical formation [185, 191, 190]. Mass-segregation mechanisms make the most massive black holes sink towards the center of the clusters, favouring the dynamical formation of massive black-hole binaries. Besides, simulations of the evolution of the merger remnants after repeated stellar collisions seem to indicate that runaway mergers at solar metallicity evolve to $\sim 100 M_{\odot}$ Wolf-Rayet stars [133]. The star rapidly loses mass and turns into a $\sim 10 M_{\odot}$ black hole, but there are hints pointing out that lower metallicities can lead to higher remnant masses.

In light of these results, a search targeting more massive systems than those considered in section 6.2 appears promising. Most of these systems would merge within the most sensitive part of the LIGO band; searching for them with complete filters for the full coalescence increases the reach of the detectors and, thus, the chance of detecting gravitational waves from faraway sources. Figure 31 illustrates the convenience of extending the inspiral searches to higher masses and frequencies. The horizon distance for standard post-Newtonian filters in the stationary-phase approximation is compared with the reach obtained with full inspiral-merger-ringdown templates. It is clear that this kind of searches provide a considerably enlarged reach, both in surveyed effective distance and in masses.

Inspiral-Merger-Ringdown Waveforms

The high-mass search intends to go up to binary systems with higher masses, therefore it requires waveforms that describe the coalescence up to higher frequencies. Diverse waveform models are used in the search, both to efficiently filter the data for signals and to assess the sensitivity of the instruments and the data analysis procedures via simulations. In the mass range that the high-mass search wants to explore, the use of full inspiral-merger-ringdown waveforms that model all of the observable signal and naturally decay away

Wolf-Rayet stars are evolved, massive stars—over $20 M_{\odot}$ —, which are losing mass rapidly by means of a very strong stellar wind

This is the distance at which the detector measures a SNR $\rho = 8$ for an optimally-oriented and optimally-located binary, i.e. an overhead, face-on orbit.

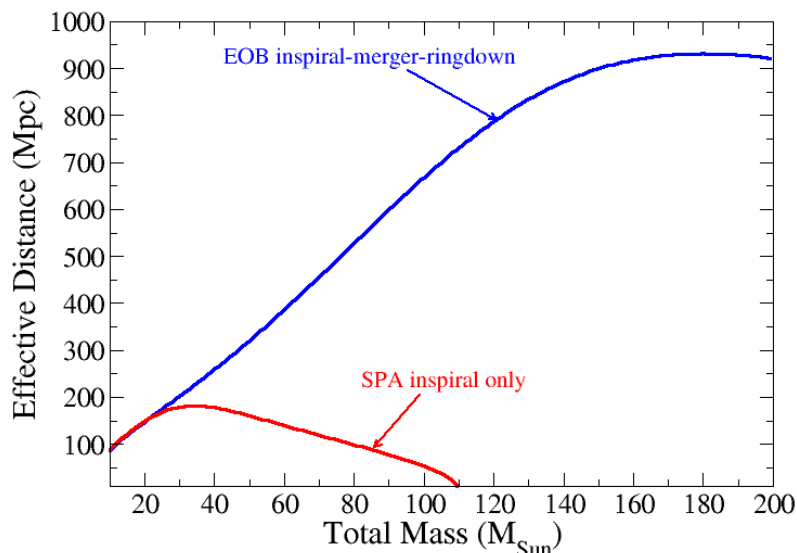


Figure 31: Expected horizon distance of the LIGO detectors for inspiral-only (red) and full inspiral-merger-ringdown signals (blue). The merger and ringdown contribute significantly to the SNR; a search employing full filters is able to explore more massive systems and to reach further.

during the ringdown phase is highly desirable. As already discussed in chapter 4, numerical relativity is now able to reveal the nature of the merger and ringdown stages of the binary black hole coalescence. The most optimal way to integrate these new results into existing data analysis codes is by means of analytical models that capture the features of the coalescence.

So far, this effort has led to two different approaches, the effective-one-body method calibrated to numerical relativity data (EOBNR) [80, 83, 98, 103] and the phenomenological models obtained by matching post-Newtonian and numerical waveforms [24, 22, 23, 25]. These approaches have already been described in section 5.1; in particular, the model developed in chapter 5 belongs to the second category. The high mass search uses EOBNR as search templates and also as injected waveforms to test the detection efficiency. The non-spinning phenomenological waveforms are used for injections and provide a check that that search pipeline can detect waveforms which are slightly different than the search templates. Future searches for systems in this mass range will make use of the spinning equivalents of the EOBNR and phenomenological models, including our model of chapter 5.

The Data Analysis Procedure

The search strategy for the high-mass search follows all the main steps of the pipeline employed for the low-mass search of section 6.2, with only a different choice for the filter waveforms and minor technical details. Data from the three detectors under consideration — H1, H2 and L1 — is read in and used as the base to compute the power spectral density. In a first filtering stage, double- or triple-coincident events above a single-detector SNR threshold of $\rho^* = 5.5$ are recorded. A subsequent second filtering stage re-filters the data with the χ^2 veto using $p = 10$ bins and $\chi_{\text{dof}} = 18$ in equation 6.10.

One particularity of the high-mass search has to do with the choice of template bank placement. The templates ought to cover the parameter space of total mass between $25 - 100 M_{\odot}$, with component masses in the range $1 - 99 M_{\odot}$. The bank is laid out using a hexagonal placement algorithm [93], such that the maximum loss in SNR would be 3%. The template spacing is determined using the metric calculated for the frequency-domain templates in the stationary phase approximation [51], as has been used in previous searches for signals from low-mass systems. Although this metric has not been calculated for signals featuring inspiral, merger and ringdown phases, it has been found that the bank gives the desired minimal match for most of the parameter space. We do not achieve exactly the desired minimal match for the highest masses. To take into account this limitation, the coincidence requirements chosen are somewhat looser than those of previous searches. This limitation should be mitigated in future searches when metrics for full inspiral-merger-ringdown waveforms become available.

After the two filtering stages mentioned above, events are required to be coincident in at least two detectors. The background is estimated via 100 five-second time slides between the two LIGO sites. All H1H2 double-coincidence events are ignored due to correlated noise. H2L1 events found when H1 was in operation are likewise discarded. These choices agree with those made for the low-mass search. The coincident candidates are ranked according to their effective SNR ρ_{eff} , and the false alarm rate (FAR) is calculated in the manner described in section 6.1.5. The three different mass categories in which the triggers are separated, due to the mass-dependent background, are chosen as $M_{\text{low}} < 50 \leq M_{\text{mid}} < 85 \leq M_{\text{high}}$. After being separated in categories according to their total mass and type of coincidence, the inverse false alarm rate is used as an intermediate statistic to finally compute the combined FAR; candidates are ranked accordingly. Potential candidates for gravitational-wave detection are identified and followed up. If no plausible candidate is found, upper limits on the rate of coalescences for systems in the considered mass range are calculated.

6.3.2 Preliminary Results of the High-Mass Search

The high-mass search analyzed the complete S5 LIGO data in a similar fashion to the second year S5 low-mass search of section 6.2. The data was split in 12 two-month long blocks, that were analyzed separately by different analysts. We report results of the analysis of playground data for months 1 and 2 of the S5 LIGO data. Figure 32 illustrates the reach of the detectors during these months. A large number of simulated signals are injected into the pipeline and analyzed in order to test the data analysis finding algorithm. In the high-mass search, EOBNR and phenomenological waveforms are injected at physical distances between 1 and 750 Mpc. These injections are considered found if they produce coincident triggers above the SNR threshold $\rho^* = 5.5$. In figure 32 we plot in blue and green the injections that were found in triple and double coincidence respectively; in black those that were missed. The line that separates the regions of found and missed injections gives an estimation of the reach of the detectors, which ranges from tens of Mpc at low masses to hundreds of Mpc at the high end of the mass range, confirming the predictions of figure 31. Rather than reaching a maximum at around total mass $M = 30 M_{\odot}$ and decreasing afterwards, like we saw in figure 28 for the low-mass search, the

The author analyzed months 1 and 2 of the S5 LIGO data, from November 4, 2005 to January 6, 2006

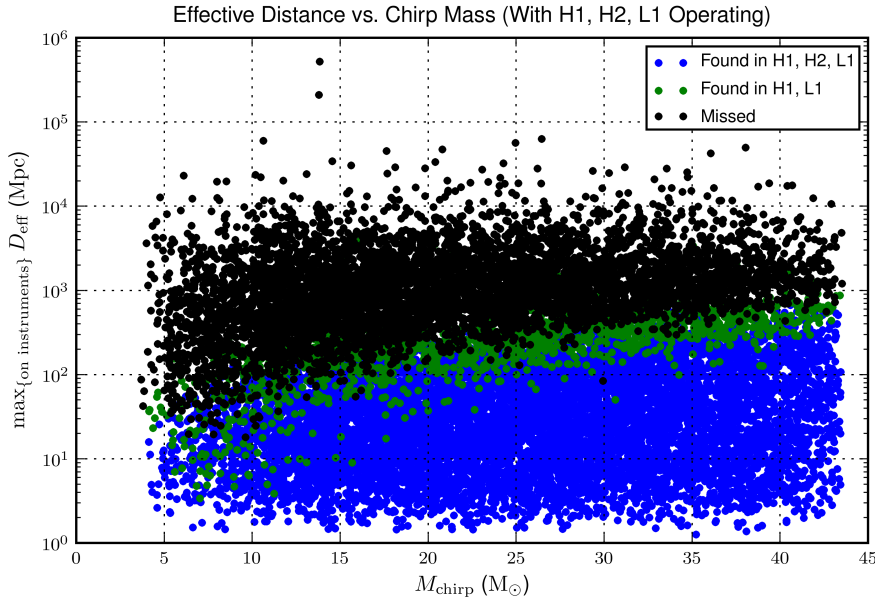


Figure 32: Found and missed injection during months 1 and 2 of the high-mass S5 LIGO search. The plot corresponds to the times when the three LIGO interferometers were operating. Double- and triple- found coincidences are compared with missed injections according to their chirp mass \mathcal{M} .

horizon distance reaches its maximum at total mass of few hundred M_{\odot} when inspiral-merger-ringdown templates are used.

As already mentioned, the data is filtered against the elements of the template bank twice; at the second filter stage the χ^2 veto is applied. This signal-based veto is very important in order to separate potential real signals from background noise. Figure 33 shows how the veto differentiates among them; we plot the value of χ^2 versus the SNR ρ for three different kinds of events: software injections, background triggers estimated via time slides and zero-lag triggers from the playground. The figure corresponds to the L1 detector; plots for H1 and H2 show a similar structure. Firstly, one should notice the efficiency of the veto in separating background and injections. The χ^2 test provides significant separation from noise for a large fraction of simulated signals in this search. Background triggers associated to glitches might be very loud and pass the SNR cut, but for the most part they present a large χ^2 value; in general, injections are correlated with lower χ^2 values. In principle we could draw a line in the ρ - χ^2 plane and discard all triggers above it. In practice, however, one should be careful when applying this procedure, since the separation between injections and background is not always perfectly clean, especially at low ρ values. Thus, stringent cuts would put us in danger of discarding real signals with slightly-above-threshold SNR. This is a well-identified issue; future search efforts in this mass range will employ new signal-based vetoes and multivariate classifiers to hopefully achieve a better separation of signal from background. In addition, figure 33 shows that among the zero-lag triggers for months 1 and 2 of S5 no obvious candidate for detection is present, for all blue crosses in the plot are consistent with the time-slided background triggers.

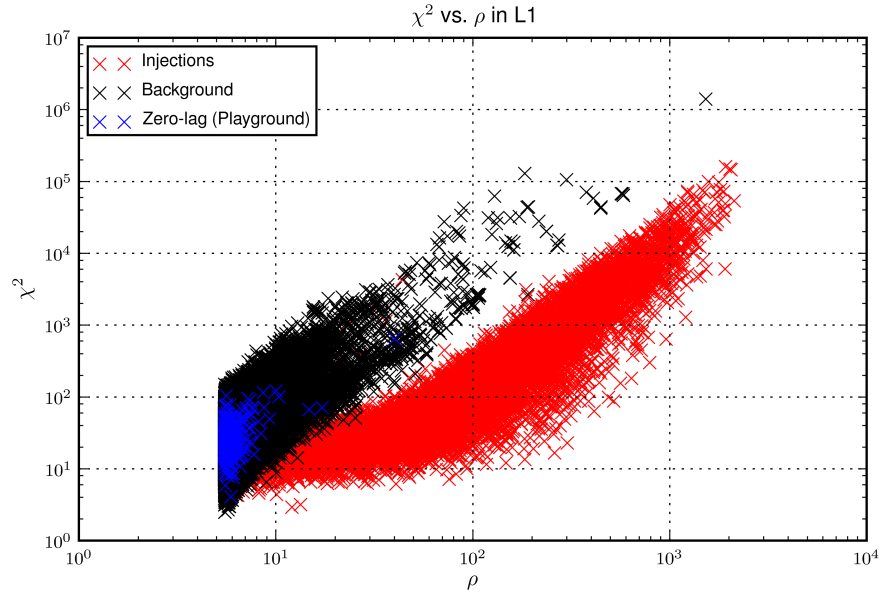


Figure 33: Plot of SNR versus χ^2 in L1 during months 1 and 2 of the high-mass S5 LIGO search. Time-slided background triggers (black) present larger χ^2 values than the injections, showing how the χ^2 veto helps discriminate between them. Additionally, we observe no obvious real candidate among the zero-lag playground triggers.

Once the data has been filtered and the triggers have been subject to the coincidence test, the next step is the ranking of the candidates in order to establish their significance. For the high-mass search this ranking is done using the false alarm statistic. As it happened in the low-mass search, the false alarm rate depends on the filter — despite the expectation for Gaussian noise in which it does not— and also on how many detectors were operating and participated in the event. For the high-mass search, we compute the false alarm rate as a discrete function of four parameters, which each coincident event possesses. Each parameter is an index for an event E . The first index, i , describes the instruments that were functioning during the event and is a member of the set $\{H_1L_1, H_2L_1, H_1H_2L_1\}$. The second index, j , indexes the instruments that participated and is also a member of the set $\{H_1L_1, H_2L_1, H_1H_2L_1\}$. The third index, k , denotes a range for the average total mass estimated for the event and is in the set $\{[25, 50), [50, 85), [85, 100)\}$. The fourth index, m , is the rank of the event. This index is determined by assigning the event with the lowest combined effective SNR defined in 6.13 the value 0 and the the next lowest, 1, etc. until all N events are ranked. We calculate the false alarm rate, ξ , for a given event by summing all background events $B \in E$ with a rank larger than that event dividing by the background time analyzed T_i .

This time is a function of the instruments that were in operation

$$\xi_{ijkl} = \sum_{m>l} B_{ijkm} / T_i. \quad (6.15)$$

This is essentially equivalent to equation 6.14 and to the calculation done for the low-mass search, but new algorithms have been developed in the high-mass search in order to parse events from the database.

In order to assess the total FAR of events, independent of the second and third indices, j , k , we use the inverse FAR ξ^{-1} as an intermediate ranking

statistic to replace combined effective SNR as the fourth index. Then the combined FAR

$$\xi_{i1} = \sum_{m>l,j,k} E_{ijkl} / T_i \quad (6.16)$$

is only a function of the detectors i that were functioning during the event and the inverse FAR computed at the previous step. The results of the FAR calculation for the zero-lag playground triggers occurred during months 1 and 2 of the high-mass S5 LIGO search are shown in figure 34. We observe values of ρ_{eff} compatible with the background; however the FAR plot shows a significant event above the $3\text{-}\sigma$ level. Such an event is eventually followed up with appropriate diagnosis tools developed by the group; the description of the full follow-up pipeline falls beyond the scope of this dissertation. Nevertheless, the true significance of this event found in the playground can only be stated after the analysis of the full data set is complete; the playground results are affected by small statistics associated to the reduced data-set that is analyzed.

Full results of the high-mass search, including in-depth description of the loudest candidates found and —if applicable— computation of upper limits on the rate of binary coalescences will be presented in in [2].

Limitations and Future Prospects

There are a number of limitations in the current approach, which will be addressed for future searches. The main limitation is that the template waveforms neglect the effects of spin. As mentioned in previous chapters of this dissertation, the statistical distribution of the spins of black holes in binaries is not well known; nevertheless there are examples of black holes in X-ray binaries which have been observed to have a large spin [181]. For a binary with spinning components, we have shown that the expected observed gravitational wave signal will differ substantially from the non-spinning case; the observed length can be different, and in the case of non-aligned spin and orbital angular momenta, there would be modulation of the amplitude and phase of the gravitational waveform due to the precession of the orbital plane. Neglecting such effects in the search templates will affect the detection efficiency for binaries with spinning components. Due to the current lack of analytical inspiral-merger-ringdown waveforms for systems with generic spins, we are not yet able to fully quantify how large an effect this is. The model presented in chapter 5 constitutes a first step towards the incorporation of spins in current GW searches and will be included in the near future.

Another limitation of the search is that, due to the shorter duration and bandwidth of the signals in comparison to searches for lower mass systems, it is harder to distinguish between genuine signals and background events. Since the signals themselves resemble short-duration glitches, tests which have previously proved very effective in the lower mass searches, such as the χ^2 -test described in 6.1.3, and the consistency between measured distances in the two Hanford detectors, are not as effective here. New approaches to the ranking of candidate events are being developed to improve this situation in the future.

This chapter has presented the current status of searches for binary coalescences with ground-based interferometers. Over the past years, significant advances, especially in waveform modelling, have opened the door to improvements in the design of the searches. In particular, the possibility of

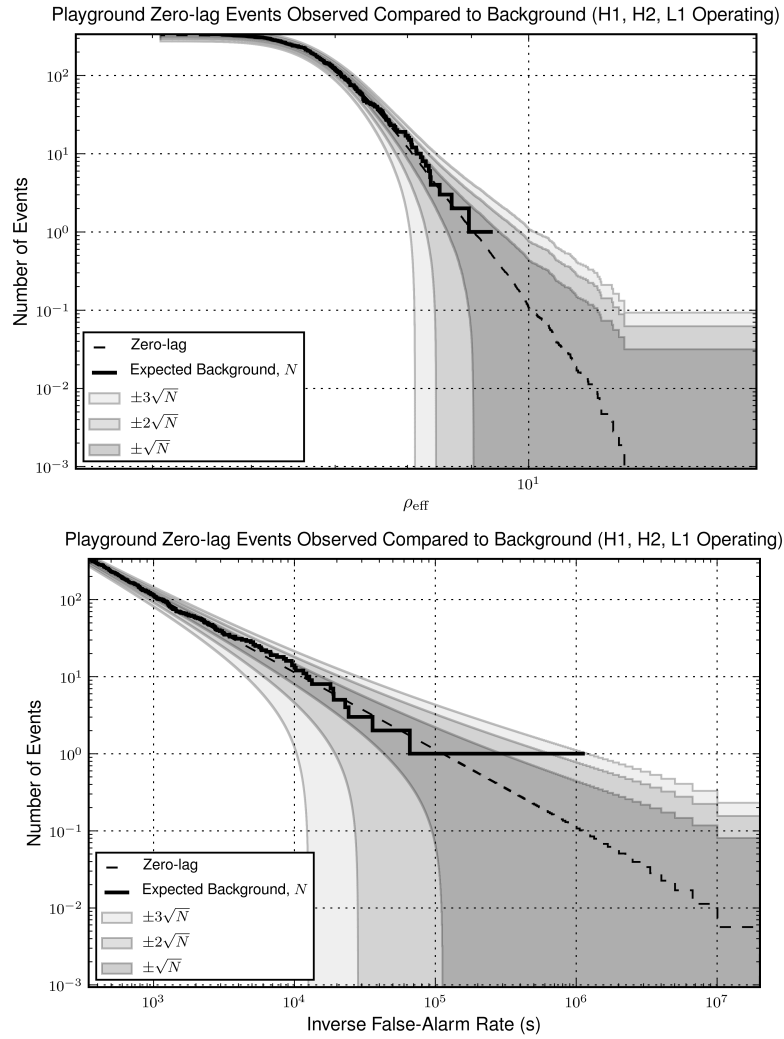


Figure 34: Playground zero-lag events observed compared to background during months 1 and 2 of the high-mass S5 LIGO search. The results correspond to the times when the three LIGO detectors were operating. The upper panel shows the number events versus ρ_{eff} , whereas the lower panel shows the false alarm rate. The apparent $3\text{-}\sigma$ significance of an event in the FAR plot is due to insufficient analyzed data in the playground. In order to establish its true significance, the event would need to be properly analyzed against the full data set.

incorporating input from numerical relativity is slowly taking form. The next chapter presents the results of the first project directly targeted to study the influence of numerical relativity waveforms into current gravitational-wave searches.

So far we have stressed the importance of binary systems of compact objects formed by black holes and/or neutron stars for testing general relativity and studying its astrophysical implications [253]. We have seen how detection of gravitational radiation from these objects is very likely with future generations of gravitational-wave interferometers. Two important advances have occurred in recent years that approach us to the goal of observing and interpreting signals from coalescing compact objects. The first is the successful construction and operation of the world-wide network of gravitational-wave interferometers described in depth in chapter 1. The second has been the success of numerical relativity in simulating the merger phase of binary black hole (BBH) coalescence introduced in chapter 4. Since the already-mentioned breakthroughs occurred in 2005, a number of numerical relativity groups around the world have successfully evolved various configurations starting from the inspiral phase all the way through the merger to the final remnant black hole. This has led to important new physical insights in BBH mergers.

Since the coalescence of black holes is among the most important targets of gravitational-wave detectors, detailed information provided by numerical simulations should be used to increase the reach and to quantify the efficacy of data analysis pipelines. Indeed the driving motivation of research on numerical simulations of black-hole binaries over the last few decades has been their use in gravitational-wave observations.

This chapter presents the results of the first project established with those specific goals. Below is the description of the scope and goals of the NINJA project as well as the contributed numerical waveforms and the construction of the simulated gravitational-wave detector data used in the analyses. The core of the author's work for NINJA, corresponding to the implementation of a search that uses the non-spinning phenomenological template bank of [24] is described in section 7.2. The chapter concludes with the discussion of the results and future directions for NINJA in sections 7.2.3 and 7.2.4.

This chapter summarizes the work of the author in the context of the NINJA collaboration, which resulted in the publications [49], [87] and [228]

7.1 THE NINJA PROJECT

Thus far, most searches for gravitational waves from BBH mergers have relied on post-Newtonian results, which are valid when the black holes are sufficiently far apart, as explained in section 3.1 of chapter 3. Within its range of validity, post-Newtonian theory provides a convenient analytic description of the expected signals produced by binary systems. The numerical relativity results, on the other hand, have not yet been synthesised into an analytic model for the merger phase covering a broad range of parameters, i.e., a wide range of mass ratios, spins and if necessary, eccentricity. As a matter of fact, one of the core results of this thesis, presented in chapter 5, is the construction of a phenomenological model for the full coalescence of non-precessing BBH systems that aims at incorporating the spins of the black holes in a simplified way.

Similarly, despite significant progress, there is not yet a complete detailed description over the full parameter space of how post-Newtonian and numerical simulations are to be matched with each other. The waveform family of chapter 5 is a first step in this direction, but more work is necessary to expand this model to generically spinning systems. On the data analysis side, many pipelines, especially ones that rely on a detailed model for the signal waveform, have made a number of choices based on post-Newtonian results, and it is important to verify that these choices are sufficiently robust. More generally, it is necessary to quantify the performance of these data analysis pipelines for both detection and parameter estimation. This is critical for setting astrophysical upper limits in case that no detection is made, for following up interesting detection candidates, and of course for interpreting direct detections. To date, available research has primarily used post-Newtonian waveforms. Numerical relativity now provides an important avenue for extending these studies to the merger phase.

*NINJA: The Numerical
INjection Analysis
Project*
[http://www.
ninja-project.org/](http://www.ninja-project.org/)

There are significant challenges to be overcome before numerical relativity results can be fully exploited in data-analysis pipelines. The NINJA project was started in the spring of 2008 with the aim of addressing these challenges and fostering close collaboration between numerical relativists and data analysts. The purpose of NINJA is to study the sensitivity of existing gravitational-wave search algorithms using numerically generated waveforms that are injected into simulated noise. Only BBH simulations are considered, leaving out results from supernova simulations or simulations containing neutron stars; the waveform data comes purely from numerical simulations; the NINJA data set is constructed using Gaussian noise to model the response of the Initial LIGO and Virgo detectors —no attempt has been made to include non-Gaussian noise transients found in real detector data.

7.1.1 Numerical Waveforms

The NINJA project studied BBH coalescence waveforms submitted by ten individuals and teams. Participation in NINJA was open to anyone and the only restrictions were that each contribution: (i) was a numerical solution of the full Einstein equations, (ii) consisted of only two waveforms, or up to five waveforms if they were part of a one-parameter family. No restrictions were placed on the accuracy of each waveform. All contributions followed the format specified in [75]. The contributed waveforms, plotted in Figures 35 and 36, cover a variety of physical and numerical parameters. Most simulations model low-eccentricity inspiral, the mass ratio $q = m_1/m_2$ ranges from 1 to 4. The initial angular frequency of the $\ell = m = 2$ mode ranges from $0.033/M$ to $0.203/M$ (where M denotes the sum of the initial black-hole masses). This initial angular frequency marks where contributors consider the waveform sufficiently clean to represent the physical system (e.g. this will be chosen after initial unphysical radiation content, often referred to as “junk radiation” in numerical relativity, is radiated away). The length of the waveforms varies between a few $100 M$ to over $4000 M$. The contributions naturally differ in accuracy, both regarding how well they capture the black-hole dynamics and in the extraction of the gravitational-wave signal.

Table 10 lists a few key parameters that distinguish the waveforms, and introduces the following tags for the different contributions and NR codes: BAM HHB [77, 156, 146, 145, 78] and BAM FAU [77, 156, 254, 78] are contribu-

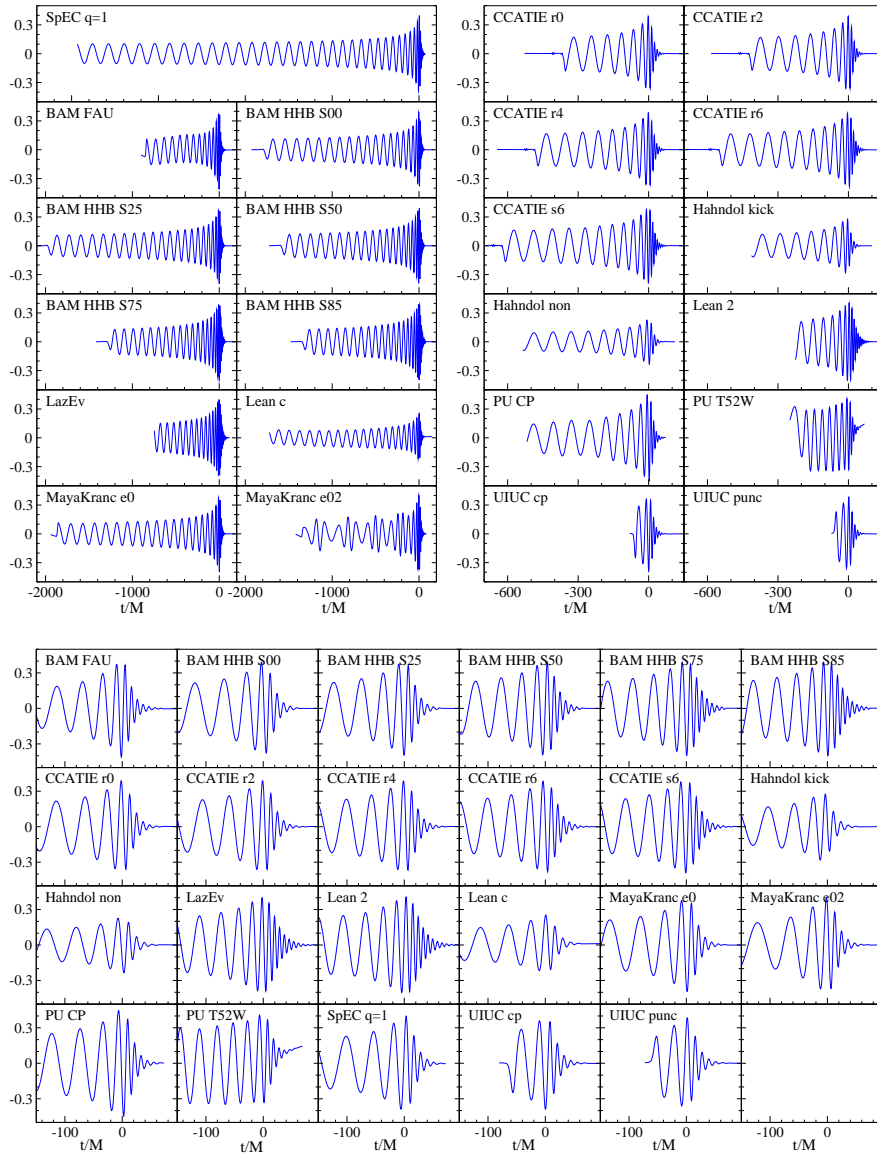


Figure 35: Summary of all submitted numerical waveforms: $r/M \operatorname{Re}(h_{22})$. The x -axis shows time in units of M and the y -axis shows the real part of the $(\ell, m) = (2, 2)$ component of the dimensionless wave strain $rh = rh_+ - irh_\times$. The top panels show the complete waveforms: the top-left panel includes waveforms that last more than about $700M$, and the top-right panel includes waveforms shorter than about $700M$. The bottom panel shows an enlargement of the merger phase for all waveforms. (Figure credit: Harald Pfeiffer)

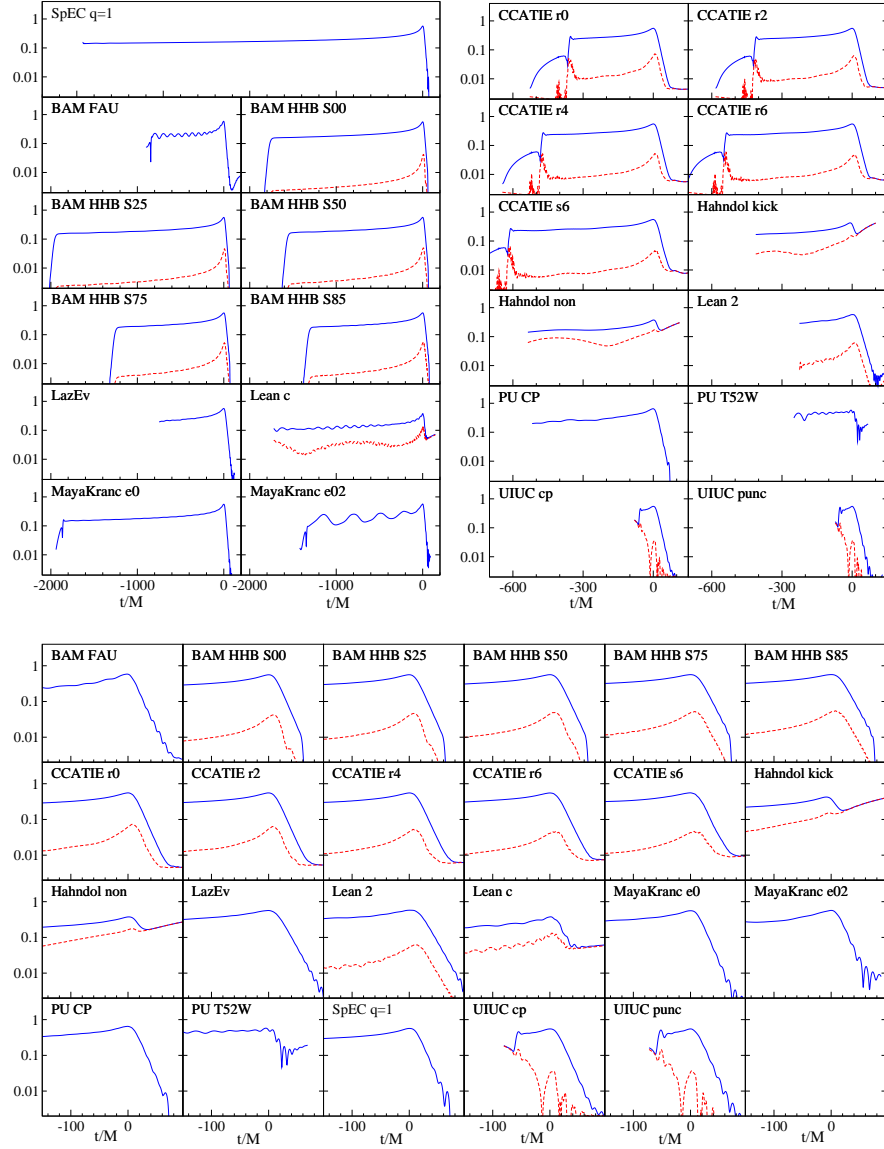


Figure 36: Distribution of power into different spherical harmonics. The blue line shows $(\sum_{\ell, m} |h_{\ell m} r/M|^2)^{1/2}$. A dashed red line, if present, shows the same sum, but *excluding* the $(\ell, m) = (2, \pm 2)$ modes. The separation between the two lines gives the relative importance of non $(2, \pm 2)$ modes. If no red line is present for a certain run, then only the $(2, \pm 2)$ modes were supplied. The layout is as in figure 35: The top panels show the complete waveforms, whereas the bottom panel shows an enlargement of the merger phase. The x-axis shows time in units of M . (Figure credit: Harald Pfeiffer)

tions using the BAM code, CCATIE is the AEI/LSU code [28, 29, 170, 206, 222], Hahndol is the Goddard Space Flight Center's code [158, 256], LazEv is the RIT code [269, 88, 96], Lean is Ulrich Sperhake's code [244, 246, 245], MayaKranc is the Georgia Tech/Penn State code [255, 153], PU stands for the Princeton University code [213, 212, 82, 214], SpEC for the Cornell/Caltech collaboration code [231, 204, 69, 232], and UIUC stands for the University of Illinois at Urbana-Champaign team [114].

The codes listed above use different formulations of the Einstein equations, gauge conditions, mesh structures, initial data and wave extraction methods; they follow either of two approaches to solving the Einstein equations: (i) the generalized harmonic formulation, which was the basis of Pretorius' initial breakthrough simulation of coalescing black holes [212], or (ii) the moving-puncture approach, following [88, 52]. Both approaches result in canonical choices for the construction of initial data, the evolution system for the Einstein equations, and the treatment of the singularity inside the black-hole horizons. Full details of each individual code are given in the references above and a comparative description of their main features is presented in [49].

The list of contributing groups to NINJA reflects the success of the project, for all research groups capable of performing NR simulations of BBH space-times did contribute their waveforms.

7.1.2 Creation of NINJA Data

The data provided by the numerical relativity groups follows the format outlined in [75], which is based on the mode decomposition of the gravitational radiation field at large distances from the source. If we specify a gravitational waveform $h_{\mu\nu}$ in the Transverse-Traceless (TT) gauge, we only need the spatial components h_{ij} . We assume that we are sufficiently far away from the source so that the $1/r$ piece dominates:

$$h_{ij} = A_{ij} \frac{M}{r} + \mathcal{O}(r^{-2}), \quad (7.1)$$

where M is the total mass of the system, r is the distance from the source, and A_{ij} is a time-dependent TT tensor. In the TT gauge, h_{ij} has two independent polarizations denoted h_+ and h_\times and the complex function $h_+ - ih_\times$ can be decomposed into modes using spin-weighted spherical harmonics $^{-2}Y_{\ell m}$ of weight -2:

$$h_+ - ih_\times = \frac{M}{r} \sum_{\ell=2}^{\infty} \sum_{m=-\ell}^{\ell} H_{\ell m}(t) \ ^{-2}Y_{\ell m}(\iota, \phi). \quad (7.2)$$

The expansion parameters $H_{\ell m}$ are complex functions of the retarded time $t - r$, however if we fix r to be the radius of the sphere at which we extract waves then $H_{\ell m}$ are functions of t only. The angles ι and ϕ are respectively the polar and azimuthal angles in a suitable coordinate system centered on the source. This decomposition is directly applicable to non-precessing binaries. Otherwise, a comparison of the waveforms requires a careful treatment of mode-mixing effects due to rotations of the frame; see for instance [137]. The numerical data contributed to NINJA is given in the form of an ASCII data file for each mode (ℓ, m) , with accompanying meta-data describing the simulation [75]. Only modes that contribute appreciably to the final waveform are included, at the discretion of the contributing group. Each data file consists of three columns: time in units of the total mass, and the real and imaginary parts of the mode coefficients $H_{\ell m}$ as a function of time. Note that the total

Table 10: Initial conditions for numerical waveforms submitted to the NINJA project. The columns list, in order from left to right, the name of the contribution or code, the name of the run where appropriate, the mass ratio $q = m_1/m_2$ where $m_1 \geq m_2$, the spins of the black holes in vector form (if only one spin is given, both spins are equal), the initial frequency of the $(\ell, m) = (2, 2)$ mode (rounded to three digits) and the initial coordinate separation of either the black-hole punctures or the excision surfaces. All binaries start out in the xy -plane with initial momenta tangent to the xy -plane. See text for the identification of each contribution. The dimensionless spins of the BAM FAU run are $(-0.634, -0.223, 0.333)$ and $(-0.517, -0.542, 0.034)$.

Code [Ref.]	Run	q	\vec{S}_i/m_i^2	$\omega_{22} M$	D/M
BAM FAU [77, 156]	[254]	1	see caption	0.06	$9.58 \hat{y}$
BAM HHB [77, 156]	S00 [146]	1	0	0.045	$12 \hat{y}$
	S25 [145]	1	$0.25 \hat{z}$	0.045	$12 \hat{y}$
	S50 [145]	1	$0.50 \hat{z}$	0.052	$11 \hat{y}$
	S75 [145]	1	$0.75 \hat{z}$	0.06	$10 \hat{y}$
	S85 [145]	1	$0.85 \hat{z}$	0.06	$10 \hat{y}$
CCATIE [28, 29, 170, 206]	r0 [206]	1	$0.6 \hat{z}, -0.6 \hat{z}$	0.079	$8 \hat{x}$
	r2 [206]	1	$0.6 \hat{z}, -0.3 \hat{z}$	0.078	$8 \hat{x}$
	r4 [206]	1	$0.6 \hat{z}, 0$	0.076	$8 \hat{x}$
	r6 [206]	1	$0.6 \hat{z}, 0.3 \hat{z}$	0.075	$8 \hat{x}$
	s6 [222]	1	$0.6 \hat{z}$	0.074	$8 \hat{x}$
HahndoL [158, 256]	kick	3	$0.2 \hat{x}, 0.022 \hat{x}$	0.078	$8.007 \hat{y}$
	non	4	0	0.070	$8.470 \hat{y}$
LazEv [269, 88]	MH [96]	1	$0.92 \hat{z}$	0.07	$8.16 \hat{x}$
Lean [244]	c	4	0	0.05	$10.93 \hat{x}$
	2	1	$0.926 \hat{z}$	0.11	$6.02 \hat{x}$
MayaKranc [255]	e0 [153]	1	0	0.05	$12 \hat{x}$
	e02 [153]	1	0	0.05	$15.26 \hat{x}$
PU [213, 212]	CP [82]	1	$0.063 \hat{z}$	0.07	$9.5 \hat{x}$
	T52W [214]	1	0	0.07	
SpEC [231]	$q = 1$ [69, 232]	1	0	0.033	$15 \hat{x}$
UIUC [114]	cp [114]	1	0	0.194	$4.790 \hat{x}$
	punc [114]	1	0	0.203	$4.369 \hat{y}$

Table 11: Characteristic duration, mass and frequencies of the waveforms summarized in table 10. The columns ΔT_{100} and $f_{i,100}$ give the duration and initial frequency of the waveform when scaled to total mass $M = 100 M_{\odot}$. $M_{30\text{Hz}}$ is the total mass of the waveform when it is scaled so that the initial frequency is 30Hz (this sets the lowest mass at which each waveform can be injected into the NINJA data).

Code	Run	q	ΔT_{100} (s)	$f_{i,100}$ (Hz)	$M_{30\text{Hz}}(M_{\odot})$
BAM FAU		1	0.54	19	65
BAM HHB	S00	1	1.03	15	48
	S25	1	1.15	15	48
	S50	1	1.03	17	56
	S75	1	0.81	19	65
	S85	1	0.87	19	65
CCATIE	r0	1	0.34	26	85
	r2	1	0.37	25	84
	r4	1	0.40	25	82
	r6	1	0.45	24	81
	s6	1	0.59	24	80
Hahndol	kick	3	0.25	25	84
	non	4	0.32	23	75
LazEv	MH	1	0.43	23	75
Lean	c	4	0.92	16	54
	2	1	0.20	36	118
MayaKranc	e0	1	1.23	16	54
	e02	1	0.74	16	54
PU	CP	1	0.29	23	75
	T52W	1	0.16	23	75
SpEC	q = 1	1	1.96	11	36
UIUC	cp	1	0.10	63	209
	punc	1	0.10	66	219

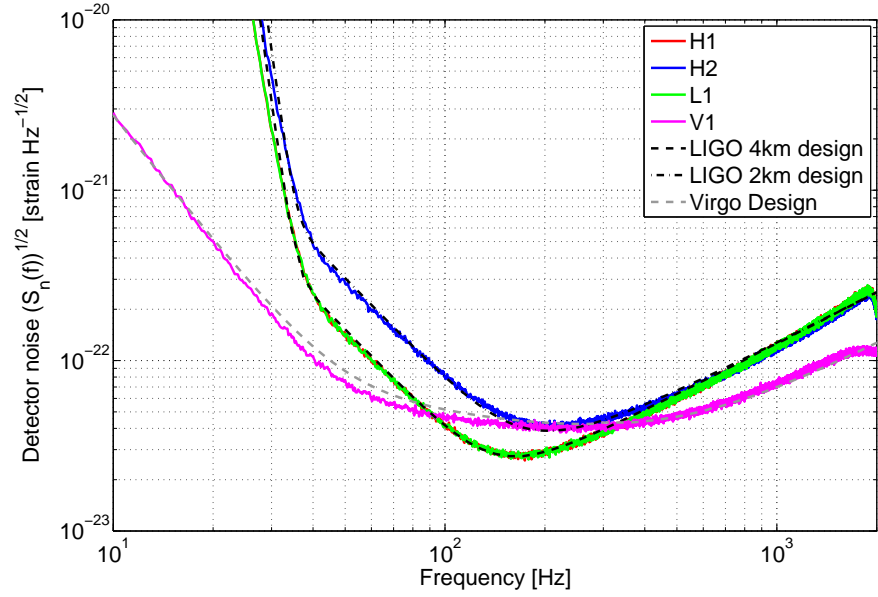


Figure 37: Design spectra of the first generation LIGO and Virgo detectors and the NINJA noise curves generated via coloured Gaussian data to mimic the response of the real detectors.

This is not true in the case of simulations which include matter fields, but we do not consider such waveforms here

See, for example, [253]

mass M scales both the time and the amplitude; thus the BBH waveforms for each simulation can be scaled to an arbitrary value of the mass. To model the signal seen by a gravitational-wave detector, we need to calculate the detector strain $h(t)$ from the above mode decomposition. To do this, we must choose particular values of the total mass, orientation and distance from the detector. Given the $H_{\ell m}$, the total mass, the distance to the source, and the angles (ι, ϕ) , we calculate $h_{+, \times}$ using equation 7.2, and use the detector response functions $F_{+, \times}$ to calculate the observed strain

$$h(t) = h_+(t)F_+(\alpha, \delta, \psi) + h_\times(t)F_\times(\alpha, \delta, \psi). \tag{7.3}$$

Here (α, δ) are sky-angles in the detector frame, ψ is the polarization angle and the time t is measured in seconds. In this analysis, we wish to simulate signals that might be observed by the Initial LIGO and Virgo detectors. Since the location and alignment of the three observatories differ, we must use the appropriate detector response and arrival time to compute the strain waveform $h(t)$ seen at each observatory. This ensures that the waveforms are coherent between the detectors and simulate a true signal.

To model the detector noise, we generated independent Gaussian noise time series $n(t)$, sampled at 4096 Hz, for each detector. This sample rate was chosen to mimic that used in LSC-Virgo searches and assures a tolerable loss in signal-to-noise ratio due to the discrete time steps. Stationary white noise time series are generated and coloured by a number of time-domain filters designed to mimic the design response of each of the LIGO and Virgo detectors. Figure 37 shows the one-sided amplitude spectral density $\sqrt{S_n(f)}$ of each time detector’s time series, where $S_n(f)$ is defined by equation 5.4.

We see from figure 37 that the noise power spectrum of the NINJA data set closely approximates the Initial LIGO design sensitivity in the frequency range of interest (30 – 10³ Hz). There is a slight discrepancy with the Virgo design

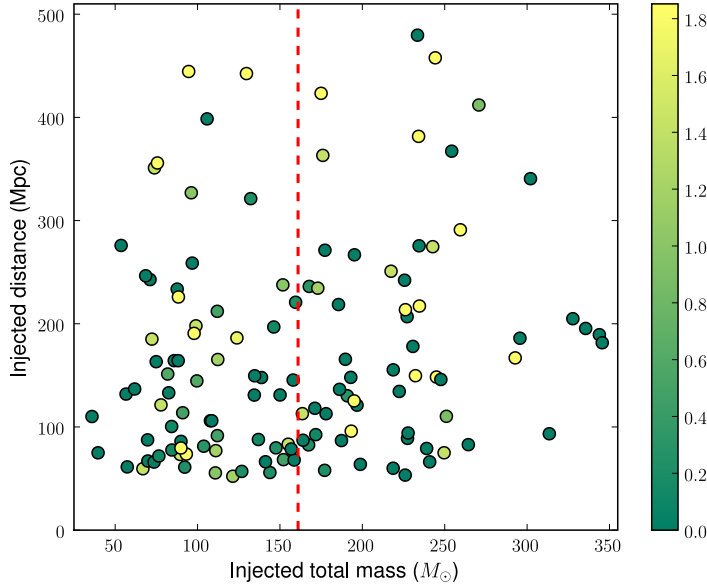


Figure 38: Total mass and distance of the 126 NINJA injections, with the colour code encoding the modulus of the dimensionless total spin $|\vec{S}_1/m_1^2 + \vec{S}_2/m_2^2|$ of the black holes. The total mass of the injected signals lies within the range $36 M_\odot \leq M \leq 460 M_\odot$ and they are located at a distance between 52 and 480 Mpc. The vertical line delimits the mass parameter space with $M < 160 M_\odot$ that the phenomenological template bank for the search described in section 7.2 covers. The full NINJA data set spans a duration of a little over 30 hours and contains a total of 126 signals injected in simulated noise, 67 of which overlap with the parameter space of our template bank.

curve at low frequencies (between approximately 20 and 150 Hz), which is an artefact of the Virgo noise generation procedure. Narrow-band features such as the violin and mirror modes were removed from the detector response used to compute the NINJA data, but were included in the calculation of the Virgo design curve. The $1/f$ tails of these narrow-band features are responsible for the small discrepancy.

Having produced the simulated detector data, we then generated a population of simulated signals using the numerical relativity data. This population was constructed to cover a broad range of masses and signal amplitudes. We required that the starting frequency of the dominant $\ell = m = 2$ mode of the signal was not more than 30 Hz, an appropriate threshold given the sensitivity curve of the Initial LIGO and Virgo detectors. This sets a minimum mass at which each waveform can be injected, which is given in Table 11. The minimum possible injection mass is therefore $36 M_\odot$. The maximum mass was chosen as $350 M_\odot$. To get a good sample of long injected waveforms, we systematically chose a lower range of masses for the longer waveforms. No restrictions were placed on the other simulation parameters, i.e., the spins, mass-ratios and eccentricities. We ensured that waveforms from all the participating groups were equitably represented by generating approximately 12 signals from the waveforms supplied by each group. The time interval between adjacent injected signals was chosen to be a random number in the range 700 ± 100 s.

Given these constraints, we generated the parameters of the signal population. The logarithm of the distance to the binary was drawn from a uniform distribution ranging from 50 Mpc to 500 Mpc, and the source locations and orientations were drawn from an isotropic distribution of angles. We then computed waveforms corresponding to this population and at the appropriate sampling rate. We required that the optimal matched filter signal-to-noise ratio of any injection be greater than five in at least one of the four simulated detectors. Any waveform that did not satisfy this constraint was discarded from the population. Subject to this condition, the distances of injected signals varied from 52 Mpc to 480 Mpc (median at 145 Mpc), the injected total mass range was $36 M_{\odot} \leq M \leq 346 M_{\odot}$ (median at $155 M_{\odot}$), with individual component masses in the range $11 M_{\odot} \leq m_i \leq 193 M_{\odot}$.

Finally, the waveforms $h(t)$ were added to the simulated detector noise $n(t)$ to generate the NINJA data set $s(t) = n(t) + h(t)$. As described above, care was taken to ensure that signals were coherently injected in the data streams from the four detectors. The data set used in this analysis consisted of a total of 126 signals injected in a total of 106 contiguous segments of noise each 1024 s long, thus spanning a duration of a little over 30 hours. Figure 38 shows the mass, spin and distance of the waveforms contained in the NINJA data set, as well as the part of the parameter space explored by the search described in section 7.2

The software for carrying out this procedure is freely available as part of the LSC Algorithm Library <http://www.lsc-group.phys.uwm.edu/lal> [178].

7.2 SEARCH WITH A PHENOMENOLOGICAL TEMPLATE BANK

Analysis of the NINJA data was open and nine groups submitted contributions using a variety of analysis techniques. Participating groups were provided with the NINJA data set containing signals embedded in noise and the parameters of the injected signals. Analysts were not given access to the raw numerical-relativity waveforms or noiseless injection data. Methods used to analyze the NINJA data include: matched-filter based searches, unmodeled waveform searches using excess-power techniques, and Bayesian model-selection and parameter-estimation techniques. For a full description of all analyses and results we refer the reader to the main NINJA paper [49]. In this section we present the results of our analysis employing a matched-filter search using phenomenological waveforms.

7.2.1 *The Non-Spinning Phenomenological Waveform Model*

Most standard searches for gravitational waves from BBHs use the PN approximation of general relativity to construct banks of templates that account for the inspiral stage of the coalescence process, and the final ringdown can also be computed via perturbative techniques. However, the full calculation of the waveform in the merger stage requires numerical methods. These numerical simulations are in general rather expensive, and it is at present not feasible to model a coalescing binary over hundreds of orbits with sufficient accuracy. It is in fact also unnecessary to do so, because PN theory provides a valid description of the system when the black holes are sufficiently separated and the gravitational field is weak. Thus, a promising approach for constructing long waveform models covering the inspiral, merger and ringdown regimes is to stitch together the results of PN and NR calculations.

One procedure for constructing such hybrid waveforms is presented in [24, 23, 22], where PN and NR waveforms are matched in an appropriate regime ($-750 \leq t/M \leq -550$) prior to the merger (M is the total mass of the binary system in solar masses). Restricted 3.5PN waveforms at mass-quadrupole order are used for the inspiral phase, as given by equation (3.1) of [23]. For the numerical part, the model is based on long unequal-mass waveforms from simulations run by the Jena group using the BAM code [77, 146, 105]. These simulations span a range of mass ratios corresponding to $0.16 \leq \eta \leq 0.25$, where $\eta = (m_1 m_2)/M^2$ is the symmetric mass ratio of the binary system. The matching of PN and NR data is performed over an overlapping region, under the assumption that both approaches to the true BBH waveform are approximately correct at the late inspiral stage. Once the hybrid waveforms are constructed, they are fit to a phenomenological model determined entirely by the physical parameters of the binary system. This fit to an analytical expression is performed in the Fourier domain, assuming a functional dependence of the form

$$u(f) = A_{\text{eff}}(f) \Psi_{\text{eff}}(f), \quad (7.4)$$

with amplitude and phase given by the following equations:

$$A_{\text{eff}}(f) \equiv C \begin{cases} (f/f_{\text{merg}})^{-7/6} & \text{if } f < f_{\text{merg}} \\ (f/f_{\text{merg}})^{-2/3} & \text{if } f_{\text{merg}} \leq f < f_{\text{ring}} \\ \omega \mathcal{L}(f, f_{\text{ring}}, \sigma) & \text{if } f_{\text{ring}} \leq f < f_{\text{cut}} \end{cases} \quad (7.5)$$

$$\Psi_{\text{eff}}(f) = 2\pi f t_0 + \varphi_0 + \sum_{k=0}^7 \psi_k f^{(k-5)/3}, \quad (7.6)$$

The phenomenological coefficients f_{merg} , f_{ring} , f_{cut} , σ and ψ_k are functions of the binary symmetric mass ratio η and total mass only and can be computed from Tables I and II of [23].

Each waveform is parameterized by the physical parameters of the system, which in the non-spinning case are solely the masses m_1 and m_2 of the black holes. As a result of the matching and fitting procedures described above, a two-dimensional template family of waveforms that attempt to model the entire coalescence of non-spinning binary black hole systems has been obtained.

7.2.2 The Search Strategy

The LSC inspiral pipeline infrastructure developed by the CBC group and described in chapter 6 has been employed to analyze the data released for the NINJA project. The pipeline, without major conceptual modifications, has been used in LSC searches for compact binaries from the third LIGO science run onward [10]. The same pipeline has been modified for the analysis of the NINJA data with the non-spinning phenomenological template family [24, 23, 22] described in section 7.2.1. Since the signals present in the simulated noise are known to be numerical simulations of BBH coalescences, the search method consists of a matched-filter technique [31] using an IMR waveform model based on hybrid NR-PN waveforms. The findings presented here concentrate solely on the simulated LIGO detectors H1, H2 and L1, although the NINJA data was generated for the simulated Virgo interferometer V1 as well.

The tuning of the pipeline was realized according to the usual choices made by the group in the analysis of real LIGO data. For our NINJA analysis, a SNR threshold $\rho^* = 5.5$ was employed, in agreement with the value currently used

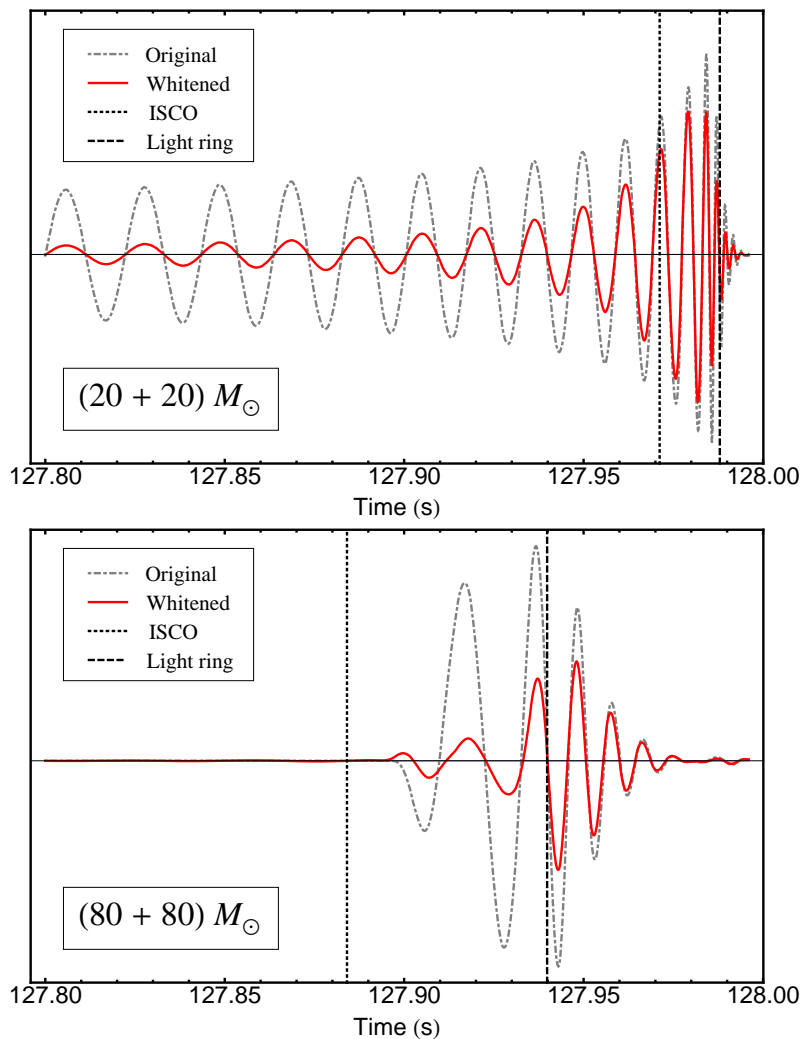


Figure 39: Two time-domain phenomenological waveforms from the template bank used in this search, corresponding to equal-mass binaries in the corners of our parameter space, namely $(20 + 20) M_{\odot}$ and $(80 + 80) M_{\odot}$ BBH systems. The original and “whitened” [99] waveforms are shown, with their amplitudes arbitrarily resized. The dotted and dashed vertical lines mark the points where the ISCO and light ring frequencies are reached. The LRD frequency is not shown, since it basically extends up to the full waveform. A matched-filter search that starts at 30 Hz and ends at the ISCO will not be able to pick the most massive binaries, since the inspiral phase of the coalescence falls below the LIGO interferometers’ detection band. It is expected that the light ring and LRD frequencies, which extend up to the BH merger and ringdown respectively, will show improved performance at recovering high-mass signals.

in recent LSC searches for binary coalescences [15]. Whenever triggers are found with comparable coalescence time and parameters—in this case, component masses—they are stored as coincident [224]. The detection statistic is the combined SNR of the single detector triggers.

Once the initial matched filter has produced a list of triggers that pass the first coincidence step, a second stage follows where data is again filtered, but only through the templates that previously matched a trigger. Additionally the

χ^2 [30] and r^2 [225] signal-based vetoes, designed to separate true inspiral signals from fluctuations in non-stationary noise, are applied. At this point an *effective SNR* $\rho_{\text{eff},i}(\rho_i, \chi_i^2)$ is calculated combining the standard SNR with the χ^2 value characterizing the mismatch between the spectral content of the template and the data. After further coincidence tests, the surviving triggers are listed as true gravitational wave candidates and constitute the output of the search. The significance of the triggers is based on the combined effective SNR, namely

$$\rho_{\text{eff}} = \sqrt{\sum_i^N (\rho_{\text{eff},i})^2}. \quad (7.7)$$

A direct comparison between the list of injections performed on the NINJA noise and the triggers found by the pipeline allows for conclusions about the sensitivity of the analysis and the relative performance of the different template banks.

The phenomenological template bank has been included in the LSC inspiral pipeline routinely used by the CBC group as a new waveform for filtering in the time domain. A search on the NINJA data has been performed, within a mass range of $20 M_\odot \leq m_1, m_2 \leq 80 M_\odot$ for the component masses, with $40 M_\odot \leq M \leq 160 M_\odot$ for the total mass of the binary. The template bank is constructed using the standard second order post-Newtonian metric, and uses a hexagonal placement algorithm in mass space with a minimal match of 0.99 [93]. The number of signals that are recovered by the pipeline depends strongly on the choice for the upper frequency cutoff used in the matched filter integral, as we have observed in our investigations with the integration stopping at the ISCO (Innermost Stable Circular Orbit, $r = 6M$), light ring (the unstable circular orbit for photons orbiting a Schwarzschild black hole, $r = 3M$) and Lorentzian ringdown (LRD) frequencies.

In Figure 39 we show two waveforms from our phenomenological template bank, which correspond to equal-mass binaries in the corners of our parameter space, namely total mass $M = 40 M_\odot$ and $160 M_\odot$. Displayed are both the original time domain waveform and its “whitened” form [99], as the initial LIGO detector perceives it, and the relative amplitudes have been arbitrarily resized. The whitened waveform is computed as the inverse Fourier transform of the original signal multiplied by the function $1/\sqrt{S_h(f)}$ in the frequency domain, where $S_h(f)$ is the one-sided noise power spectral density of the simulated LIGO detectors. In each plot the vertical lines correspond to the ISCO and light ring frequencies. In our searches we have started filtering against the phenomenological templates at either 30 or 40 Hz and we have stopped the integration at the three frequencies discussed in the above paragraph. It is evident that whereas a cut at the ISCO frequency still retains a good portion of the inspiral signal for low-mass binaries, it is insufficient for higher masses. The light ring and LRD frequencies, on the other hand, extend roughly up to the BH merger and to the Lorentzian tail (from the decay of the quasi-normal modes of the ringdown), respectively, and are therefore expected to produce better results for a matched-filter search for high-mass signals.

The Lorentzian ringdown frequency is defined as 1.2 times the fundamental ringdown frequency of Berti, Cardoso and Will, Phys. Rev. D 73 064030 (2006).

Table 12: Results of the search for NINJA signals using the non-spinning phenomenological template bank. There were 126 injections performed into the analyzed data for H1, H2 and L1, 67 of which fell within the mass range of our phenomenological template bank ($M < 160 M_{\odot}$). We explicitly show that a much better efficiency in trigger recovery is achieved when the cutoff frequency is pushed beyond the ISCO frequency, up to the light ring and Lorentzian ringdown frequencies. Likewise we observe improved efficiency in finding the signals that lie within the mass range of our template bank. In both cases the signal-based vetoes have little influence in the rejection of triggers, confirming their efficiency in separating inspiral-like signals from other kind of glitches.

<i>Frequency Cutoff</i>	ISCO	LightRing	LRD	LRD
<i>Filter Start Frequency</i>	30 Hz	30 Hz	30 Hz	40 Hz
Complete set of 126 NINJA Injections				
<i>Found Single (H1, H2, L1)</i>	78, 54, 69	94, 66, 90	92, 61, 87	93, 60, 86
<i>Found Coincidence</i>	59	78	81	80
<i>Found Second Coincidence</i>	59	78	80	79
Reduced set of 67 NINJA Injections with $M < 160 M_{\odot}$				
<i>Found Single (H1, H2, L1)</i>	40, 17, 32	55, 41, 50	55, 41, 50	56, 40, 50
<i>Found Coincidence</i>	30	47	48	47
<i>Found Second Coincidence</i>	30	47	48	47

7.2.3 Efficiency for Detection

The main results of our search for numerical relativity signals injected in simulated LIGO noise employing a phenomenological template bank are presented in Table 12. We show here a summary of the found triggers at different stages of the pipeline for several runs, with the starting frequency for the matched-filter integral being either 30 or 40Hz and the integration stopping at three different frequencies —ISCO, light ring and LRD— displayed in ascending order. We have separated our results in two sections, according to performance in recovering the full set of 126 NINJA injections and the reduced set of 67 injections whose total mass falls below $160 M_{\odot}$. This choice is motivated by the construction of the phenomenological bank.

A time window of 120 ms has been used in order to cluster the triggers found by the pipeline in a single detector. Similarly the coincidence has been determined within a 80 ms injection window. Given these choices for the parameters used in clustering the triggers, we report recovery of 80/126 triggers in double or triple coincidence for the full injection set and 48/67 triggers for the reduced set with $M < 160 M_{\odot}$. These are triggers that survive the second coincidence stage (including the signal-based vetoes) for our best run, which corresponds to the matched-filter integral starting at 30Hz and ending at the LRD frequency. The number of recovered triggers in the full mass range is compatible with the results quoted by other participants in the NINJA project employing searches with higher-order corrections PN templates extended up to larger frequencies. The efficiency of the search improves, however, when

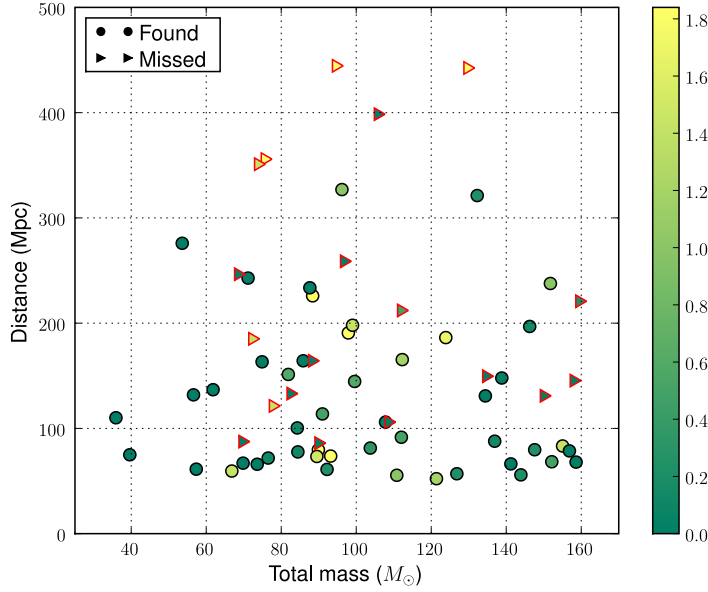


Figure 40: Found and missed injections in the mass region $32 M_{\odot} \leq M \leq 160 M_{\odot}$ as a function of their total mass and distance for our best search, starting at 30 Hz and stopping at the LRD frequency. The circles represent triggers that were recorded as either double or triple coincidences after the second stage (including the signal-based vetoes), whereas the triangles represent missed injections. The colour code displayed in the vertical scale represents the modulus of the dimensionless total spin $|\vec{S}_1/m_1^2 + \vec{S}_2/m_2^2|$ of the black holes. The red border of the triangles serves solely as visual aid to facilitate their quick identification as missed injections.

we restrict ourselves to signals with masses overlapping those of our template bank. It is worthwhile noting that among the triggers recovered by the pipeline we find not only non-spinning simulations but also signals with non-precessing spins, such as the CCATIE and BAM_BBH waveforms (except in the case of equal $S/m^2 = 0.25$ spins aligned in the z -direction, which we discuss later). This supports existing evidence for the fact that non-spinning templates should be able to detect non-precessing spinning signals with moderate individual spins. The capability of non-spinning templates for recovering signals with precession and large spins could however be compromised, as we discuss below. Due to the low statistics of the present analysis, these statements should be taken with the appropriate reservations.

Figure 40 provides an overview of the found and missed injections corresponding to total mass below $160 M_{\odot}$. The colour code encodes the modulus of the dimensionless total spin $|\vec{S}_1/m_1^2 + \vec{S}_2/m_2^2|$ of the black holes, and gives an indication of the injections that significantly deviate from the non-spinning case modelled by the phenomenological waveforms. We observe how signals located at distances above 350Mpc are systematically lost, giving us an indication of the distance reach of the pipeline; nevertheless, several nearby injections are missed as well. In order to track down the missed injections in the mass region below $160 M_{\odot}$, a compilation of their relevant physical parameters and associated information is given in Table 13. A similar analysis of the missed and found injections has been recently performed by the

Here S is the modulus of the angular momentum \vec{S} (which in this particular BAM simulation is the same for both black holes).

Table 13: Overview of the 19 missed injections with total mass below $160 M_{\odot}$ for the best run reported. The ID column stores an index that identifies each of the injections of the NINJA set. The last column displays the modulus of the sum of the black holes individual spins. Among the missed signals we stress the presence of waveforms with eccentricity, large spins and precession and also those injected at distances further than 350 Mpc. Note that the IDs enclosed in asterisks correspond to signals also reported as missed in [50], where a Bayesian inference search on the NINJA data using a Nested Sampling algorithm is presented.

ID	NR Simulation	Tot. mass (M_{\odot})	Distance (Mpc)	Eff. dist. H / L (Mpc)	η	Tot. Spin $ \sum \vec{S}_i/m_i^2 $
136	LazEv	94.6	444.5	15831.9 / 2941.3	0.25	1.84
141	LazEv	75.6	355.8	1047.2 / 746.6	0.25	1.84
142	LazEv	129.7	442.5	2221.8 / 1537.7	0.25	1.84
59	CC	69.7	87.5	469.2 / 1573.0	0.25	0
41	BAM_HHB_S25	112.0	212.1	1150.8 / 802.2	0.25	0.5
47	BAM_HHB_S00	150.0	131.0	648.5 / 908.0	0.25	0
27	BAM_FAU	77.8	121.3	764.1 / 741.1	0.25	1.43
29	BAM_FAU	72.3	185.1	1325.7 / 885.4	0.25	1.43
30	BAM_FAU	73.9	351.1	896.9 / 771.4	0.25	1.43
114	PU_T52W	82.6	133.1	364.0 / 320.2	0.25	0
116	PU_T52W	88.2	164.2	654.7 / 533.7	0.25	0
118	PU_T52W	90.0	86.0	1055.4 / 452.3	0.25	0
120	PU_T52W	108.6	106.0	202.0 / 205.9	0.25	0
125	PU_T52W	96.8	258.8	463.8 / 464.7	0.25	0
126	PU_T52W	105.8	398.5	1175.2 / 1797.1	0.25	0
64	GSFC_X4	134.7	149.6	1320.4 / 856.0	0.16	0
68	GSFC_X3	160.0	220.8	819.3 / 1123.2	0.1875	0.222
76	GSFC_X4	158.0	145.4	722.2 / 558.5	0.16	0
95	Lean_c138	68.6	246.5	333.9 / 407.7	0.16	0
Total number of missed injections: 19						

Birmingham group in [50], applying Bayesian inference on the NINJA data using a Nested Sampling algorithm. The work of Aylott explores how different waveform families affect the confidence of detection of NR waveforms. Their Bayes factor B is a metric for assessing the level of confidence that a signal has been detected, and their defined thresholds for $\log_{10} B$ allow for classification of the signals as found or missed. The IDs displayed in bold type in our Table 13 correspond to signals that are reported as missed by the Birmingham group in Table 2 of [50]; 12 of our 19 missed injections are also lost by them, a correlation that seems worth following up. Future versions of the NINJA project will certainly benefit from combined searches and cross-checks of this kind between different DA methods.

Signals with large eccentricity, such as the Princeton $e \gtrsim 0.5$ PU_T52W run are invariably lost by our pipeline. Likewise, the phenomenological templates are not able to pick up signals with considerable spin, such as the equal-mass, spinning waveforms from LazEv with individual spins of equal

value $S/m^2 = 0.92$ aligned along the z -axis and BAM_FAU with precessing spins $S/m^2 = 0.75$ outside the xy -plane and misaligned with respect to the z -direction. Our template bank was developed to search for signals in which spin is unimportant and no precession is present, so these results are understandable. Further work targeted to incorporating spins within the phenomenological model is desirable and will be undertaken in the future. The missed GSFC signals with mass ratio 1 : 3 and 1 : 4 correspond to runs with few orbits before merger and moreover they are injected at total masses bordering on the edge of our template bank, which could explain them being lost. More bewildering is however the fact that the pipeline misses a couple of long equal-mass non-spinning simulations injected at rather close distances, such as SpEC, which is also missed by the search reported in [50], and BAM_HHB_spp00. A look at the columns of Table 13 that list the *effective distance* in H and L (the distance to an equivalent source with optimal location and orientation) indicates that it might be the poor orientation of these injections that prevents the pipeline from finding them. Aside from these individual cases, which would need a careful follow-up that is below the scope of this paper, we can justify the rest of missed injections as those either placed at large distances, presenting large spin values and/or precession and containing few orbits before merger.

Among the obvious improvements that a search with phenomenological templates could benefit from we can mention the following. Firstly, and once the technical issue with the generation of high-mass templates is resolved, the search would clearly improve with the use of a template bank that fully covers the parameter space of the signals searched for. Additionally, the inclusion of the fourth interferometer V1 in our pipeline shall provide a larger number of recovered triggers, in the manner reported by the search using EOBNR templates that is described in Section 4.1.3 of [49]. Both improvements will be most likely incorporated to searches with the phenomenological template bank in future realizations of the NINJA project.

7.2.4 Accuracy for Parameter Estimation

The number of found versus missed triggers is not the only relevant metric for assessing the performance of the standard GW searches. If astrophysically relevant statements are to be made from GW observations, the ability of accurately estimate the physical parameters of the measured signals is crucial. The inspiral pipeline returns estimated values for the individual and total masses of the detected system, effective distance, coalescence time and event duration, among others. Figure 41 shows two parameter estimation plots for the phenomenological search on the NINJA injections. The left panel displays the fractional difference for recovery of the chirp mass of the system. The vertical colour bar encodes the total mass in solar masses. We report substantial improvement in parameter estimation with respect to LIGO/Virgo standard searches that make use of PN templates, which we can see in Figure 8 of the NINJA paper [49]. While standard PN searches recover most of the injections with a fractional difference in chirp mass of 0.5 or above, the left panel of our Figure 41 shows an overall better accuracy, with the exception of one outlier. Using the phenomenological template bank, the chirp mass is recovered within a 20% accuracy for values of \mathcal{M} below $40 M_{\odot}$ and $\sim 40\%$ for signals with larger chirp mass. In any case, it should not be forgotten that the PN searches reported in [49] make use of banks with masses up to $90 M_{\odot}$.

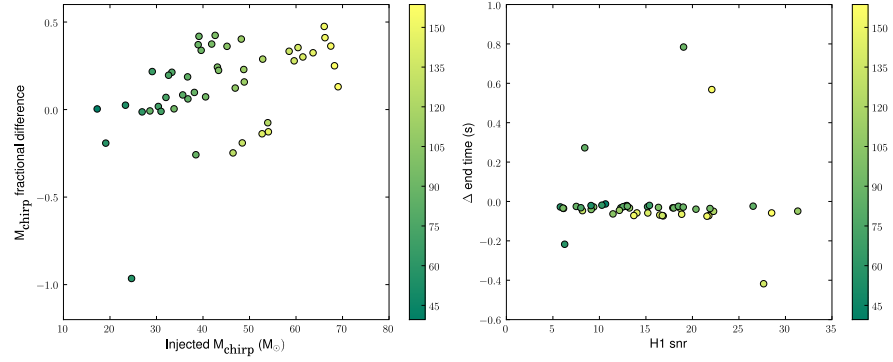


Figure 41: Accuracy in the recovery of chirp mass and end time (left and right panel respectively) of the reduced set of NINJA injections with total mass below $160 M_{\odot}$ using the phenomenological template bank. In both plots, the colour scale is given by the total mass of the system. The chirp mass, a common quantity in data analysis which is defined as $\mathcal{M} = (m_1 m_2)^{3/5} (M)^{-1/5}$, is typically recovered within a 20%–40% accuracy, depending on the chirp mass and total mass of the system. The results for parameter estimation with our IMR bank constitute a significant improvement over current LIGO/Virgo searches with standard PN templates.

only. The outlier that can be spotted at $\mathcal{M} \sim 30 M_{\odot}$ corresponds to a SpEC waveform injected at 132Mpc with total mass $56.6 M_{\odot}$. For this particular injection the accuracy in parameter recovery is rather poor, and further work to understand this behaviour will be undertaken in the future.

The panel in the right shows the accuracy in end time recovery of the found signals, with the colour code again displaying the total mass of the system. The injection time of the numerical waveforms corresponds to the maximum of their amplitude, which happens roughly at the merger of the two black holes. Current PN templates stop before that point while IMR templates extend beyond the merger into the ringdown. The sign convention for Δt_{end} corresponds to the injected minus the recovered parameters, so that a trigger that presents a positive value $\Delta t_{\text{end}} > 0$ indicates that the signal was really injected at a *later* time than the value recorded by our pipeline. Most of the signals displayed in the left panel of Figure 41 are recovered at a time within a few hundredths of second from the injected end time value, with the outliers corresponding partially to signals with larger total mass. These results are consistent with the other IMR search reported in the NINJA paper. Again we expect that the use of a template bank overlapping the mass region of the injections would lead to a reduction of the outliers, but certain improvement with respect to the left panel in Figure 8 of [49] can still be acknowledged.

Even though the number of total recovered triggers for the phenomenological search on the NINJA data is similar to the results quoted by the standard PN searches, there is a reasonable indication that the use of a full IMR template bank helps the estimation of the physical signal parameters. In view of these and other coincident results quoted in [49, 50, 115], we conclude that searches that attempt to recover and estimate the physical parameters of BBH signals in the mass range $10^2 - 10^3 M_{\odot}$ would profit from using an IMR template bank that fully models the inspiral, merger and ringdown of the binary system. This is of crucial important for future LIGO/Virgo searches

that aim at targeting coalescences of compact objects in the above-mentioned range, for which a full template bank adapted to arbitrarily high masses (and ideally also to non-zero spin values) needs to be developed. Attempts in this direction are already underway within the LIGO/Virgo collaboration.

7.3 LOOKING AHEAD: THE NINJA 2 PROJECT

The second NINJA project, aimed at testing the gravitational wave analysis pipelines' sensitivity to numerical waveforms will build upon the success of the first NINJA project while extending it to be a more systematic test, using real GW detector data and will proceed in a similar manner as for NINJA 1, by building a collaboration of all interested researchers to tackle this problem. Other NINJA projects, including one focused on matter, are envisioned to occur in parallel, although not using real data.

<https://www.ninja-project.org/doku.php?id=ninja2:home>

The ultimate goal of this sort of projects is to develop an optimal search and parameter estimation approach for the full BBH coalescence, including rapidly spinning black holes. NINJA 2, the second phase of the NINJA project, expected to start in summer 2010, is widely regarded as the key means by which these investigations will be conducted by the international community. The scope of NINJA 2 will be much broader than NINJA 1: longer and more numerous spinning and non-spinning signals —including the model developed by the author and introduced in chapter 5— will be injected in old LIGO data containing glitches and non-Gaussian features, which make the analyses more realistic.

The analysis of the NINJA 2 data will be a challenging task so far never explored by the current search pipelines: extension to spins and injection of full IMR waveforms. The presence of spins increases the dimensionality of the problem from 9 to 15. The study of how this enlarged parameter space impacts the searches poses a challenge, which will have to be undertaken by parts, first understanding the effect of including non-precessing spin templates and later addressing the general, misaligned spin case, as the corresponding NR simulations become available. Furthermore, accurate estimation of the physical parameters of the binary is crucial in order to maximize the science exploitation of the data. Extensive parameter estimation studies are needed in order to establish the reliability of our search pipelines for recovering the correct physical information of the binary systems.

The final goal is to identify and conceptually develop a full analysis approach for BBH detection and parameter estimation that can be ported into the LSC-Virgo analysis. The techniques and analyses needed to bring the full NINJA 2 project to completion fall outside the scope of this thesis, but some of the methods developed in this work will be of direct relevance for forecoming research in this direction.

Experimental evidence exists to support the existence of both solar-mass and supermassive black holes with masses ranging between $\sim 1.4 - 20 M_{\odot}$ and $\sim 10^5 - 9 M_{\odot}$ respectively. Gravitational-wave searches targeted to observing the former have been discussed in chapter 6. Detection of the latter should be enabled once the space antenna LISA flies. Quite to the contrary, the existence of intermediate-mass black holes (IMBHs) with masses of roughly $10^{2-4} M_{\odot}$ has not yet been corroborated observationally, despite the high interest that these objects have for astrophysics. Our understanding of formation and evolution of supermassive black holes, as well as galaxy evolution modeling and cosmography would dramatically change if an IMBH was observed. From a point of view of traditional photon-based astronomy, which relies on the monitoring of innermost stellar kinematics, the *direct* detection of an IMBH does not seem plausible until the next-generation telescopes start operating within the next decade. However, the prospect of detection and characterization of an IMBH has good chances in lower-frequency gravitational-wave astrophysics with ground-based detectors such as LIGO, Virgo and the future Einstein Telescope. The prospects for IMBH detection and characterization with ground-based gravitational-wave observatories would not only provide us with a robust test of general relativity, but would also corroborate the existence of these systems. Such detections should allow astrophysicists to probe the stellar environments of IMBHs and their formation processes.

This chapter discusses the mechanisms that might give rise to one or more IMBHs inside globular stellar clusters, and provides an estimation of the expected event rates for binaries of IMBHs that future gravitational-wave observatories might observe; the waveform model developed in chapter 5 is employed to estimate the sensitivity of the detector to these systems; finally, we explore the implications that a detection would have.

This chapter summarizes the work presented in [39]

8.1 FORMATION OF AN INTERMEDIATE-MASS BLACK HOLE

By following the stellar dynamics at the center of our Galaxy, we have now the most well-established evidence for the existence of a SMBH. The close examination of the Keplerian orbits of the S-stars has revealed the nature of the central dark object located at the Galactic Center. By following S2 (SO₂), the mass of SgrA* was estimated to be about $3.7 \times 10^6 M_{\odot}$ within a volume with radius no larger than 6.25 light-hours [234, 128]. More recent data based on 16 years of observations set the mass of the central SMBH to $\sim 4 \times 10^6 M_{\odot}$ [111, 129, 130, 131].

These also called SO-stars, where the letter “S” stands simply for source

Massive black holes in a lower range of masses may exist in smaller stellar systems such as globular clusters. These are called intermediate-mass black holes because their masses range between $M \sim 10^{2-4} M_{\odot}$, if we assume that they follow the observed correlations between SMBHs and their host stellar environments. Nevertheless, the existence of IMBHs has never been confirmed, though we have some evidences that could favor them.

See [184, 183] and references therein

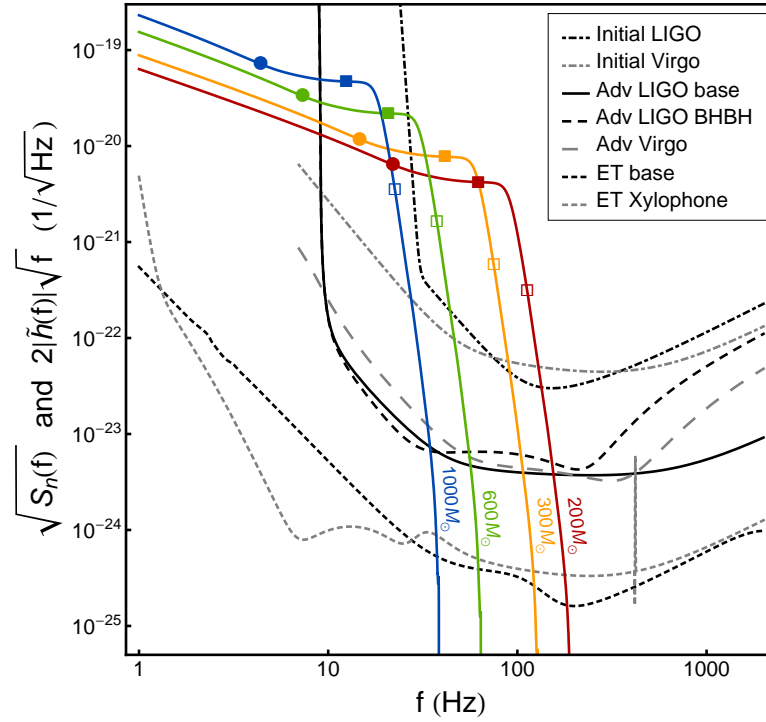


Figure 42: Amplitude of equal-mass, non-spinning BBH systems scaled to various total masses of the IMBH binary compared with the sensitivity curves of various detectors. The sources are optimally oriented and placed at 100 Mpc of the detectors. The symbols on top of the waveforms mark various stages of the BBH evolution: solid circles represent f_{ISCO} , squares the f_{LR} and open squares f_{LRD} (see section). The sensitivity curves of current and future ground-based detectors are shown as well.

If we wanted to apply the same detection technique to detect IMBHs in globular clusters as we do with SMBHs in galactic centers, ultra-precise astronomy would be required, since the sphere of influence of an IMBH is \sim few arc seconds. The number of stars enclosed in that volume is only a few. Currently, with adaptive optics, one can aspire to have a couple of measurements of velocities if the target is about \sim 5 kpc away in the time basis of 10 yrs. The measures depend on a number of factors, such as the required availability of a bright reference star, in order to have a good astrometric reference system. Also, the sensitivity limits correspond to a K-band magnitude of \sim 15 — B-MS stars at 8 kpc, like e.g. S2 in our Galactic Center.

This means that, in order to detect an IMBH or, at least, a massive dark object in a globular cluster center with traditional astronomy, one has to resort to the Very Large Telescope interferometer and to one of the next-generation instruments, the VSI or GRAVITY [132, 112]. In this case we can hope to improve the astrometric accuracy by a factor of \sim 10. Only in that scenario we would be in the position of following closely the kinematics around a potential IMBH, so as to determine its mass.

Incidentally, gravitational-wave astronomy could contribute to IMBH detection. Current and future ground-based interferometers are sensitive to the frequencies associated to the late inspiral, merger and ringdown of coalescing binaries of IMBHs. Figure 42 illustrates this fact. Systems with total mass

This is, by following the stellar dynamics around it

above $600 M_{\odot}$ fall almost completely below the 40 Hz “seismic wall” of the initial LIGO detectors; however they will become very interesting sources for the second generation of GW interferometers and the proposed Einstein Telescope. Indeed, they will also be seen by the future space-borne LISA.

Next section 8.2 expands the astrophysical context to this problem and gives a description of the different efforts made to address the evolution of a black-hole binary in a stellar cluster, from its birth, to the final coalescence. In section 8.3 we compute the reach of the detectors for systems of IMBH binaries, which is needed for the calculation of the expected event rates presented in section 8.4.

8.2 LIFE OF A MASSIVE BINARY

The aim of this section is not to give a detailed explanation of the processes of formation of IMBHs and binaries of IMBHs (BBHs), but a description of the global picture so as to introduce the two different scenarios that play a role in the formation of BBHs.

8.2.1 Birth

Up to now, the IMBH formation process which has drawn more attention is that of a young cluster in which the most massive stars sink down to the center due to mass segregation. There, a high-density stellar region builds and stars start to physically collide. One of them gains more and more mass and forms a runaway star whose mass is much larger than that of any other star in the system. Later, that runaway star may collapse and form an IMBH [210, 123, 209, 121].

In particular, Freitag *et al.* [122, 121] described the requirements from the point of view of the host cluster to form an IMBH in the center of the system. By starting with a cluster of main-sequence stars with a determined initial-mass function, the authors find that, after the cluster reaches core-collapse due to mass segregation in the system, if there are not *too hard* binaries, the time to reach core collapse is shorter than 3 Myrs and the environmental velocity dispersion is not much larger than $\sim 500 \text{ km s}^{-1}$, the runaway formation of a very massive star (VMS) is possible. Not yet well understood are the later evolution of the VMS and the conditions to impose upon it, so that it does not evolve into a super-massive star (SMS) in this particular scenario. Also not completely clear are the factors that could limit the mass of such an object so that it could collapse and turn into an IMBH. The process depends on a number of factors and assumptions, such as e.g. the role of metallicity, stellar winds and the collisions on to the runaway star from a certain mass upwards. On the other hand, Suzuki *et al.* [248] investigated the process of growing up of a runaway particle by coupling direct N–body simulations with smooth particle hydrodynamics (SPH) to analyze the evolution of the star and found that stellar winds would not inhibit the formation of a very massive star. More recently, the effects of the stellar evolution on the runaway collision product have been considered by analyzing the succession of collisions from a dynamical evolution [133]. It is found that for low-metallicity models, the final remnant of the merger tree is expected to explode as a supernova, and in their high-metallicity models the possibility of forming an IMBH is negligible and end up with a mass of 10–14 M_{\odot} at the onset of carbon burning. Nevertheless,

A very massive star (VMS) is a star of mass larger than $\gg 100 M_{\odot}$

See for instance [37, 38, 33] and references therein

See e.g. [56], though it is rather unclear how to extrapolate their results (which are limited to stars with masses of maximum $150 M_{\odot}$) to the masses found in the runaway scenario, which are typically at least one order of magnitude larger

these develop an extended envelope, so that the probability of further collisions is higher. The authors did not change the masses accordingly in the dynamical simulation. In any case, self-consistent direct-summation N-body simulations with evolution of the runaway process are called in to investigate the final outcome. Hence, assuming that they form, we can theoretically explain the formation of a binary of two IMBHs (BBH) in a cluster in two different ways.

(i) *The double-cluster channel:*

In this scenario, two clusters born in a cluster of clusters, such as those found in the Antennæ galaxy, are gravitationally bound and doomed to collide. When this happens, the IMBHs sink down to the center of the resulting merged stellar system due to dynamical friction. They form a BBH whose semi-major axis continues to shrink due to slingshot ejections of stars coming from the stellar system. In each of the processes, a star removes a small fraction of the energy and angular momentum of the BBH, which becomes harder. At later stages in the evolution of the BBH, GW radiation takes over efficiently and starts to circularize, though one can expect these systems to have a residual eccentricity when entering the LISA band [35]. This detector will typically be able to see systems of binaries of IMBHs out to a few Gpc. For this channel and volume, the authors estimated an event rate of $4 - 5 \text{ yr}^{-1}$.

(ii) *The single-cluster channel:*

Gürkan *et al.* [138] added a fraction of primordial binaries to the initial configuration in the scenario of formation of a runaway star in a stellar cluster. In their simulations they find that not one, but two very massive stars form in rich clusters with a binary fraction of 10%. Fregeau *et al.* [120] investigated the possibility of emission of GWs by such a BBH and estimated that LISA and Advanced LIGO can detect tens of them depending on the distribution of cluster masses and their densities. More recently, Gair *et al.* [124] addressed the event rate that the proposed Einstein Telescope could see and quoted a few to a few thousand events of comparable-mass IMBH mergers of the single-cluster channel.

See [35] for a detailed explanation of the process

8.2.2 *Growing Up (Shrinking Down): The role of triaxiality on Centrophilic Orbits*

In the case of the double-cluster channel, the cluster, which is in rotation, results from the merger of the two initial clusters and may develop a triaxiality sufficient to produce enough centrophilic orbits. These *boxy* orbits are typical of systems that do not possess a symmetry around any of their axes [57]. On the contrary to loop orbits, a characteristic of spherically symmetric or axisymmetric systems, boxy orbits bring stars arbitrarily close to the center of the system, since it oscillates independently along the three different axes. Therefore, such stars, due to the fact of being potential sling-shots, can feed the process of shrinkage of the BBH semi-major axes by removing energy and angular momentum out of it after a strong interaction. In the strong triaxial systems of [57], the rotation caused in the process of merger creates an unstable structure in the form of a bar. Within the bar the angular momentum will not be conserved and thus the BBH loss-cone is full due to the stars on centrophilic orbits, independently of the number of stars N_* . In the models of [35], the initial conditions are a realistic parabolic merger of two stellar clusters. The resulting merged cluster does not show the strong axisymmetry of [57]. In the simulations we address for the results of this work, the BBH of

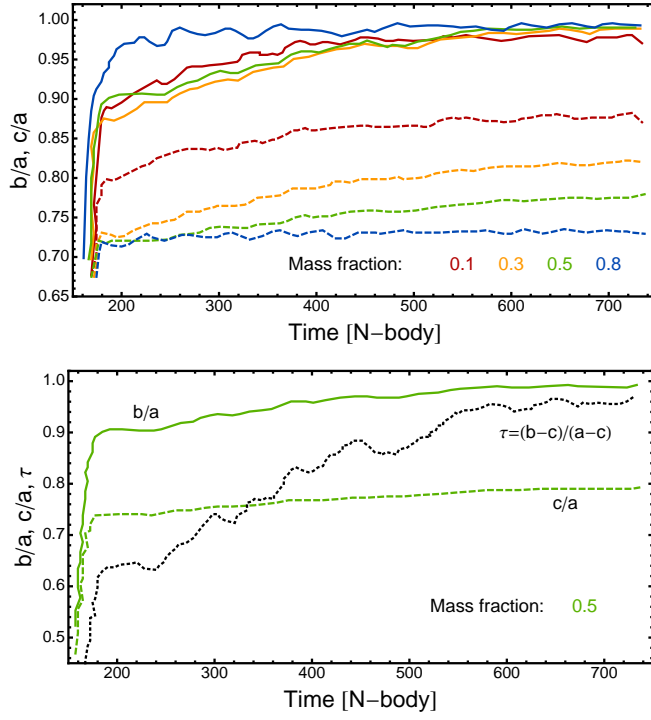


Figure 43: Triaxiality of the resulting merged cluster for different mass fractions (upper panel) and the mass fraction 0.5. We calculate the semi-major axes of the ellipsoid of inertia a , b and c (where $a > b > c$) according to four different mass fractions which, in turn, are distributed on the basis of the amount of gravitational energy. The shorter the distance to the center of the resulting cluster, the lower the mass fraction. Displayed are b/a (solid lines) and c/a (dashed lines). The lower panel shows the shape indicators for the mass fraction 0.5, together with the evolution of the parameter τ , an indicator for the triaxiality of the system, which tends to one as time elapses; i.e. the system tends to be oblate. The evolution of τ is similar for the rest of mass fractions

IMBHs is not stalling, in spite of the reduced number of centrophilic orbits due to the architecture of the stellar system.

In Figure 43 we show the role of the cluster symmetry explicitly by depicting the evolution of the triaxiality of the cluster formed as a result of the merger of the two clusters for our fiducial model in the case of the double-cluster channel. After a merger which is the result of a parabolic orbit, the final system is oblate rather than prolate; i.e. $a \sim b > c$, where a , b and c are the cluster axes. At the outskirts the resulting merged cluster is flatter and at the center the binary of IMBHs makes it rather spherical. Amaro-Seoane *et al.* [36] addressed the single-cluster channel scenario after the formation of the IMBHs and used additional simulations to further evolve the BBH. They used scattering experiments of three bodies including relativistic precession to 1st post-Newtonian order, as well as radiation reaction caused by GW, so that they did not have to integrate every single star in the cluster to understand the posterior evolution of the BBH. In their work, between the strong encounters, a and e of the BBH were evolved by resorting to the quadrupole formulæ of [203].

This is the reference model of [35]

The BBH will have completely circularized when it reaches the frequencies probed by Advanced LIGO and the ET, because the emission of GWs takes over the dynamics of the system.

8.2.3 *Death*

While the emission of GWs is present all the time from the very first moment in which the BBH is formed, the amplitude and frequency of the waves is initially so low that no present or planned detector would be able to register any information from the system. Only when the semi-major axis shrinks sufficiently, the frequency increases enough so as to *enter* the LISA band, which we assume starts at 10^{-4} Hz. The BBH then crosses the entire detector window during its inspiral phase, as we can see in Figure 44. We depict the evolution of a BBH of mass $439.2 + 439.2 M_{\odot}$. The reason for this particular choice of masses is to give the reader a point of reference to understand the whole picture. Recently, Amaro-Seoane *et al.* [34] included the effect of rotation of the host cluster and addressed the dynamical evolution of the global system. The authors have shown that LISA will see the system of Figure 44 with a median SNR of few tens. The fact that the system merges outside its band prevents LISA from observing the loudest part of the BBH coalescence. In order to follow the system at this early stage of its evolution in the LISA band, a simple post-Newtonian approach suffices for modeling the GW radiation. We are far enough from the highly relativistic regime and only the inspiral phase of the BBH coalescence is visible to the space antenna.

As the binary system depicted in Figure 44 leaves the LISA band and enters the strong field regime, higher order post-Newtonian corrections and eventually input from numerical relativity simulations need to be considered in order to model the GW waveform. Three reference frequencies in the evolution of a compact BBH that approaches its merger are the innermost stable circular orbit (f_{ISCO}) defined in equation 2.7 of a test particle orbiting a Schwarzschild black hole, the light-ring frequency (f_{LR}) corresponding to the smallest unstable orbit of a photon orbiting a Kerr black hole and the fundamental ringdown frequency (f_{FRD}) of the decay of the quasi-normal modes computed by [59].

For the binary system shown in Figure 44, the values of these three frequencies are $f_{\text{ISCO}}|_{878.4M_{\odot}} \simeq 5$ Hz, $f_{\text{LR}}|_{878.4M_{\odot}} \simeq 14.2$ Hz and $f_{\text{FRD}}|_{878.4M_{\odot}} \simeq 21.4$ Hz. Should such a binary exist at a distance of 100 Mpc, and if it was to be detected with Advanced LIGO, it would produce a sky-averaged SNR of ~ 450 , assuming a low frequency cut-off of 10 Hz. To that total SNR, the contribution of parts of the inspiral happening before the system reaches the characteristic frequencies f_{ISCO} , f_{LR} and f_{FRD} would be 0%, 37% and 95% respectively. It is immediately noticed that, for the binaries of IMBHs of interest in this study, most of the SNR that these binaries will produce in Advanced LIGO comes from the last stages of the the BBH coalescence.

We can estimate the time that the binary system takes to evolve from $f = 0.01$ Hz, a frequency where the BBH can be seen by LISA, to the lower cut-off frequency of 10 Hz of Advanced LIGO or of 1 Hz of the ET. A lower order approximation based on the Newtonian quadrupole formula [203] leads

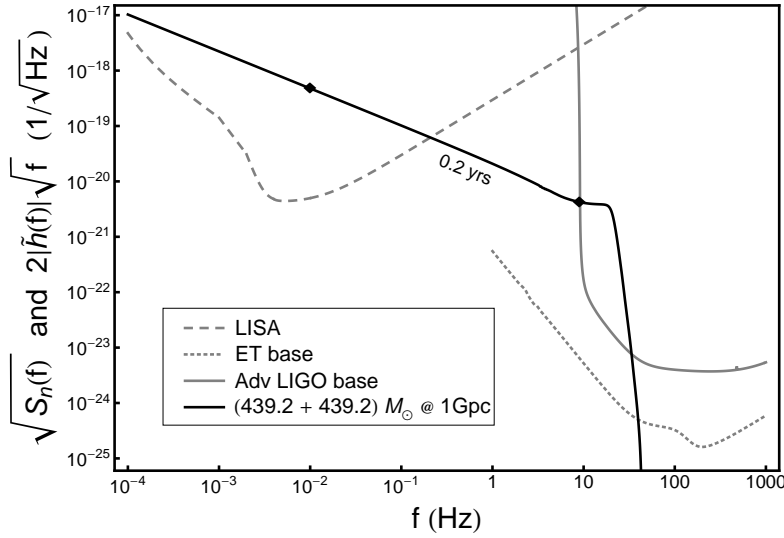


Figure 44: Amplitude of the GW emitted by a system of two equal-mass IMBHs of total mass $878.4 M_{\odot}$ placed at 100 Mpc as seen by different GW observatories. Note that we have multiplied $|\tilde{h}(f)|$ by a factor $2\sqrt{f}$, with f the frequency of the system. From left to right we depict the sensitivity windows of the future space-borne LISA (dashed, grey curve), the Einstein Telescope (dotted, grey curve) and Advanced LIGO (solid, grey line starting sharply at 10 Hz). The strain of the BBH of IMBHs spends most of its inspiral in the LISA band, whilst the ringdown and merger occur at higher frequencies, only observable by ground-based detectors. Notably, the ET captures an important extent of the inspiral as well as the whole ringdown and merger. The averaged SNR produced by this system would be $\text{SNR}_{\text{LISA}} = 854$, $\text{SNR}_{\text{ET}} = 7044$ and $\text{SNR}_{\text{AdvLIGO}} = 450$. The BBH system spends approximately 0.2 yrs to go from $f = 0.01$ Hz (well into the LISA band) up to the lower cut-off frequency of Advanced LIGO, 10 Hz. These two points are pinpointed on the plot

to the following expression for the evolution of the frequency in terms of the chirp mass \mathcal{M} and frequency of the system

$$\frac{df}{dt} = \frac{96}{5} \pi^{8/3} \mathcal{M}^{5/3} f^{11/3}. \quad (8.1)$$

We find a delay of only 0.2 yrs (80 days) for a BBH with total mass $M = 878.4 M_{\odot}$ to go from 0.01 Hz to the beginning of the ET band —taken to be at 1 Hz— and almost similar numbers to the beginning of the Advanced LIGO band —at 10 Hz.

In view of these figures, LISA could be used as an *alarm* to prepare ground-based detectors to register in detail the final coalescence, the death of the BBH as such, by adjusting their “sweet spots” to the particular BBH. The high accuracy of which LISA is capable for parameter estimation during the inspiral phase could be combined with the information obtained from the large-SNR triggers that the BBH merger and ringdown will produce in Advanced LIGO or ET to achieve a more complete characterization of the system.

The evolution of the system is extraordinarily quick in the late inspiral phase, which explains the fast evolution from 1 to 10 Hz

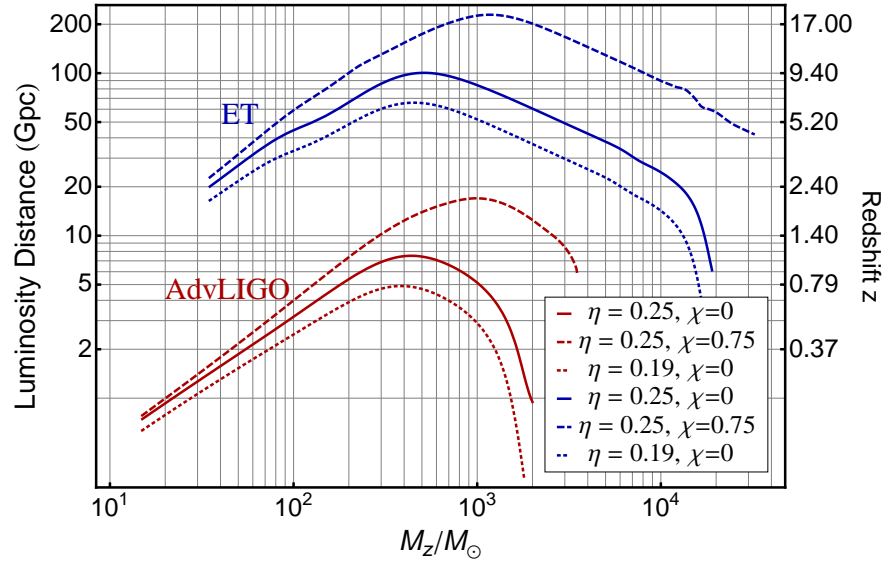


Figure 45: Sky-averaged horizon distance versus redshifted mass for three binary configurations obtained with the design sensitivity curves of Advanced LIGO and the Einstein Telescope. The dashed line corresponds to the hang-up configuration with $\chi_{1,2} = 0.75$.

8.3 HORIZON DISTANCE AND SIGNAL-TO-NOISE RATIO

A commonly-used quantity to estimate the reach of a detector is the horizon distance. It is defined as the distance at which a detector measures an $\text{SNR} = 8$ for an optimally-oriented and optimally-located binary, i.e. an overhead, face-on orbit. Non-optimally located and oriented sources are detected with $\text{SNR} = 8$ at closer distances. At the large distances that Advanced LIGO and the ET are expected to survey, the calculation of the horizon distance needs to take into account the redshift and, thus, a cosmological model needs to be assumed. For the results shown here, we adopt the standard ΛCDM universe with parameters given by the first five years of the WMAP sky survey [154]. These are $\Omega_\Lambda = 0.73$, $\Omega_b = 0.046$, $\Omega_c = 0.23$, $H_0 = 70.5 \text{ km s}^{-1} \text{ Mpc}^{-1}$ and $t_0 = 13.72 \text{ Gyr}$.

Using the full inspiral-merger-ringdown waveforms described in chapter 5 and the corresponding redshift function $z(d)$ for the ΛCDM model, we compute the sky-averaged horizon distance for non-spinning systems with symmetric mass ratio $\eta = 0.25, 0.1875$ and for an equal-mass system with spins $\chi_{1,2} = 0.75$ aligned in the direction of the angular momentum. The results can be seen in figure. 45 for the Advanced LIGO and the ET. We plot the horizon distance for IMBH binaries in Gpc and z versus the redshifted — observed— total mass $M_z \equiv M(1+z)$. Firstly, we observe how the detectors’ reach depends on the spins of the binary. “Loud” configurations, such as the hang-up case, can increase the observed distance by a factor of $\sim 2\text{--}3$. In the mass range of interest regarding IMBH binaries, i.e. total mass between 200 and $2 \times 10^4 M_\odot$, we can see that Advanced LIGO will be able to survey cosmological distances up to $z \approx 2$. The Einstein Telescope will be able to probe much larger distances, possibly up to $z > 10$. This opens the possibility of studying seed black hole formation that will provide information about the formation of structure in the early Universe.

Averaging for the whole sky corresponds to dividing the optimal value by 2.26

This is the “hang-up” configuration

This result is confirmed in [220], although they do not consider the variation of M with z

See Gair et al. [125]

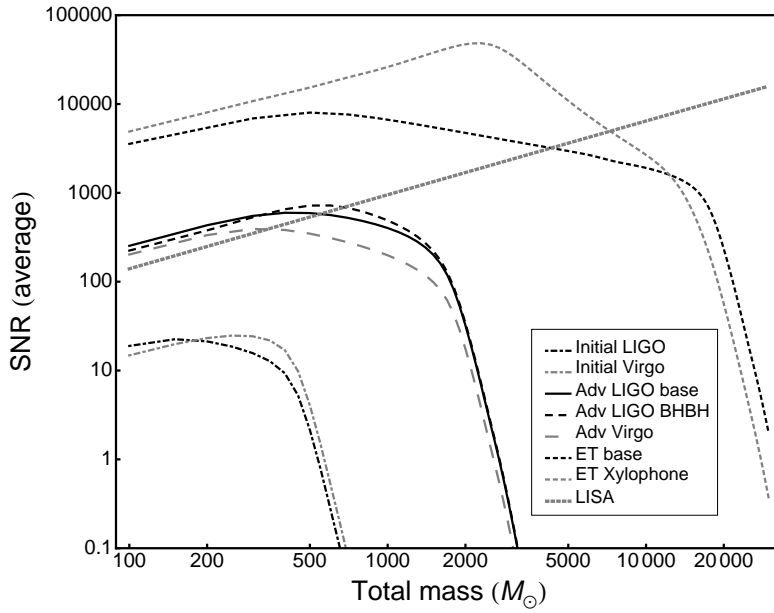


Figure 46: Signal-to-noise ratio as a function of the total mass of the BBH for the present and future generations of GW detectors and LISA. The sources are placed at a distance of 100 Mpc and the SNRs are angle-averaged

In Figure 46 we show the angle-averaged SNR expected for these sources in current and future gravitational-wave detectors as a function of the total mass of the system. The sources are placed at a distance of 100 Mpc simply because this is an easily scalable number. The redshift $z = 0.023$ in this case can therefore be neglected. For more distant sources however, the total mass $M_z = (1 + z) M$ would need to be considered, as we do in figure 45.

Unsurprisingly, the SNRs calculated for the third generation of ground-based detectors beat the expectations for initial and Advanced Virgo and LIGO at all masses. SNRs of the order of 10 are expected for current LIGO and Virgo interferometers for binaries with total mass up to a few hundreds of solar masses at 100 Mpc. The first-generation detectors are most sensitive to neutron star binaries and stellar-mass black holes, hence they miss most of the inspiral part of an IMBH binary coalescence and can only see a fraction of its merger and ringdown phases. Advanced LIGO and Virgo will be able to measure averaged SNRs of the order of 10^{2-3} at 100 Mpc, with a maximal response to BBH systems with total mass in the range of 400 to 1000 M_\odot . For the Einstein Telescope the SNR values are expected to lie within the 10^{3-5} range, and it is expected to be sensitive to binaries with total masses of the order of $10^4 M_\odot$, a significantly larger range than that surveyed by Advanced LIGO and Virgo. It is noticeable how the ET xylophone configuration increases the detectability of binaries with masses above 600 M_\odot with respect to the broadband ET configuration. This is due to its improved sensitivity precisely at frequencies in the range of 1 – 30 Hz, which is where systems of mass above hundreds of solar masses accumulate most of their SNR. As for LISA, IMBH binaries with masses of hundreds of solar masses will be seen by the space antenna with a moderate SNR — it is only at masses above tens of thousands of solar masses that LISA will start taking over the ground-based observatories, as can be seen in Figure 46. Although the space antenna will

The xylophone configuration is described in [151]

See Figure 42

Some studies also include mild eccentricities, see [34]

be most sensitive to BBH binaries with masses in the range of $10^{6-7} M_{\odot}$, the possibility that it can act as a complementary observatory to the Einstein Telescope for IMBH binaries is a very promising one. Parameter accuracy studies for IMBHs in LISA are already available using the inspiral part of the coalescence. There are indications that masses and sky positions will be recovered with a high accuracy level. In order to complete the characterization of IMBHs with the information given by the second and third generations of ground-based detectors, a comprehensive study of parameter recovery that takes the BBH coalescence into account is very much desirable.

8.4 EVENT RATES

These are typically stellar black holes merging with IMBHs

Miller [182] estimated for the first time the event rate for *intermediate-mass* mergers of IMBHs in clusters by calculating the luminosity distance for the inspiral, merger and ringdown [118] out to which these three stages can be detected with a SNR ratio larger than 10. With no cosmological corrections, the maximum distance for the detector was found to be 3 Gpc ($z \sim 0.53$). The event rate was calculated as

$$R = \int \frac{4\pi}{3} D(M)^3 \nu(M) n_{\text{ng}} f(M) dM \quad (8.2)$$

In this equation n_{ng} is the number density of globular clusters, which was taken to be $n_{\text{ng}} \sim 8h^3/\text{Mpc}^3$, as in the work of [210]. The rate of coalescence of stellar-mass compact objects with the IMBH is $\nu(M)$ and $f(M) = dN/dM$ is the mass distribution of massive enough black holes in clusters. Obviously, $\int f(M) dM = f_{\text{tot}} < 1$. Therefore, everything boils down to the calculation of the maximum distance to which the detector, in this specific case LISA, can observe these sources; i.e. the observable volume of the detector. The estimation of [118] is used in [182] to find that a few per year should be detectable during the last phase of their inspiral. Two years later, Will [264] revisited the problem using matched filtering for the parameter estimation, an updated curve for the sensitivity of the detector and restricted post-Newtonian waveforms to calculate an analytical expression for the luminosity distance D_L . He finds that the detection rate for binaries in a mass range of $10 M_{\odot} - 100 M_{\odot}$ is of about 1 per Myr.

A more detailed and updated analysis is given by Fregeau *et al.* [120]. They calculated the number of events that LISA and Advanced LIGO could see from the single-cluster channel. In their estimation, they assume that the very massive stars formed in the runaway scenario do not merge into one, but evolve separately; each of them eventually form an individual IMBH, following the numerical results of the Monte Carlo experiments of [138]. They find a generalized form for the event rate observed at $z = 0$

This is equation 2 in [120]

$$R = \frac{dN_{\text{event}}}{dt_0} = \int_0^{z_{\text{max}}} \frac{d^2 M_{\text{SF}}}{dV_c dt_e} g_{\text{cl}} g \frac{dt_e}{dt_0} \frac{dV_c}{dz} \times \int_{M_{\text{cl, min}}}^{M_{\text{cl, max}}} \frac{dN_{\text{cl}}^2}{dM_{\text{SF, cl}} dM_{\text{cl}}} dM_{\text{cl}} dz. \quad (8.3)$$

In this expression, $d^2 M_{\text{SF}}/dV_c dt_e$ is the star formation rate (SFR) per unit of comoving volume per unit of local time; g_{cl} is the fraction of mass that goes into the massive clusters of interest; g is the fraction of massive clusters

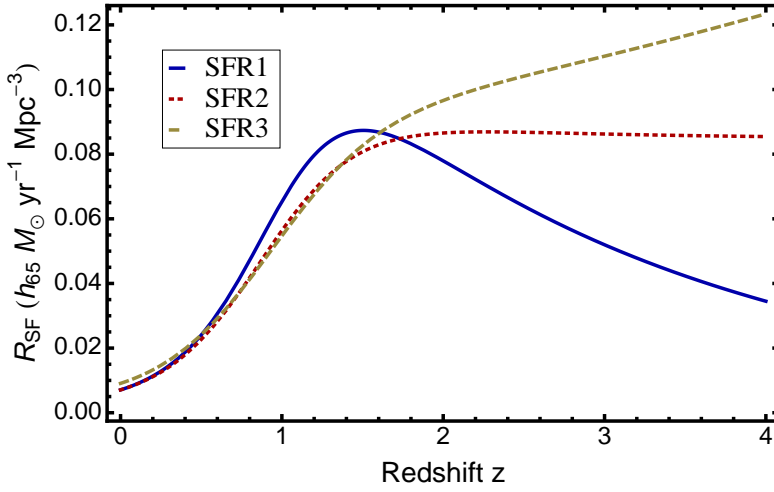


Figure 47: Three parameterizations of the stellar formation rate per unit comoving volume compared in the calculation of the event rates. We assume a Λ -dominated cosmology with $H_0 = 70.5 \text{ km s}^{-1} \text{ Mpc}^{-1} = 65 h_{65}$, $\Omega_\Lambda = 0.73$ and $\Omega = 0.27$. The three stellar formation rate functions increase with the redshift until $\sim z = 2$; for larger distances they exhibit different behaviours: SFR1 decreases, SFR2 keeps approximately constant and SFR3 increase. Nevertheless, the rates integrand is not too strongly dependent on the particular functional form for redshifts $z > 2$.

which form IMBHs; $dt_e/dt_0 = (1+z)^{-1}$ is the relation between local and observed time; dV_c/dz is the change of comoving volume with redshift; and $dN_{\text{cl}}^2/dM_{\text{SF,cl}}dM_{\text{cl}}$ is the distribution function of clusters over individual cluster mass M_{cl} and total star-forming mass in clusters $M_{\text{SF,cl}}$.

We calculate the event rate using the values for $D_L(M_z)$ that we obtained in section 8.3 for Advanced LIGO and the ET, which are based on the waveform model of chapter 5 and depend on the mass ratio and spins of the binary. We consider three different cases, corresponding to the three different configurations shown in figure 45. In addition, we compare three different parameterizations of the stellar formation rate per unit comoving volume, $R_{\text{SF},1,2,3}(z)$ as given by equations 4, 5 and 6 of [208]. The three models are depicted in figure 47; they are similar for close distances until $\sim z = 2$, differing from there on. For the distribution of cluster masses, the factor can be expressed as

$$\frac{dN_{\text{cl}}^2}{dM_{\text{SF,cl}}dM_{\text{cl}}} = \frac{f(M_{\text{cl}})}{\int M_{\text{cl}} f(M_{\text{cl}}) dM_{\text{cl}}}. \quad (8.4)$$

We take $dN_{\text{cl}}/dM_{\text{cl}} \propto 1/M_{\text{cl}}^2$, following the power-law form observed for young star clusters in the Antenna. The validity of assuming the same law for the larger volume of the Universe surveyed by Advanced LIGO or the ET is, however, a generalization not based on direct observations. Unfortunately, a more precise distribution function based on measured data is at present not known. Thus, we should take this premise with care. By assuming an efficiency factor of $f_{\text{GC}} \sim 2 \times 10^{-3}$, based in the results of [138], we can set the values for the limits based on the masses of the IMBHs and the observable volume

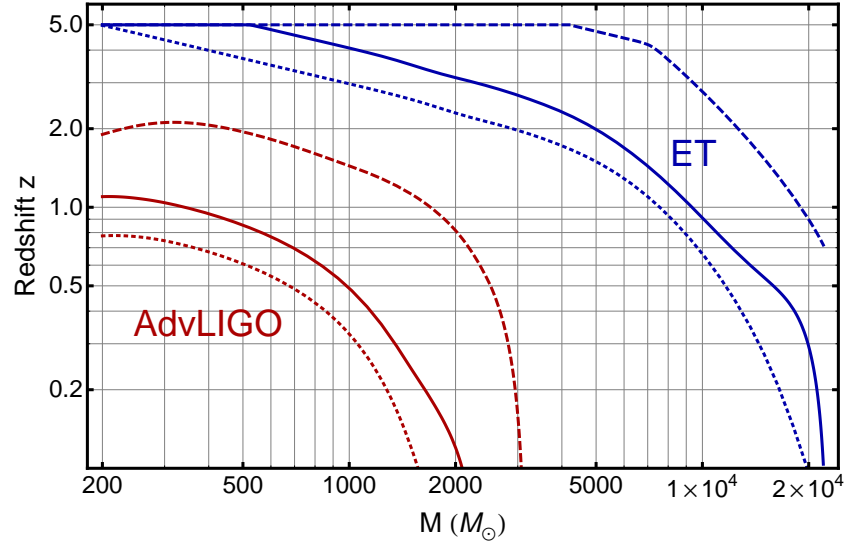


Figure 48: Sky-averaged reach of the Advanced LIGO and the ET detectors up to $z = 5$ versus intrinsic total mass of the IMBH binary. Red lines are for Advanced LIGO and blue are for the ET. The solid, dotted, dashed curves represent the same physical configurations displayed in figure 45.

—i.e. the maximum redshift z_{\max} — of the detector of interest. The integral can now be expressed as

$$R = \frac{f_{\text{GC}} g_{\text{cl}}}{\ln(M_{\text{cl}, \max}) / \ln(M_{\text{cl}, \min})} \int_{M_{\text{IMBHB}, \min}}^{M_{\text{IMBHB}, \max}} \frac{dM_{\text{IMBHB}}}{M_{\text{IMBHB}}^2} \times \int_0^{z_{\max}} \text{SFR}_i(z) F(z) \frac{1}{(1+z)} \frac{dV_c}{dz} dz, \quad (8.5)$$

where $M_{\text{IMBHB}, \max}$ (\min) is the range of total mass of the IMBH binary that we are considering, $\text{SFR}_i(z)$, $i = 1, 2, 3$ is any of the three considered stellar formation rates of [208] displayed in figure 47 and

$$F(z) = \frac{\sqrt{\Omega_M(1+z)^3 + \Omega_k(1+z)^2 + \Omega_\Lambda}}{(1+z)^{3/2}} \quad (8.6)$$

is the factor that relates the stellar formation rate function in different cosmologies with respect to the Einstein-de Sitter Universe. The maximum value z_{\max} in the integral on z is a function of the mass of the IMBH system, its configuration —mass ratio, spin— and the particular waveform model used in the calculation of the horizon distance. The results employing the waveform model of chapter 5 can be seen in figure 45.

The maximum values for $D_L(M_z)$ obtained with the ET range between $z \sim 5.5$ and $z \sim 17$. This implies that the ET will be able to probe the different proposed scenarios to produce the first generation of black hole seeds, as pointed out by [237]. We note that the values for z that we obtain are significantly larger than assumed in [237]. However, at these very large cosmological distances the stellar formation rate is unknown. We therefore set a maximum cut-off value of $z_{\max} = 5$ in the computation of the integral when $D_L(M_z)$ exceeds this value. The value of $z_{\max}(M_{\text{IMBH}})$ that we have used in the computation of the rates integral is shown in figure 48 for our three particular physical configurations.

Following the definition of IMBH, we take M_{IMBHB} from 200 to $2 \times 10^4 M_\odot$

Table 14: Event rates formed in the single-cluster channel for IMBH binaries potentially observable by Advanced LIGO and the ET per year. We take $g = 0.1$, $g_{\text{cl}} = 0.1$ as standard values.

Detector	Configuration	$R \left[\left(\frac{g}{0.1} \right) \left(\frac{g_{\text{cl}}}{0.1} \right) \text{yr}^{-1} \right]$
Advanced LIGO	$\eta = 0.25, \chi = 0$	48
	$\eta = 0.25, \chi = 0.75$	283
	$\eta = 0.19, \chi = 0$	16
Einstein Telescope	$\eta = 0.25, \chi = 0$	868
	$\eta = 0.25, \chi = 0.75$	940
	$\eta = 0.19, \chi = 0$	741

We have evaluated the integral 8.5 for the three stellar formation rates of figure 47 and the three configurations of figure 45 for Advanced LIGO and the ET. In agreement with [120], we find that the event rate does not depend strongly on the assumed stellar formation rate; the differences are negligible for Advanced LIGO and of a $\sim 15\%$ for the ET. We therefore quote the results found for $\text{SFR}_2(z)$ only.

The event rates do, however, depend on the spins and mass ratio of the binary. As expected, “loud” configurations like the hang-up case increase the event rate by a factor of ~ 6 in the case of Advanced LIGO. Smaller mass ratios decrease the rate, the difference between $\eta = 0.25$ and $\eta = 0.1875$ being of a factor of 3. The differences are not so extreme in the case of the ET, due to the fact that we are cutting off z_{max} at a value of 5 and, thus, neglecting contributions at higher redshift; we lack observational data to make statements about the stellar formation rate at larger values of z . Assuming that IMBH binary systems exhibit comparable masses, as it was found in [138], and random spin values, we can estimate the single-channel event rate roughly as $\sim 100 \text{ yr}^{-1}$ for Advanced LIGO and $\sim 850 \text{ yr}^{-1}$ for the ET. The exact computation of the rates would imply further integration on the mass ratios and spins of the binary system. At present it is not clear what those distribution might be, therefore we simply summarize our results for all configurations under consideration in table 14. These rates assume formation of IMBH binaries in the single-cluster channel.

So far, we have concentrated on the single-cluster channel scenario. Amaro-Seoane *et al.* [35] gave a prescription to calculate an estimate of the event rates for the double-cluster channel by resorting to the detailed calculation of [120]. This was based in the fact that the only difference between both astrophysical scenarios in terms of the event calculation involves (i) the fact that in the double-cluster channel one has one single IMBH in one cluster and (ii) these two clusters have to collide so that the IMBHs form a BBH when they sink to the center due to dynamical friction.

As explained in section 4 of [35], the connection between the event rate estimation of the two channels is

$$\Gamma^{\text{doub}} = P_{\text{merg}} g \Gamma^{\text{sing}}, \quad (8.7)$$

This is the function that keeps constant after $z = 2$

where Γ^{doub} is the event rate of the double-cluster channel, Γ^{sing} of the single-channel and P_{merg} is the probability for two clusters to collide in the scenario of [35]. They find $P_{\text{merg}} \in [0.1, 1]$.

The two different works assumed that the probability that a cluster gets into the runaway phase is g . Fregeau *et al.* [120] took this value as a parameter because of the large uncertainties and set it to 0.1 as an example. Nevertheless, as proven in the simulations of [122], it could be *as large as* 0.5. We therefore can define the (absolute) *optimistic* upper limit and *pessimistic* lower limit of the event rates for Advanced LIGO and the ET by assigning all parameters their maximum and minimum values and summing the contributions of the two channels:

$$\Gamma_{\text{Adv. LIGO}}^{\text{total}} \in [(0) 1.1 \times 10^2, 3 \times 10^3] \text{ yr}^{-1} \quad (8.8)$$

$$\Gamma_{\text{ET}}^{\text{total}} \in [(0) 9.35 \times 10^2, 2.55 \times 10^4] \text{ yr}^{-1} \quad (8.9)$$

Even though the optimistic upper limit is to be taken carefully, these event rates are obviously more than encouraging to address the problem of detection and characterization of systems of IMBH binaries with of GWs. On the other hand, one should bear in mind that the existence of IMBHs altogether has not yet been corroborated, so that the pessimistic estimate is still somewhat optimistic. This is why we have added a (0) in the previous rates as the absolute lower limit.

8.5 SUMMARY AND CONCLUSIONS

The existence of IMBHs is a subject of particular interest in theoretical astrophysics. Even though we do not have any evidence of these objects so far, a number of theoretical works have addressed their formation in dense stellar clusters. If we were to follow the same techniques that have led us to discover the SMBH in our Galaxy, we would need the Very Large Telescope interferometer and next-generation instruments, such as the VSI or GRAVITY, which should be operative in the next ~ 10 yrs. An alternative, or even complementary way of discovering IMBHs is via their emission of GWs when they are in a BBH system.

The identification and characterization of these systems relies on accurate waveform modeling of their GW emission, which has been made possible due to the success of numerical relativity in simulating the last orbits of the BBH coalescence and the coupling of these results to analytical post-Newtonian calculations of the inspiral phase, as we discuss in this dissertation.

We have computed the sky-averaged horizon distance corresponding to Advanced LIGO and the proposed ET and the space-based LISA. The results show that binaries with total mass around to $500 M_{\odot}$ will be seen by Advanced LIGO at redshifts as high as $z = 1$ in the non-spinning case and $z = 2$ if the spin is significant. The ET will see IMBH binaries up to tens of thousands of solar masses up to cosmological distances above $z = 5$ and as high as $z > 15$ for particularly loud configurations. This could open the door to exploration of seed black hole formation and other discoveries in the early Universe.

We have revisited the event rate of BBHs for Advanced LIGO and the ET and found hundreds to tens of hundreds per year for the former and rates one order of magnitude larger for the latter. The first of these predictions should be able to be tested within five years after Advanced LIGO comes into operation.

The observations of Advanced LIGO and the ET in the intermediate-mass range could be complementary to those of LISA, which is expected to detect these systems with moderate SNRs and to be more sensitive to SMBH binaries instead. More remarkably, in principle if LISA and the ET are operative at the same time, they could complement each other and be used to track a particular event.

Current LIGO and Virgo matched-filter searches for BBH coalescences are solely targeted to stellar-mass black holes, for those are one of the types of systems that first-generation ground-based detectors are most sensitive to. The elevated rates of IMBHs events that we predict for Advanced LIGO and Virgo and the ET based on our improved waveforms should bring these more massive systems to the attention of the GW data analysis community. Future matched filter searches specifically targeted towards detections of IMBH binaries with ground-based detectors should be able to shed light into the question of their existence and corroborate or invalidate the current theoretical estimations on their event rate.

Advanced ground-based detectors are designed to be able to operate in different modes so that their sensitivity can be tuned to various kinds of astrophysical objects. Considering the importance of an eventual detection of an IMBH binary, the design of an optimized Advanced LIGO configuration for systems with $M \sim 10^{2-4} M_{\odot}$ would be desirable in order to increase the possibility of observing such a system. In case an IMBH binary coalescence was detected, the recovery and study of the physical parameters of the system could serve to test general relativity and prove or reject other alternative theories, such as scalar-tensor type or massive graviton theories.

The *direct* identification of an IMBH with GWs will be a revolutionary event not only due to the uncertainty that surrounds their existence and their potential role to test general relativity. The information encoded in the detection will provide us with a detailed description of the environment of the BBH/IMBH.

The information which we will recover from the data analysis of these systems, once they have been detected with GWs, will provide us with restrictions on the models which will constrain the various unknowns. Also, by combining this information with that from forthcoming instruments such as the Very Large Telescope interferometer and next-generation observatories, as e.g. VSI or GRAVITY, we will have a more accurate description of the stellar environment surrounding the IMBH. Thanks to an accurate identification of the system, we will be in position to “reverse-engineer” the astrophysical history of the stellar cluster, since this will leave a fingerprint in the detected IMBHs.

This dissertation has provided a global picture of the problem of modelling and detecting the gravitational-wave signature associated to binaries of black holes. Black-hole binary systems can be approached as a purely theoretical challenge, in the sense that they constitute one of the simplest non-trivial problems to be solved in General Relativity. From that point of view, analytical and numerical methods are needed to arrive to a full solution for the metric of the space-time, a solution that even nowadays is available only for a reduced subset of the most general parameter space. We have presented a full model for the coalescence of black hole binaries that covers a particular subset of the full parameter space, as a first step towards a further generalization. Our phenomenological waveform model for non-precessing, spinning binaries belongs precisely in the category of work targeted towards a proper theoretical understanding of gravitational-wave sources.

But black-hole binaries are also among the most fascinating objects that astrophysicists expect to observe in our Universe. Direct measurement of the gravitational-wave emission of such objects would turn into a revolution in the field of astronomy. With that goal, an international scientific community is gathered around the LIGO and Virgo gravitational-wave detectors, developing the necessary tools to properly analyze and understand their data. We have presented the results of the latest search for low-mass binary black-hole coalescence on LIGO data and have introduced preliminary results of an ongoing search for more massive systems with total mass up to hundreds of solar masses. But this is by no means the end; the Enhanced and Advanced configurations of the detectors hold great promise for detection of a binary system, perhaps of a pair of black holes. The incorporation of up-to-date results in waveform models for searches of black-hole binary coalescences is, thus, another major focus of this dissertation.

Upon entering the era of gravitational-wave astronomy, the detectors will turn into observatories. Their data will not only confirm or confound our expectations about the Universe around us, but they also should allow us to test current hypotheses about expected and conjectured astrophysical populations. In this sense, predictions such as the existence of intermediate-mass black hole binaries, the astrophysical background of which has also been discussed in this dissertation, could eventually be ascertained. We have revisited the expected astrophysical rates for these kind of objects and stated the prospect for their detection with gravitational-wave astronomy.

We currently find ourselves on the verge of finishing the analyses of the enhanced interferometers' output and entering a time of preparation for the data from the advanced detectors. Collaborations will be formed to devise and design the most promising data analysis strategies and techniques; input from scientists working in electromagnetic counterparts will be sought; faster, automatized searches will be run. Some of the results obtained in this dissertation will be employed in this challenge. The final reward will be sensational.

BIBLIOGRAPHY

- [1] ABADIE, J. ET AL. (THE LIGO SCIENTIFIC COLLABORATION AND THE VIRGO COLLABORATION), “Predictions for the Rates of Compact Binary Coalescences Observable by Ground-based Gravitational-wave Detectors”, (2010). (Cited on page 34.)
- [2] ABADIE, J. ET AL. (THE LIGO SCIENTIFIC COLLABORATION AND THE VIRGO COLLABORATION), “Search for gravitational waves from black hole binary inspiral, merger and ringdown”, (2010). In preparation. (Cited on pages 110 and 115.)
- [3] ABADIE, J. ET AL. (LIGO SCIENTIFIC COLLABORATION AND VIRGO COLLABORATION), “Sensitivity to Gravitational Waves from Compact Binary Coalescences Achieved during LIGO’s Fifth and Virgo’s First Science Run”, arXiv e-print, (mar 2010). [arXiv:1003.2481]. (Cited on page 79.)
- [4] ABBOTT, B. ET AL. (LIGO SCIENTIFIC COLLABORATION), “Search for gravitational waves from galactic and extra-galactic binary neutron stars”, *Phys. Rev. D*, 72, 082001, (2005). (Cited on pages 95 and 100.)
- [5] ABBOTT, B. P. ET AL. (LIGO SCIENTIFIC COLLABORATION), “Analysis of LIGO data for gravitational waves from binary neutron stars”, *Phys. Rev. D*, 69, 122001, (2004). (Cited on pages 95 and 100.)
- [6] ABBOTT, B. P. ET AL. (LIGO SCIENTIFIC COLLABORATION), “Search for gravitational waves from primordial black hole binary coalescences in the galactic halo”, *Phys. Rev. D*, 72, 082002, (2005). (Cited on pages 95 and 100.)
- [7] ABBOTT, B. P. ET AL. (LIGO SCIENTIFIC COLLABORATION), “Search for gravitational waves from binary black hole inspirals in LIGO data”, *Phys. Rev. D*, 73, 062001, (2006). (Cited on pages 95 and 100.)
- [8] ABBOTT, B. P. ET AL. (THE LIGO SCIENTIFIC COLLABORATION), *Tuning matched filter searches for compact binary coalescence*, (2007). URL (cited on April 13, 2010): <http://www.ligo.caltech.edu/docs/T/T070109-01.pdf>. (Cited on page 103.)
- [9] ABBOTT, B. P. ET AL. (THE LIGO SCIENTIFIC COLLABORATION AND THE VIRGO COLLABORATION), “Beating the Spin-Down Limit on Gravitational Wave Emission from the Crab Pulsar”, *Astrophys. J. Lett.*, 683(1), L45–L49, (2008). (Cited on page 28.)
- [10] ABBOTT, B. P. ET AL. (THE LIGO SCIENTIFIC COLLABORATION), “Search for gravitational waves from binary inspirals in S3 and S4 LIGO data”, *Phys. Rev. D*, 77, 062002, (2008). (Cited on pages 65, 95, 100, 102, and 127.)
- [11] ABBOTT, B. P. ET AL. (THE LIGO SCIENTIFIC COLLABORATION), “Search of S3 LIGO data for gravitational wave signals from spinning black hole and neutron star binary inspirals”, *Phys. Rev. D*, 78, 042002, (2008). (Cited on page 65.)
- [12] ABBOTT, B. P. ET AL. (THE LIGO SCIENTIFIC COLLABORATION AND THE VIRGO COLLABORATION), “An Upper Limit on the Stochastic Gravitational-Wave Background of Cosmological Origin”, *Nature*, 460, 990, (2009). (Cited on page 28.)
- [13] ABBOTT, B. P. ET AL. (THE LIGO SCIENTIFIC COLLABORATION), “LIGO: The Laser Interferometer Gravitational-Wave Observatory”, *Rep. Prog. Phys.*, 72, 076901, (2009). (Cited on pages 69 and 95.)
- [14] ABBOTT, B. P. ET AL. (THE LIGO SCIENTIFIC COLLABORATION), “Search for gravitational wave ringdowns from perturbed black holes in LIGO S4 data”, *Phys. Rev. D*, 80, 062001, (2009). (Cited on page 50.)
- [15] ABBOTT, B. P. ET AL. (THE LIGO SCIENTIFIC COLLABORATION), “Search for Gravitational Waves from Low Mass Binary Coalescences in the First Year of LIGO’s S5 Data”, *Phys. Rev. D*, 79, 122001, (2009). (Cited on pages 65, 102, 103, 105, 107, 109, and 128.)
- [16] ABBOTT, B. P. ET AL. (THE LIGO SCIENTIFIC COLLABORATION), “Search for Gravitational Waves from Low Mass Compact Binary Coalescence in 186 Days of LIGO’s fifth Science Run”, *Phys. Rev. D*, 80, 047101, (2009). (Cited on pages 65 and 101.)
- [17] ABRAHAMS, A. M. AND EVANS, C. R., “Reading off gravitational radiation waveforms in numerical relativity calculations: Matching to linearized gravity”, *Phys. Rev. D*, 37, 318–332, (1988). (Cited on page 66.)
- [18] ABRAHAMS, A. M. AND EVANS, C. R., “Gauge invariant treatment of gravitational radiation near the source: Analysis and numerical simulations”, *Phys. Rev. D*, 42, 2585–2594, (1990). (Cited on page 66.)

- [19] ACERNESE, F. ET AL., “Virgo status”, *Class. Quantum Grav.*, 25, 184001, (2008). (Cited on page 69.)
- [20] “Advanced LIGO anticipated sensitivity curves”. URL (cited on April 13, 2010): <https://dcc.ligo.org/cgi-bin/DocDB/ShowDocument?docid=2974>. (Cited on page 79.)
- [21] AGUIAR, O. D., ANDRADE, L. A., BARROSO, J. J., BORTOLI, F., CARNEIRO, L. A., CASTRO, P. J., COSTA, C. A., COSTA, K. M. F., DE ARAUJO, J. C. N., DE LUCENA, A. U., DE PAULA, W., DE REY NETO, E. C., DE SOUZA, S. T., FAUTH, A. C., FRAJUÇA, C., FROSSATI, G., FURTADO, S. R., MAGALHAES, N. S., MARINHO, R. M., MELO, J. L., MIRANDA, O. D., OLIVEIRA, N. F., RIBEIRO, K. L., STELLATI, C., VELLOSO, W. F. AND WEBER, J., “The Brazilian gravitational wave detector Mario Schenberg: status report”, *Class. Quantum Grav.*, 23(8), S239–S244, (2006). (Cited on page 16.)
- [22] AJITH, P., “Gravitational-wave data analysis using binary black-hole waveforms”, *Class. Quantum Grav.*, 25, 114033, (2008). (Cited on pages 66, 71, 91, 111, and 127.)
- [23] AJITH, P., BABAK, S., CHEN, Y., HEWITSON, M., KRISHNAN, B., SINTES, A. M., WHELAN, J. T., BRÜGMANN, B., DIENER, P., DORBAND, N., GONZALEZ, J., HANNAM, M., HUSA, S., POLLNEY, D., REZZOLLA, L., SANTAMARÍA, L., SPERHAKE, U. AND THORNBURG, J., “A template bank for gravitational waveforms from coalescing binary black holes: I. non-spinning binaries”, *Phys. Rev. D*, 77, 104017, (2008). (Cited on pages 66, 71, 85, 91, 111, and 127.)
- [24] AJITH, P., BABAK, S., CHEN, Y., HEWITSON, M., KRISHNAN, B., WHELAN, J. T., BRÜGMANN, B., DIENER, P., GONZÁLEZ, J., HANNAM, M., HUSA, S., KOPPITZ, M., POLLNEY, D., REZZOLLA, L., SANTAMARÍA, L., SINTES, A. M., SPERHAKE, U. AND THORNBURG, J., “Phenomenological template family for black-hole coalescence waveforms”, *Class. Quantum Grav.*, 24, S689–S699, (2007). (Cited on pages 71, 91, 111, 117, and 127.)
- [25] AJITH, P., HANNAM, M., HUSA, S., CHEN, Y., BRÜGMANN, B., DORBAND, N., MÜLLER, D., OHME, F., POLLNEY, D., REISSWIG, C., SANTAMARÍA, L. AND SEILER, J., ““Complete” gravitational waveforms for black-hole binaries with non-precessing spins”, (2009). (Cited on pages 66, 71, 87, 91, and 111.)
- [26] ALCUBIERRE, M., *Introduction to 3+1 Numerical Relativity*, (Oxford University Press, 2008). (Cited on pages 60 and 62.)
- [27] ALCUBIERRE, M. AND BRÜGMANN, B., “Simple excision of a black hole in 3+1 numerical relativity”, *Phys. Rev. D*, 63(10), 104006, (2001). (Cited on page 60.)
- [28] ALCUBIERRE, M. ET AL., “Towards a stable numerical evolution of strongly gravitating systems in general relativity: The conformal treatments”, *Phys. Rev. D*, 62, 044034, (2000). (Cited on pages 121 and 122.)
- [29] ALCUBIERRE, M. ET AL., “Gauge conditions for long-term numerical black hole evolutions without excision”, *Phys. Rev. D*, 67, 084023, (2003). (Cited on pages 121 and 122.)
- [30] ALLEN, B., “A χ^2 time-frequency discriminator for gravitational wave detection”, *Phys. Rev. D*, 71, 062001, (2005). (Cited on pages 98, 99, 103, and 129.)
- [31] ALLEN, B., ANDERSON, W. G., BRADY, P. R., BROWN, D. A. AND CREIGHTON, J. D. E., “FINDCHIRP: An algorithm for detection of gravitational waves from inspiraling compact binaries”, (2005). (Cited on pages 103 and 127.)
- [32] ALVI, K., “Energy and angular momentum flow into a black hole in a binary”, *Phys. Rev. D*, 64, 104020, (2001). (Cited on page 42.)
- [33] AMARO-SEOANE, P., “Dynamics of dense gas-star systems. Black holes and their precursors”, (2004). (Cited on page 139.)
- [34] AMARO-SEOANE, P., EICHHORN, C., PORTER, E. AND SPURZEM, R., “Binaries of massive black holes in rotating clusters: Dynamics, gravitational waves, detection and the role of eccentricity”, *Mon. Not. R. Astron. Soc.*, 401, 2268–2284, (2009). (Cited on pages 142 and 146.)
- [35] AMARO-SEOANE, P. AND FREITAG, M., “Intermediate-Mass Black Holes in Colliding Clusters: Implications for Lower Frequency Gravitational-Wave Astronomy”, *Astrophys. J. Lett.*, 653, L53–L56, (2006). (Cited on pages 140, 141, 149, and 150.)
- [36] AMARO-SEOANE, P., MILLER, M. C. AND FREITAG, M., “Gravitational Waves from Eccentric Intermediate-Mass Black Hole Binaries”, *Astrophys. J. Lett.*, 692, L50–L53, (2009). (Cited on page 141.)
- [37] AMARO-SEOANE, P. AND SPURZEM, R., “The loss-cone problem in dense nuclei”, *Mon. Not. R. Astron. Soc.*, 327, 995–1003, (2001). (Cited on page 139.)

- [38] AMARO-SEOANE, P., SPURZEM, R. AND JUST, A., “Super-Massive Stars: Dense Star-Gas Systems”, in *Lighthouses of the Universe: The Most Luminous Celestial Objects and Their Use for Cosmology, Proceedings of the MPA/ESO/MPE/USM Joint Astronomy Conference Held in Garching, Germany, 6–10 August 2001*, p. 376. Springer, (2002). (Cited on page 139.)
- [39] AMARO-SEOANE, P. AND SANTAMARÍA, L., “Detection of IMBHs with ground-based gravitational wave observatories: A biography of a binary of black holes, from birth to death”, (2009). (Cited on page 137.)
- [40] APOSTOLATOS, T. A., CUTLER, C., SUSSMAN, G. J. AND THORNE, K. S., “Spin induced orbital precession and its modulation of the gravitational wave forms from merging binaries”, *Phys. Rev. D*, 49, 6274–6297, (1994). (Cited on pages 40, 41, and 108.)
- [41] ARNOWITT, R., DESER, S. AND MISNER, C. W., “The Dynamics of General Relativity”, in WITTEN, L., ed., *Gravitation: An Introduction to Current Research*, pp. 227–265, (Wiley, New York, 1962). (Cited on page 54.)
- [42] ARUN, K. G., BUONANNO, A., FAYE, G. AND OCHSNER, E., “Higher-order spin effects in the amplitude and phase of gravitational waveforms emitted by inspiraling compact binaries: Ready-to-use gravitational waveforms”, *Phys. Rev. D*, 79, 104023, (2009). (Cited on pages 41, 45, and 46.)
- [43] ARUN, K. G., IYER, B. R., SATHYAPRAKASH, B. S. AND SUNDARARAJAN, P. A., “Parameter estimation of inspiralling compact binaries using 3.5 post-Newtonian gravitational wave phasing: The non-spinning case”, *Phys. Rev. D*, 71, 084008, (2005). (Cited on pages 41, 44, and 45.)
- [44] ASHBY, N., “Relativity in the Global Positioning System”, *Living Rev. Relativity*, 6(1), (2003). URL (cited on April 13, 2010): <http://www.livingreviews.org/lrr-2003-1>. (Cited on page 3.)
- [45] ASHTEKAR, A. AND KRISHNAN, B., “Isolated and dynamical horizons and their applications”, *Living Rev. Relativity*, 7, 10, (2004). URL (cited on April 13, 2010): <http://www.livingreviews.org/lrr-2004-10>. (Cited on page 75.)
- [46] ASTONE, P., BASSAN, M., BONIFAZI, P., CARELLI, P., CASTELLANO, M. G., CAVALLARI, G., COCCIA, E., COSMELLI, C., FAFONE, V., FRASCA, S., MAJORANA, E., MODENA, I., PALLOTTINO, G. V., PIZZELLA, G., RAPAGNANI, P., RICCI, F. AND VISCO, M., “Long-term operation of the Rome “Explorer” cryogenic gravitational wave detector”, *Phys. Rev. D*, 47(2), 362–375, (1993). (Cited on page 15.)
- [47] ASTONE, P., BASSAN, M., BONIFAZI, P., CARELLI, P., COCCIA, E., COSMELLI, C., FAFONE, V., FRASCA, S., MARINI, A., MAZZITELLI, G., MINENKOV, Y., MODENA, I., MODESTINO, G., MOLETI, A., PALLOTTINO, G. V., PAPA, M. A., PIZZELLA, G., RAPAGNANI, P., RICCI, F., RONGA, F., TEREZI, R., VISCO, M. AND VOTANO, L., “The gravitational wave detector NAUTILUS operating at $T = 0.1$ K”, *Astropart. Phys.*, 7(3), 231–243, (1997). (Cited on page 15.)
- [48] “Australian International Gravitational Observatory”. URL (cited on April 13, 2010): <http://www.gravity.uwa.edu.au/>. (Cited on page 19.)
- [49] AYLOTT, B. ET AL., “Testing gravitational-wave searches with numerical relativity waveforms: Results from the first Numerical INjection Analysis (NINJA) project”, *Class. Quantum Grav.*, 26, 165008, (2009). (Cited on pages 70, 117, 121, 126, 133, and 134.)
- [50] AYLOTT, B., VEITCH, J. AND VECCHIO, A., “Bayesian inference on the Numerical INjection Analysis (NINJA) data set using a nested sampling algorithm”, *Class. Quantum Grav.*, 26, 114011, (2009). (Cited on pages 132, 133, and 134.)
- [51] BABAK, S., BALASUBRAMANIAN, R., CHURCHES, D., COKELAER, T. AND SATHYAPRAKASH, B., “A template bank to search for gravitational waves from inspiralling compact binaries I: physical models”, *Class. Quantum Grav.*, 23, 5477–5504, (2006). (Cited on page 112.)
- [52] BAKER, J. G., CENTRELLA, J., CHOI, D.-I., KOPPITZ, M. AND VAN METER, J., “Gravitational wave extraction from an inspiraling configuration of merging black holes”, *Phys. Rev. Lett.*, 96, 111102, (2006). (Cited on pages 33, 53, 63, 65, 69, and 121.)
- [53] BAKER, J. G., VAN METER, J. R., MCWILLIAMS, S. T., CENTRELLA, J. AND KELLY, B. J., “Consistency of post-Newtonian waveforms with numerical relativity”, (2006). (Cited on page 70.)
- [54] BAUMGARTE, T. W. AND SHAPIRO, S. L., “On the Numerical Integration of Einstein’s Field Equations”, *Phys. Rev. D*, 59, 024007, (1999). (Cited on page 57.)
- [55] BEETLE, C., “Approximate Killing Fields as an Eigenvalue Problem”, arXiv e-print, (2008). [arXiv:0808.1745 [gr-qc]]. (Cited on pages 74 and 75.)

- [56] BELKUS, H., VAN BEVER, J. AND VANBEVEREN, D., “The Evolution of Very Massive Stars”, *Astrophys. J.*, 659, 1576–1581, (2007). (Cited on page 139.)
- [57] BERCEZIK, P., MERRITT, D., SPURZEM, R. AND BISCHOF, H.-P., “Efficient Merger of Binary Supermassive Black Holes in Non-Axisymmetric Galaxies”, *Astron. J.*, 642, L21, (2006). (Cited on page 140.)
- [58] BERTI, E., CARDOSO, V., GONZALEZ, J. A., SPERHAKE, U. AND BRÜGMANN, B., “Multipolar analysis of spinning binaries”, *Class. Quantum Grav.*, 25, 114035, (2008). (Cited on page 45.)
- [59] BERTI, E., BUONANNO, A. AND WILL, C. M., “Testing general relativity and probing the merger history of massive black holes with LISA”, *Class. Quant. Grav.*, 22, S943–S954, (2005). (Cited on page 142.)
- [60] BERTI, E. ET AL., “Inspirational, merger and ringdown of unequal mass black hole binaries: A multipolar analysis”, *Phys. Rev. D*, 76, 064034, (2007). (Cited on page 67.)
- [61] BILDSTEN, L., “Gravitational radiation and rotation of accreting neutron stars”, *Astrophys. J.*, 501, L89, (1998). (Cited on page 28.)
- [62] BISWAS, R., BRADY, P. R., CREIGHTON, J. D. E. AND FAIRHURST, S., “The Loudest Event Statistic: General Formulation, Properties and Applications”, *Class. Quantum Grav.*, 26, 175009, (2009). (Cited on page 105.)
- [63] BLAIR, D. G., IVANOV, E. N., TOBAR, M. E., TURNER, P. J., VAN KANN, F. AND HENG, I. S., “High Sensitivity Gravitational Wave Antenna with Parametric Transducer Readout”, *Phys. Rev. Lett.*, 74(11), 1908–1911, (1995). (Cited on page 15.)
- [64] BLANCHET, L., “Gravitational Radiation from Post-Newtonian Sources and Inspiralling Compact Binaries”, *Living Rev. Relativity*, 9(4), (2006). URL (cited on April 13, 2010): <http://www.livingreviews.org/lrr-2006-4>. (Cited on pages 31, 40, and 41.)
- [65] BLANCHET, L., BUONANNO, A. AND FAYE, G., “Higher-order spin effects in the dynamics of compact binaries II. Radiation field”, *Phys. Rev. D*, 74, 104034, (2006). (Cited on pages 41 and 42.)
- [66] BLANCHET, L., DAMOUR, T., ESPOSITO-FARÈSE, G. AND IYER, B. R., “Gravitational radiation from inspiralling compact binaries completed at the third post-Newtonian order”, *Phys. Rev. Lett.*, 93, 091101, (2004). (Cited on page 41.)
- [67] BLANCHET, L., FAYE, G., IYER, B. R. AND SINHA, S., “The third post-Newtonian gravitational wave polarisations and associated spherical harmonic modes for inspiralling compact binaries in quasi-circular orbits”, *Class. Quantum Grav.*, 25, 165003, (2008). (Cited on pages 41, 44, and 45.)
- [68] BONA, C., MASSO, J., SEIDEL, E. AND STELA, J., “A New formalism for numerical relativity”, *Phys. Rev. Lett.*, 75, 600–603, (1995). (Cited on page 60.)
- [69] BOYLE, M. ET AL., “High-accuracy comparison of numerical relativity simulations with post-Newtonian expansions”, *Phys. Rev. D*, 76, 124038, (2007). (Cited on pages 42, 63, 65, 70, 121, and 122.)
- [70] BOYLE, M. ET AL., “High-accuracy numerical simulation of black-hole binaries: Computation of the gravitational-wave energy flux and comparisons with post-Newtonian approximants”, *Phys. Rev. D*, 78, 104020, (2008). (Cited on page 70.)
- [71] BRADY, P. R., CREIGHTON, J. D. E. AND WISEMAN, A. G., “Upper limits on gravitational-wave signals based on loudest events”, *Class. Quantum Grav.*, 21, S1775–S1781, (2004). (Cited on page 105.)
- [72] BRADY, P. R. AND FAIRHURST, S., “Interpreting the results of searches for gravitational waves from coalescing binaries”, *Class. Quantum Grav.*, 25(10), 1050002, (2008). (Cited on pages 105 and 106.)
- [73] BRANDT, S. AND BRÜGMANN, B., “A Simple Construction of Initial Data for Multiple Black Holes”, *Phys. Rev. Lett.*, 78(19), 3606–3609, (1997). (Cited on page 61.)
- [74] BRILL, D. R. AND LINDQUIST, R. W., “Interaction Energy in Geometrostatics”, *Phys. Rev.*, 131(1), 471–476, (1963). (Cited on page 61.)
- [75] BROWN, D. A., FAIRHURST, S., KRISHNAN, B., MERCER, R. A., KOPPARAPU, R. K., SANTAMARÍA, L. AND WHELAN, J. T., “Data formats for numerical relativity waves”, arXiv e-print, (2007). [arXiv:0709.0093 [gr-qc]]. (Cited on pages 118 and 121.)
- [76] BRÜGMANN, B., GONZALEZ, J. A., HANNAM, M., HUSA, S. AND SPERHAKE, U., “Exploring black hole superkicks”, *Phys. Rev. D*, 77, 124047, (2008). (Cited on page 66.)
- [77] BRÜGMANN, B., GONZÁLEZ, J. A., HANNAM, M., HUSA, S., SPERHAKE, U. AND TICHY, W., “Calibration of Moving Puncture Simulations”, *Phys. Rev. D*, 77, 024027, (2008). (Cited

- on pages 63, 64, 66, 118, 122, and 127.)
- [78] BRÜGMANN, B., TICHY, W. AND JANSEN, N., “Numerical simulation of orbiting black holes”, *Phys. Rev. Lett.*, 92, 211101, (2004). (Cited on page 118.)
 - [79] BULIK, T. AND BELCZYŃSKI, K., “Constraints on the Binary Evolution from Chirp Mass Measurements”, *Astrophys. J. Lett.*, 589, L37–L40, (2003). (Cited on page 110.)
 - [80] BUONANNO, A. AND DAMOUR, T., “Effective one-body approach to general relativistic two-body dynamics”, *Phys. Rev. D*, 59, 084006, (1999). (Cited on pages 70 and 111.)
 - [81] BUONANNO, A., CHEN, Y. AND DAMOUR, T., “Transition from inspiral to plunge in precessing binaries of spinning black holes”, *Phys. Rev. D*, 74, 104005, (2006). (Cited on page 41.)
 - [82] BUONANNO, A., COOK, G. B. AND PRETORIUS, F., “Inspirals, merger and ring-down of equal-mass black-hole binaries”, *Phys. Rev. D*, 75, 124018, (2007). (Cited on pages 70, 121, and 122.)
 - [83] BUONANNO, A. AND DAMOUR, T., “Transition from inspiral to plunge in binary black hole coalescences”, *Phys. Rev. D*, 62, 064015, (2000). (Cited on pages 70 and 111.)
 - [84] BUONANNO, A. ET AL., “Toward faithful templates for non-spinning binary black holes using the effective-one-body approach”, *Phys. Rev. D*, 76, 104049, (2007). (Cited on page 70.)
 - [85] BUONANNO, A. ET AL., “Effective-one-body waveforms calibrated to numerical relativity simulations: coalescence of non-spinning, equal-mass black holes”, *Phys. Rev. D*, 79, 124028, (2009). (Cited on page 70.)
 - [86] BUONANNO, A., IYER, B., OCHSNER, E., PAN, Y. AND SATHYAPRAKASH, B. S., “Comparison of post-Newtonian templates for compact binary inspiral signals in gravitational-wave detectors”, (2009). (Cited on pages 42 and 81.)
 - [87] CADONATI, L. ET AL., “Status of NINJA: the Numerical INjection Analysis project”, *Class. Quantum Grav.*, 26(11), 114008, (2009). (Cited on pages 70 and 117.)
 - [88] CAMPANELLI, M., LOUSTO, C. O., MARRONETTI, P. AND ZLOCHOWER, Y., “Accurate evolutions of orbiting black-hole binaries without excision”, *Phys. Rev. Lett.*, 96, 111101, (2006). (Cited on pages 33, 53, 63, 65, 69, 121, and 122.)
 - [89] CAMPANELLI, M., LOUSTO, C. O., NAKANO, H. AND ZLOCHOWER, Y., “Comparison of Numerical and Post-Newtonian Waveforms for Generic Precessing Black-Hole Binaries”, *Phys. Rev. D*, 79, 084010, (2009). (Cited on page 70.)
 - [90] CAMPANELLI, M., LOUSTO, C. O., ZLOCHOWER, Y., KRISHNAN, B. AND MERRITT, D., “Spin Flips and Precession in Black-Hole-Binary Mergers”, *Phys. Rev. D*, 75, 064030, (2007). (Cited on page 75.)
 - [91] CAO, Z.-J., YO, H.-J. AND YU, J.-P., “A Reinvestigation of Moving Punctured Black Holes with a New Code”, *Phys. Rev. D*, 78, 124011, (2008). (Cited on page 63.)
 - [92] CHU, T., PFEIFFER, H. P. AND SCHEEL, M. A., “High accuracy simulations of black hole binaries: spins anti-aligned with the orbital angular momentum”, *Phys. Rev. D*, 80, 124051, (2009). (Cited on page 65.)
 - [93] COKELAER, T., “Gravitational waves from inspiralling compact binaries: hexagonal template placement and its efficiency in detecting physical signals”, *Phys. Rev. D*, 76, 102004, (2007). (Cited on pages 97, 103, 112, and 129.)
 - [94] COLLINS, H., *Gravity’s shadow: the search for gravitational waves*, (University of Chicago Press, 2004). (Cited on page 9.)
 - [95] CORINALDESI, E. AND PAPAPETROU, A., “Spinning test particles in general relativity. 2”, *Proc. R. Soc. London, Ser. A*, 64, 259–268, (1952). (Cited on page 74.)
 - [96] DAIN, S., LOUSTO, C. O. AND ZLOCHOWER, Y., “Extra-Large Remnant Recoil Velocities and Spins from Near-Extremal-Bowen-York-Spin Black-Hole Binaries”, *Phys. Rev. D*, 78, 024039, (2008). (Cited on pages 121 and 122.)
 - [97] DAMOUR, T., “Coalescence of two spinning black holes: An effective one-body approach”, *Phys. Rev. D*, 64, 124013, (2001). (Cited on page 41.)
 - [98] DAMOUR, T., IYER, B. R. AND SATHYAPRAKASH, B. S., “Improved filters for gravitational waves from inspiralling compact binaries”, *Phys. Rev. D*, 57, 885–907, (1998). (Cited on pages 70, 73, and 111.)
 - [99] DAMOUR, T., IYER, B. R. AND SATHYAPRAKASH, B. S., “Frequency-domain P-approximant filters for time-truncated inspiral gravitational wave signals from compact binaries”, *Phys. Rev. D*, 62, 084036, (2000). (Cited on pages 128 and 129.)

- [100] DAMOUR, T., IYER, B. R. AND SATHYAPRAKASH, B. S., “A comparison of search templates for gravitational waves from binary inspiral”, *Phys. Rev. D*, 63, 044023, (2001). (Cited on pages 41 and 44.)
- [101] DAMOUR, T., IYER, B. R. AND SATHYAPRAKASH, B. S., “A comparison of search templates for gravitational waves from binary inspiral: 3.5-PN update”, *Phys. Rev. D*, 66, 027502, (2002). (Cited on pages 41 and 44.)
- [102] DAMOUR, T., IYER, B. R. AND SATHYAPRAKASH, B. S., “Erratum: Comparison of search templates for gravitational waves from binary inspiral: 3.5PN update [Phys. Rev. D 66, 027502 (2002)]”, *Phys. Rev. D*, 72(2), 029901, (2005). (Cited on pages 41 and 44.)
- [103] DAMOUR, T., JARANOWSKI, P. AND SCHÄFER, G., “On the determination of the last stable orbit for circular general relativistic binaries at the third post-Newtonian approximation”, *Phys. Rev. D*, 62, 084011, (2000). (Cited on pages 70 and 111.)
- [104] DAMOUR, T., JARANOWSKI, P. AND SCHÄFER, G., “Dimensional regularization of the gravitational interaction of point masses”, *Phys. Lett. B*, 513, 147–155, (2001). (Cited on page 41.)
- [105] DAMOUR, T., NAGAR, A., HANNAM, M., HUSA, S. AND BRÜGMANN, B., “Accurate Effective-One-Body waveforms of inspiralling and coalescing black-hole binaries”, *Phys. Rev. D*, 78, 044039, (2008). (Cited on page 127.)
- [106] DE WAARD, A., BENZAIM, Y., FROSSATI, G., GOTTARDI, L., VAN DER MARK, H., FLOKSTRA, J., PODT, M., BASSAN, M., MINENKOV, Y., MOLETI, A., ROCCHI, A., FAFONE, V. AND PALLOTTINO, G. V., “MiniGRAIL progress report 2004”, *Class. Quantum Grav.*, 22(10), S215–S219, (2005). (Cited on page 16.)
- [107] DREYER, O., KRISHNAN, B., SHOEMAKER, D. AND SCHNETTER, E., “Introduction to Isolated Horizons in Numerical Relativity”, *Phys. Rev. D*, 67, 024018, (2003). (Cited on pages 74 and 75.)
- [108] DROZ, S., KNAPP, D. J., POISSON, E. AND OWEN, B. J., “Gravitational waves from inspiraling compact binaries: Validity of the stationary-phase approximation to the Fourier transform”, *Phys. Rev. D*, 59, 124016, (1999). (Cited on page 103.)
- [109] ECHEVERRIA, F., “Gravitational-wave measurements of the mass and angular momentum of a black hole”, *Phys. Rev. D*, 40(10), 3194–3203, (1989). (Cited on page 50.)
- [110] EINSTEIN, A., “Zur allgemeinen Relativitätstheorie”, *Sitzungsber. K. Preuss. Akad. Wiss.*, 778–786, (1915). (Cited on page 9.)
- [111] EISENHAUER, F. ET AL., “SINFONI in the Galactic Center: Young Stars and Infrared Flares in the Central Light-Month”, *Astrophys. J.*, 628, 246–259, (2005). (Cited on page 137.)
- [112] EISENHAUER, F. ET AL., “GRAVITY: getting to the event horizon of Sgr A*”, in *Optical and Infrared Interferometry*, Proc. SPIE, vol. 7013, (2008). (Cited on page 138.)
- [113] ESTABROOK, F. B. AND WAHLQUIST, H. D., “Response of Doppler spacecraft tracking to gravitational radiation”, *General Relativity and Gravitation*, 6, 439–447, (1975). (Cited on page 14.)
- [114] ETIENNE, Z. B., FABER, J. A., LIU, Y. T., SHAPIRO, S. L. AND BAUMGARTE, T. W., “Filling the holes: Evolving excised binary black hole initial data with puncture techniques”, *Phys. Rev. D*, 76, 101503, (2007). (Cited on pages 63, 121, and 122.)
- [115] FARR, B., FAIRHURST, S. AND SATHYAPRAKASH, B. S., “Searching for binary coalescences with inspiral templates: Detection and parameter estimation”, *Class. Quantum Grav.*, 26, 114009, (2009). (Cited on page 134.)
- [116] FAYE, G., BLANCHET, L. AND BUONANNO, A., “Higher-order spin effects in the dynamics of compact binaries. I: Equations of motion”, *Phys. Rev. D*, 74, 104033, (2006). (Cited on page 42.)
- [117] FINN, L. S., “The response of interferometric gravitational wave detectors”, *Phys. Rev.*, D79, 022002, (2009). (Cited on page 14.)
- [118] FLANAGAN, É. É. AND HUGHES, S. A., “Measuring gravitational waves from binary black hole coalescences. I. Signal to noise for inspiral, merger, and ringdown”, *Phys. Rev. D*, 57, 4535–4565, (1998). (Cited on page 146.)
- [119] FORWARD, R. L., “Multidirectional, multipolarization antennas for scalar and tensor gravitational radiation.”, *Gen. Relativ. Gravit.*, 2, 149–159, (1971). (Cited on page 16.)
- [120] FREGEAU, J. M., LARSON, S. L., MILLER, M. C., O’SHAUGHNESSY, R. AND RASIO, F. A., “Observing IMBH-IMBH Binary Coalescences via Gravitational Radiation”, *Astrophys. J. Lett.*, 646, L135–L138, (2006). (Cited on pages 140, 146, 149, and 150.)

- [121] FREITAG, M., GÜRKAN, M. A. AND RASIO, F. A., “Runaway collisions in young star clusters - II. Numerical results”, *Mon. Not. R. Astron. Soc.*, 368, 141–161, (2006). (Cited on page 139.)
- [122] FREITAG, M., RASIO, F. A. AND BAUMGARDT, H., “Runaway collisions in young star clusters - I. Methods and tests”, *Mon. Not. R. Astron. Soc.*, 368, 121–140, (2006). (Cited on pages 139 and 150.)
- [123] GÜRKAN, M. A., FREITAG, M. AND RASIO, F. A., “Formation of Massive Black Holes in Dense Star Clusters. I. Mass Segregation and Core Collapse”, *Astrophys. J.*, 604, 632–652, (2004). (Cited on page 139.)
- [124] GAIR, J. R., MANDEL, I., MILLER, M. C. AND VOLONTERI, M., “Exploring intermediate and massive black-hole binaries with the Einstein Telescope”, arXiv e-print, (jul 2009). [arXiv:0907.5450]. (Cited on page 140.)
- [125] GAIR, J. R., MANDEL, I., SESANA, A. AND VECCHIO, A., “Probing seed black holes using future gravitational-wave detectors”, *Class. Quant. Grav.*, 26, 204009, (2009). (Cited on page 144.)
- [126] GALAVIZ, P., BRUEGMANN, B. AND CAO, Z., “Numerical evolution of multiple black holes with accurate initial data”, (2010). (Cited on page 63.)
- [127] “GEO600 detector”. URL (cited on April 13, 2010): <http://www.geo600.org/>. (Cited on pages 18 and 19.)
- [128] GHEZ, A. M. ET AL., “The First Measurement of Spectral Lines in a Short-Period Star Bound to the Galaxy’s Central Black Hole: A Paradox of Youth”, *Astrophys. J.*, 586, L127–L131, (2003). (Cited on page 137.)
- [129] GHEZ, A. M., SALIM, S., HORNSTEIN, S. D., TANNER, A., LU, J. R., MORRIS, M., BECKLIN, E. E. AND DUCHÊNE, G., “Stellar Orbits around the Galactic Center Black Hole”, *Astrophys. J.*, 620, 744–757, (2005). (Cited on page 137.)
- [130] GHEZ, A. M., SALIM, S., WEINBERG, N. N., LU, J. R., DO, T., DUNN, J. K., MATTHEWS, K., MORRIS, M. R., YELDA, S., BECKLIN, E. E., KREMENEK, T., MILOSAVLJEVIC, M. AND NAIMAN, J., “Measuring Distance and Properties of the Milky Way’s Central Supermassive Black Hole with Stellar Orbits”, *Astrophys. J.*, 689, 1044–1062, (2008). (Cited on page 137.)
- [131] GILLESSEN, S., EISENHAUER, F., TRIPPE, S., ALEXANDER, T., GENZEL, R., MARTINS, F. AND OTT, T., “Monitoring Stellar Orbits Around the Massive Black Hole in the Galactic Center”, *Astrophys. J.*, 692, 1075–1109, (2009). (Cited on page 137.)
- [132] GILLESSEN, S., PERRIN, G., BRANDNER, W., STRAUBMEIER, C., EISENHAUER, F., RABIER, S., ECKART, A., LENA, P., GENZEL, R., PAUMARD, T. AND HIPPLER, S., “GRAVITY: the adaptive-optics-assisted two-object beam combiner instrument for the VLTI”, in *Advances in Stellar Interferometry*, Proc. SPIE, vol. 6268, (2006). (Cited on page 138.)
- [133] GLEBBEEK, E., GABUROV, E., DE MINK, S. E., POLS, O. R. AND PORTEGIES ZWART, S. F., “The evolution of runaway stellar collision products”, *Astron. Astrophys.*, 497, 255–264, (2009). (Cited on pages 110 and 139.)
- [134] GOLDBERGER, W. D. AND ROTHSTEIN, I. Z., “An effective field theory of gravity for extended objects”, *Phys. Rev. D*, 73, 104029, (2006). (Cited on page 74.)
- [135] GOPAKUMAR, A., HANNAM, M., HUSA, S. AND BRÜGMANN, B., “Comparison between numerical relativity and a new class of post-Newtonian gravitational-wave phase evolutions: the non-spinning equal-mass case”, *Phys. Rev. D*, 78, 064026, (2008). (Cited on page 70.)
- [136] GROTE, H. (LIGO SCIENTIFIC), “The status of GEO 600”, *Class. Quantum Grav.*, 25, 114043, (2008). (Cited on page 69.)
- [137] GUALTIERI, L., BERTI, E., CARDOSO, V. AND SPERHAKE, U., “Transformation of the multipolar components of gravitational radiation under rotations and boosts”, *Phys. Rev. D*, 78, 044024, (2008). (Cited on page 121.)
- [138] GÜRKAN, M. A., FREGEAU, J. M. AND RASIO, F. A., “Massive Black Hole Binaries from Collisional Runaways”, *Astrophys. J. Lett.*, 640, L39–L42, (2006). (Cited on pages 140, 146, 147, and 149.)
- [139] HAHN, S. G. AND LINDQUIST, R. W., “The two-body problem in geometrodynamics”, *Ann. Phys.*, 29, 304–331, (1964). (Cited on pages 33 and 53.)
- [140] HANNAM, M., HUSA, S., BRÜGMANN, B., GONZÁLEZ, J. A., SPERHAKE, U. AND MURCHADHA, N. Ó., “Where do moving punctures go?”, *J. Phys.: Conf. Ser.*, 66(1), 012047, (2007). (Cited on page 62.)

- [141] HANNAM, M., HUSA, S., POLLNEY, D., BRÜGMANN, B. AND MURCHADHA, N. Ó., “Geometry and Regularity of Moving Punctures”, *Phys. Rev. Lett.*, 99(24), 241102, (2007). (Cited on page 62.)
- [142] HANNAM, M., “Status of black-hole-binary simulations for gravitational- wave detection”, *Class. Quantum Grav.*, 26, 114001, (2009). (Cited on page 70.)
- [143] HANNAM, M. ET AL., “The Samurai Project: verifying the consistency of black- hole-binary waveforms for gravitational-wave detection”, *Phys. Rev. D*, 79, 084025, (2009). (Cited on pages 65 and 70.)
- [144] HANNAM, M. ET AL., “Gravitational waveforms from equal-mass black-hole binaries with non-precessing spins”, (2010). In preparation. (Cited on pages 65 and 66.)
- [145] HANNAM, M., HUSA, S., BRÜGMANN, B. AND GOPAKUMAR, A., “Comparison between numerical-relativity and post-Newtonian waveforms from spinning binaries: the orbital hang-up case”, *Phys. Rev. D*, 78, 104007, (2008). (Cited on pages 65, 66, 70, 118, and 122.)
- [146] HANNAM, M., HUSA, S., SPERHAKE, U., BRÜGMANN, B. AND GONZÁLEZ, J. A., “Where post-Newtonian and numerical-relativity waveforms meet”, *Phys. Rev. D*, 77, 044020, (2008). (Cited on pages 66, 70, 118, 122, and 127.)
- [147] HARTE, A. I., “Approximate spacetime symmetries and conservation laws”, *Class. Quantum Grav.*, 25, 205008, (2008). (Cited on pages 74 and 75.)
- [148] HELMSTROM, C. W., *Statistical Theory of Signal Detection*, (Pergamon Press, London, 1968), 2 edition. (Cited on page 95.)
- [149] HELMSTROM, C. W., *Elements of signal detection and estimation*, (Prentice-Hall, Inc., Upper Saddle River, NJ, USA, 1995). (Cited on page 72.)
- [150] HERRMANN, F., SILBERHOLZ, J., BELLONE, M., GUERBEROFF, G. AND TIGLIO, M., “Integrating Post-Newtonian Equations on Graphics Processing Units”, *Class. Quantum Grav.*, 27, 032001, (2010). (Cited on page 40.)
- [151] HILD, S., CHELKOWSKI, S., FREISE, A., FRANC, J., MORGADO, N., FLAMINIO, R. AND DESALVO, R., “A Xylophone Configuration for a third Generation Gravitational Wave Detector”, *Class. Quantum Grav.*, 27, 015003, (2010). (Cited on pages 25 and 145.)
- [152] HINDER, I., “The Current Status of Binary Black Hole Simulations in Numerical Relativity”, (2010). (Cited on page 70.)
- [153] HINDER, I., VAISHNAV, B., HERRMANN, F., SHOEMAKER, D. AND LAGUNA, P., “Universality and Final Spin in Eccentric Binary Black Hole Inspirals”, *Phys. Rev. D*, 77, 081502, (2008). (Cited on pages 63, 121, and 122.)
- [154] HINSHAW, G. ET AL. (WMAP), “Five-Year Wilkinson Microwave Anisotropy Probe (WMAP) Observations: Data Processing, Sky Maps, & Basic Results”, *Astrophys. J. Suppl.*, 180, 225–245, (2009). (Cited on page 144.)
- [155] HULSE, R. A. AND TAYLOR, J. H., “Discovery of a pulsar in a binary system”, *Astrophys. J. Lett.*, 195, L51–L53, (1975). (Cited on page 31.)
- [156] HUSA, S., GONZALEZ, J. A., HANNAM, M., BRÜGMANN, B. AND SPERHAKE, U., “Reducing phase error in long numerical binary black hole evolutions with sixth order finite differencing”, *Class. Quantum Grav.*, 25, 105006, (2008). (Cited on pages 74, 118, and 122.)
- [157] HUSA, S., HANNAM, M., GONZALEZ, J. A., SPERHAKE, U. AND BRÜGMANN, B., “Reducing eccentricity in black-hole binary evolutions with initial parameters from post-Newtonian inspiral”, *Phys. Rev. D*, 77, 044037, (2008). (Cited on pages 64 and 66.)
- [158] IMBIRIBA, B. ET AL., “Evolving a puncture black hole with fixed mesh refinement”, *Phys. Rev. D*, 70, 124025, (2004). (Cited on pages 63, 121, and 122.)
- [159] JASIULEK, M., “A new method to compute quasi-local spin and other invariants on marginally trapped surfaces”, *Class. Quantum Grav.*, 26, 245008, (2009). (Cited on pages 74 and 75.)
- [160] KALOGERA, V., BELCZYNSKI, K., KIM, C., O’SHAUGHNESSY, R. AND WILLEMS, B., “Formation of double compact objects”, *Phys. Rep.*, 442, 75–108, (2007). (Cited on page 35.)
- [161] KALOGERA, V. ET AL., “Erratum: “The Cosmic Coalescence Rates for Double Neutron Star Binaries (Ap), 601, L179 [2004]”, *Astrophys. J. Lett.*, 614, L137–L138, (2004). (Cited on page 109.)
- [162] KALOGERA, V., KIM, C., LORIMER, D. R., BURGAY, M., D’AMICO, N., POSSENTI, A., MANCHESTER, R. N., LYNE, A. G., JOSHI, B. C., MCLAUGHLIN, M. A., KRAMER, M., SARKISSIAN, J. M. AND CAMILO, F., “The Cosmic Coalescence Rates for Double Neutron Star Binaries”, *Astrophys. J.*, 601, L179–L182, (2004). Erratum-ibid. 614 (2004) L137. (Cited on pages 35 and 109.)

- [163] KALOGERA, V., NARAYAN, R., SPERGEL, D. N. AND TAYLOR, J. H., “The Coalescence Rate of Double Neutron Star Systems”, *Astrophys. J.*, 556, 340, (2001). (Cited on page 105.)
- [164] KERR, R. P., “Gravitational Field of a Spinning Mass as an Example of Algebraically Special Metrics”, *Phys. Rev. Lett.*, 11, 237–238, (1963). (Cited on page 34.)
- [165] KIDDER, L. E., “Coalescing binary systems of compact objects to postNewtonian 5/2 order. 5. Spin effects”, *Phys. Rev. D*, 52, 821–847, (1995). (Cited on page 41.)
- [166] KIM, C., KALOGERA, V. AND LORIMER, D. R., “Effect of PSR J0737-3039 on the DNS Merger Rate and Implications for GW Detection”, *ArXiv e-prints*, (2006). (Cited on page 35.)
- [167] KIUCHI, K., SEKIGUCHI, Y., SHIBATA, M. AND TANIGUCHI, K., “Longterm general relativistic simulation of binary neutron stars collapsing to a black hole”, *Phys. Rev. D*, 80, 064037, (2009). (Cited on page 103.)
- [168] KOKKOTAS, K. D. AND SCHMIDT, B., “Quasi-Normal Modes of Stars and Black Holes”, *Living Rev. Relativity*, 2(2), (1999). URL (cited on April 13, 2010): <http://www.livingreviews.org/lrr-1999-2>. (Cited on page 48.)
- [169] KOPPARAPU, R. K., HANNA, C., KALOGERA, V., O’SHAUGHNESSY, R., GONZALEZ, G., BRADY, P. R. AND FAIRHURST, S., “Host Galaxies Catalog Used in LIGO Searches for Compact Binary Coalescence Events”, *Astrophys. J.*, 675(2), 1459–1467, (2008). (Cited on pages 105, 106, and 109.)
- [170] KOPPITZ, M. ET AL., “Getting a kick from equal-mass binary black hole mergers”, *Phys. Rev. Lett.*, 99, 041102, (2007). (Cited on pages 121 and 122.)
- [171] KRAMER, M. ET AL., “Tests of general relativity from timing the double pulsar”, *Science*, 314, 97–102, (2006). (Cited on page 31.)
- [172] KYRIAN, K. AND SEMERÁK, O., “Spinning test particles in a Kerr field - II”, *Mon. Not. R. Astron. Soc.*, 382, 1922–1932, (2007). (Cited on page 75.)
- [173] “Laser Interferometer Gravitational-wave Observatory”. URL (cited on April 13, 2010): <http://www.ligo.caltech.edu/>. (Cited on pages 18 and 19.)
- [174] LEAVER, E. W., “An Analytic representation for the quasi normal modes of Kerr black holes”, *Proc. R. Soc. London, Ser. A*, 402, 285–298, (1985). (Cited on pages 48 and 49.)
- [175] LINDBLOM, L., OWEN, B. J. AND BROWN, D. A., “Model Waveform Accuracy Standards for Gravitational Wave Data Analysis”, *Phys. Rev. D*, 78, 124020, (2008). (Cited on pages 72 and 73.)
- [176] LOUSTO, C. O., NAKANO, H., ZLOCHOWER, Y. AND CAMPANELLI, M., “Statistical studies of Spinning Black-Hole Binaries”, (2009). (Cited on page 40.)
- [177] LOVELACE, G., OWEN, R., PFEIFFER, H. P. AND CHU, T., “Binary-black-hole initial data with nearly-extremal spins”, *Phys. Rev. D*, 78, 084017, (2008). (Cited on pages 74 and 75.)
- [178] “LSC Algorithm Library”. URL (cited on April 13, 2010): <http://www.lsc-group.phys.uwm.edu/lal>. (Cited on page 126.)
- [179] MANCHESTER, R. N., HOBBS, G. B., TEOH, A. AND HOBBS, M., “The Australia Telescope National Facility Pulsar Catalogue”, *Astron. J.*, 129(4), 1993–2006, (2005). (Cited on page 108.)
- [180] MAUCELI, E., GENG, Z. K., HAMILTON, W. O., JOHNSON, W. W., MERKOWITZ, S., MORSE, A., PRICE, B. AND SOLOMONSON, N., “The Allegro gravitational wave detector: Data acquisition and analysis”, *Phys. Rev. D*, 54(2), 1264–1275, (1996). (Cited on page 15.)
- [181] MCCLINTOCK, J. E., SHAFEE, R., NARAYAN, R., REMILLARD, R. A., DAVIS, S. W. AND LI, L.-X., “The Spin of the Near-Extreme Kerr Black Hole GRS 1915+105”, *Astrophys. J.*, 652, 518, (2006). (Cited on page 115.)
- [182] MILLER, M. C., “Gravitational Radiation from Intermediate-Mass Black Holes”, *Astrophys. J.*, 581, 438–450, (2002). (Cited on page 146.)
- [183] MILLER, M. C., “Intermediate-mass black holes as LISA sources”, *Class. Quantum Grav.*, 26(9), 094031, (2009). (Cited on page 137.)
- [184] MILLER, M. C. AND COLBERT, E. J. M., “Intermediate-Mass Black Holes”, *Int. J. Mod. Phys. D*, 13, 1–64, (2004). (Cited on page 137.)
- [185] MILLER, M. C. AND LAUBURG, V. M., “Mergers of Stellar-Mass Black Holes in Nuclear Star Clusters”, *Astrophys. J.*, 692, 917–923, (2009). (Cited on page 110.)
- [186] NAGY, G., ORTIZ, O. E. AND REULA, O. A., “Strongly hyperbolic second order Einstein’s evolution equations”, *Phys. Rev. D*, 70, 044012, (2004). (Cited on page 57.)
- [187] NAKAMURA, T., OOHARA, K. AND KOJIMA, Y., “General Relativistic Collapse to Black Holes and Gravitational Waves from Black Holes”, *Prog. Theor. Phys. Suppl.*, 90, 1–218,

- (1987). (Cited on page 57.)
- [188] NIELSEN, A., JASIULEK, M., SCHNETTER, E. AND KRISHNAN, B., (2010). In preparation. (Cited on page 74.)
- [189] “Numerical INjection Analysis project”. URL (cited on April 13, 2010): <http://www.ninja-project.org>. (Cited on page 70.)
- [190] O’LEARY, R. M., KOCSIS, B. AND LOEB, A., “Gravitational waves from scattering of stellar-mass black holes in galactic nuclei”, *Mon. Not. R. Astron. Soc.*, 395, 2127–2146, (2009). (Cited on page 110.)
- [191] O’LEARY, R. M., O’SHAUGHNESSY, R. AND RASIO, F. A., “Dynamical interactions and the black-hole merger rate of the Universe”, *Phys. Rev. D*, 76(6), 061504, (2007). (Cited on page 110.)
- [192] OLIYNYK, T. A., “Cosmological post-Newtonian expansions to arbitrary order”, (2009). (Cited on page 74.)
- [193] OROSZ, J. A., MCCLINTOCK, J. E., NARAYAN, R., BAILYN, C. D., HARTMAN, J. D., MACRI, L., LIU, J., PIETSCH, W., REMILLARD, R. A., SHPORER, A. AND MAZEH, T., “A 15.65-solar-mass black hole in an eclipsing binary in the nearby spiral galaxy M 33”, *Nature*, 449, 872–875, (2007). (Cited on page 110.)
- [194] O’SHAUGHNESSY, R., KALOGERA, V. AND BELCZYNSKI, K., “Binary compact object coalescence rates: The role of elliptical galaxies”, arXiv e-print, (aug 2009). [arXiv:0908.3635]. (Cited on page 110.)
- [195] O’SHAUGHNESSY, R., KIM, C., FRAGOS, T., KALOGERA, V. AND BELCZYNSKI, K., “Constraining Population Synthesis Models via the Binary Neutron Star Population”, *Astrophys. J.*, 633, 1076–1084, (2005). (Cited on page 109.)
- [196] O’SHAUGHNESSY, R., KIM, C., KALOGERA, V. AND BELCZYNSKI, K., “Constraining Population Synthesis Models via Empirical Binary Compact Object Merger and Supernova Rates”, *Astrophys. J.*, 672, 479–488, (2008). (Cited on pages 35 and 109.)
- [197] OWEN, B. J., “Search templates for gravitational waves from inspiraling binaries: Choice of template spacing”, *Phys. Rev. D*, 53, 6749–6761, (1996). (Cited on page 97.)
- [198] OWEN, B. J. AND SATHYAPRAKASH, B. S., “Matched filtering of gravitational waves from inspiraling compact binaries: Computational cost and template placement”, *Phys. Rev. D*, 60, 022002, (1999). (Cited on page 103.)
- [199] PAN, Y. ET AL., “Effective-one-body waveforms calibrated to numerical relativity simulations: coalescence of non-precessing, spinning, equal-mass black holes”, (2009). (Cited on page 70.)
- [200] PAPAPETROU, A., “Spinning test particles in general relativity”, *Proc. R. Soc. London, Ser. A*, 209, 248–258, (1951). (Cited on page 74.)
- [201] PAPOULIS, A. AND UNNIKRISHNA PILLAI, S., *Probability, Random Variables and Stochastic Processes*, (McGraw Hill Higher Education, 2002), 4 edition. (Cited on page 72.)
- [202] PENROSE, R. AND RINDLER, W., *Spinors and Space-time: Two-spinor calculus and relativistic fields*, (Press Syndicate of the University of Cambridge, 1986). (Cited on page 66.)
- [203] PETERS, P. C., “Gravitational Radiation and the Motion of Two Point Masses”, *Phys. Rev.*, 136, 1224–1232, (1964). (Cited on pages 141 and 142.)
- [204] PFEIFFER, H. P. ET AL., “Reducing orbital eccentricity in binary black hole simulations”, *Class. Quantum Grav.*, 24, S59–S82, (2007). (Cited on page 121.)
- [205] POISSON, E., “Gravitational waves from inspiraling compact binaries: The quadrupole-moment term”, *Phys. Rev. D*, 57, 5287–5290, (1998). (Cited on page 41.)
- [206] POLLNEY, D. ET AL., “Recoil velocities from equal-mass binary black-hole mergers: a systematic investigation of spin-orbit aligned configurations”, *Phys. Rev. D*, 76, 124002, (2007). (Cited on pages 63, 65, 66, 121, and 122.)
- [207] POLLNEY, D., REISSWIG, C., SCHNETTER, E., DORBAND, N. AND DIENER, P., “High accuracy binary black hole simulations with an extended wave zone”, (2009). (Cited on pages 63, 66, and 67.)
- [208] PORCIANI, C. AND MADAU, P., “On the Association of Gamma-Ray Bursts with Massive Stars: Implications for Number Counts and Lensing Statistics”, *Astrophys. J.*, 548, 522–531, (2001). (Cited on pages 147 and 148.)
- [209] PORTEGIES ZWART, S. F., BAUMGARDT, H., HUT, P., MAKINO, J. AND McMILLAN, S. L. W., “Formation of massive black holes through runaway collisions in dense young star clusters”, *Nature*, 428, 724–726, (2004). (Cited on page 139.)

- [210] PORTEGIES ZWART, S. F. AND McMILLAN, S. L. W., “Black Hole Mergers in the Universe”, *Astrophys. J. Lett.*, 528, L17–L20, (2000). (Cited on pages 139 and 146.)
- [211] PORTO, R. A. AND ROTHSTEIN, I. Z., “Spin(1)Spin(2) Effects in the Motion of Inspiralling Compact Binaries at Third Order in the Post-Newtonian Expansion”, *Phys. Rev. D*, 78, 044012, (2008). (Cited on page 74.)
- [212] PRETORIUS, F., “Evolution of binary black hole spacetimes”, *Phys. Rev. Lett.*, 95, 121101, (2005). (Cited on pages 33, 53, 61, 63, 65, 69, 121, and 122.)
- [213] PRETORIUS, F., “Numerical Relativity Using a Generalized Harmonic Decomposition”, *Class. Quantum Grav.*, 22, 425–452, (2005). (Cited on pages 63, 65, 121, and 122.)
- [214] PRETORIUS, F. AND KHURANA, D., “Black hole mergers and unstable circular orbits”, *Class. Quantum Grav.*, 24, S83–S108, (2007). (Cited on pages 121 and 122.)
- [215] PRODI, G. A. ET AL., “Initial operation of the gravitational wave detector AURIGA”. Prepared for 2nd Edoardo Amaldi Conference on Gravitational Waves, Geneva, Switzerland, 1-4 Jul 1997. (Cited on page 15.)
- [216] REGGE, T. AND WHEELER, J., “Stability of a Schwarzschild Singularity”, *Phys. Rev.*, 108, 1063–1069, (1957). (Cited on page 48.)
- [217] REGGE, T. AND WHEELER, J. A., “Stability of a Schwarzschild singularity”, *Phys. Rev.*, 108, 1063–1069, (1957). (Cited on page 66.)
- [218] REISSWIG, C., BISHOP, N. T., POLLNEY, D. AND SZILAGYI, B., “Unambiguous determination of gravitational waveforms from binary black hole mergers”, *Phys. Rev. Lett.*, 103, 221101, (2009). (Cited on page 67.)
- [219] REISSWIG, C., BISHOP, N. T., POLLNEY, D. AND SZILAGYI, B., “Characteristic extraction in numerical relativity: binary black hole merger waveforms at null infinity”, *Class. Quantum Grav.*, 27, 075014, (2010). (Cited on page 67.)
- [220] REISSWIG, C. ET AL., “Gravitational-wave detectability of equal-mass black-hole binaries with aligned spins”, *Phys. Rev. D*, 80, 124026, (2009). (Cited on pages 51, 66, and 144.)
- [221] REZZOLLA, L., DORBAND, E. N., REISSWIG, C., DIENER, P., POLLNEY, D., SCHNETTER, E. AND SZILÁGYI, B., “Spin Diagrams for equal-mass black-hole binaries with aligned spins”, (2007). (Cited on page 65.)
- [222] REZZOLLA, L. ET AL., “Spin Diagrams for Equal-Mass Black-Hole Binaries with Aligned Spins”, *Astrophys. J.*, 679, 1422–1426, (2008). (Cited on pages 121 and 122.)
- [223] REZZOLLA, L. ET AL., “The final spin from the coalescence of aligned-spin black-hole binaries”, *Astrophys. J.*, 674, L29–L32, (2008). (Cited on pages 65 and 86.)
- [224] ROBINSON, C. A. K., SATHYAPRAKASH, B. S. AND SENGUPTA, A. S., “A geometric algorithm for efficient coincident detection of gravitational waves”, *Phys. Rev. D*, 78, 062002, (2008). (Cited on pages 103 and 128.)
- [225] RODRÍGUEZ, A., “Reducing false alarms in searches for gravitational waves from coalescing binary systems”, (2007). (Cited on pages 103 and 129.)
- [226] RUBBO, L. J., CORNISH, N. J. AND POUJADE, O., “Forward modeling of space-borne gravitational wave detectors”, *Phys. Rev. D*, 69, 082003, (2004). (Cited on page 14.)
- [227] SANTAMARÍA, L., OHME, F., AJITH, P., BRÜGMANN, B., DORBAND, N., HANNAM, M., HUSA, S., MÖSTA, P., MÜLLER, D., POLLNEY, D., REISSWIG, C., SEILER, J. AND KRISHNAN, B., “Matching post-Newtonian and numerical relativity waveforms: systematic errors and a new phenomenological model for non-precessing black hole binaries”, (2010). To be submitted. (Cited on page 69.)
- [228] SANTAMARÍA, L., KRISHNAN, B. AND WHELAN, J. T., “Searching for numerically-simulated signals of black hole binaries with a phenomenological template family”, *Class. Quantum Grav.*, 26, 114010, (2009). (Cited on page 117.)
- [229] SATHYAPRAKASH, B. S. AND DHURANDHAR, S. V., “Choice of filters for the detection of gravitational waves from coalescing binaries”, *Phys. Rev. D*, 44, 3819–3834, (1991). (Cited on page 103.)
- [230] SATHYAPRAKASH, B. AND SCHUTZ, B. F., “Physics, Astrophysics and Cosmology with Gravitational Waves”, *Living Rev. Relativity*, 12(2), (2009). URL (cited on April 13, 2010): <http://www.livingreviews.org/lrr-2009-2>. (Cited on page 30.)
- [231] SCHEEL, M. A. ET AL., “Solving Einstein’s equations with dual coordinate frames”, *Phys. Rev. D*, 74, 104006, (2006). (Cited on pages 66, 121, and 122.)
- [232] SCHEEL, M. A. ET AL., “High-accuracy waveforms for binary black hole inspiral, merger, and ringdown”, *Phys. Rev. D*, 79, 024003, (2009). (Cited on pages 63, 67, 70, 121, and 122.)

- [233] SCHNITTMAN, J. D., “Spin-orbit resonance and the evolution of compact binary systems”, *Phys. Rev. D*, 70(12), 124020, (2004). (Cited on page 40.)
- [234] SCHODEL, R. ET AL., “Stellar dynamics in the central arcsecond of our galaxy”, *Astrophys. J.*, 596, 1015–1034, (2003). (Cited on page 137.)
- [235] SCHUTZ, B., *A First Course in General Relativity*, (Cambridge University Press, 2009), 2nd edition. (Cited on page 11.)
- [236] SEARLE, A. C., SCOTT, S. M., MCCLELLAND, D. E. AND FINN, L. S., “Optimal location of a new interferometric gravitational wave observatory”, *Phys. Rev. D*, 73(12), 124014, (2006). (Cited on page 22.)
- [237] SESANA, A., GAIR, J., MANDEL, I. AND VECCHIO, A., “Observing Gravitational Waves from the First Generation of Black Holes”, *Astrophys. J. Lett.*, 698, L129–L132, (2009). (Cited on page 148.)
- [238] SHADDOCK, D. A., “An overview of the Laser Interferometer Space Antenna”, *Publ. Astron. Soc. Australia*, 26, 128–132, (2009). (Cited on page 69.)
- [239] SHIBATA, M. AND NAKAMURA, T., “Evolution of three-dimensional gravitational waves: Harmonic slicing case”, *Phys. Rev. D*, 52(10), 5428–5444, (1995). (Cited on page 57.)
- [240] SHIBATA, M., KYUTOKU, K., YAMAMOTO, T. AND TANIGUCHI, K., “Gravitational waves from black hole-neutron star binaries I: Classification of waveforms”, *Phys. Rev. D*, 79, 044030, (2009). (Cited on page 103.)
- [241] SMARR, L. L., “Gauge Conditions, Raidation Formulae, and the Two Black Hole Collision”, in SMARR, L. L., ed., *Sources of Gravitational Radiation*, pp. 245–274, (Cambridge University Press, Cambridge, UK, 1979). (Cited on page 53.)
- [242] SMARR, L. L. AND YORK, JR., J. W., “Kinematical Conditions in the Construction of Spacetime”, *Phys. Rev. D*, 17(10), 2529–2551, (1978). (Cited on page 53.)
- [243] SMARR, L. L. AND YORK, JR., J. W., “Radiation Gauge in General Relativity”, *Phys. Rev. D*, 17(8), 1945–1956, (1978). (Cited on page 53.)
- [244] SPERHAKE, U., “Binary black-hole evolutions of excision and puncture data”, *Phys. Rev. D*, 76, 104015, (2007). (Cited on pages 63, 121, and 122.)
- [245] SPERHAKE, U., CARDOSO, V., PRETORIUS, F., BERTI, E. AND GONZALEZ, J. A., “The high-energy collision of two black holes”, *Phys. Rev. Lett.*, 101, 161101, (2008). (Cited on page 121.)
- [246] SPERHAKE, U. ET AL., “Eccentric binary black-hole mergers: The transition from inspiral to plunge in general relativity”, *Phys. Rev. D*, 78, 064069, (2008). (Cited on page 121.)
- [247] STUART, A., KEITH ORD, K. AND ARNOLD, S., *Kendall’s Advanced Theory of Statistics, Volume 2A: Classical Inference and and the Linear Model*, (Wiley, 2009), 6 edition. (Cited on page 72.)
- [248] SUZUKI, T. K., NAKASATO, N., BAUMGARDT, H., IBUKIYAMA, A., MAKINO, J. AND EBISUZAKI, T., “Evolution of Collisionally Merged Massive Stars”, *Astrophys. J.*, 668, 435–448, (2007). (Cited on page 139.)
- [249] “TAMA300 detector”. URL (cited on April 13, 2010): <http://tamago.mtk.nao.ac.jp/>. (Cited on page 19.)
- [250] TAYLOR, J. H. AND WEISBERG, J. M., “A new test of general relativity: Gravitational radiation and the binary pulsar PS R 1913+16”, *Astrophys. J.*, 253, 908–920, (1982). (Cited on pages 3 and 31.)
- [251] TEUKOLSKY, S. A., “Rotating black holes: Separable wave equations for gravitational and electromagnetic perturbations”, *Phys. Rev. Lett.*, 29, 1114–1118, (1972). (Cited on page 49.)
- [252] TEUKOLSKY, S. A., “Perturbations of a rotating black hole. 1. Fundamental equations for gravitational electromagnetic and neutrino field perturbations”, *Astrophys. J.*, 185, 635–647, (1973). (Cited on page 86.)
- [253] THORNE, K. S., “Gravitational radiation”, in HAWKING, S. W. AND ISRAEL, W., eds., *Three hundred years of gravitation*, 9, pp. 330–458, (Cambridge University Press, Cambridge, 1987). (Cited on pages 29, 103, 117, and 124.)
- [254] TICHY, W. AND MARRONETTI, P., “The final mass and spin of black hole mergers”, *Phys. Rev. D*, 78, 081501, (2008). (Cited on pages 118 and 122.)
- [255] VAISHNAV, B., HINDER, I., HERRMANN, F. AND SHOEMAKER, D., “Matched Filtering of Numerical Relativity Templates of Spinning Binary Black Holes”, *Phys. Rev. D*, 76, 084020, (2007). (Cited on pages 121 and 122.)

- [256] VAN METER, J. R., BAKER, J. G., KOPPITZ, M. AND CHOI, D.-I., “How to move a black hole without excision: gauge conditions for the numerical evolution of a moving puncture”, *Phys. Rev. D*, 73, 124011, (2006). (Cited on pages 63, 121, and 122.)
- [257] “Virgo detector”. URL (cited on April 13, 2010): <http://www.virgo.infn.it/>. (Cited on pages 18 and 19.)
- [258] VISHVESHWARA, C., “Scattering of gravitational radiation by a Schwarzschild black-hole”, *Nature*, 227, 936–938, (1970). (Cited on page 48.)
- [259] WALD, R. M., *General Relativity*, (University Of Chicago Press, 1984). (Cited on pages 10 and 12.)
- [260] WALTHER, B., BRÜGMANN, B. AND MÜLLER, D., “Numerical black hole initial data with low eccentricity based on post-Newtonian orbital parameters”, *Phys. Rev. D*, 79, 124040, (2009). (Cited on page 74.)
- [261] WEBER, J., “Observation of the Thermal Fluctuations of a Gravitational-Wave Detector”, *Phys. Rev. Lett.*, 17(24), 1228–1230, (1966). (Cited on page 15.)
- [262] WEBER, J., “Evidence for Discovery of Gravitational Radiation”, *Phys. Rev. Lett.*, 22(24), 1320–1324, (1969). (Cited on page 15.)
- [263] WEBER, J., “Anisotropy and Polarization in the Gravitational-Radiation Experiments”, *Phys. Rev. Lett.*, 25(3), 180–184, (1970). (Cited on page 15.)
- [264] WILL, C. M., “On the Rate of Detectability of Intermediate-Mass Black Hole Binaries Using LISA”, *Astrophys. J.*, 611, 1080–1083, (2004). (Cited on page 146.)
- [265] WILLKE, B. ET AL., “The GEO-HF project”, *Class. Quantum Grav.*, 23(8), S207–S214, (2006). (Cited on page 21.)
- [266] YORK, JR., J. W., “Kinematics and Dynamics of General Relativity”, in SMARR, L. L., ed., *Sources of Gravitational Radiation*, pp. 83–126, (Cambridge University Press, Cambridge, UK, 1979). (Cited on page 54.)
- [267] ZERILLI, F., “Gravitational Field of a Particle Falling in a Schwarzschild Geometry Analyzed in Tensor Harmonics”, *Phys. Rev. D*, 2, 2141–2160, (1970). (Cited on page 48.)
- [268] ZERILLI, F. J., “Effective potential for even parity Regge-Wheeler gravitational perturbation equations”, *Phys. Rev. Lett.*, 24, 737–738, (1970). (Cited on page 66.)
- [269] ZLOCHOWER, Y., BAKER, J. G., CAMPANELLI, M. AND LOUSTO, C. O., “Accurate black hole evolutions by fourth-order numerical relativity”, *Phys. Rev. D*, 72, 024021, (2005). (Cited on pages 63, 121, and 122.)

CURRICULUM VITÆ

PERSONAL

Lucía Santamaría Lara
Born on July 23th, 1982 in Burgos, Spain
Nationality: Spanish

EDUCATION

PhD in Physics (2005-2010)
Albert-Einstein-Institut, Potsdam, Germany
Adviser: Prof. Bernard F. Schutz
University affiliation: Mathematisch-Naturwissenschaftliche Fakultät,
Universität Potsdam

Licenciado en Física (MSc in Physics) (2000-2005)
University of Salamanca, Spain

High School with Honors (1998-2000)
Secondary School “Conde Diego Porcelos”, Burgos, Spain

RESEARCH FELLOWSHIPS, GRANTS AND AWARDS

DAAD (German Academic Exchange Service)
Scholarship for graduate studies in Germany (2006/2009)

DAAD (German Academic Exchange Service)
Scholarship for intensive language courses, Goethe Institute
Munich (Autumn 2006)

CERN (European Organization for Nuclear Research)
Research summership, LHCb experiment (Summer 2005)
Adviser: Prof. Clara Matteuzzi

DESY (German Electron Synchrotron)
Research summership, HERMES experiment (Summer 2004)
Adviser: Dr. Ingrid Gregor

Spanish Ministry of Education
Grant for undergraduate research. Department of Optics, Uni-
versity of Salamanca (2004/2005)
Adviser: Prof. Luis Roso

Spanish Ministry of Education
Scholarship for language courses, London (Summer 2003)

Spanish Ministry of Education
Extraordinary Award for High School Studies (June 2000)

SEMINARS AND CONTRIBUTED TALKS

*Black-hole binary coalescence: phenomenological models for non-
precessing systems and astrophysics of intermediate-mass bina-
ries*

Department Seminar, Caltech, CA, USA (02/2010)

Department Seminar, UWM, WI, USA (10/2009)

Department Seminar, RIT, NY, USA (10/2009)

A new phenomenological waveform family for modeling non-precessing spinning black-hole binaries

NRDA09, Potsdam, Germany (07/2009)

8th Edoardo Amaldi Conference on Gravitational Waves, NYC, USA (06/2009)

The NINJA project: preliminary results

Spanish Relativity Meeting ERE08, Salamanca, Spain (09/2008)

Numerical Modeling of Astrophysical Sources of Gravitational Radiation, Valencia, Spain (09/2008)

The NINJA project: an Overview

Department Seminar, University of Columbia, NYC, USA (08/2008)

Searching for numerically-simulated signals with a phenomenological template family

NRDA08, Syracuse, USA (08/2008)

Incorporating Numerical Relativity Waveforms into Gravitational Wave Data Analysis

Pacific Coast Gravity Meeting, UCSB, Santa Barbara, USA (03/2008)

GWDAA12, MIT, Cambridge, USA (12/2007)

Interplay between Numerical Relativity and Gravitational Wave Data Analysis

Workshop, KAVLI Institute for Theoretical Physics, Santa Barbara, USA (01/2008)

Numerical Relativity meets Gravitational Wave Data Analysis

Spanish Relativity Meeting ERE07, Tenerife, Spain (09/2007)

Numerical evolutions of Brillwaves

Spanish Relativity Meeting ERE06, Palma, Spain (09/2006)

PUBLICATIONS

1. L. SANTAMARÍA, F. OHME, P. AJITH, B. BRÜGMANN, N. DORBAND, M. HANNAM, S. HUSA, P. MÖSTA, D. POLLNEY, C. REISSWIG, J. SEILER AND B. KRISHNAN, “Matching post-Newtonian and numerical relativity waveforms: systematic errors and a new phenomenological model for non-precessing black hole binaries,” to be submitted to *Phys. Rev. D*, 2010.
2. P. AMARO-SEOANE AND L. SANTAMARÍA, “Detection of IMBHs with ground-based gravitational wave observatories: A biography of a binary of black holes, from birth to death,” *astro-ph.C0/0910.0254*, 2009.
3. P. AJITH, M. HANNAM, S. HUSA, Y. CHEN, B. BRUEGMANN, N. DORBAND, D. MUELLER, F. OHME, D. POLLNEY, C. REISSWIG, L. SANTAMARÍA AND J. SEILER, ““Complete” gravitational waveforms for black-hole binaries with non-precessing spins,” *gr-qc/0909.2867*, 2009.
4. L. SANTAMARÍA, B. KRISHNAN AND J. T. WHELAN, “Searching for numerically-simulated signals of black hole binaries with a phenomenological template family,” *Class. Quant. Grav.*, vol. 26, p. 114010, 2009.
5. L. CADONATI *ET AL.*, “Status of NINJA: the Numerical INjection Analysis project,” *Class. Quant. Grav.*, vol. 26, no. 11, p. 114008 (13pp), 2009.
6. B. AYLOTT *ET AL.*, “Testing gravitational-wave searches with numerical relativity waveforms: Results from the first Numerical INjection Analysis (NINJA) project,” *Class. Quant. Grav.*, vol. 26, p. 165008, 2009.
7. P. AJITH, S. BABAK, Y. CHEN, M. HEWITSON, B. KRISHNAN, A. M. SINTES, J. T. WHELAN, B. BRÜGMANN, P. DIENER, N. DORBAND, J. GONZALEZ, M. HANNAM, S. HUSA, D. POLLNEY, L. REZZOLLA, L. SANTAMARÍA, U. SPERHAKE AND J. THORNBURG, “A template bank for gravitational waveforms from coalescing binary black holes: I. non-spinning binaries,” *Phys. Rev. D*, vol. 77, p. 104017, 2008.
8. D. A. BROWN, S. FAIRHURST, B. KRISHNAN, R. A. MERCER, R. K. KOPPARAPU, L. SANTAMARÍA AND J. T. WHELAN, “Data formats for numerical relativity waves.” 2007.
9. P. AJITH, S. BABAK, Y. CHEN, M. HEWITSON, B. KRISHNAN, J. T. WHELAN, B. BRÜGMANN, P. DIENER, J. GONZÁLEZ, M. HANNAM, S. HUSA, M. KOPPITZ, D. POLLNEY, L. REZZOLLA, L. SANTAMARÍA, A. M. SINTES, U. SPERHAKE AND J. THORNBURG, “Phenomenological template family for black-hole coalescence waveforms,” *Class. Quantum Grav.*, vol. 24, pp. S689–S699, 2007.

Publications with the LIGO and Virgo Scientific Collaborations

10. J. ABADIE AND OTHERS (THE LIGO SCIENTIFIC COLLABORATION AND THE VIRGO COLLABORATION), “Predictions for the rates of compact binary coalescences observable by ground-based gravitational-wave detectors,” 2010.

11. J. ABADIE AND OTHERS (THE LIGO SCIENTIFIC COLLABORATION AND THE VIRGO COLLABORATION), “Search for gravitational waves from black hole binary inspiral, merger and ringdown,” 2010. In preparation.
12. J. ABADIE *ET AL.* (THE LIGO SCIENTIFIC COLLABORATION), “Search for gravitational-wave inspiral signals associated with short Gamma-Ray Bursts during LIGO’s fifth and Virgo’s first science run,” 2010.
13. B. P. ABBOTT *ET AL.* (THE LIGO SCIENTIFIC COLLABORATION AND THE VIRGO COLLABORATION), “Searches for gravitational waves from known pulsars with S5 LIGO data,” *Astrophys. J.*, vol. 713, pp. 671–685, 2010.
14. B. P. ABBOTT *ET AL.* (THE LIGO SCIENTIFIC COLLABORATION AND THE VIRGO COLLABORATION), “Search for gravitational-wave bursts associated with gamma-ray bursts using data from LIGO Science Run 5 and Virgo Science Run 1,” 2009.
15. B. P. ABBOTT *ET AL.* (THE LIGO SCIENTIFIC COLLABORATION), “Search for Gravitational Waves from Low Mass Compact Binary Coalescence in 186 Days of LIGO’s fifth Science Run,” *Phys. Rev.*, vol. D80, p. 047101, 2009.
16. B. P. ABBOTT *ET AL.* (THE LIGO SCIENTIFIC COLLABORATION), “Einstein@Home search for periodic gravitational waves in early S5 LIGO data,” *Phys. Rev.*, vol. D80, p. 042003, 2009.
17. B. P. ABBOTT *ET AL.* (THE LIGO SCIENTIFIC COLLABORATION), “Search for gravitational wave ringdowns from perturbed black holes in LIGO S4 data,” *Phys. Rev.*, vol. D80, p. 062001, 2009.
18. B. P. ABBOTT *ET AL.* (THE LIGO SCIENTIFIC COLLABORATION), “Search for gravitational-wave bursts in the first year of the fifth LIGO science run,” *Phys. Rev.*, vol. D80, p. 102001, 2009.
19. B. P. ABBOTT *ET AL.* (THE LIGO SCIENTIFIC COLLABORATION), “Stacked Search for Gravitational Waves from the 2006 SGR 1900+14 Storm,” *Astrophys. J.*, vol. 701, pp. L68–L74, 2009.
20. B. P. ABBOTT *ET AL.* (THE LIGO SCIENTIFIC COLLABORATION), “Search for High Frequency Gravitational Wave Bursts in the First Calendar Year of LIGO’s Fifth Science Run,” *Phys. Rev.*, vol. D80, p. 102002, 2009.
21. B. P. ABBOTT *ET AL.* (THE LIGO SCIENTIFIC COLLABORATION), “First LIGO search for gravitational wave bursts from cosmic (super)strings,” *Phys. Rev.*, vol. D80, p. 062002, 2009.
22. B. P. ABBOTT *ET AL.* (THE LIGO SCIENTIFIC COLLABORATION), “Search for Gravitational Waves from Low Mass Binary Coalescences in the First Year of LIGO’s S5 Data,” *Phys. Rev.*, vol. D79, p. 122001, 2009.
23. B. P. ABBOTT *ET AL.* (THE LIGO SCIENTIFIC COLLABORATION AND THE VIRGO COLLABORATION), “An Upper Limit on the Stochastic Gravitational-Wave Background of Cosmological Origin,” *Nature*, vol. 460, p. 990, 2009.

COLOPHON

This thesis was typeset with $\text{\LaTeX} 2_{\epsilon}$ using Robert Slimbach's *Minion* and Hermann Zapf's *Euler* type faces. The figures were produced with the python-based *matplotlib* plotting package and the *Mathematica* software.

Final Version as of April 13, 2010 at 13:36.

